Magnetohydrodynamic Modeling of Space Plasmas with Pressure Anisotropy

by

Xing Meng

A dissertation submitted in partial fulfillment
of the requirements for the degree of
Doctor of Philosophy
(Atmospheric and Space Sciences and Scientific Computing)
in the University of Michigan
2013

Doctoral Committee:

Professor Tamas I. Gombosi, Co-Chair
Research Scientist Gábor Tóth, Co-Chair
Associate Professor Michael W. Liemohn
Professor Kenneth G. Powell
Associate Research Scientist Bartholomeus van der Holst

ACKNOWLEDGEMENTS

This dissertation has been made possible with the help from many people in many ways, whom I would like to acknowledge and thank.

Foremost, I would like to express my deepest gratitude to my research advisors, Prof. Tamas Gombosi and Dr. Gábor Tóth, for guiding me, educating me, supporting me, and encouraging me throughout my graduate study. I am really fortunate to have them as my mentors, and I have enjoyed so much working with them. With their enthusiasm, patience and knowledge, they have shown me how to do good research and how to be a good scientist. It is impossible to count how many things they have taught me, but what I have learned will continuously benefit me in my future career.

I would like to thank the rest of my dissertation committee: Prof. Mike Liemohn, Prof. Kenneth Powell, and Dr. Bart van der Holst, for serving on my committee and their insightful comments. Dr. Bart van der Holst, especially, has worked with me and provided me a lot of help on the anisotropic MHD solar wind model presented in Chapter V.

I would also like to acknowledge my collaborators at Goddard: Dr. Alex Glocer and Dr. Mei-Ching Fok, who have contributed greatly to the development, testing and validation of the coupling between Anisotropic BATS-R-US and the CRCM presented in Chapter IV. I appreciate their kindness and patience in answering my numerous questions during the project.

My thanks go to the rest of professors, scientists, and research fellows in the CSEM group as well, who have helped me through either the courses they taught, or the

useful conversations we had.

I am grateful to the administrative staff in our department, for helping me through a lot of tedious processes, and to the IT support staff, for fixing every issue I have had with my computer.

I would like to thank my officemates and other fellow graduate students in our department, with whom I have had a great time. I also want to thank my friends at Michigan, and those who are not, for accompanying me and supporting me.

Last but not the least, I would like to thank my parents, my grandparents, and the rest of my family, for their love, understanding and spiritual support throughout the years.

TABLE OF CONTENTS

LIST OF FIGURES

Figure

LIST OF TABLES

Table

LIST OF APPENDICES

Appendix

ABSTRACT

Magnetohydrodynamic Modeling of Space Plasmas with Pressure Anisotropy

by

Xing Meng

Co-Chairs: Tamas I. Gombosi and Gábor Tóth

The present generation of global 3D magnetohydrodynamic (MHD) simulations of the Sun-Earth environment is based on the assumption that the plasma pressure is isotropic. This assumption, however, is an inadequate description of space plasmas, such as plasmas in the Earth's magnetosheath and inner magnetosphere, as well as in the solar corona, where strong magnetic fields give rise to highly anisotropic plasma pressures. Specifically, particle collisions are not frequent enough to balance the particle motions along and perpendicular to the magnetic field, thus the corresponding parallel and perpendicular pressure components are different.

This dissertation research, therefore focuses on extending the University of Michigan MHD space physics code BATS-R-US to account for pressure anisotropy. The analytical model is developed by studying the formulation of anisotropic MHD under both classical and semirelativistic approximations, in particular, deriving the dispersion relation and characteristic wave speeds for semirelativistic anisotropic MHD. The software implementation of the new model, Anisotropic BATS-R-US, is verified through numerical tests.

Several applications of Anisotropic BATS-R-US are considered in this work. The

first application is to simulate the quiet time terrestrial magnetosphere and validate the results with satellite measurements. Pressure anisotropy is found to widen the magnetosheath, enhance the nightside plasma pressure, and reduce the flow speed in the magnetotail. In the second application, Anisotropic BATS-R-US is coupled with two ring current models, respectively, to conduct global magnetospheric simulations during geomagnetic disturbed times. The simulation results indicate the importance of pressure anisotropy in controlling the nightside magnetic field topology. Finally, Anisotropic BATS-R-US is applied to simulate the solar corona and heliosphere, in which pressure anisotropy results in faster solar wind speeds close to the Sun. This application has the potential to capture the anisotropic heating mechanism that has not been addressed by isotropic MHD models.

CHAPTER I

Introduction

This chapter contains three parts. In the first part, I present the motivation of this thesis study by reviewing current understandings of the solar-terrestrial environment, particularly the research of pressure anisotropy in space plasmas. In the second part, I introduce the Space Weather Modeling Framework that this dissertation research builds on. In the final part, I overview the content of this dissertation.

1.1 Motivation

1.1.1 The Sun-Earth environment

Although the earliest sightings of the auroras and the application of compasses can be dated back to thousands of years ago, the emergence of the solar-terrestrial physics discipline was not until the eighteenth century, when an instrument maker found that the compass is always in motion, which led to the discovery of the diurnal variation of the geomagnetic field. Since then, especially since the mid-twentieth century when rockets and spacecrafts began to provide opportunities of space exploration, the understanding of the Sun-Earth environment has been advanced significantly.

Today we know that the Sun-Earth environment is a complex and highly-coupled system with various physical processes going on. While not every process is fully understood, the overall picture is clear: the Sun is very dynamic and provides the

major energy source for the physical processes in the solar-terrestrial environment; the interplanetary space between the Sun and the Earth is filled with tenuous magnetized plasma primarily originating from the Sun; This space plasma is called the solar wind, which propagates from the surface of the Sun throughout the solar system; the interaction between the solar wind and the intrinsic magnetic field of the Earth forms the terrestrial magnetosphere; the lower extension of the magnetosphere towards the Earth is the ionosphere, which is also part of the upper atmosphere and contains neutral and ionized particles; the activities on the Sun can cause variations in the solar wind that disturbs the terrestrial magnetosphere and the ionosphere.

This thesis research mainly deals with the terrestrial magnetosphere, and the last part of this research is about the solar corona and the solar wind. Below I present major physics processes and discuss outstanding issues in these regions, with emphasis on the magnetospheric part.

1.1.1.1 The solar corona and the solar wind

The *solar corona* is the uppermost layer of the solar atmosphere. Below it we have the photosphere, the chromosphere, and the transition layer. The most important feature of the solar corona is its very high temperatures of more than 10^6 K, in contrast to about 5800 K in the photosphere. This temperature increase occurs within 500 km, which is very small compared to the solar radius. The problem of how the coronal plasmas are heated in such a short distance has been a hot research topic, but it is still not fully solved. The corona is highly structured. For instance, coronal holes are the dark regions appearing in x-ray observations where open magnetic field configurations dominate; streamers are long-lived regions extending from the base of the corona to several solar radii in the visible view of the corona, and are found to represent closed loops of magnetic field. A schematic plot of the coronal structures is shown in Figure 1.1.

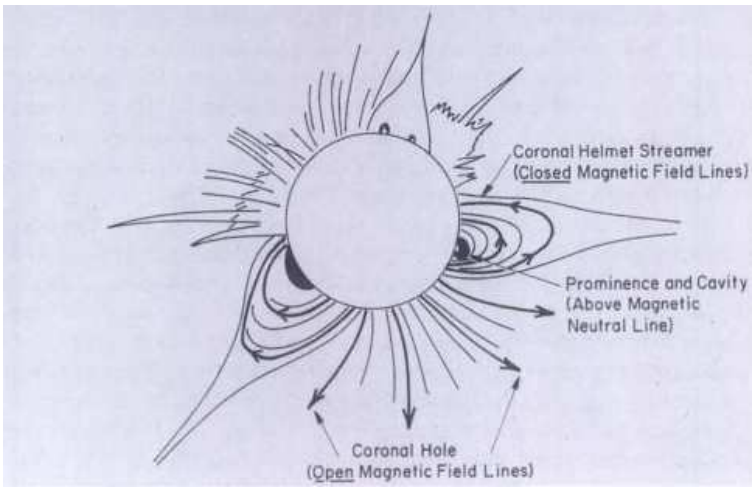

Figure 1.1: An illustration of the solar corona from *Kivelson and Russell* [1995].

The *solar wind* is the extension of the solar corona into the interplanetary space. It starts subsonically at the base of the corona and accelerates to supersonic speeds. There are two types of solar wind with different origins. The solar wind originating from coronal holes with open magnetic field lines is the fast solar wind with speed larger than 600 km/s, while the solar wind originating from the closed magnetic field line regions is the slow solar wind with speed smaller than 350 km/s typically. Although the origin of the fast solar wind is clear, the formation and acceleration of the slow solar wind is still under investigation. The composition of the solar wind plasma is mostly protons and electrons. The solar wind plasma is also magnetized, and the interplanetary magnetic field (IMF) is the extension of the solar magnetic field. The *current sheet* separates the fields and plasma flows from different hemispheres. The region of space influenced by the solar wind is the *heliosphere* extending far beyond the planetary orbits.

The solar corona, and consequently the solar wind have both temporal and spatial variations. The most important long-term variation is due to the *solar cycle*, which has an average period of about 11 years as characterized by the number of sunspots on the solar surface. During a solar cycle, the solar magnetic field changes significantly. Near solar maximum, the solar magnetic field is not dipolelike, and the coronal holes

are restricted to the polar regions; near solar minimum, the solar magnetic field is approximately a dipole, and the coronal holes extend to lower heliographic latitudes. The spatially varying solar corona results in recurring solar wind structures as the Sun rotates. More specifically, faster solar wind streams catch up with slower streams at low heliographic latitudes and leads to the formation of a high-pressure region that separates the fast and slow solar wind regions. This is the *corotating interaction region* (CIR). Short-term solar activities such as *coronal mass ejections* (CMEs) lead to non-recurring variations in the solar wind. During CMEs, large amounts of coronal material with speeds that can reach 2000 km/s are ejected from the Sun to the interplanetary medium. CMEs have been studied intensively, yet their physical origin is not clear.

1.1.1.2 The terrestrial magnetosphere

The intrinsic magnetic field of the Earth can be approximated by a magnetic dipole. The interaction between the solar wind plasma and the geomagnetic dipole field was first studied by *Chapman and Ferraro* [1930], who proposed that the solar wind stream is in effect a highly conducting body, and a current system is generated at the surface of this conducting body as it approaches the terrestrial dipole field. The Chapman-Ferraro model, though too simple to describe the real situation, reveals the fundamental physics behind the solar wind-Earth interaction and establishes the base for later research.

In today's understanding, the interaction between the supermagnetosonic solar wind and the geomagnetic field forms the *magnetosphere*, as displayed in Figure 1.2. The five main current systems that are important in controlling the dynamics of the magnetosphere are shown in Figure 1.3.

The supermagnetosonic solar wind results in the bow shock, which slows down the solar wind ahead of the Earth. The bow shock is a fast shock, and its location is

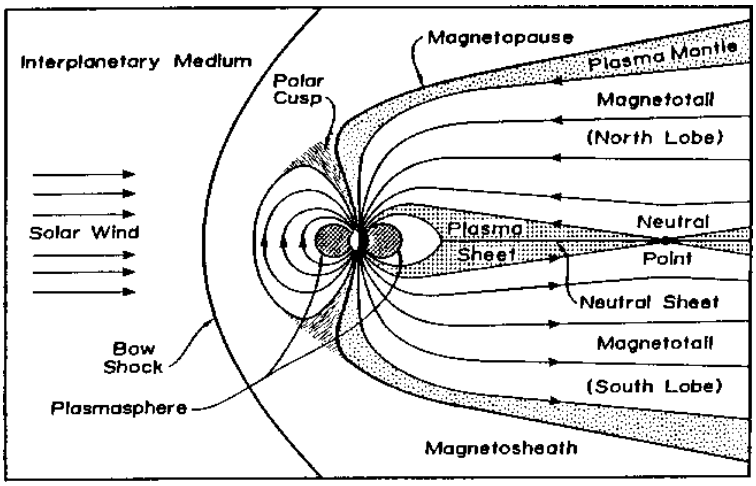

Figure 1.2: A schematic noon-midnight meridian cross section of the terrestrial magnetosphere from *Russell* [1972].

determined by the shape and size of the magnetopause, which is approximately a tangential discontinuity that separates the shocked solar wind from the region dominated by the terrestrial magnetic dipole field. The magnetopause current, also called the Chapman-Ferraro current, flows around the magnetopause and generates a magnetic field that prevents the terrestrial dipole field from penetrating into the solar wind. At the magnetopause, the total pressure of the shocked solar wind is balanced by the total pressure inside of the magnetosheath, thus the position of the magnetopause varies with solar wind conditions. The region between the bow shock and the magnetopause is the magnetosheath, which can extend down to the atmosphere in the two polar cusps. It is filled with compressed and heated solar wind plasmas with stronger magnetic field than in the ambient solar wind. The magnetosheath, together with the bow shock and the magnetopause, form a complex plasma environment, in which many physical processes occur. Those processes that have been heavily studied but not well understood include the dayside magnetic reconnection, energetic particle acceleration, waves and turbulence, plasma instabilities, chaos and fractals, foreshock cavities, hot flow anomalies, dawn-dusk asymmetry, temperature anisotropy, and so on [*Russell*, 1994; *Song and Russell*, 1997; *Pudovkin et al.*, 2002; *Lucek et al.*, 2005].

The effects of pressure anisotropy on this region will be explored in Chapter III.

In the nightside magnetosphere, the magnetic field lines are highly stretched along the solar wind flow direction, and they form the magnetotail. In a simplified scenario, the magnetic field lines reconnect at the neutral line. The center of the magnetotail contains hot and dense plasmas, which is called the plasma sheet. The plasma mantle is the expansion of the magnetosheath plasma as the field lines are convected downward along the magnetotail. The very low density regions between the plasma sheet and the plasma mantle are the two magnetotail lobes. The tail current system relates to the tail magnetic field. It consists of the neutral sheet current pointing from dawn to dusk in the current sheet, which is closed by the tail current pointing from dusk to dawn in the tail magnetosheath. The magnetotail stores the energy in the magnetosphere, and plays an important role during substorms. A lot of research work have been focused on the tail magnetic reconnection, which is probably the most important process in the magneotail and even in the magnetosphere. By now we only have a rough picture of how the tail magnetic reconnection works and incomplete understandings of the reconnection rate, the energy release and conversion, and the contribution to global magnetospheric dynamics. The tail magnetic reconnection rate will be discussed in Chapter III.

The nearly dipolar closed field line region around the Earth is the inner magnetosphere. This region is perhaps the most intensively studied part in the magnetosphere, given the large amount of interesting phenomena there and its direct coupling with the upper atmosphere that could affect human activities. The inner magnetosphere contains the plasmasphere, the ring current, and the radiation belts. The plasmasphere is composed of the coldest particles (eV-energy), mostly hydrogen ions, of the inner magnetosphere. Examples of active research topics include plasmapause formation, plasmasphere refilling and erosion, drainage plumes, and plasmaspheric wind. The ring current is composed of 10 to 200 keV particles that are geomagnetically trapped

between 3 and 6 Earth radii, and it is formed due to the gradient-curvature drift. The drift path of a ring current particle is not necessarily closed due to the convection and corotational electric fields. These electric fields normally point from dawn to dusk near the equatorial plane, and cause the particles drifting sunward. Since the gradient-curvature drift is energy-dependent and proportional to the square of geocentric distance, while the electric drift is independent of particle energy and proportional to the cubic of geocentric distance, at larger geocentric distances and/or for particle with lower energies, the particles are sunward drifting and deflected around the Earth, and form the partial ring current. The ring current is a critical factor during geomagnetic storms. The strength of the ring current affects the magnetic field on the surface of the Earth, which is characterized by the Dst index. Numerous work on the ring current have been carried out [*Daglis et al.*, 1999; *Daglis*, 2001, 2006], and major open disputes are the mass driver for strong current, the role of oxygen ions, the contribution from electrons, the large-scale morphology, the efficiency of charge exchange, and the effects of wave scattering. In Chapter IV I will investigate the ring current dynamics affected by ion temperature anisotropy. The radiation belt contains relativistic electrons and very energetic ions of MeV energies, and is also a hot research area especially after the recent discovery by the Radiation Belt Storm Probe that reveals a previously unknown radiation region [*Baker et al.*, 2013].

The remaining two current systems connect the magnetosphere with the ionosphere and thus important in the magnetosphere-ionosphere coupling. The field-aligned currents, also called Birkeland currents, consist of Region 1 currents flowing outward from the ionosphere to the magnetosphere, and Region 2 currents flowing in the opposite direction. The field-aligned currents are closed by the partial ring current in the low latitude magnetosphere, therefore the strength of the field-aligned currents is related to the strength of the nightside equatorial plasma pressure in the inner magnetosphere. This will be demonstrated in Chapter IV. The last current sys-

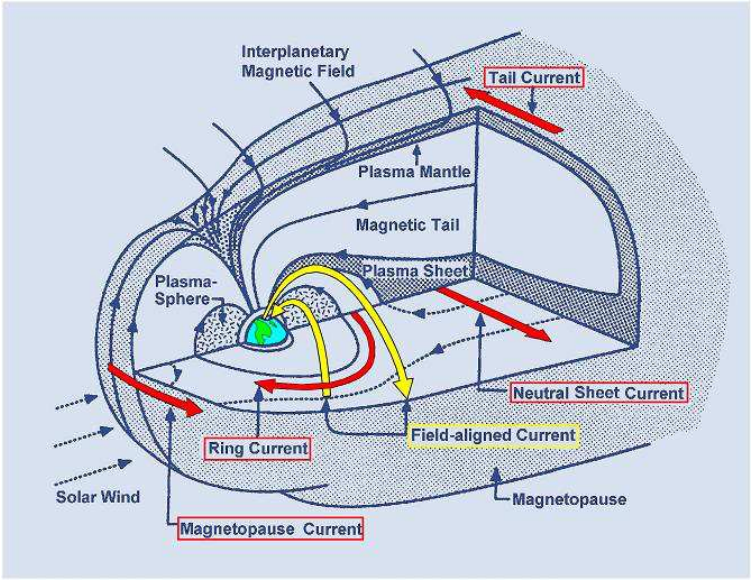

Figure 1.3: An illustration of the current systems in the terrestrial magnetosphere, from *Russell et al.* [1995].

tem, the ionospheric currents (Hall and Pedersen currents, not shown in the figure), close the field-aligned currents in the polar ionosphere.

The solar wind-magnetosphere-ionosphere coupling leads to several types of geomagnetic activities. The best understood one is the *quiet time diurnal variation*, which refers to systematic variations in each magnetic field component measured in midlatitude ground-based magnetometers on geomagnetic quiet days. This variation is essentially due to the Hall currents in the ionosphere.

Variations in the solar wind can cause large and prolonged disturbances of the magnetosphere, and lead to another type of geomagnetic activity, *geomagnetic storms*. Geomagnetic storms relate closely to solar activities, and many of them follow solar flares or coronal mass ejections (CMEs). A typical geomagnetic storm event begins with a sudden compression of the magnetosphere, causing the magnetopause current to increase. Then several hours of southward IMF enhances the dayside magnetic reconnection between the solar wind magnetic field and the geomagnetic field, which increases the penetration of the solar wind motional electric field into the magne-

tosphere. Consequently, the magnetospheric convection increases. The strengthened duskward electric field increases the number of particles injected into the ring current. Thus the ring current increases, and the horizontal component of the surface magnetic field decreases. In the ionosphere, increased precipitation of charged particles from the magnetosphere can result in variations in the electric current systems and lead to aurora activity. As soon as the southward IMF weakens, the reconnection rate decreases, which weakens the electric fields and consequently the particle injection into the ring current. As a result, the ring current starts to decay. The recovery of a storm can last for several days. Therefore, during geomagnetic storms, the energy input from the solar wind is deposited into the magnetosphere and dissipates in the magnetosphere-ionosphere system. During large geomagnetic storms, *magnetospheric substorms* often develop.

Substorms belong to a different type of geomagnetic activity, and refer to time periods of enhanced energy input from the solar wind into the magnetosphere and the subsequent energy dissipation processes in the magnetosphere. Comparing to storms, substorms usually have much shorter durations of several hours. A typical substorm follows the growth phase, expansion phase, and the recovery phase. During substorms, auroral activities increase, and the ionospheric currents enhance.

There are a lot of open questions regarding geomagnetic storms and especially substorms. For example, the differences between storms caused by various sources, the relation between storms and substorms, the trigger of substorms, and the substorm timing are not clear. I will analyze two particular storm/substorm events in Chapter IV.

The modern development of the solar-terrestrial physics led to the emergence of a new term *space weather* in 1990s. The conditions on the Sun determine the conditions in the solar wind, which impact the conditions in the terrestrial magnetosphere, and

furthermore, the ionosphere and the thermosphere. These conditions can influence the performance of space-borne and ground-based technological systems or can endanger human life or health, and are referred to as space weather.

Space weather can impact telecommunication systems operating on the ground and in space, power grids and oil pipelines, satellite operations, global navigation satellite systems, airplane radios, and the health of astronauts, airplane crews and passengers. As human activities rely more and more on the technology systems that could be affected by space weather, the study of the solar-terrestrial environment, especially the development of predictive space weather models, has become important.

Currently our knowledge of the solar-terrestrial environment has achieved an unprecedented high level. We have a physical explanation, sometimes more than one interpretations, for almost every phenomenon observed. However, what we know is far from complete, and there are still lots of unknowns or debates that mostly relate to the details of some physical processes as mentioned earlier. One such question is about the pressure anisotropy of space plasmas.

1.1.2 Pressure anisotropy of space plasmas

1.1.2.1 What is pressure anisotropy?

Pressure anisotropy, or alternatively, temperature anisotropy, refers to different thermal pressures/temperatures perpendicular and parallel to the magnetic field. Pressure anisotropy arises naturally in a low density magnetized plasma, where the gyration and the field-aligned motion of the particles are not coupled by collisions. The magnetic field provides the preferred orientation, while particle collisions tend to drive the plasma towards isotropy by evenly distributing the parallel and perpendicular momenta with respect to the magnetic field. Without enough collisions, the parallel and perpendicular pressures can be different. Space plasmas, our primary interest, are basically collisionless, which means that pressure anisotropy could play

an important role. In fact, a large amount of in-situ and remote observational data has shown plasma pressure or temperature anisotropy in the solar corona [*Kohl et al.*, 1998, 2006; *Li et al.*, 1998; *Antonucci et al.*, 2000; *Telloni et al.*, 2007] and the solar wind [*Hundhausen*, 1968; *Feldman et al.*, 1974; *Marsch et al.*, 1982, 2004; *Gary et al.*, 2001, 2002; *Kasper et al.*, 2003; *Hellinger et al.*, 2006], as well as in the magnetosheath [*Crooker et al.*, 1976; *Phan et al.*, 1994], the ring current region [*Lui and Hamilton*, 1992; *De Michelis et al.*, 1999], and the magnetotail [*DeCoster and Frank*, 1979; *Takahashi and E. W. Hones*, 1988] of the Earth's magnetosphere.

In the presence of pressure anisotropy, plasma pressure can be expressed by a tensor as [*Chew et al.*, 1956; *Gombosi*, 1991]

$$\mathbf{P} = p_{\perp}\mathbf{I} + (p_{\parallel} - p_{\perp})\mathbf{bb} \tag{1.1}$$

where $\mathbf{I}$ is the identity tensor and $\mathbf{b} = \mathbf{B}/|\mathbf{B}|$ is the unit vector along the magnetic field $\mathbf{B}$. $p_{\parallel}$ and $p_{\perp}$ describe the parallel and perpendicular thermal pressure components with respect to the magnetic field. Equation (1.1) is a generalized expression for anisotropic pressure, and thus valid for both ions and electrons. In real space plasmas, electron pressure anisotropy is much less important than ion pressure anisotropy, since electrons respond to perturbations much more rapidly than ions due to their small mass, as a result their momentum distribution tends to be less anisotropic than ions'.

The difference between parallel and perpendicular pressures cannot be arbitrarily large, because it is bounded by plasma instabilities. In space plasmas, ion pressure anisotropy can cause several types of instabilities, including the firehose, mirror, ion-cyclotron and Harris instabilities [*Chandrasekhar et al.*, 1958; *Barnes*, 1966; *Kennel and Petschek*, 1966; *Soper and Harris*, 1965; *Gary*, 1976]. The first three instabilities are related to anisotropic ion pressure only, while the Harris instability is also related to anisotropic electron pressure, and it is not considered in this dissertation study.

The firehose instability can be viewed as an analogue of the violent motion of a firehose with water flowing through rapidly. It arises when the ion parallel pressure is sufficiently large that a small perturbation perpendicular to the magnetic field grows. The mirror instability occurs when the ion perpendicular pressure gets too large, and part of the particles are trapped in small magnetic "mirrors" formed by the perturbed magnetic field. A typical observational feature is the anti-phased variations in the magnetic field strength and the plasma number density. The ion cyclotron instability is also driven by the too large ion perpendicular pressure. It is a resonant instability that occurs when the electric field vector of the ion cyclotron wave rotates synchronously with the particle gyration.

1.1.2.2 Modeling space plasmas with anisotropic pressure

Though being observed frequently, the role of the pressure anisotropy in space plasmas is not fully understood. To address this issue, numerical modeling has been carried out in the past few decades. In particular, for the solar wind and the terrestrial magnetosphere, where our primary research interest lies, empirical and/or physics-based models have been developed to account for pressure anisotropy.

For solar wind modeling, proton temperature anisotropy has been included in several MHD models. The earliest work can be dated back to about forty years ago. *Leer and Axford* [1972] developed a one-dimensional (1D) steady state solar wind model with isotropic electron temperature and anisotropic proton temperature that allows for extended coronal proton-heating. The model itself does not solve for the magnetic field, but the solar wind solutions are obtained for the cases of a purely radial and a spiral magnetic field, and the solutions at 1 AU are reasonable. At about the same time, *Whang* [1972] also developed a 1D steady state solar wind model including proton thermal anisotropy, which assumes the same isotropic temperature for electrons and protons within a radial distance of 0.4 AU, while different temper-

atures for electrons and protons, as well as proton temperature anisotropy beyond 0.4 AU. The calculated solar wind solution at 1 AU agrees well with observations. Both models are pioneers in simulating proton temperature anisotropy in the solar wind.

More work has been done after 1990s. *Hu et al.* [1997] presented a 1D time-dependent fast solar wind model with isotropic electron temperature and anisotropic proton temperature. The model includes momentum and heat input to the solar wind by Alfvén waves, additional momentum input to the protons, and additional heat input to both electrons and protons. The high-speed solar wind solutions they obtained match most of the empirical constraints from observations. This model was further extended to solve the 16-moment bi-Maxwellian equations by *Li* [1999], who has found that the inclusion of proton parallel and perpendicular heat flux densities greatly affect proton temperature anisotropy. More recently, *Li et al.* [2004] reported the first 2D Alfvén wave turbulence-driven solar wind model with proton temperature anisotropy. They obtained solutions for both fast and slow solar wind, and found that the average proton temperature in the anisotropic case is lower than in the isotropic case. *Chandran et al.* [2011] developed a 1D solar wind model including proton temperature anisotropy, pitch-angle scattering from mirror and firehose instabilities, and kinetic Alfvén wave turbulence, based on theories of linear wave damping and nonlinear stochastic heating. They have found consistency between their model results and a number of measurements. All these studies provide valuable understanding to the modeling of solar wind with anisotropic proton temperature. However, these 1D or 2D models still cannot reveal the complete picture of the spatially and temporally varying solar wind, which could only be provided by time-dependent 3D global models of the corona and heliosphere.

For terrestrial magnetospheric modeling, pressure anisotropy has been investigated with empirical, equilibrium and MHD models, all of which are major branches

of magnetospheric modeling techniques. One widely used empirical model is the Tsyganenko geomagnetic field model, based on which several studies considered anisotropic pressure. For instance, *Horton et al.* [1993] derived the plasma pressure tensors from the Tsyganenko models; *Lui et al.* [1994] obtained the perpendicular and parallel pressure distributions in force equilibrium with magnetic stresses from the Tsyganenko models for the quiet time nightside magnetosphere, and found the deduced pressure profiles are in good agreement with observations.

Equilibrium modeling has also been adopted to address pressure anisotropy. *Cheng* [1992a] obtained self-consistent magnetospheric equilibria with anisotropic pressure by solving the inverse equilibrium equation. *Zaharia et al.* [2004] computed 3D force-balanced magnetospheric configurations with their 3D equilibrium code and applied them to magnetic storm simulations. *Wu et al.* [2009] extended a friction code equilibrium solver to include pressure anisotropy. These studies provide very interesting insight of how anisotropic pressures modify the magnetic field and current configuration in the inner magnetosphere. Yet the equilibrium modeling relies on empirical models of the pressure distribution as initial inputs, thus it is not as self-consistent as MHD modeling.

Since no global magnetospheric MHD model capturing pressure anisotropy has been developed (to our knowledge), MHD modeling with anisotropic pressure has been focused on localized models. A heavily studied topic is the anisotropic MHD modeling of the magnetosheath. *Erkaev et al.* [1999] presented a 3D steady state MHD model of the magnetosheath flow near the subsolar line with anisotropic pressure. *Denton and Lyon* [2000] studied the effects of pressure anisotropy using a 2D fluid model of the magnetosheath. More recently, *Samsonov et al.* [2007] validated their 3D anisotropic MHD model of the magnetosheath by comparing the model results to Cluster data. The magnetotail has also been simulated with a 3D anisotropic MHD model by *Hesse and Birn* [1992]. These regional MHD models significantly

contribute to the numerical modeling of magnetospheric plasmas with anisotropic pressure, however they cannot reveal the global impacts of pressure anisotropy.

The above review of past studies implies the lack of 3D global MHD models that can resolve plasma pressure anisotropy for both the solar wind and terrestrial magnetosphere. In other words, the 3D global MHD models of the solar wind and the magnetosphere have been assuming isotropic plasma pressure so far. More advanced models are needed to represent the real space plasmas where pressure anisotropy could arise, which would be not only a new tool to study the effects of pressure anisotropy in the solar-terrestrial environment, but also a step forward towards better space weather prediction models. This motivates the development of a 3D global anisotropic MHD model, Anisotropic BATS-R-US, which is the fundamental code modification task of this dissertation research.

1.2 Technique

The present research tools for studying the Sun-Earth environment range from remote-sensing to in-situ observations, and from plasma theories to computational models. These techniques have different strengths and weaknesses, and thus can complement each other to provide better understanding of the physical processes that we are interested in. Observations directly supply the plasma data of the space environment, which can validate theoretical and computational models, but the observational data are often largely limited by the locations of the satellites, the time of the measurements, and the accuracy of the instruments. The theoretical approach is the most rigorous way to understand the phenomena that we observe, yet the correctness of theoretical space plasma models relies on the support from observational data. The computational modeling of the space environment can provide complete pictures of the dynamics of space plasmas and can be predictive. However, the numerical models are usually developed based on theoretical models, and are validated against

actual measurements. In this dissertation research, the major tool used is numerical modeling, while the other two approaches are also applied as supplements. More specifically, I first develop an analytical model, upon which I build a computational model, which is then validated through observational data.

This dissertation research is conducted with the Space Weather Modeling Framework developed at the University of Michigan. This is a software framework that uses different models for different domains of the solar-terrestrial system to account for disparate temporal and spatial scales on the Sun, in the heliosphere, and in the magnetosphere.

1.2.1 The Space Weather Modeling Framework

The Space Weather Modeling Framework (SWMF) [*Tóth et al.*, 2005, 2012] is a highly integrated toolkit of various numerical models for the solar-terrestrial space. It contains several components corresponding to different physics domains from the Sun to the Earth, and each component is represented by one or more physics models with appropriate wrappers and couplers. The components, or more typically, a subset of the components, can be compiled and linked to the core of the framework to form a single executable, or the components can be compiled into individual executables and used as stand-alone models.

The current components of the SWMF are described as follows: the Eruptive Event (EE) generator is responsible for creating a CME; the Solar Corona (SC) describes the corona out to about 25 solar radii; the Inner Heliosphere (IH) extends from about 20 solar radii to the orbit of the Earth and has been extended to 30 AU; the Outer Heliosphere (OH) extends from about 30 AU to 1000 AU; the Solar Energetic Particle (SP) domain consists of one or more field lines along which the energetic particles accelerate and diffuse; the Global Magnetosphere (GM) domain surrounds the Earth and extends to about 30 Earth radii on the dayside, a few hundred Earth

	Component name	ID	Physics-based / empirical models
1.	Eruptive Event Generator	EE	BATS-R-US / breakout, flux-rope
2.	Solar Corona	SC	BATS-R-US
3.	Inner Heliosphere	IH	BATS-R-US
4.	Outer Heliosphere	OH	BATS-R-US
5.	Solar Energetic Particles	SP	Kota, FLAMPA
6.	Global Magnetosphere	GM	BATS-R-US / Tsyganenko
7.	Inner Magnetosphere	IM	RCM, CRCM, HEIDI, RAM-SCB
8.	Radiation Belt	RB	RBE
9.	Polar Wind	PW	PWOM
10.	Ionosphere Electrodynamics	IE	RIM / Weimer
11.	Upper Atmosphere	UA	GITM / MSIS, IRI

Table 1.1: Physics-based and empirical models of the SWMF [*Tóth et al.*, 2012].

radii on the nightside, and about 60-100 Earth radii in the orthogonal directions; the Inner Magnetosphere (IM) models the closed field line region around the Earth; the Radiation Belt (RB) has the same domain as IM but it models the relativistic electrons; the Polar Wind (PW) models the open field line region near the Earth; the Ionospheric Electrodynamics (IE) model is a two dimensional spherical surface at a nominal ionospheric altitude; the Upper Atmosphere (UA) contains the thermosphere and the ionosphere from around 90 km to 600 km altitude for the Earth. A few more components are under development, for instance the Plasmasphere (PS). The SWMF components are listed in Table 1.1. As the table shows, several components can be represented by the BATS-R-US model [*Powell et al.*, 1999; *Gombosi et al.*, 2004], which is also the most computationally expensive model in the SWMF.

1.2.2 The BATS-R-US MHD model

The magnetohydrodynamics (MHD) description of magnetized plasmas has been widely used in many applications by both the modeling and theoretical communities. Most space plasmas can be well approximated by MHD. This motivated the development of the Block-Adaptive Tree Solarwind Roe-type Upwind Scheme (BATS-R-US) as the core model of the SWMF, which is a three-dimensional (3D) MHD model that

solves a variety of MHD equation sets, including ideal MHD, semirelativistic MHD, Hall MHD, multi-species MHD, multi-fluid MHD, and MHD with Alfvén wave heating and electron thermal heat conduction. These different types of MHD approximations are based on different assumptions and simplifications, and can be applied to simulate space plasmas according to locations and physical processes of interest.

BATS-R-US uses a block-adaptive grid with either Cartesian or generalized coordinates including spherical and cylindrical grids. Each block has the same number of cells, but the blocks can have different sizes in terms of the volume of physical space that they occupy. The block-based Adaptive Mesh Refinement (AMR) algorithm allows different grid resolutions at different locations in the computational domain. Starting with an initial mesh consisting of blocks of equal size, selected blocks are divided or coarsened according to regions of interest. For a 3D grid that the original AMR algorithm was designed for, the refinement of a block results in eight equal-sized "children" blocks, while the coarsening process merges eight "children" blocks into a single block, thus the grid resolution is increased or reduced by a factor of 2. The recent development of the Block-Adaptive Tree Library (BATL) [*Tóth et al.*, 2012] generalizes the AMR algorithm to a 1, 2, or 3 dimensional grid, which greatly extends the capabilities of BATS-R-US.

BATS-R-US has various options for spatial and temporal discretization schemes. The spatial discretization in BATS-R-US is based on a finite volume discretization of the MHD equations with up to fifth order accurate slope limiters. Available numerical flux functions include the Rusanov or local Lax-Friedrichs [*Rusanov*, 1961], HLLE [*Harten et al.*, 1983], Artificial Wind [*Sokolov et al.*, 2002], HLLD [*Miyoshi and Kusano*, 2005], Roe [*Roe*, 1981] and Godunov [*Godunov*, 1959] fluxes. BATS-R-US can use local time stepping or time accurate mode. The local time stepping is usually used to solve steady state problems, and the steady state solution is often used as an initial condition for a time accurate simulation. In time accurate simulations, various time

stepping schemes are available, including the explicit, point-implicit, semi-implicit, and fully implicit schemes, as well as the explicit/implicit scheme [*Tóth et al.*, 2006] that can advance some of the blocks explicitly, while the rest of the blocks implicitly.

1.2.3 Coronal and heliospheric simulations

One important application of the SWMF is to perform coronal and inner heliospheric simulations with the SC and IH components. We can run the SC component in stand-alone mode to simulate the solar corona, or run the coupled SC-IH components to simulate the solar wind and the IMF solution in the inner heliosphere. When CMEs are modeled, the EE component is also required to initialize them.

Being represented by BATS-R-US, the SC component contains several coronal MHD models that have been or are being developed: semi-empirical MHD [*Cohen et al.*, 2007], two-temperature (proton and electron) MHD with Alfvén wave heating [*van der Holst et al.*, 2010], MHD with Alfvén wave turbulence heating [*Sokolov et al.*, 2013], and so on. Although any one of these models can be and have been used to describe the corona, newer models are preferred as they contain more physics and rely less on empirical models and tunable parameters. The SC component can use the Cartesian or spherical coordinate system in the Heliographic Rotating (HGR) frame. The inner boundary of SC is usually driven by the density, pressure, velocity, magnetic field, and for newer models, also Alfvén wave energy density defined just above the photosphere. The temperature and mass density at the inner boundary may vary with longitude and latitude to achieve the most realistic solar wind near the Sun and further out. The velocity components at the inner boundary should maintain line-tying of the magnetic field. The magnetic field at the inner boundary may be obtained from synoptic magnetograms, or a simple dipole (possibly with a few higher order terms) may be assumed. The outer boundary of SC is well beyond the sonic point of the solar wind, and the flow at the outer boundary is usually faster than

the fast magnetosonic speed of the plasma, so no information is propagating inward. Sometimes, however, when a CME passes the outer boundary of SC, the solar wind speed may become subfast for short periods of time. During such periods, the SC component needs to receive the outer boundary condition from the IH component.

The IH component is also represented by BATS-R-US, more specifically, ideal single-fluid MHD or two-temperature MHD models. It usually uses Cartesian coordinates in the Heliographic Inertial (HGI) or HGR frame (the rotating frame only works out to about 1 AU). IH obtains its inner boundary conditions from SC. The flow at the outer boundary of IH is always superfast. The IH component provides the outer boundary conditions for the SC component when the flow at the outer boundary of SC is not superfast, as mentioned before. IH can also provide the upstream boundary conditions for the GM component that is used for Sun-to-Earth SWMF simulations.

The domain of the EE component is embedded in SC, and it is responsible for creating a CME. The EE component can be represented by either a physics-based model of flux emergence from the convection zone, or by much simpler, and less expensive empirical models that insert an unstable flux rope into the steady solar corona solution, or insert an arcade and apply shearing motion at the lower boundary of the corona model. EE provides boundary and/or initial conditions for SC.

For quiet time periods without CMEs, assuming the corona condition does not change much during one or more Carrington rotations, we typically run SC or SC-IH in steady state mode to achieve a steady coronal and heliospheric solution for a whole Carrington rotation. For time periods with CMEs, we need to run coupled EE-SC-IH simulations in time accurate mode, so that the propagation of the CME is tracked and the CME arrival at the Earth is captured.

1.2.4 Global magnetospheric simulations

Another important application of the SWMF is planetary magnetospheric modeling with primarily the GM component. In particular, for Earth's magnetospheric simulations, the GM component is basically represented by BATS-R-US. Similar to SC and IH, there are several options of MHD equation sets that BATS-R-US solves, from ideal MHD to multifluid MHD, as mentioned in section 1.2.2. The GM component can use Geocentric Solar Magnetic (GSM) or Geocentric Solar Ecliptic (GSE) coordinate system, and a Cartesian or spherical mesh. The upstream boundary conditions are obtained from the IH component or from satellite measurements. At the other outer boundaries one can usually assume zero gradient for the plasma variables since these boundaries are far enough from the Earth to have no significant effect on the dynamics near the Earth. The inner boundary of GM is a spherical surface usually at 2 to 3 Earth radii from the center of the Earth.

The GM component can run in stand-alone mode, but more typically it is coupled with the IE component for terrestrial magnetospheric simulations. In the current version of the SWMF, the IE component is represented by the Ridley Ionosphere Model (RIM) [*Ridley et al.*, 2004], which is an electric potential solver on a two-dimensional (2D) spherical surface at around 110 km above the surface of the Earth. IE obtains the field-aligned currents from GM to generate an auroral precipitation pattern, which is then used with the solar illumination to calculate Hall and Pedersen conductances. The IE component provides the electric potential to the GM component, which is used by GM to calculate the electric field and the corresponding plasma velocities as the inner boundary condition of GM.

Given that MHD is not appropriate in describing the inner magnetospheric dynamics that is characterized by particles with energies in the order of keV or even MeV, the IM component of the SWMF is also required to couple with the GM and IE components, especially for simulating the magnetosphere during geomagnetic dis-

turbed times. The IM component solves equations describing the motion of keV-energy ions and electrons in the closed field line region, which contribute to the ring current, and can be represented by several kinetic models as shown in Table 1.1. IM obtains the geometrical and plasma information about the closed field lines from GM and the electric potential solution from IE, while it provides the density and pressure corrections along the closed field lines to GM.

For standard global magnetospheric simulations, the coupled GM-IE model is run in steady state mode for a few thousand iterations until the magnetospheric solution reaches an approximate steady state. Then GM-IE is switched to time accurate mode, and if necessary, coupled with IM, thus the solution advances with time.

1.3 Dissertation Outline

For this dissertation research, my work includes analytical model development, software implementation and science applications of Anisotropic BATS-R-US, an extension of the standard BATS-R-US MHD model including pressure anisotropy [*Meng et al.*, 2012a,b].

The development of the analytical model starts from studying the formulation of anisotropic MHD to obtain the appropriate set of equations that is both physically adequate to describe plasmas with pressure anisotropy and computationally inexpensive to perform large-scale 3D simulations. Both the non-conservative/conservative form and classical/semirelativistic form of the equation set are investigated to take care of different situations. To calculate characteristic wave speeds that are needed by numerical fluxes, I solve the eigenvalue problem of the characteristic matrix for the equation set. Deriving formulas for the instabilities are a substantial part of the work. During the software implementation, the anisotropic MHD equations are discretized in various temporal and spatial schemes and implemented into the BATS-R-US code. To verify Anisotropic BATS-R-US, a large set of numerical tests are designed and

carried out.

Anisotropic BATS-R-US has many potential applications, and several of them are considered in this thesis work. First, Anisotropic BATS-R-US is applied to terrestrial magnetospheric simulations. I perform quiet time magnetospheric simulations with Anisotropic BATS-R-US and compare the results with satellite measurements across the magnetosheath and magnetotail. This also serves as validation tests for Anisotropic BATS-R-US. To better represent the inner magnetosphere where MHD description is not appropriate, especially during geomagnetic disturbed time, I couple Anisotropic BATS-R-US with inner magnetospheric kinetic models. The coupled models are applied to simulate geomagnetic storms, and the results are validated through comparisons with satellite and ground based magnetometer observations in the near-Earth magnetosphere.

Second, Anisotropic BATS-R-US is applied to coronal and heliospheric modeling. I perform idealized coronal simulations and compare the results with previous 1D and 2D modeling results. Real Carrington rotation simulations are also carried out, with comparisons to satellite observations at various locations in the heliosphere. This part of work is still undergoing, thus the results presented in this dissertation are preliminary.

The rest of the dissertation is organized as follows. Chapter II presents the development and implementation of Anisotropic BATS-R-US. Chapter III describes the quiet time magnetospheric simulations performed with Anisotropic BATS-R-US. Chapter IV describes the coupling between Anisotropic BATS-R-US and inner magnetospheric models, as well as the geomagnetic storm simulations performed with the coupled models. Chapter V applies Anisotropic BATS-R-US to solar wind simulations. Chapter VI concludes the dissertation and proposes future work. The contents of Chapter II and III are published in *Meng et al.* [2012a] and *Meng et al.* [2012b], respectively, while the content of Chapter IV has been submitted to the Journal of

Geophysical Research.

CHAPTER II

The Development of Anisotropic BATS-R-US

MHD with anisotropic pressure was first investigated by *Chew et al.* [1956]. They start from the Boltzmann equation and obtain the Chew-Goldberger-Low (CGL) approximation, also known as the double-adiabatic model, which is valid for single-fluid collisionless plasma with strong magnetic field and neglects the pressure transport along magnetic field lines. Later on *Hau and Sonnerup* [1993] and *Hau et al.* [1993] proposed the double-polytropic model as a more generalized description, which recovers the CGL model as a limiting case. We derive our transport equations by taking the moments of the generalized kinetic equation presented by *Gombosi and Rasmussen* [1991]. We include the electron pressure as well, which is assumed to be isotropic.

As an important extension to the classical (non-relativistic) case, we also study and implement the semirelativistic formulation. The semirelativistic approximation assumes that the plasma flow speed and the sound speed are nonrelativistic, while the Alfvén speed is relativistic. This is applicable for the case when the classical Alfvén speed is comparable or even larger than the speed of light, for example in Jupiter's and Saturn's magnetospheres due to strong planetary magnetic fields. For problems with moderate Alfvén speeds, the semirelativistic form of the MHD equations is still useful because it allows larger explicit time steps and reduces the numerical diffusion for some schemes [*Tóth et al.*, 2011] by artificially reducing the speed of light,

which is known as the "Boris correction" in the space plasma modeling community [*Boris*, 1970]. For single-fluid ideal MHD, the semirelativistic equation set as well as characteristic waves were presented in *Gombosi et al.* [2002].

This chapter first presents the MHD equations for both classical and semirelativistic cases with anisotropic ion pressure and isotropic electron pressure in Section 2.1. Then in Section 2.2 the characteristic waves are explored for the semirelativistic approximation. The classical case and the case without electron pressure are also obtained. Section 2.3 describes the implementation of Anisotropic BATS-R-US. In section 2.4, we present verification tests for Anisotropic BATS-R-US. Section 2.5 contains the summary for Chapter II.

2.1 Equations

According to equation (1.1), with anisotropic ion pressure and isotropic electron pressure, the pressure tensor can be written as

$$\mathbf{P} = (p_\perp + p_e)\mathbf{I} + (p_\parallel - p_\perp)\mathbf{bb} \tag{2.1}$$

where p_e denotes electron pressure, and $p_\parallel$ and $p_\perp$ represent the parallel and perpendicular ion pressures. The average ion scalar pressure thus can be expressed as

$$p = \frac{2p_\perp + p_\parallel}{3} \tag{2.2}$$

which is the trace of the ion pressure tensor divided by 3.

2.1.1 Non-relativistic equations

We start with the equation set for non-relativistic MHD in the primitive-variable form

$$\frac{\partial \rho}{\partial t} + (\mathbf{u}\cdot\nabla)\rho + \rho(\nabla\cdot\mathbf{u}) = 0 \tag{2.3}$$

$$\rho\frac{\partial \mathbf{u}}{\partial t} + \rho(\mathbf{u}\cdot\nabla)\mathbf{u} + \nabla(p_\perp + p_e) + \nabla\cdot\left[(p_\parallel - p_\perp)\mathbf{bb}\right] + \frac{1}{\mu_0}\mathbf{B}\times(\nabla\times\mathbf{B}) = 0 \tag{2.4}$$

$$\frac{\partial \mathbf{B}}{\partial t} + \nabla\times[-(\mathbf{u}\times\mathbf{B})] = 0 \tag{2.5}$$

$$\frac{\partial p_\parallel}{\partial t} + (\mathbf{u}\cdot\nabla)p_\parallel + p_\parallel(\nabla\cdot\mathbf{u}) + 2p_\parallel\mathbf{b}\cdot(\mathbf{b}\cdot\nabla)\mathbf{u} = 0 \tag{2.6}$$

$$\frac{\partial p_\perp}{\partial t} + (\mathbf{u}\cdot\nabla)p_\perp + 2p_\perp(\nabla\cdot\mathbf{u}) - p_\perp\mathbf{b}\cdot(\mathbf{b}\cdot\nabla)\mathbf{u} = 0 \tag{2.7}$$

$$\frac{\partial p_e}{\partial t} + (\mathbf{u}\cdot\nabla)p_e + \frac{5}{3}p_e(\nabla\cdot\mathbf{u}) = 0 \tag{2.8}$$

where ρ and $\mathbf{u}$ represent the density and velocity, μ_0 is the permeability of vacuum, and the polytropic index is taken to be 5/3. Note that we assume that the ion and electron velocities are equal, thus we do not consider Hall MHD for this study. Also, the collision terms which describe the interactions between ions and electrons as well as wave scatterings are all neglected. Therefore, we are dealing with an "ideal" three-temperature MHD approximation, i.e., considering the ion parallel pressure, ion perpendicular pressure and electron pressure separately.

Compared to the isotropic MHD equations, the continuity equation (2.3) and the induction equation (2.5) remain the same. The momentum equation (2.4) contains the pressure tensor (2.1) instead of the scalar pressure in the isotropic case. The ion pressure components have their individual evolution equations (2.6) and (2.7). In the absence of collision terms, the ratio between the two pressure components might achieve unrealistic values. When implementing the equations into BATS-R-US, we add a relaxation term to the right-hand-sides of (2.6) and (2.7) to limit the

ion pressure anisotropy to the range allowed by the various instabilities. This will be discussed later.

For the convenience of implementation into BATS-R-US and the consistency with the isotropic MHD model, we adopt the average ion pressure p as one of our primitive variables, and solve

$$\frac{\partial p}{\partial t} + 2p(\nabla \cdot \mathbf{u}) + (\mathbf{u} \cdot \nabla)p - \frac{1}{3}p_{\parallel}(\nabla \cdot \mathbf{u}) + (p_{\parallel} - p)\mathbf{b} \cdot (\mathbf{b} \cdot \nabla)\mathbf{u} = 0 \qquad (2.9)$$

which is obtained by linearly combining the parallel (2.6) and perpendicular (2.7) ion pressure equations according to relation (2.2). Mathematically, we can use either $p_{\parallel}$ or $p_{\perp}$ as the other ion pressure variable as they make no difference. However, given $p_{\perp}$ is larger than $p_{\parallel}$ in most places where ion pressure anisotropy exists in the terrestrial magnetosphere where we will first apply Anisotropic BATS-R-US to simulate, the chance of $p_{\parallel}$ becoming negative when solving for p and $p_{\perp}$ is larger than the chance of $p_{\perp}$ getting negative when solving for p and $p_{\parallel}$. In favor of numerical computation, we choose to solve $p_{\parallel}$ instead of $p_{\perp}$.

2.1.2 Conservative form

The conservative form of the equations is required in order to capture correct jump conditions across discontinuities, for instance, the Earth's bow shock. We have density ρ, momentum $\rho\mathbf{u}$, magnetic field $\mathbf{B}$, and total energy density

$$e = \frac{\rho u^2}{2} + \frac{\mathbf{B}^2}{2\mu_0} + \frac{3}{2}(p + p_e) \qquad (2.10)$$

as conservative variables, and the conservative equations can be written as

$$\frac{\partial \rho}{\partial t} + \nabla \cdot (\rho \mathbf{u}) = 0 \qquad (2.11)$$

$$\frac{\partial \rho \mathbf{u}}{\partial t} + \nabla \cdot \left[\rho \mathbf{u}\mathbf{u} + p_\perp \mathbf{I} + p_e \mathbf{I} + (p_\parallel - p_\perp)\mathbf{b}\mathbf{b} - \frac{1}{\mu_0}\left(\mathbf{B}\mathbf{B} - \frac{B^2}{2}\mathbf{I} \right) \right] = 0 \qquad (2.12)$$

$$\frac{\partial \mathbf{B}}{\partial t} + \nabla \times [-(\mathbf{u} \times \mathbf{B})] = 0 \qquad (2.13)$$

$$\frac{\partial e}{\partial t} + \nabla \cdot \left[\mathbf{u} \left(e + p_\perp + p_e + \frac{\mathbf{B}^2}{2\mu_0} \right) + \mathbf{u} \cdot ((p_\parallel - p_\perp)\mathbf{b}\mathbf{b} - \frac{\mathbf{B}\mathbf{B}}{2\mu_0}) \right] = 0 \qquad (2.14)$$

The parallel and electron pressure equations (2.6) and (2.8) are still needed to calculate $p_\parallel$ and p_e. This means that the jump conditions across a discontinuity cannot be fully determined from the conservation relations, because we do not know how to distribute the total thermal energy (obtained from the conservative quantity e) among the parallel ion, perpendicular ion and electron pressures. The problem of insufficient jump relations for discontinuities in an anisotropic plasma has been discussed by many earlier studies [*Abraham-Shrauner*, 1967; *Lynn*, 1967; *Neubauer*, 1970], in which various additional assumptions were applied to supplement the jump relations. *Hudson* [1970] discussed types of discontinuities for an anisotropic plasma, and pointed out that the assumptions made for a general case may not be suitable for discontinuities in the solar wind. There are also detailed analysis of Rankine-Hugoniot relations modified by the pressure anisotropy for shocks in space [*Chao and Goldstein*, 1972; *Lyu and Kan*, 1986]. A relatively new solution to the problem was proposed by *Erkaev et al.* [2000] and *Vogl et al.* [2001a,b], in which mirror and firehose instability criteria were applied to constrain the ratio between parallel and perpendicular pressures downstream of the shock. We apply a similar approach of utilizing instabilities.

2.1.3 Instabilities

The three types of instabilities that we consider are the firehose, mirror and ion cyclotron instabilities that can be present in plasmas with ion pressure anisotropy.

The Harris instability mentioned in Section 1.1.2.1 is also associated with electron pressure anisotropy and thus is not considered in our model.

The firehose instability [*Lazar and Poedts*, 2009a,b; *Gary et al.*, 1998] arises when the ion parallel pressure is large enough so that

$$\frac{p_{\parallel}}{p_{\perp}} > 1 + \frac{\mathbf{B}^2}{\mu_0 p_{\perp}} \tag{2.15}$$

The mirror and ion cyclotron instabilities arise when the ion perpendicular pressure is sufficiently large. These two instabilities, especially their behaviors in space plasma regimes, have been investigated by many researchers [*Tajiri*, 1967; *Gary*, 1976, 1992]. The criterion for the mirror instability is

$$\frac{p_{\perp}}{p_{\parallel}} > 1 + \frac{\mathbf{B}^2}{2\mu_0 p_{\perp}} \tag{2.16}$$

For the ion cyclotron instability, the general form can be written as

$$\frac{p_{\perp}}{p_{\parallel}} > 1 + C_1 \left(\frac{\mathbf{B}^2}{2\mu_0 p_{\parallel}} \right)^{C_2} \tag{2.17}$$

where C_1 and C_2 are constants, which vary from study to study. *Anderson et al.* [1994] gave $C_1 = 0.85$ and $C_2 = 0.48$, while *Gary et al.* [1994] presented three different sets of constants based on three growth rates. Also, *Denton et al.* [1994] extracted the threshold from measurements. In our code we use $C_1 = 0.3$ and $C_2 = 0.5$ for magnetosphere simulations as it gives reasonable agreement with measurements.

When the instability criteria are satisfied, the strong wave-particle interaction tends to drive the system towards isotropy. The ratio of ion perpendicular to ion parallel pressure of a stable plasma is limited by the lower bound provided by the firehose stability threshold (2.15) and the upper bound provided by the mirror and ion cyclotron stability criteria (2.16) and (2.17). The incomplete equation set in

conservative form is thus augmented by instability thresholds, which constrain the solution to be physically reasonable.

It is important to note that the mirror and ion cyclotron instabilities are kinetic phenomena that are not captured by the anisotropic MHD equations. The firehose instability is correctly represented by the fluid equations, but its growth rate is limited by the grid resolution. To take into account the effect of these instabilities, we add a right-hand-side source term to (2.6) if any of the instability conditions is fulfilled [*Hesse and Birn*, 1992; *Birn et al.*, 1995; *Samsonov et al.*, 2001]:

$$\frac{\delta p_{\parallel}}{\delta t} = \frac{\overline{p}_{\parallel} - p_{\parallel}}{\tau} \tag{2.18}$$

where $\overline{p}_{\parallel}$ is the marginally unstable ion parallel pressure obtained from (2.15), (2.16) or (2.17), respectively, which are described in Appendix A. This source term relaxes the ion pressure anisotropy towards a stable state at a time rate τ. The value of τ depends on the growth rate of instabilities, which in turn depends on the plasma state as well as the spatial scales. The details will be explored according to the applications of Anisotropic BATS-R-US in the following chapters. We can also explicitly set τ to a constant value that is small relative to the typical dynamical time scales of the problem.

The source term is applied in a split manner at the end of the time step and it is discretized point-implicitly for the sake of numerical stability as

$$p_{\parallel}^{n+1} = p_{\parallel}^{*} + \frac{\Delta t}{\tau}(\overline{p}_{\parallel} - p_{\parallel}^{n+1}) \tag{2.19}$$

which can be solved for $p_{\parallel}^{n+1}$ to obtain the update

$$p_{\parallel}^{n+1} = p_{\parallel}^{*} + \frac{(\overline{p}_{\parallel} - p_{\parallel}^{*})\Delta t}{\Delta t + \tau} \tag{2.20}$$

where Δt is the time step, and time levels $*$ and $n+1$ correspond to the incomplete and final updates, respectively.

2.1.4 Semirelativistic equations

To obtain the semirelativistic form, we follow the steps in *Gombosi et al.* [2002] for semirelativistic MHD with isotropic pressure. We re-derive the equations while keeping the electric force in the momentum equation and the displacement current in Ampere's law. Only the momentum equation (2.4) needs to be modified from the classical case, which can be written as

$$\begin{aligned} \frac{\partial \mathbf{u}}{\partial t} &+ \gamma_A^2(\mathbf{I}+\frac{V_A^2}{c^2}\mathbf{bb})\cdot\left[(\mathbf{u}\cdot\nabla)\mathbf{u}+\frac{1}{\rho}\nabla(p_\perp+p_e)+\frac{1}{\rho}\nabla\cdot\left[(p_\parallel-p_\perp)\mathbf{bb}\right]\right] \\ &+ \gamma_A^2\frac{1}{\mu_0\rho}\mathbf{B}\times\left[\nabla\times\mathbf{B}-\frac{1}{c^2}\mathbf{u}\times(\nabla\times\mathbf{E})-\frac{1}{c_0^2}\mathbf{u}\nabla\cdot\mathbf{E}\right]=0 \end{aligned} \tag{2.21}$$

where the Alfvén factor

$$\gamma_A = \frac{1}{\sqrt{1+\frac{V_A^2}{c^2}}} \tag{2.22}$$

was introduced with the classical Alfvén speed $V_A = B/\sqrt{\mu_0\rho}$. c_0 is the true value of the speed of light, while c is the artificially lowered speed of light. The electric field $\mathbf{E}$ can be obtained from Ohm's law

$$\mathbf{E} = -\mathbf{u}\times\mathbf{B} \tag{2.23}$$

Hence, our primitive-variable equation set of the semirelativistic MHD with anisotropic ion pressure and isotropic electron pressure is composed of equations (2.3), (2.5) - (2.8) and (2.21). Note that when V_A^2 is much smaller than c^2, the equation set reduces to the classical form. In equation (2.21), the last term $\frac{1}{c_0^2}\mathbf{u}\nabla\cdot\mathbf{E}$ can be dropped because that it is basically u^2/c_0^2 smaller than the $\nabla\times\mathbf{B}$ term, and $u^2 << c_0^2$ is true for the semirelativistic limit. This simplification will be used for the derivation

of characteristic waves.

In the conservative form of semirelativistic MHD, both the momentum and energy equations are different from the non-relativistic equations. The momentum equation (2.12) is replaced with

$$\frac{\partial \left[\rho \mathbf{u} + \mathbf{E} \times \mathbf{B}/(\mu_0 c^2)\right]}{\partial t} + \nabla \cdot \left[\rho \mathbf{u}\mathbf{u} + (p_\perp + p_e)\mathbf{I} + (p_\parallel - p_\perp)\mathbf{b}\mathbf{b} + \frac{B^2\mathbf{I}}{2\mu_0} + \frac{E^2\mathbf{I}}{2\mu_0 c^2} - \frac{\mathbf{B}\mathbf{B}}{\mu_0} - \frac{\mathbf{E}\mathbf{E}}{\mu_0 c^2}\right] = 0 \tag{2.24}$$

and the energy equation (2.14) changes to

$$\frac{\partial \left[e + E^2/(2\mu_0 c^2)\right]}{\partial t} + \nabla \cdot \left[\mathbf{u}\left(e + p_\perp + p_e - \frac{\mathbf{B}^2}{2\mu_0}\right) + (p_\parallel - p_\perp)\mathbf{u} \cdot \mathbf{b}\mathbf{b} + \frac{\mathbf{E} \times \mathbf{B}}{\mu_0}\right] = 0 \tag{2.25}$$

where $E = |\mathbf{E}|$ is the magnitude of the electric field.

2.2 Characteristic Wave Speeds

The numerical discretization of the anisotropic MHD equations requires characteristic wave speeds. The maximum wave propagation speed determines the maximum stable explicit time step according to the Courant-Friedrichs-Lewy (CFL) stability condition. The maximum wave speed is also required for the Rusanov (or local Lax-Friedrichs) scheme [*Rusanov*, 1961], while the fastest left and right wave speeds are needed for the Harten-Lax-van Leer (HLL) scheme [*Harten et al.*, 1983].

To find the characteristic waves, we need to solve for the eigenvalue problem of a set of nine equations. We solve the semirelativisitic case, and then obtain the classical limit by taking $\gamma_A = 1$. In order to obtain the characteristic matrix, we write the

equation set in a quasi-linear form in one dimension:

$$\frac{\partial \mathbf{U}}{\partial t} + \mathbf{M}_x \frac{\partial \mathbf{U}}{\partial x} = 0 \tag{2.26}$$

The variables $\mathbf{U} = (\rho, \mathbf{u}, \mathbf{B}, p_\parallel, p_\perp, p_e)$ only depend on x and t. We utilize the MAPLE software to extract the coefficients from equations (2.3), (2.5) - (2.8) and (2.21), and form the 9×9 characteristic matrix. Because the characteristic wave speeds do not depend on the coordinate system, we simplify our problem by setting $B_z = 0$, i.e., the coordinate system is rotated such that the magnetic field lies in the $x - y$ plane. The final characteristic matrix $\mathbf{M}_x$ can be written as

$$\begin{pmatrix}
u_x & \rho & 0 & 0 & 0 & 0 & 0 & 0 & 0 \\
0 & \gamma_A^2 u_x + \chi_{11} & \chi_{12} & 0 & \kappa_1 & 0 & \eta_{11} & \eta_{12} & \eta_{13} \\
0 & \chi_{21} & \gamma_A^2 u_x + \chi_{22} & 0 & \kappa_2 & 0 & \eta_{21} & \eta_{22} & \eta_{23} \\
0 & \chi_{31} & \chi_{32} & \gamma_A^2 u_x + \chi_{33} & \kappa_3 & \nu & 0 & 0 & 0 \\
0 & B_y & -B_x & 0 & u_x & 0 & 0 & 0 & 0 \\
0 & 0 & 0 & -B_x & 0 & u_x & 0 & 0 & 0 \\
0 & p_\parallel (1 + 2b_x^2) & 2p_\parallel b_x b_y & 0 & 0 & 0 & u_x & 0 & 0 \\
0 & p_\perp (2 - b_x^2) & -p_\perp b_x b_y & 0 & 0 & 0 & 0 & u_x & 0 \\
0 & \frac{5}{3} p_e & 0 & 0 & 0 & 0 & 0 & 0 & u_x
\end{pmatrix} \tag{2.27}$$

where

$$\chi = \frac{\gamma_A^2}{\mu_0 \rho c^2} \begin{pmatrix}
B_x^2 u_x - B_y^2 u_x & 2B_x B_y u_x & 0 \\
2B_x B_y u_x & B_y^2 u_x - B_x^2 u_x & 0 \\
-B_y^2 u_z & B_x B_y u_z & -B_x^2 u_x - B_x B_y u_y
\end{pmatrix} \tag{2.28}$$

$$\kappa = \frac{\gamma_A^2}{\mu_0 \rho c^2} \begin{pmatrix} (c^2 - u_x^2)B_y + (2\mu_0 \rho c^2 B^{-2} + 1)B_y b_x^2 (p_\perp - p_\parallel)\rho^{-1} \\ (u_x^2 - c^2)B_x + \left(b_y^2 + (b_y^2 - b_x^2)\mu_0 \rho c^2 B^{-2}\right) B_x^2 (p_\perp - p_\parallel)\rho^{-1} \\ -B_y u_x u_z \end{pmatrix} \tag{2.29}$$

$$\nu = \frac{\gamma_A^2}{\mu_0 \rho c^2} \left[(u_x^2 - c^2)B_x + B_y u_x u_y - \mu_0 c^2 B_x B^{-2}(p_\perp - p_\parallel)\right] \tag{2.30}$$

$$\eta = \begin{pmatrix} b_x^2 \rho^{-1} & \gamma_A^2 b_y^2 \rho^{-1} & \gamma_A^2 \rho^{-1}(1 + V_{A,x}^2 c^{-2}) \\ b_x b_y \rho^{-1} & -\gamma_A^2 b_x b_y \rho^{-1} & \gamma_A^2 b_x b_y \rho^{-1} V_A^2 c^{-2} \\ 0 & 0 & 0 \end{pmatrix} \tag{2.31}$$

We use the notation $b_y = B_y/B$. With the help of MAPLE and after some complicated algebra, the characteristic equation $\det(\mathbf{M}_x - \mathbf{I}\lambda) = 0$ is reduced to the following form:

$$(\lambda - u_x)^3 P_2(\lambda) P_4(\lambda) = 0 \tag{2.32}$$

where the wave speed λ is one of the eigenvalues of $\mathbf{M}_x$. u_x is the flow velocity along the direction x. P_2 and P_4 are second- and fourth-order polynomials:

$$P_2 = \lambda(\lambda - u_x) + \gamma_A^2 \left[\lambda(\mathbf{u}\cdot\mathbf{b})b_x \frac{V_A^2}{c^2} - u_x(\lambda - u_x) - \left(V_A^2 + \frac{p_\perp - p_\parallel}{\rho}\right) b_x^2\right] \tag{2.33}$$

$$\begin{aligned} P_4 = {} & (\lambda - u_x)^4 - \left(a^2 + \frac{2p_\perp - 3p_\parallel}{\rho} + \frac{2p_\parallel - p_\perp}{\rho} b_x^2\right)(\lambda - u_x)^2 \\ & -(c^2 - \lambda^2)\frac{V_A^2}{c^2}\left[(\lambda - u_x)^2 - a^2 b_x^2\right] \\ & - \left[\frac{{p_\perp}^2 - 3p_\perp p_\parallel}{\rho^2}(1 - b_x^2) + \frac{3{p_\parallel}^2}{\rho^2} b_x^2 - \frac{5p_e}{3\rho}\left(\frac{4p_\parallel - p_\perp}{\rho} b_x^2 - \frac{3p_\parallel}{\rho}\right)\right] b_x^2 \end{aligned} \tag{2.34}$$

where

$$a^2 = \frac{3p_\parallel + \frac{5}{3}p_e}{\rho} \tag{2.35}$$

is defined as the sound speed and $b_x = B_x/B$.

Equation (2.32) is the dispersion relation, whose roots λ describe the corresponding characteristic waves. Three of the roots are identical:

$$\lambda_{1,2,3} = u_x \tag{2.36}$$

They represent three entropy waves related to the three pressures $p_\parallel$, $p_\perp$ and p_e. In the classical limit, the entropy waves remain the same.

2.2.1 Alfvén waves

The roots of $P_2 = 0$ correspond to a pair of Alfvén waves:

$$\begin{aligned}\lambda_{4,5} &= \frac{1}{2}\gamma_A^2\left[u_x - \frac{V_A^2}{c^2}(\mathbf{u}\cdot\mathbf{b})b_x\right] + \frac{u_x}{2} \\ &\pm \sqrt{\gamma_A^2\left(V_{A,x}^2 + \frac{p_\perp - p_\parallel}{\rho}b_x^2 - u_x^2\right) + \left[\frac{1}{2}\gamma_A^2\left(u_x - \frac{V_A^2}{c^2}(\mathbf{u}\cdot\mathbf{b})b_x\right) + \frac{u_x}{2}\right]^2}\end{aligned} \tag{2.37}$$

where $V_{A,x} = V_A b_x = \sqrt{B_x^2/\mu_0\rho}$. Although the formula is quite complicated, there is no p_e dependence, which means that the presence of the electron pressure does not affect the Alfvén wave solutions. This is expected, since the electron pressure is isotropic, which can be viewed as an analog to the isotropic pressure in single-fluid MHD, and only contributes to the longitudinal (compressional) waves.

In the classical limit with $V_A \ll c$ and γ_A^2 approaching 1, the Alfvén wave speeds reduce to

$$\lim_{V_A \ll c} \lambda_{4,5} = u_x \pm \sqrt{\frac{\frac{1}{\mu_0}B_x^2 + (p_\perp - p_\parallel)b_x^2}{\rho}} \tag{2.38}$$

This is consistent with Baranov's results [*Baranov*, 1970]. Compared to isotropic MHD, pressure anisotropy enters the expression as the difference between the parallel and perpendicular pressures. $\lambda_{4,5}$ contains an imaginary part if the condition (2.15) is fulfilled, and then the firehose instability will arise.

2.2.2 Fast and slow magnetosonic waves

The remaining four roots of $P_4 = 0$ in (2.34) are associated with magnetosonic waves. The equation itself is very complicated, so are the roots. It is much simpler to look into the classical limit first, as the terms proportional to V_A^2/c^2 will vanish. The resulting equation has only fourth- and second-order terms of $\lambda - u_x$, which can be easily solved:

$$\begin{aligned}
\lim_{V_A \ll c} \lambda_{6,7,8,9} &= u_x \pm \frac{1}{\sqrt{2\rho}} \left\{ \frac{B^2}{\mu_0} + 2p_\perp + \frac{5}{3}p_e + (2p_\parallel - p_\perp) b_x^2 \right. \\
&\pm \left[\left(\frac{B^2}{\mu_0} + 2p_\perp + \frac{5}{3}p_e + (2p_\parallel - p_\perp) b_x^2 \right)^2 \right. \\
&+ 4 \left(\frac{1}{4} {p_\perp}^2 b_x^2 (1 - b_x^2) - 3 p_\parallel p_\perp b_x^2 (2 - b_x^2) + 3 {p_\parallel}^2 b_x^4 \right. \\
&+ \left. \left. \left. \frac{5}{3} p_e (4 p_\parallel b_x^2 - p_\perp b_x^2 - 3 p_\parallel) b_x^2 - \left(3p_\parallel + \frac{5}{3}p_e \right) \frac{B_x^2}{\mu_0} \right) \right]^{1/2} \right\}^{1/2} \qquad (2.39)
\end{aligned}$$

where we substituted a^2 back from (2.35). The second $\pm$ corresponds to fast(+) and slow(−) magnetosonic waves, respectively. For each type, there are two waves propagating symmetrically along opposite directions with respect to the bulk flow speed u_x, corresponding to the first $\pm$ sign. With the pressure anisotropy, the magnetosonic wave speeds are much more complicated than in the isotropic case. In the case of neglecting the electron pressure, we recover the formula obtained by *Baranov* [1970].

Next we consider the semirelativistic case. The general case requires the solution of a general fourth-order polynomial. While this can be done, it is very expensive. To obtain an approximation, we study some special cases that have simpler solutions. First we take the zero flow velocity assumption, i.e. $\mathbf{u} = 0$. We define

$$\overline{a}^2 = a^2 \left(1 + \frac{V_{A,x}^2}{c^2} \right) + \frac{2p_\perp - 3p_\parallel}{\rho} + \frac{2p_\parallel - p_\perp}{\rho} b_x^2 \qquad (2.40)$$

related to the sound speed, and

$$\epsilon = \frac{b_x^2}{\rho^2}\left[3p_\parallel p_\perp(2-b_x^2) - p_\perp^2(1-b_x^2) - 3p_\parallel^2 b_x^2 - \frac{5p_e}{3}\left(4p_\parallel b_x^2 - p_\perp b_x^2 - 3p_\parallel\right)\right] \tag{2.41}$$

to include the extra terms related to the pressure anisotropy and the direction of the magnetic field. The eigenvalues $\lambda_{6,7,8,9}$ for no flow approximation are

$$\lim_{u_x\to 0}\lambda_{6,7} = \pm\frac{1}{\sqrt{2}}\sqrt{\gamma_A^2(\overline{a}^2+V_A^2) - \sqrt{\gamma_A^4(\overline{a}^2+V_A^2)^2 - 4\gamma_A^2(a^2V_{A,x}^2+\epsilon)}} \tag{2.42}$$

and

$$\lim_{u_x\to 0}\lambda_{8,9} = \pm\frac{1}{\sqrt{2}}\sqrt{\gamma_A^2(\overline{a}^2+V_A^2) + \sqrt{\gamma_A^4(\overline{a}^2+V_A^2)^2 - 4\gamma_A^2(a^2V_{A,x}^2+\epsilon)}} \tag{2.43}$$

corresponding to the slow and fast magnetosonic wave speeds, respectively.

Another special case is when the magnetic field is parallel to the x direction, i.e. $b_x = 1$. This simplifies the eigenvalues to be

$$\lim_{b_x\to 1}\lambda_{6,7} = u_x \pm a \tag{2.44}$$

$$\lim_{b_x\to 1}\lambda_{8,9} = \gamma_A^2 u_x \pm \gamma_A V_A\sqrt{1+\frac{p_\perp - p_\parallel}{V_A^2\rho} - \gamma_A^2\frac{u_x^2}{c^2}} \tag{2.45}$$

The last special case we consider is when the magnetic field is perpendicular to the x direction, i.e., $b_x = 0$. In this case the wave speeds become

$$\lim_{b_x\to 0}\lambda_{6,7} = u_x \tag{2.46}$$

$$\lim_{b_x\to 0}\lambda_{8,9} = \gamma_A^2 u_x \pm \gamma_A\sqrt{\frac{2p_\perp + (5/3)p_e}{\rho} + V_A^2\left(1-\gamma_A^2\frac{u_x^2}{c^2}\right)} \tag{2.47}$$

Based on the special cases and the approximate formulas for the isotropic case [*Gom-*

bosi et al., 2002], we construct the following approximate slow and fast magnetosonic wave speeds for the general case:

$$\begin{aligned}\tilde{\lambda}_{6,7} &= u_x \pm \tilde{c}_s \\ &= u_x \pm \frac{1}{\sqrt{2}}\sqrt{\gamma_A^2(\overline{a}^2+\overline{V}_A^2) - \sqrt{\gamma_A^4(\overline{a}^2+\overline{V}_A^2)^2 - 4\gamma_A^2(a^2\overline{V}_{A,x}^2+\epsilon)}}\end{aligned} \tag{2.48}$$

and

$$\begin{aligned}\tilde{\lambda}_{8,9} &= \gamma_A^2 u_x \pm \tilde{c}_f \\ &= \gamma_A^2 u_x \pm \frac{1}{\sqrt{2}}\sqrt{\gamma_A^2(\overline{a}^2+\overline{V}_A^2) + \sqrt{\gamma_A^4(\overline{a}^2+\overline{V}_A^2)^2 - 4\gamma_A^2(a^2\overline{V}_{A,x}^2+\epsilon)}}\end{aligned} \tag{2.49}$$

where we defined

$$\overline{V}_A^2 = V_A^2\left(1-\gamma_A^2\frac{u_x^2}{c^2}\right) \text{ and } \overline{V}_{A,x}^2 = V_{A,x}^2\left(1-\gamma_A^2\frac{u_x^2}{c^2}\right) \tag{2.50}$$

Equations (2.48) and (2.49) reduce to the special cases in the corresponding limits. First of all, they reduce to the classical magnetosonic wave speeds (2.39) for the case of Alfvén speed negligible compared to the artificially reduced speed of light, i.e., $V_A \ll c$ and $\gamma_A \to 1$,$\overline{V}_A \to V_A$, $\overline{V}_{A,x} \to V_{A,x}$. Secondly, for $u_x = 0$, equations (2.42) and (2.43) are recovered. Lastly, when substituting $b_x = 1$ or $b_x = 0$ for the parallel and perpendicular magnetic field limits, (2.48) and (2.49) are consistent with (2.44),(2.45), and (2.46), (2.47), respectively.

In order to check the accuracy, we compare the exact solutions of $P_4 = 0$ with the values given by the approximate formulas. The relative error is evaluated as the difference between the approximate and exact solutions and then divided by the exact solution:

$$\xi_{s+} = \frac{\tilde{\lambda}_6 - \lambda_6}{\lambda_6}, \quad \xi_{s-} = \frac{\tilde{\lambda}_7 - \lambda_7}{\lambda_7}, \quad \xi_{f+} = \frac{\tilde{\lambda}_8 - \lambda_8}{\lambda_8}, \quad \xi_{f-} = \frac{\tilde{\lambda}_9 - \lambda_9}{\lambda_9} \tag{2.51}$$

We investigate the errors statistically by generating 10^5 random points in a 6-dimensional variable space of u_x, B, b_x, $p_\parallel$, $p_\perp$ and p_e, while fixing $\rho = 1$, $c = 1$, and $\mu_0 = 1$. Recall the definition of semirelativistic MHD, the bulk flow velocity u_x and the sound speed a should always be much smaller than the speed of light c, yet the Alfvén speed V_A can exceed c. We thus limit variable ranges to be $0 < u_x < c/3$, $0 < a < c/3$, $0 < V_A < 3c$, $0 < b_x < 1$ and $0 < p_\perp < 5p_\parallel$ that covers the physically reasonable range of anisotropy. The relative errors are shown in Figure 2.1. For the right going fast speed λ_8, the errors are within 5%. This is the most important eigenvalue, since λ_8 is the largest wave speed (for $u_x > 0$) that determines the explicit time step and it is also used in the Rusanov and HLL schemes. The HLL scheme also uses λ_9, but it does not contribute much when its value approaches zero. So we are interested in the errors of λ_9 away from zero, which are acceptable. The plot of ξ_{f+} also shows that the points are mainly in the positive part, which means that $\tilde{\lambda}_8$ overestimates the exact fast speed in almost every case with very few exceptions. This in turn ensures that the CFL condition based on $\tilde{\lambda}_8$ is sufficiently safe to maintain stability. When both u_x and a lie between $c/3$ and c, the errors are found to be within 20%. Overall, the approximate formulas are accurate enough for our purposes within the parameter range of interest.

2.3 Implementation

We implement both the classical and semirelativistic MHD equations with anisotropic ion pressure and isotropic electron pressure into the BATS-R-US code, and name the new model Anisotropic BATS-R-US. The implementation of the various temporal and spatial discretization schemes have been reported in detail during the development of BATS-R-US [*Powell et al.*, 1999; *De Zeeuw et al.*, 2000; *Tóth et al.*, 2006; *Tóth et al.*, 2012], and here we only describe those parts of the algorithm that are specific to the anisotropic pressure.

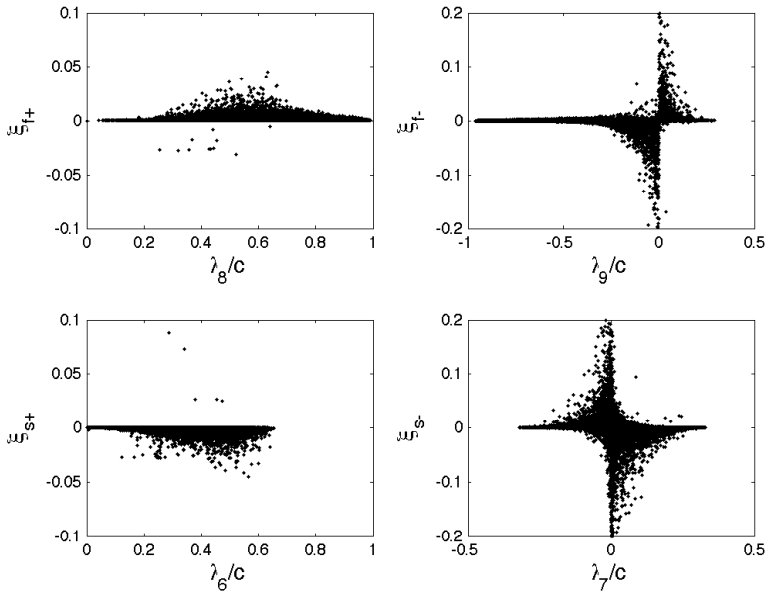

Figure 2.1: The relative error of the approximate semirelativistic magnetosonic wave formulas (2.48) and (2.49). The dots are 0.1 million random variable sets in a 6-dimensional space. The calculation of the error is based on (2.51).

We solve the conservative form of the continuity, momentum, induction and energy equations: (2.11)-(2.14) in the classical case, and (2.11), (2.13), (2.24), (2.25) in the semirelativistic case. The pressure equations (2.6), (2.9) and (2.8) cannot be cast into full conservation form, so they are solved in the following non-conservative form:

$$\frac{\partial p_\parallel}{\partial t} + \nabla \cdot (p_\parallel \mathbf{u}) = -2p_\parallel \mathbf{b} \cdot (\mathbf{b} \cdot \nabla)\mathbf{u} \tag{2.52}$$

$$\frac{\partial p}{\partial t} + \nabla \cdot (p\mathbf{u}) = (p - p_\parallel)\mathbf{b} \cdot (\mathbf{b} \cdot \nabla)\mathbf{u} - \left(p - \frac{p_\parallel}{3}\right) \nabla \cdot \mathbf{u} \tag{2.53}$$

$$\frac{\partial p_e}{\partial t} + \nabla \cdot (p_e \mathbf{u}) = -\frac{2}{3} p_e \nabla \cdot \mathbf{u} \tag{2.54}$$

The above equations have pure divergence terms on the left hand sides where we use the usual flux formulation of the finite volume schemes. The right hand sides of equations (2.52), (2.53) and (2.54) consist of the gradient and divergence of the velocity multiplied by some terms. These coefficient terms are simply taken at the cell

centers, while the gradient and divergence of the velocity are evaluated analogously to the fluxes used in the conservative equations. In particular, we use a limited reconstruction procedure with second or third order accurate slope limiters to obtain the left and right states in the primitive variables. At resolution changes we use the algorithm of *Sokolov et al.* [2006]. The left and right velocities are averaged as

$$\bar{\mathbf{u}} = \frac{\mathbf{u}_L + \mathbf{u}_R}{2} \tag{2.55}$$

for the Rusanov scheme, and

$$\bar{\mathbf{u}} = \frac{\lambda_+ \mathbf{u}_L - \lambda_- \mathbf{u}_R}{\lambda_+ - \lambda_-} \tag{2.56}$$

for the HLL scheme, where λ_- and λ_+ are the most negative and most positive wave speeds, respectively. The wave speeds are calculated with the exact formula (2.39) in the classical case, while for the semirelativistic case, the approximate magnetosonic wave speed formulas (2.48) and (2.49) are applied. Finally, the divergence and gradient of the velocity are obtained by integrating $\bar{\mathbf{u}}$ over the surface of the cell in the usual finite volume manner.

BATS-R-US can either solve for the energy density e or the ion pressure p or use a hybrid approach and solve for both. In the hybrid scheme the energy equation can be used near shock waves to get the correct energy jump conditions, while the pressure equation provides more accurate and robust solution in regions where the thermal energy density is a small fraction of the total energy density. In grid cells where the energy equation is used, p^* calculated from (2.53) is overwritten by the pressure calculated from the energy density using (2.10), while the opposite is done in grid cells where the pressure equation is used. The parallel and electron pressures $p_\parallel$ and p_e are always computed from equations (2.52) and (2.54), respectively. Finally, the parallel pressure has to be corrected according to (2.20) if any of the instability

conditions (2.15) to (2.17) are satisfied.

The full algorithm can be summarized as following:

1. Reconstruct the left and right states using limited slopes of the primitive variables.

2. Calculate the Rusanov or HLL fluxes and the face centered values of the velocity from the left and right states.

3. Calculate the divergence of the fluxes and the divergence and gradient of the velocity by integrating over the cell faces.

4. Convert the classical momentum and energy densities to the semirelativistic variables in the semirelativistic case.

5. Apply the fluxes and source terms to update the variables.

6. Convert the semirelativistic momentum and energy densities back to the classical variables in the semirelativistic case.

7. Either overwrite pressure based on energy or the other way around.

8. Calculate the instability limits.

9. Apply the relaxation term to the parallel pressure.

To achieve second order accuracy in time, we apply a two-stage Runge-Kutta scheme. We can also use an implicit or explicit/implicit time stepping algorithm as described in *Tóth et al.* [2006]. In all cases, the instability limits and the relaxation terms are only applied after the full time step is completed.

2.4 Numerical tests

To verify Anisotropic BATS-R-US, a large set of numerical tests have been designed and carried out, including solving the relativistic and classical equations, solving for energy density or pressure, using Rusanov and HLL schemes, uniform and non-uniform meshes, as well as explicit and implicit time stepping schemes. Here we present tests involving the propagation of characteristic MHD waves on a 1D mesh and the simulation of the firehose instability. We use a grid convergence study to establish the accuracy of the scheme. In all tests we use the HLL scheme and normalized the units of the magnetic field so that $\mu_0 = 1$. We do not use the pressure relaxation term for the tests.

2.4.1 Magnetosonic wave propagation tests

We have performed magnetosonic wave propagation tests for many different magnetic field orientations both for classical and semirelativistic cases. Small perturbations are applied on a uniform background state, and then the simulated wave speeds are compared with the analytic solution.

As a specific example, we describe a test with magnetosonic waves propagating perpendicular to the background magnetic field in the semirelativistic approximation. In this case, the analytic solution for the fast wave speed is given by equation (2.47), while the slow wave speed given by equation (2.46) is equal to the flow speed u_x. We compute on a 1D domain ranging from $x = -30$ to $x = +30$ with periodic boundary conditions, and set the uniform background as $\rho = 1$, $u_x = 12$, $u_y = u_z = 0$, $B_x = B_z = 0$, $B_y = 30$, $p_\parallel = 14$, $p = 16$, $p_e = 12$, $c = 30$. The density, pressure, and magnetic field perturbations are sinusoidal waves centered at $x = 0$ and limited within $-3 < x < 3$: $\delta\rho = 0.01\cos(2\pi x/12)$, $\delta p_\parallel = 0.14\cos(2\pi x/12)$, $\delta p = 0.16\cos(2\pi x/12)$, $\delta p_e = 0.195\cos(2\pi x/12)$, and $\delta B_y = 0.3\cos(2\pi x/12)$. For each perturbation, the maximum magnitude is around 1% of the background value. A pair of excited fast

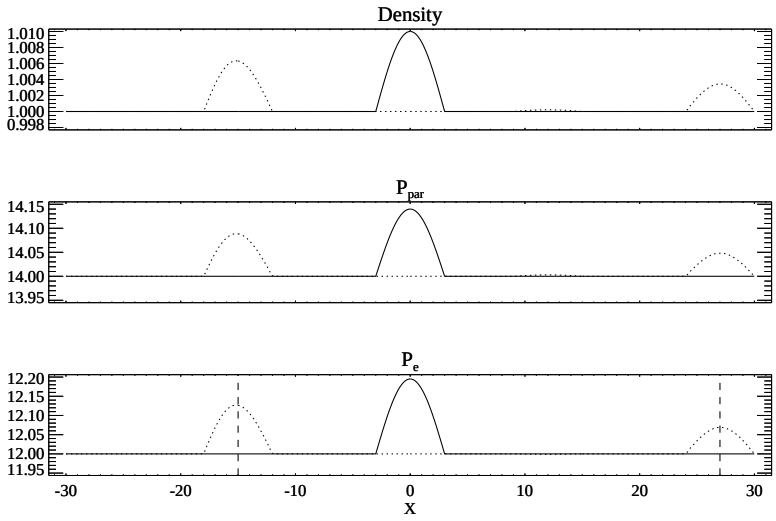

Figure 2.2: A pair of fast waves are generated from the initial center perturbation (solid lines). The two waves move in opposite directions at speeds -15 and $+27$, respectively. The dotted lines show the waves at the final time $t = 1$. The vertical dashed lines show where the center of the wave should be at $t = 1$ based on the analytic formula (2.47).

waves thus propagate along $+x$ and $-x$ directions asymmetrically with velocities $\lambda_8 = 27$ and $\lambda_9 = -15$ respectively. To minimize discretization errors, we used 3,000 grid cells. Figure 2.2 shows the density, ion parallel pressure and electron pressure at the initial and final times. The numerical propagation speeds of the pair of fast waves agree well with the analytic values.

2.4.2 Alfvén wave propagation and firehose instability tests

We did Alfvén wave propagation tests similar to the magnetosonic wave tests by posing perturbations on the velocity and magnetic field. As mentioned in section 2.2.1, the electron pressure does not affect the Alfvén wave speed. The propagation speed was compared to the analytical solution, and we found good agreement in all tests.

Here we show a test of the firehose instability in the classical limit, which can be triggered from the Alfvén mode by increasing the parallel pressure. Within the

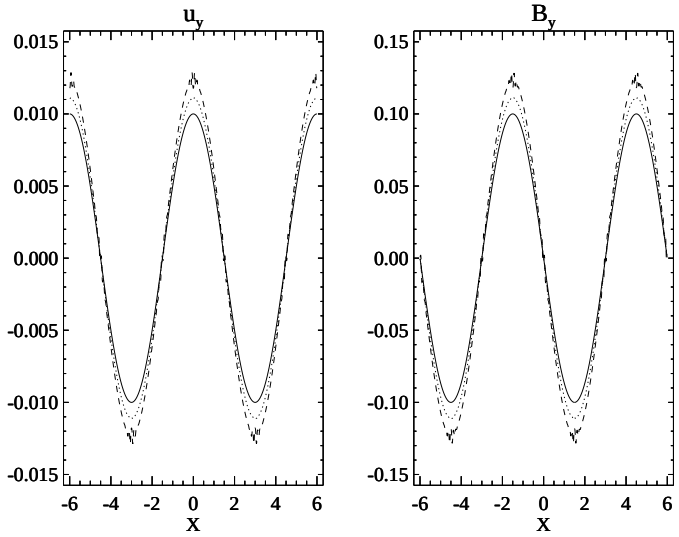

Figure 2.3: Firehose instability test, growing wave pattern at t=0s(solid line), t=0.1s(dot line), and t=0.2s(dash line)

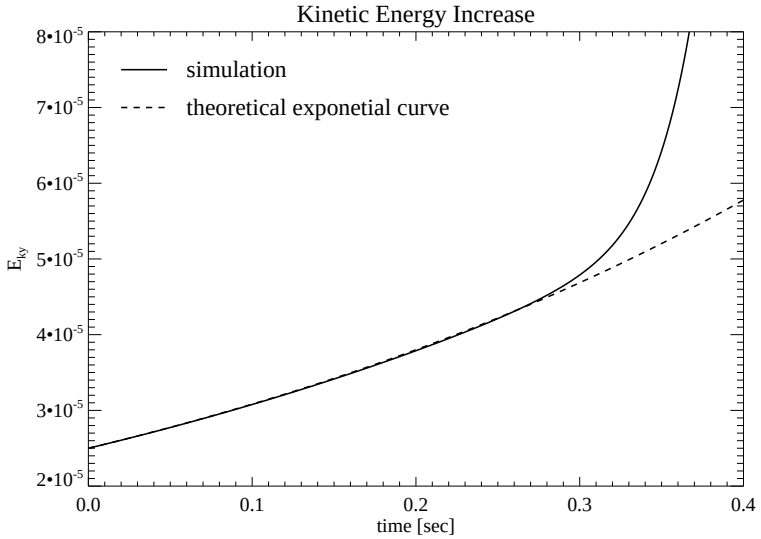

Figure 2.4: The y-direction kinetic energy growth against time for the firehose instability test. The growth curve is plotted as the solid line, while the dash line represents the theoretical exponential growth rate.

domain $-6 < x < 6$, we have a uniform background with $\rho = 1$, $u_x = u_y = u_z = 0$, $B_x = 10$, $B_y = B_z = 0$, $p_\parallel = 104$, $p = 110/3$, $p_e = 10$. According to the wave speed formula (2.38), the calculated Alfvén speed is $\sqrt{-1}$. This means that the perturbations in u_y and B_y will be shifted by 90 degrees. We apply the following perturbations: $\delta u_y = 0.01\cos(2\pi x/6)$ and $\delta B_y = 0.1\cos(2\pi x/6 + \pi/2)$. Instead of propagation, the perturbations start to grow exponentially. Figure 2.3 shows three snapshots of the growing instability. There are small oscillations near the local extrema at $t = 0.2$. These are caused by the numerical errors that introduce short wave length perturbations which grow much faster than the original perturbation. Figure 2.4 shows the growth of the y-direction kinetic energy $E_{ky} = \rho u_y^2/2$ as a function of time. The analytical growth rate is overplot for comparison. The agreement is very good up to $t = 0.25$. After this time, the growth of the kinetic energy exceeds the theoretical rate, because the short wavelength perturbation overtake the growth trend.

2.4.3 Grid convergence tests

In order to check the accuracy of the numerical scheme, we did several grid convergence studies. The test involving circularly polarized Alfvén wave propagation is presented in *Tóth et al.* [2012].

First, we show a test for sound waves propagating along the magnetic field. For convenience we only consider the classical limit, of which the exact solution can be easily calculated. The sound wave is excited in the domain $-5 < x < 5$ of zero-flow plasma with the magnetic field parallel to the wave propagation direction: $\rho = 1$, $u_x = u_y = u_z = 0$, $B_x = 10$, $B_y = B_z = 0$, $p_\parallel = p = 5$ and $p_e = 6$. The perturbations are of the order 10^{-6} in magnitude: $\delta\rho = 10^{-7}\cos(2\pi x/5)$, $\delta u_x = 5\times 10^{-7}\cos(2\pi x/5)$, $\delta p_\parallel = \delta p = 1.5\times 10^{-6}\cos(2\pi x/5)$, and $\delta p_e = 10^{-6}\cos(2\pi x/5)$. The resulting wave is a pure sound wave with speed $a = 5$. The test is performed on 1D grids with 100, 200, 400, 800 and 1600 cells, and with the monotonized central (MC) and Koren slope

limiters, respectively. The boundary conditions are periodic. The final time is set to $t = 5$, so the wave propagates 5 full wave lengths. We compare the final state to the initial perturbed state as the exact solution. The relative error is calculated for each grid resolution, which is the absolute difference between the numerical solution and the exact solution then divided by the absolute value of the exact solution. Figure 2.5 confirms that the scheme converges to the analytic solution at the expected convergence rate.

Second, as an interesting extension of the propagating semirelativistic magnetosonic wave test, we generate a pair of nonlinear fast waves by increasing the magnitudes of perturbations to be ten times the ones used in the test before and using cos^2 perturbations instead of cos, while other parameters remain the same. The nonlinear feature of the waves can be clearly seen from Figure 2.6. Similar to the sound wave test, this test is performed with 100, 200, 400, 800 and 1600 cells. The final state of the simulation with 3200 cells is regarded as the reference solution to which other results are compared. Figure 2.7 shows the convergence rates which are essentially second order. Note that the steepening of the waves creates a non-smooth solution by the end of the simulation so that second order accuracy is not necessarily expected.

2.5 Summary

We describe the equation set for the non-relativistic and semirelatvistic MHD with anisotropic ion pressure and isotropic electron pressure, a three-temperature plasma. The semirelativistic equation set is useful when the classical Alfvén speed is comparable or exceed the speed of light. It is also suitable for the artificially reduced speed of light often used in space plasma modeling.

To build a numerical model, we need to determine the characteristic speeds. We solve for the semirelativistic speeds first and obtain the non-relativistic solutions as a limiting case. With two more equations compared to the isotropic single-fluid MHD,

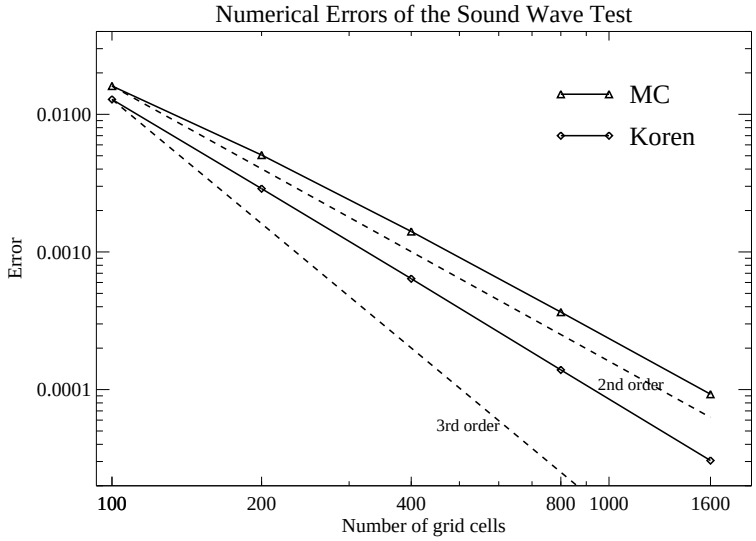

Figure 2.5: Convergence study for the sound wave test. The two curves are results of the monotonized central (MC) and Koren limiters. The dashed lines indicate the second and third order convergence rates, respectively.

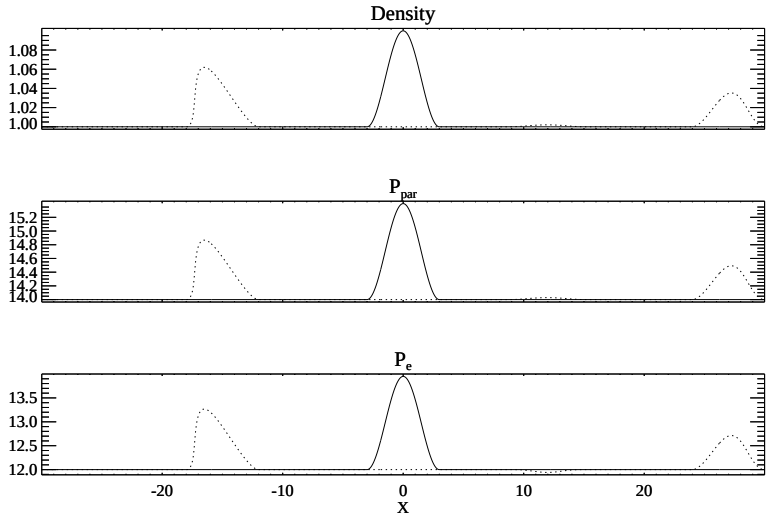

Figure 2.6: A pair of nonlinear semirelativistic fast waves are excited from the initial center perturbation (solid lines). The dotted lines show the waves at the final time $t = 1$. The plot shows the simulation with 3200 cells.

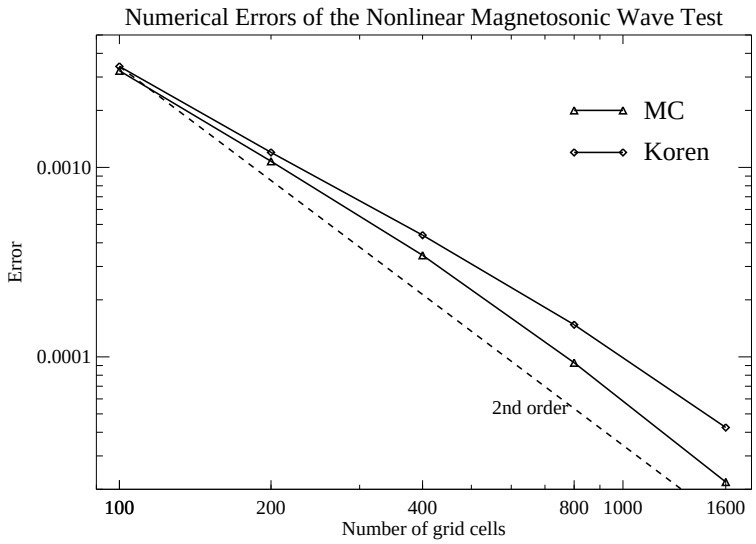

Figure 2.7: Convergence study for the nonlinear propagating semirelativistic wave test. The two curves are results of the monotonized central (MC) and Koren limiters. The dashed line indicates the second order convergence rate.

the resulting dispersion relation contains nine characteristic waves. Three of them are entropy waves corresponding to three temperatures, two of them are the Alfvén waves, while the remaining four are fast and slow magnetosonic waves. We calculate the exact speed for the Alfvén wave and derive the approximate magnetosonic wave speeds for the semirelativistic case. The accuracy of the approximate formulas are demonstrated by comparing them to the exact solution. For the classical case, we obtain the exact formulas for all wave speeds.

Instabilities play an important role in limiting ion pressure anisotropy. The fluid equations correctly describe the firehose instability, but the mirror and ion cyclotron instabilities can only be fully captured by a kinetic model. We use a source term in the parallel pressure equation to relax the solution towards the marginally unstable state whenever any of the stability conditions are violated. The instability conditions also augment the incomplete set of conservation laws to establish physically reasonable jump conditions across discontinuities.

In order to verify our theory and implementation, we performed several numerical

tests. Both the magnetosonic and the Alfvén wave speeds were checked through wave propagation tests. We also simulated the firehose instability and compared it with the analytical solution. These tests demonstrate that we have successfully developed a numerical model solving the classical and semirelativistic MHD equations with anisotropic ion pressure and isotropic electron pressure. This model, Anisotropic BATS-R-US, will be further validated through terrestrial magnetospheric simulations in the next chapter.

CHAPTER III

Global Magnetospheric Simulations with Anisotropic BATS-R-US

In the previous chapter we have reported in detail the implementation and verification of Anisotropic BATS-R-US. In this chapter, we apply Anisotropic BATS-R-US to Earth's quiet time magnetospheric simulations, which also serve as model validation tests. Since the electron pressure plays a minor role compared to the ion pressure in the terrestrial magnetosphere, we do not consider electron pressure in our magnetospheric modeling. In this case Anisotropic BATS-R-US solves single-fluid anisotropic MHD equations under the double adiabatic approximation [*Chew et al.*, 1956] with an additional pressure anisotropy limiting term.

The following content of this chapter is divided into four parts. We begin with describing the equation set that Anisotropic BATS-R-US solves in the absence of electron pressure, as well as the improved pressure anisotropy limiting term specific to magnetospheric simulations in Section 3.1. Then we present a variety of magnetospheric simulations performed with Anisotropic BATS-R-US in Section 3.2 for idealized simulations and in Section 3.3 for measured solar wind and IMF conditions as inputs. Finally we evaluate the model and conclude the chapter in Section 3.4.

3.1 Methods

3.1.1 Equations

Neglecting the electron pressure, Anisotropic BATS-R-US solves the following equations in the classical limit:

$$\frac{\partial \rho}{\partial t} + \nabla \cdot (\rho \mathbf{u}) = 0 \tag{3.1}$$

$$\frac{\partial \rho \mathbf{u}}{\partial t} + \nabla \cdot \left[\rho \mathbf{u}\mathbf{u} + p_\perp \mathbf{I} + (p_\parallel - p_\perp)\mathbf{b}\mathbf{b} - \frac{1}{\mu_0}\left(\mathbf{B}\mathbf{B} - \frac{B^2}{2}\mathbf{I} \right) \right] = 0 \tag{3.2}$$

$$\frac{\partial \mathbf{B}}{\partial t} + \nabla \times [-(\mathbf{u} \times \mathbf{B})] = 0 \tag{3.3}$$

$$\frac{\partial p_\parallel}{\partial t} + \nabla \cdot (p_\parallel \mathbf{u}) + 2 p_\parallel \mathbf{b} \cdot (\mathbf{b} \cdot \nabla)\mathbf{u} = \frac{\delta p_\parallel}{\delta t} \tag{3.4}$$

$$\frac{\partial p}{\partial t} + \nabla \cdot (p \mathbf{u}) + \frac{2}{3} p_\perp (\nabla \cdot \mathbf{u}) + \frac{2}{3}(p_\parallel - p_\perp)\mathbf{b} \cdot (\mathbf{b} \cdot \nabla)\mathbf{u} = 0 \tag{3.5}$$

where ρ, $\mathbf{u}$ and $\mathbf{B}$ are the density, velocity and magnetic field, respectively. $\mathbf{b} = \mathbf{B}/|\mathbf{B}|$ is defined as the unit vector along the magnetic field. $p_\parallel$ represents the parallel pressure component with respect to the magnetic field, while p is the average scalar pressure. μ_0 denotes the permeability of vacuum. We take the polytropic index to be 5/3. The corresponding semirelativistic equations without electron pressure can also be easily obtained by neglecting the electron pressure term, for instance in equation (2.21), thus they are not repeated in this chapter.

The conversion between the average scalar pressure and the pressure components can be expressed as

$$p = \frac{2p_\perp + p_\parallel}{3} \tag{3.6}$$

Compared to the ideal MHD equations, the momentum equation (3.2) and the average scalar pressure equation (3.5) are changed. Each of them contains a new term resulting from the difference between $p_\parallel$ and $p_\perp$: $(p_\parallel - p_\perp)\mathbf{b}\mathbf{b}$ in (3.2) and $\frac{2}{3}(p_\parallel - p_\perp)\mathbf{b} \cdot (\mathbf{b} \cdot \nabla)\mathbf{u}$ in (3.5). These two new terms are eliminated in the case of

pressure isotropy, thus the equations reduce to the standard ideal MHD equations as $p_\perp = p$. The right-hand-side of (3.4) is the pressure relaxation term that will be discussed shortly. In the absence of the pressure relaxation term, (3.4) and (3.5) are equivalent to the double adiabatic equations.

As mentioned in Chapter II, capturing jump conditions across a discontinuity relies on acquiring conservation laws of the system. Therefore, we need to solve the conservative form of the equation set for the bow shock region. Only the pressure equations (3.4) and (3.5) are not in a conservation form. The conservation of energy density e provides the conservative equation that replaces the average scalar pressure equation (3.5) as:

$$\frac{\partial e}{\partial t} + \nabla \cdot \left[\mathbf{u} \left(e + p_\perp + \frac{\mathbf{B}^2}{2\mu_0} \right) + \mathbf{u} \cdot \left((p_\parallel - p_\perp)\mathbf{bb} - \frac{\mathbf{BB}}{2\mu_0} \right) \right] = 0 \tag{3.7}$$

with

$$e = \frac{\rho u^2}{2} + \frac{\mathbf{B}^2}{2\mu_0} + \frac{3}{2}p \tag{3.8}$$

Compared to isotropic MHD, the total energy density equation also contains the additional term introduced by the pressure difference of the parallel and perpendicular components.

Since the parallel pressure equation (3.4) cannot be written in an appropriate conservative form, the system is closed by solving equation (3.4) and using the instability criteria to bound the parallel pressure jump across the bow shock, similar to the bounded anisotropic fluid model proposed by *Denton et al.* [1994].

Apart from supplementing the jump conditions, the plasma instabilities associated with anisotropic pressure limit the pressure anisotropy throughout the magnetosphere. For completeness, we repeat the criteria for the firehose, the mirror, and the ion cyclotron instabilities that are considered in Anisotropic BATS-R-US. The

firehose instability occurs when [*Gary et al.*, 1998; *Lazar and Poedts*, 2009a,b]

$$\frac{p_{\parallel}}{p_{\perp}} > 1 + \frac{\mathbf{B}^2}{\mu_0 p_{\perp}} \tag{3.9}$$

The mirror and ion cyclotron instability criteria are [*Tajiri*, 1967; *Gary*, 1976, 1992]

$$\frac{p_{\perp}}{p_{\parallel}} > 1 + \frac{\mathbf{B}^2}{2\mu_0 p_{\perp}} \tag{3.10}$$

and

$$\frac{p_{\perp}}{p_{\parallel}} > 1 + C_1 \left(\frac{\mathbf{B}^2}{2\mu_0 p_{\parallel}} \right)^{C_2} \tag{3.11}$$

respectively, where we use $C_1 = 0.3$ and $C_2 = 0.5$ as they are close to the average values derived from observations in the magnetosphere [*Anderson et al.*, 1996; *Gary et al.*, 1995].

The latter two instabilities involve kinetic effects and thus cannot be fully described by MHD. Moreover, the grid resolution that we normally apply in global MHD simulations may not be fine enough to resolve even hydromagnetic instabilities. The effect of these instabilities is represented by the collision term of the parallel pressure equation (3.4):

$$\frac{\delta p_{\parallel}}{\delta t} = \frac{\overline{p}_{\parallel} - p_{\parallel}}{\tau} \tag{3.12}$$

where $\overline{p}_{\parallel}$ is the marginally unstable parallel pressure from (A.5), (A.13) or (A.18). We call (3.12) the pressure relaxation term due to the instabilities, with the relaxation time τ relates to their growth rates. In regions stable for all types of instabilities, the relaxation term (3.12) is zero. In unstable regions, the pressure relaxation term pushes the parallel pressure so that the plasma reaches the marginally unstable states over time τ. In the case when both the mirror and ion cyclotron instabilities are present, only the one that gives larger $\delta p_{\parallel}/\delta t$ is applied. The details of how we set τ will be addressed in Section 3.1.2.

In addition to the pressure relaxation term applied in the unstable regions, we introduce a global pressure relaxation term that applies everywhere to represent other possible mechanisms constraining the plasma pressure anisotropy in the real magnetosphere. We write the global relaxation term as

$$\frac{\delta p_{\parallel}}{\delta t} = \frac{p - p_{\parallel}}{\tau_g} \tag{3.13}$$

where τ_g is the global relaxation time. In unstable regions, both (3.12) and (3.13) are computed, and the one with larger absolute value, which changes $p_{\parallel}$ more, is applied. To minimize the effect of the global relaxation term on the unstable regions, we set τ_g to be of the order of 100 seconds in quiet time magnetospheric simulations. According to the idealized simulations we performed, shown in Section 3.2, the typical relaxation time τ due to the instabilities is much lower than 100 seconds.

3.1.2 Anisotropy relaxation time

We have implemented two types of relaxation time τ for the instability induced relaxation term (3.12). First, τ can be set to a constant value homogeneously in the computational domain. For magnetospheric simulations, typical values are of the order of 10 seconds, as we shall see later. Second, τ can be set based on the growth rates of the instabilities.

For the firehose instability, the growth rate can be calculated from the dispersion relation of the Alfvén wave in a plasma with anisotropic pressure written as [*Baranov*, 1970]

$$\frac{\omega^2}{k_{\parallel}^2} = \frac{1}{\rho}\left(\frac{B^2}{\mu_0} + p_{\perp} - p_{\parallel}\right) \tag{3.14}$$

When the firehose instability is excited, i.e., equation (3.9) is satisfied, the growth rate is given by

$$\gamma_f = k_{\parallel}\sqrt{\frac{\Delta p_f}{\rho}} \tag{3.15}$$

where $k_\parallel = k\cos\theta = (2\pi/\lambda)\cos\theta$ with θ representing the angle between the wave number $\mathbf{k}$ and the magnetic field, and $\Delta p_f = p_\parallel - p_\perp - B^2/\mu_0$.

As the growth rate γ_f varies with the wavelength λ, we are seeking the wavelength that grows fastest. However, according to (3.15), the growth rate becomes infinity when the wavelength approaches zero. This is because the growth rate (3.15) is derived from the MHD theory that is only valid in the long-wavelength limit, i.e. the wavelength is much longer than the mean particle Larmor radius. Taking the finite Larmor radius effects into account, *Hall* [1979, 1981] showed that the growth rate is

$$\gamma_{f_{FLR}} = k_\parallel \sqrt{\frac{1}{\rho}\left\{\Delta p_f - \frac{1}{3\rho\Omega_i^2}\left[\frac{1}{4}p_\perp(p_\parallel - p_\perp)k_\perp^2 + p_\parallel\left(p_\perp - \frac{p_\parallel}{4}\right)k_\parallel^2\right]\right\}} \tag{3.16}$$

where ρ is plasma density, $\Omega_i = qB/m$ is ion gyrofrequency, and $k_\perp = k\sin\theta$. After some algebra, we found the maximum growth occurs when $\theta = 0$, for $p_\parallel/p_\perp < 4$, which shall hold true for the firehose instability in the magnetosphere. The corresponding fastest growing wavelength is obtained as

$$\lambda_f = 2\pi r_i \sqrt{\frac{6p_\parallel(p_\perp - p_\parallel/4)}{p_\perp \Delta p_f}} \tag{3.17}$$

where $r_i = mv_\perp/(qB)$ is the ion Larmor radius.

Based on the fastest growth rate, we write the relaxation time of the firehose instability as

$$\tau_f = \frac{1}{\gamma_{f_{FLR}}(\lambda_f)} = \frac{2}{\Omega_i}\frac{\sqrt{p_\parallel(p_\perp - p_\parallel/4)}}{\Delta p_f} \tag{3.18}$$

In our single-fluid model, Ω_i is taken to be the gyrofrequency of a proton.

A similar approach is applied to obtain the relaxation time for the mirror instability. The fluid description of this instability based on the MHD analysis yields the

following growth rate [*Southwood and Kivelson*, 1993]

$$\gamma_m = k_\perp \sqrt{\frac{2p_\perp \Delta p_m}{p_\parallel \rho}} \tag{3.19}$$

where $k_\perp = k \sin\theta = (2\pi/\lambda)\sin\theta$ and $\Delta p_m = (p_\perp - p_\parallel) - B^2 p_\parallel/(2\mu_0 p_\perp)$. Again the growth rate γ_m increases monotonically with k. Unfortunately, given the complicated expression for the growth rate with the finite Larmor radius effects [*Hall*, 1980], it is difficult to find the maximum growth rate. However, Hall calculated the fastest growing wavelength assuming low pressure anisotropy and high plasma beta as

$$\lambda_m = \frac{3\sqrt{5}\pi}{2} r_i \tag{3.20}$$

This is close to the typical values found from the full kinetic analysis by *Pokhotelov et al.* [2004], as shown in their Figure 1.

Given λ_m is an order of magnitude larger than the ion gyroradius, we approximate the maximum growth rate from the long-wavelength MHD analysis by substituting (3.20) into (3.19). The relaxation time for the mirror instability is thus written as

$$\tau_m = \frac{1}{\gamma_m(\lambda_m)} = \frac{3\sqrt{5}}{4\Omega_i} \sqrt{\frac{p_\parallel}{2\Delta p_m}} \tag{3.21}$$

For the ion cyclotron instability, its growth rate varies with both the wavelength and the instability criterion (C_1 and C_2 in (3.11)) [*Gary et al.*, 1994]. In reality, the ion cyclotron instability can arise in the magnetosheath and the closed field line region near the Earth. However, the mirror instability often dominates over the ion cyclotron instability in the magnetosheath as observed and modeled [*Phan et al.*, 1994; *Shoji et al.*, 2009], which we have already taken care of. The only concern is for the inner magnetosphere. A good estimation of the relaxation time for the ion cyclotron instability should probably relate to the bouncing period of the particles

traveling along the field lines. For sake of simplicity we approximate the growth rate based on observations in the magnetosphere [*Anderson et al.*, 1996] and theories [*Märk*, 1974; *Gary et al.*, 1993, 1995] as

$$\tau_{ic} = \frac{10^2}{\Omega_i} \tag{3.22}$$

Although the relaxation times (3.18), (3.21) and (3.22) have a physical basis, they are only approximations to reality, as is the relaxation term (3.12). An underlying assumption is that the time rate of the change in the parallel pressure is the same as the growth rate of an instability. However, these simplifications are appropriate for our MHD model in terms of both computational cost and physical accuracy.

3.2 Idealized Magnetospheric Simulations

To validate the anisotropic BATS-R-US code, we perform global magnetospheric simulations including idealized (this section) and real magnetosphere cases (next section). All the simulations in these two sections are produced from coupling BATS-R-US with the ionospheric electric potential solver Ridley Ionosphere Model (RIM) [*Ridley et al.*, 2004], i.e., the GM and IE components of the SWMF.

Our model validation starts with simulating the magnetosphere under idealized conditions to exclude unnecessary factors that complicate the system. First, we neglect the rotation of the Earth. Second, we assume the magnetic axis aligns with the ecliptic North direction. Third, we use constant solar wind and interplanetary magnetic field (IMF) conditions through the simulations: number density $\rho_{sw} = 5\,/\text{cc}$, temperature $T_{sw} = 10^5\,\text{K}$, velocity $u_{xsw} = -400\,\text{km/s}$, $u_{ysw} = u_{zsw} = 0$ and purely southward IMF $B_{zsw} = -5\,\text{nT}$ or northward IMF $B_{zsw} = 5\,\text{nT}$. The input solar wind pressure is assumed to be isotropic. Finally, for the ionosphere we apply constant Pedersen conductance 5 mho and neglect Hall conductance.

The computational domain is a three-dimensional box in GSM coordinates. With the Earth at the origin, the box covers from -224 to 32 Earth radii (R_E) in the X direction and from -64 to $64\,\mathrm{R}_E$ in the Y and Z directions. The inner boundary is the surface of a sphere surrounding the Earth at a radius of $2.5\,\mathrm{R}_E$, where the density is set to be 28 /cc. Taking advangtage of the adaptive mesh refinement (AMR) in BATS-R-US, we set the finest resolution of $1/4\,\mathrm{R}_E$ near the Earth and the coarsest resolution of $4\,\mathrm{R}_E$ far down the tail. We take the Boris factor to be 0.01, i.e. the reduced speed of light is 3000 km/s. We use the Sokolov scheme [*Sokolov et al.*, 2002] with the Koren limiter [*Koren*, 1993] in all idealized runs. We do not apply the global pressure relaxation term (3.13), so the pressure anisotropy is only limited by the instabilities, if present, based on (3.12).

3.2.1 Southward IMF case

To investigate the effects of the pressure relaxation term (3.12) we compute four runs identically except with different relaxation times. One of them uses the growth-rate dependent relaxation times for the three instabilities as (3.18), (3.21) and (3.22); The other three use a constant relaxation time of $\tau = 10\,\mathrm{s}$, $100\,\mathrm{s}$, ∞ (no relaxation term at all) for all three instabilities. For comparison, we also produce a run using standard BATS-R-US with isotropic pressure. All five runs starts with 5000 iterations in steady state mode before they are switched to time accurate mode lasting for 4 hours in physical time. We analyze the results at the end of the simulations.

First we examine the pressure anisotropy. Figure 3.1 shows the pressure anisotropy ratio $p_\perp/p_\parallel$. We extract the solutions in the noon-midnight meridional plane $Y = 0$ (left column) and the equatorial plane $Z = 0$ (right column) from the four runs with different relaxation times. To have a better visualization for all cases, the color scale is saturated for $p_\perp/p_\parallel > 4$. In the $\tau = 100\,\mathrm{s}$ and $\tau = \infty$ cases, $p_\perp/p_\parallel$ reaches a maximum of 15 and 200 in the magnetosheath, respectively, which are highly unrealistic values.

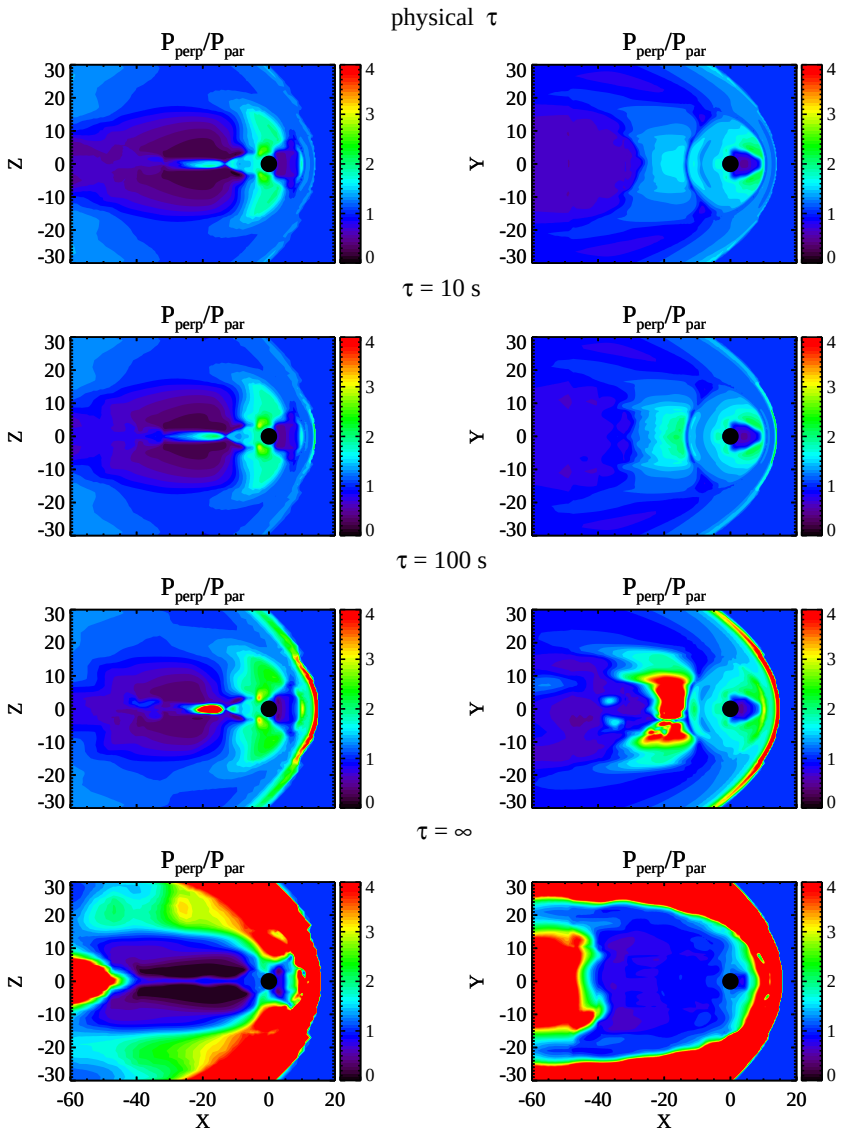

Figure 3.1: The pressure anisotropy ratio $p_\perp/p_\parallel$ in the $Y = 0$ plane (left column) and the $Z = 0$ plane (right column) from the idealized magnetospheric simulations using anisotropic BATS-R-US in the southward IMF case. The four rows are from runs with different pressure relaxation time τ. From top to bottom: growth-rate based τ, $\tau = 10\,\mathrm{s}$, $\tau = 100\,\mathrm{s}$, $\tau = \infty$ (no pressure relaxation).

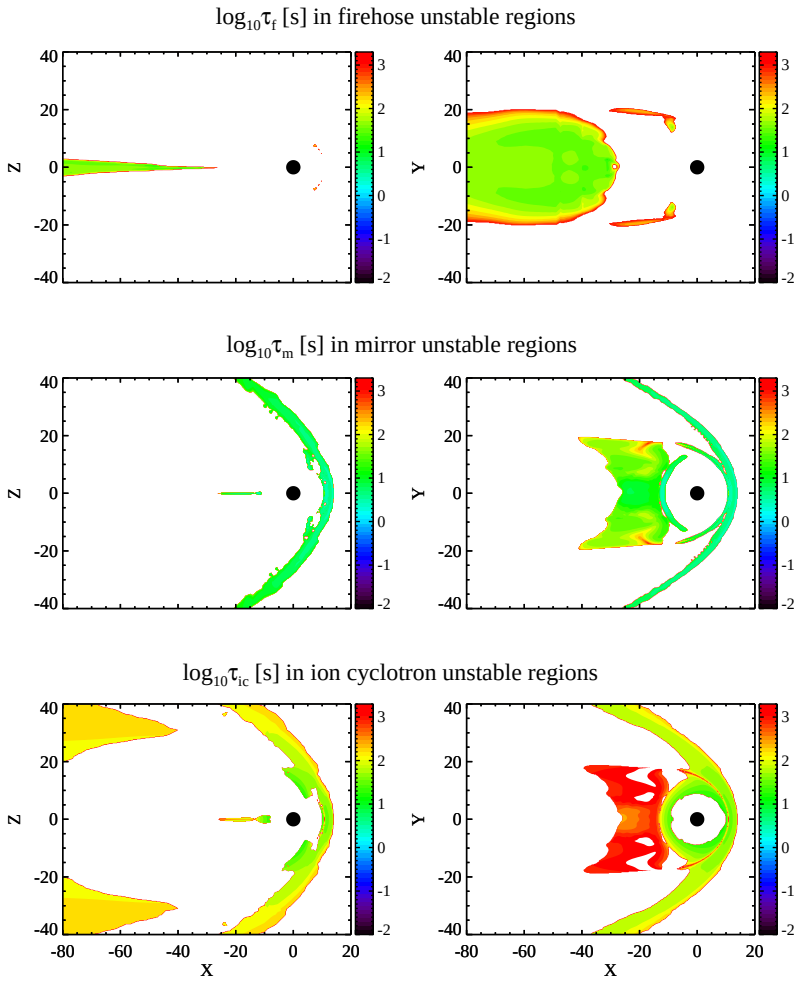

Figure 3.2: The logarithmic τ contour in the $Y = 0$ plane (left column) and the $Z = 0$ plane (right column) of the three instabilities from the growth-rate based τ run for the southward IMF case. τ is given in seconds. The white regions are stable for the respective instability.

The $\tau = 10\,\mathrm{s}$ case gives a little higher $p_\perp/p_\parallel$ compared to the growth-rate based τ case, thus an appropriate constant τ should be a few seconds. Essentially, three regions develop highly perpendicular pressure: the magnetosheath; the cusps; and the magnetotail reconnection site. These regions are filled with compressed flow, thus the perpendicular pressure increases [*Hesse and Birn*, 1992].

Next we look into the spatial variation of τ in the growth-rate based τ case, as displayed in Figure 3.2. We plot τ for three instabilities as color contours on the noon-midnight meridional plane and the equatorial plane. The white regions are stable with infinite τ. The relaxation term (3.12) is only applied in the unstable regions as colored with the corresponding τ value. The firehose instability (first row) only arises in very limited regions of the dayside magnetosphere and in the distant tail, with τ_f varying from about 10 seconds to hundreds of seconds. Both the mirror (middle row) and ion cyclotron instabilities exist throughout the magnetosheath and in the tail reconnection region. In the magnetosheath and the tail reconnection region, τ_m (around a few seconds) is much smaller than τ_{ic} (hundreds of seconds). Compared to the mirror instability region, the ion cyclotron instability region extends into the inner magnetosphere, but it does not include the region very close to the Earth. This is probably due to the strong magnetic field near the Earth that stabilizes the plasma, as can be seen in the stability condition (3.11).

To have more insight into the differences between anisotropic and isotropic MHD in global models, we compare the results from these two types of simulations. For anisotropic MHD we refer to the run with growth-rate based relaxation time unless otherwise specified. The most prominent distinctions are:

1. The width and shape of the magnetosheath.

   Previous 2D and 3D anisotropic MHD simulations of the magnetosheath [*Erkaev et al.*, 1999; *Denton and Lyon*, 2000; *Samsonov and Pudovkin*, 2000] have observed a thicker magnetosheath than isotropic MHD simulations give. Our

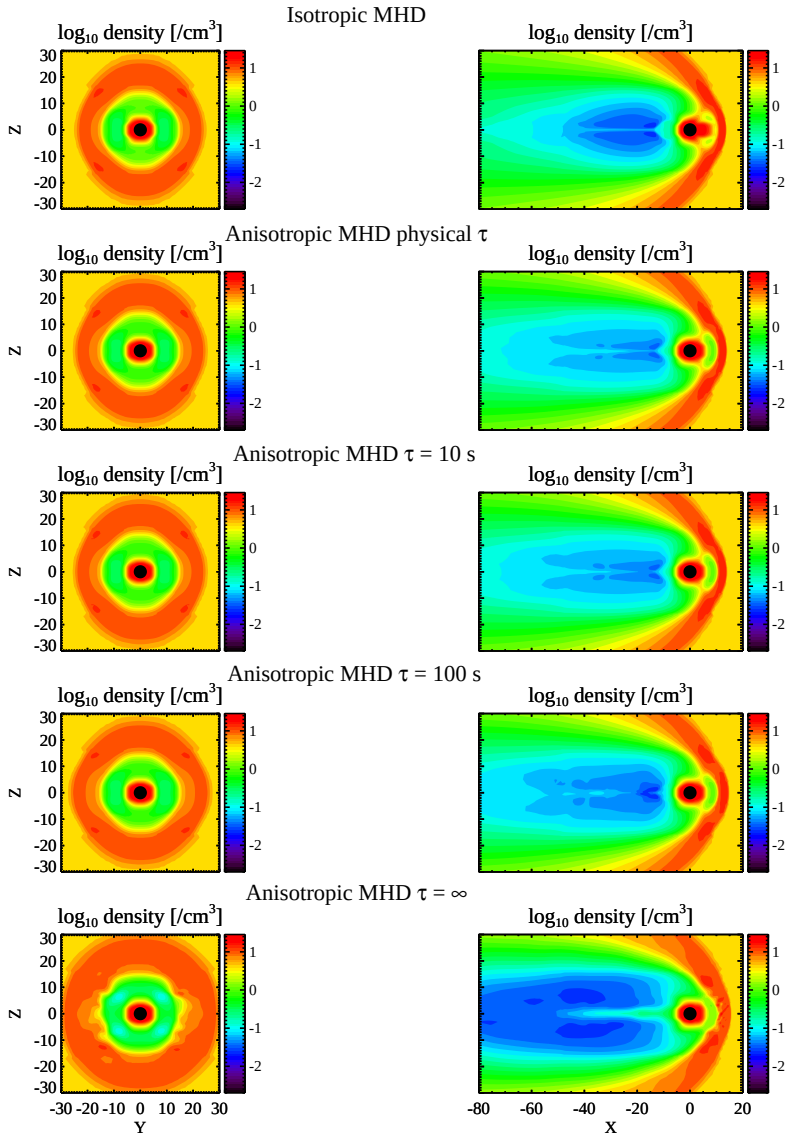

Figure 3.3: The logarithmic density contour in the $X = 0$ plane (left column) and the $Y = 0$ plane (right column) from the idealized magnetospheric simulations in the southward IMF case. From the top to the bottom row: isotropic MHD, anisotropic MHD with physical τ based on the growth rates, anisotropic MHD with $\tau = 10\,\mathrm{s}$, anisotropic MHD with $\tau = 100\,\mathrm{s}$ and anisotropic MHD with $\tau = \infty$.

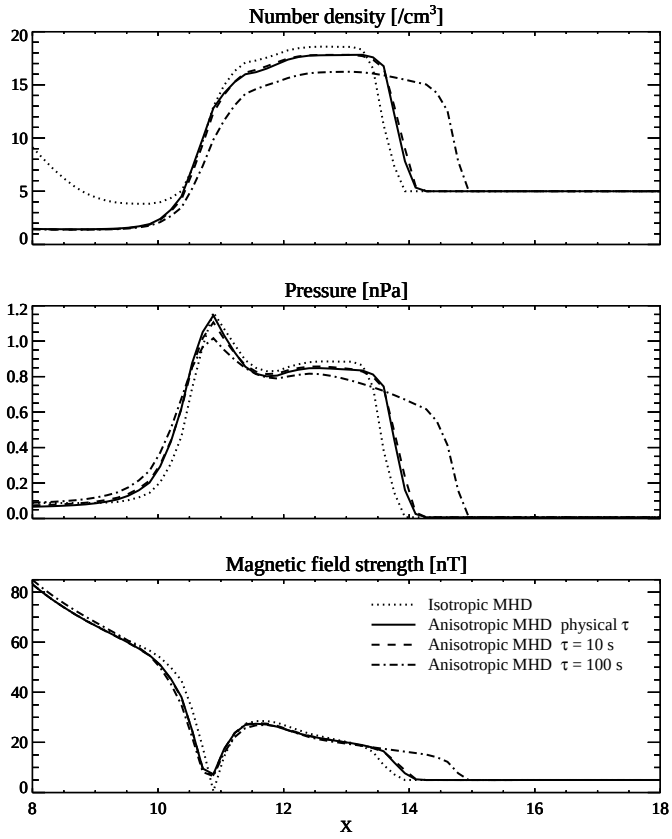

Figure 3.4: The number density (top panel), pressure (middle panel) and magnetic field strength (bottom panel) profiles of the dayside magnetosheath along the x-axis from the idealized magnetospheric simulations in the southward IMF case. Different lines represent different runs as indicated in the figure.

results agree with it. Moreover, with global simulations, we are able to examine the effects of pressure anisotropy on the shape of the whole magnetosphere.

Figure 3.3 shows density contours in the $X = 0$ and $Y = 0$ planes. As the constant relaxation time τ increases, i.e. higher pressure anisotropy is allowed in the system, the magnetosheath, shown as the red region, becomes thicker. At the same time, the magnetosheath grows faster in the Y direction than in the Z direction, such that the boundary of the magnetosphere in the $X = 0$ cut changes from an oval to a circle. This is due to the larger pressure along the Y direction than the one along the Z direction, since the pressure perpendicular to the magnetic field, which is mostly along the Z direction, is larger than the pressure parallel to the magnetic field in the magnetosheath.

The thickening of the magnetosheath can also be identified in Figure 3.4 that shows the variations of the variables along the X axis. The $\tau = \infty$ case is not shown as it is too far from the reality. The density and pressure profiles of different τ and their comparisons with isotropic MHD results clearly indicate the trend of the increasing width of the sub-solar magnetosheath. For the realistic $\tau = 10\,\mathrm{s}$ setting, represented by the dashed line, the profiles are very close to the profiles of the growth-rate based τ case represented by the solid line. Both cases are reasonably close to the isotropic MHD solution shown by the dotted line except the region inside the magnetosphere, where isotropic MHD produces higher density. Compared to the isotropic case, the anisotropic MHD simulation with growth-rate based τ slightly widens the subsolar magnetosheath. Figure 3.4 also indicates that the anisotropic MHD model yields smaller density and pressure across the magnetosheath.

2. The speed of the earthward plasma jet from the tail.

   The standard isotropic MHD simulation generates high-speed plasma jets from

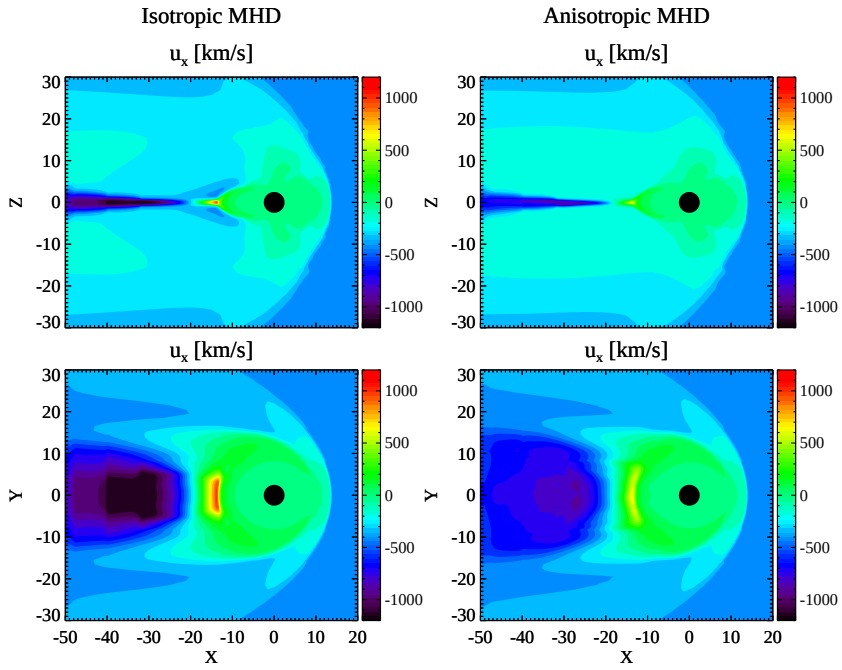

Figure 3.5: The x-direction velocity contour in the $Y = 0$ plane (top row) and the $Z = 0$ plane (bottom row) from the idealized magnetospheric simulations with isotropic MHD (left column) and anisotropic MHD with growth-rate based τ (right column) in the southward IMF case.

the tail reconnection site towards the Earth and the far tail. The speed reaches a highly unrealistic value of 1000 km/s, as Figure 3.5 shows in the left column. Observations give the typical tail flow speed smaller than 300 km/s during quiet time [*Baumjohann and Pashmann*, 1989], as also shown in our February 2009 event later. Higher speeds are only observed intermittently [*Angelopoulos et al.*, 1994]. The anisotropic MHD simulation shown in the right column significantly reduces this speed to about half. As these plasma jets are produced directly by the tail magnetic reconnection, slower jets imply a weaker reconnection. A qualitatively similar behavior was observed by *Birn et al.* [2001], who have found that pressure anisotropy leads to reduced growth rate of magnetic islands in their study for the Geospace Environment Modeling (GEM) magnetic reconnection challenge.

3. The magnitude and distribution of the nightside plasma pressure.

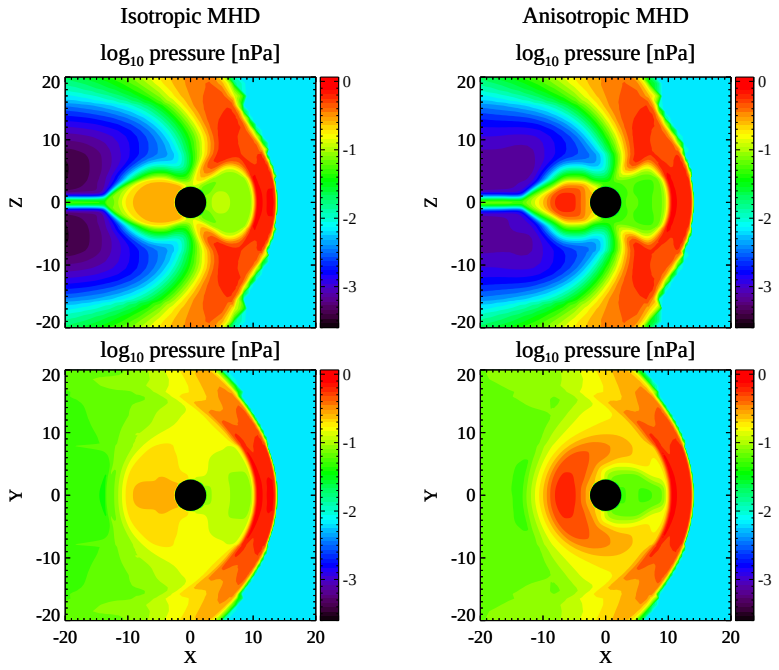

Figure 3.6: The logarithmic pressure contour in the $Y = 0$ plane (top) and the $Z = 0$ plane (bottom) from the idealized magnetospheric simulations with isotropic MHD (left column) and anisotropic MHD with growth-rate based τ (right column) in the southward IMF case.

Figure 3.6 displays pressure contours in the $Y = 0$ and $Z = 0$ planes. First, the nightside plasma pressure of the anisotropic MHD simulation is stronger than that in the isotropic MHD simulation. This agrees with the empirical modeling result reported by *Lui et al.* [1994], who found the inclusion of pressure anisotropy in empirical magnetic field models increases the plasma pressure in the quiet time nightside magnetosphere. In our anisotropic MHD simulation, the nightside pressure is mostly contributed by the perpendicular pressure given $p_\perp/p_\parallel > 1$ in this region (see Figure 3.1). Unlike the anisotropic MHD case, in which the perpendicular pressure can evolve differently from the parallel pressure, the traditional isotropic MHD forces the pressure in the inner magnetosphere to be isotropic thus limits the magnitude of the pressure, which directly affects the field-aligned currents in the ionosphere as we shall see later.

Second, compared to the pressure distribution from the isotropic MHD simu-

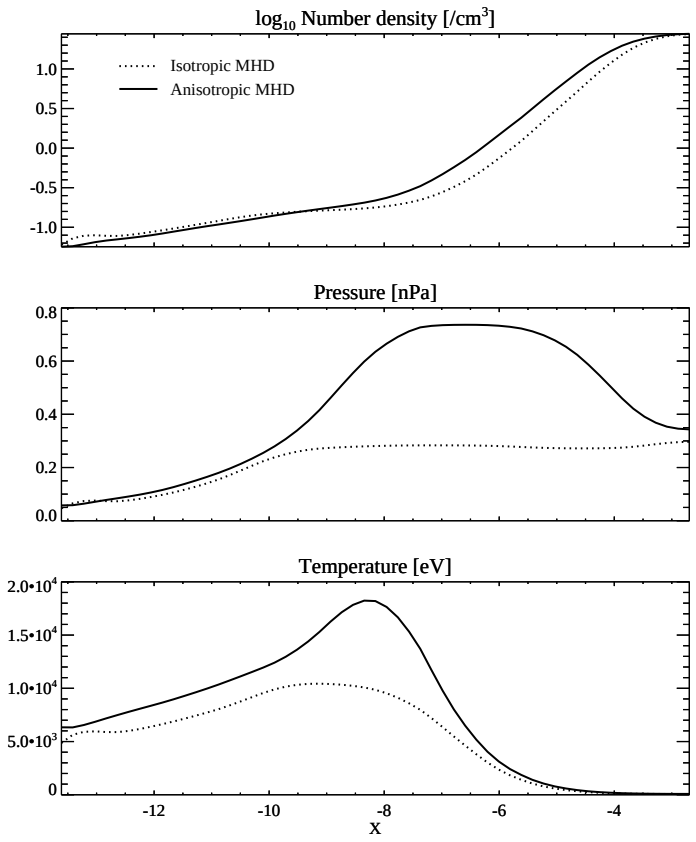

Figure 3.7: The number density (top panel), pressure (middle panel) and temperature (bottom panel) profiles of the nightside magnetosphere along the X-axis from the idealized magnetospheric simulations with isotropic MHD (dotted line) and anisotropic MHD with growth-rate based τ (solid line) in the southward IMF case. For the anisotropic MHD case, we plot the scalar pressure as defined by equation (3.6) and the corresponding scalar temperature.

lation, the anisotropic MHD simulation has a peak in average scalar pressure at around $-7\,\mathrm{R}_E$. A clearer view is given by the middle panel of Figure 3.7, in which the nightside pressure profiles are extracted along the X axis from the two simulations denoted by the dotted and the solid lines, respectively. The anisotropic MHD simulation has almost three times larger pressure at $-7\,\mathrm{R}_E$ than the isotropic MHD simulation does. The latter shows no peak in the pressure distribution. This difference leads to different pressure gradients, and furthermore different ring current patterns in the two simulations. Figure 3.7 also shows the density and temperature profiles along the X axis in the nightside. For the anisotropic MHD case, the average scalar temperature is plotted. The anisotropic MHD run produces hotter nightside plasma.

4. The magnitudes of the field-aligned currents and the cross polar cap potential.

   The anisotropic MHD simulation generates stronger region 2 currents compared to the isotropic simulation, as shown by the ionospheric view over the northern hemisphere in the left column of Figure 3.8. This is expected from the stronger nightside pressure in the anisotropic MHD simulation, since the nightside plasma contributes to the region 2 currents through the partial ring current. In addition, the cross polar cap potential shown in the right column of Figure 3.8 is slightly less in the anisotropic MHD case (the lower plot) than in the isotropic MHD case (the upper plot).

5. The pattern of the ring current.

   As mentioned before, the different pressure distributions from the anisotropic MHD and isotropic MHD simulations result in different ring current patterns in these two cases. In general, the anisotropic MHD case will give stronger ring current as the pressure gradient is larger than that of the isotropic case. A stricter analysis should consider the individual contributors to the ring cur-

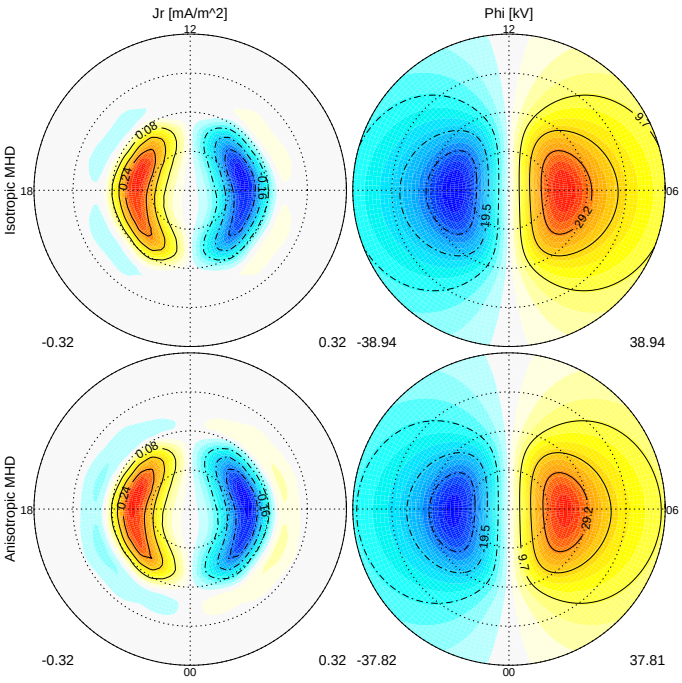

Figure 3.8: The ionospheric field-aligned currents (left column) and cross polar cap potential (right column) of the northern hemisphere from the idealized magnetospheric simulations with isotropic MHD (top) and anisotropic MHD with growth-rate based τ (bottom) in the southward IMF case.

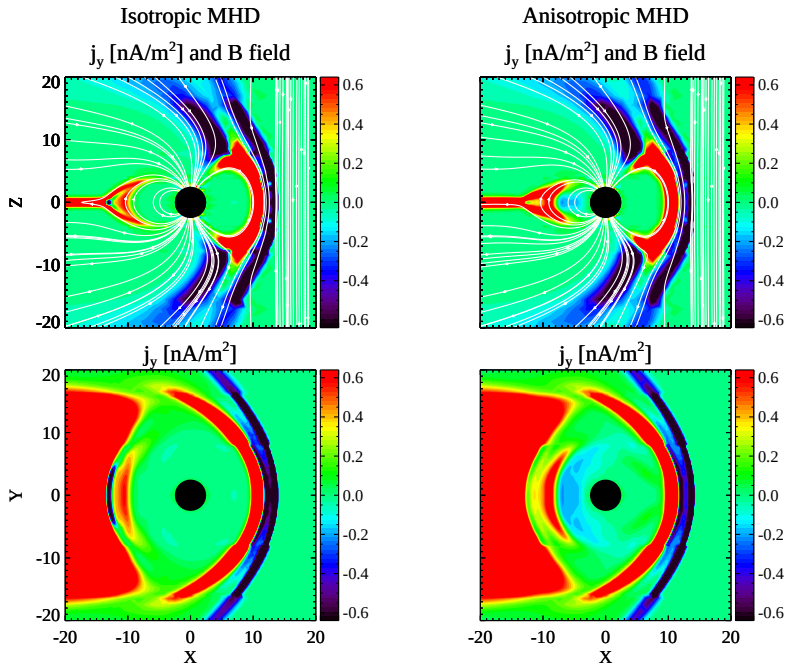

Figure 3.9: The Y-direction current density contour in the $Y = 0$ plane (top row) and the $Z = 0$ plane (bottom row) from the idealized magnetospheric simulations with isotropic MHD (left column) and anisotropic MHD with growth-rate based τ (right column) in the southward IMF case. The field lines are shown in the $Y = 0$ plane.

rent. For isotropic MHD, only the gradient of the pressure plays a role. For anisotropic MHD, both the gradient of the perpendicular pressure and another term involving the difference between the perpendicular and parallel pressures contribute to the ring current. The additional term in anisotropic MHD introduces an eastward ring current, which make the original westward ring current peak away from the equator, as found by *Cheng* [1992b] and confirmed by *Zaharia et al.* [2004] in their equilibrium model. Our anisotropic MHD simulation produces the same phenomenon.

In Figure 3.9, the Y-direction current density, as an indicator of the ring current density, is shown in the meridional and equatorial planes. The color scale is saturated for j_y above $0.64\,n\mathrm{A/m^2}$ and below $-0.64\,n\mathrm{A/m^2}$. The westward current (in red) at around $-9\,\mathrm{R}_E$ is much more prominent in the anisotropic MHD case. It peaks away from the equator and extends to higher latitude along

the field lines. Meanwhile an eastward current (in blue) peaked at the equator at around $-7\,\mathrm{R}_E$ appears in the anisotropic MHD case, which is contributed from both the perpendicular pressure gradient and the additional pressure anisotropy term. The magnitude of the eastward current (around $0.3\,n\mathrm{A/m^2}$) is smaller than the observed values (about $1\,n\mathrm{A/m^2}$) from *Lui and Hamilton* [1992]. The discrepancy is expected given the lack of an inner magnetospheric model.

3.2.2 Northward IMF case

For the northward IMF case, we also perform a set of five runs. All parameters remain the same as the southward IMF case except the change in the IMF orientation.

The pressure anisotropy in the meridional and equatorial planes is shown in Figure 3.10. Again we observe highly perpendicular pressure in the magnetosheath and in the vicinity of the Earth. Increased relaxation time τ leads to increased pressure anisotropy. The $\tau = 10\,\mathrm{s}$ run is most similar to the growth-rate based τ run. In the $\tau = 100\,\mathrm{s}$ and $\tau = \infty$ simulations, the maximum of $p_\perp/p_\parallel$ is much larger than 4 such that the anisotropy ratio is saturated on the color scale.

Figure 3.11 displays the spatial variation of τ. Most of it is very similar to the southward IMF case, except no mirror instability is excited in the close tail. The magnitude of τ varies between less than 1 second to hundreds of seconds, depending on the location.

The effect of pressure anisotropy on the width of the magnetosheath is shown in Figure 3.12. Similar to the southward IMF case, the increased pressure anisotropy results in a thicker magnetosheath. However, compared to Figure 3.4, the width of the magnetosheath is more sensitive to pressure anisotropy in the northward IMF case, as the same amount of relaxation time τ results in a larger change of the magnetosheath position in the northward IMF case than in the southward IMF case. An exception occurs when $\tau = 100\,\mathrm{s}$, which does not seem to widen the magnetosheath more for

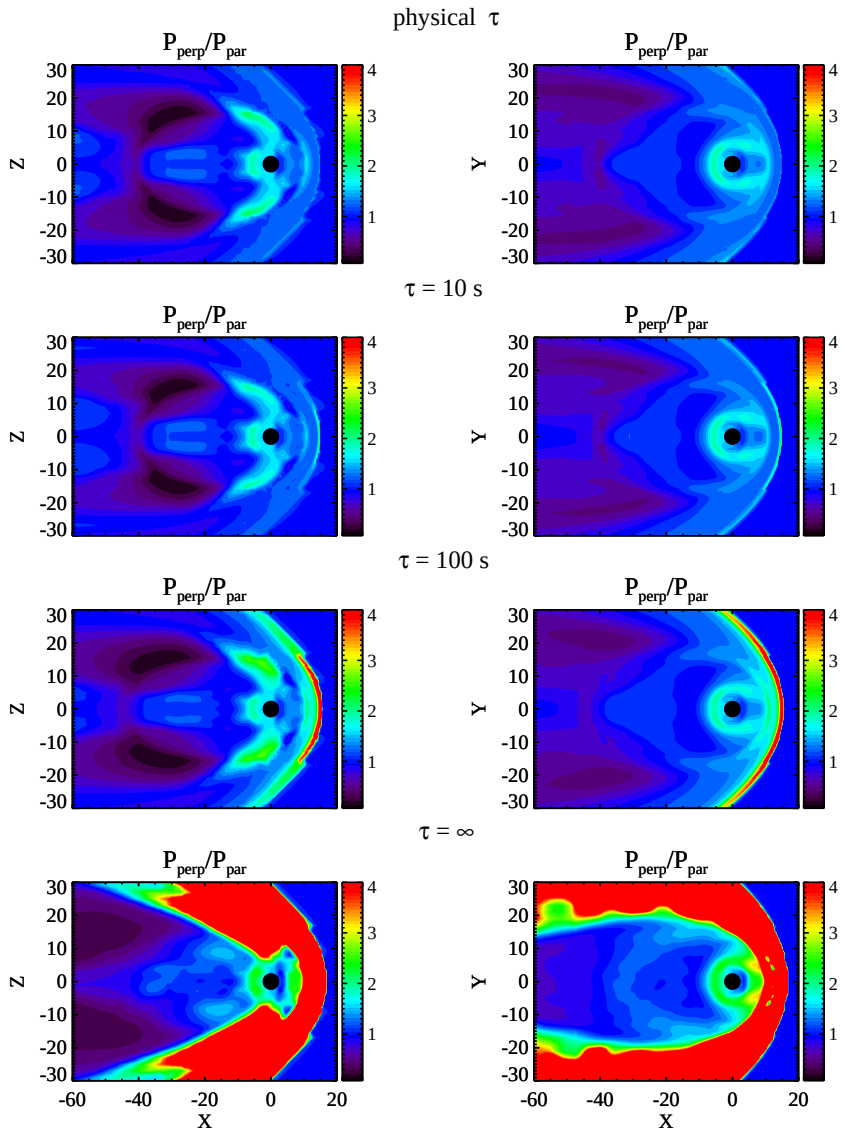

Figure 3.10: Same as Figure 3.1 for the northward IMF case.

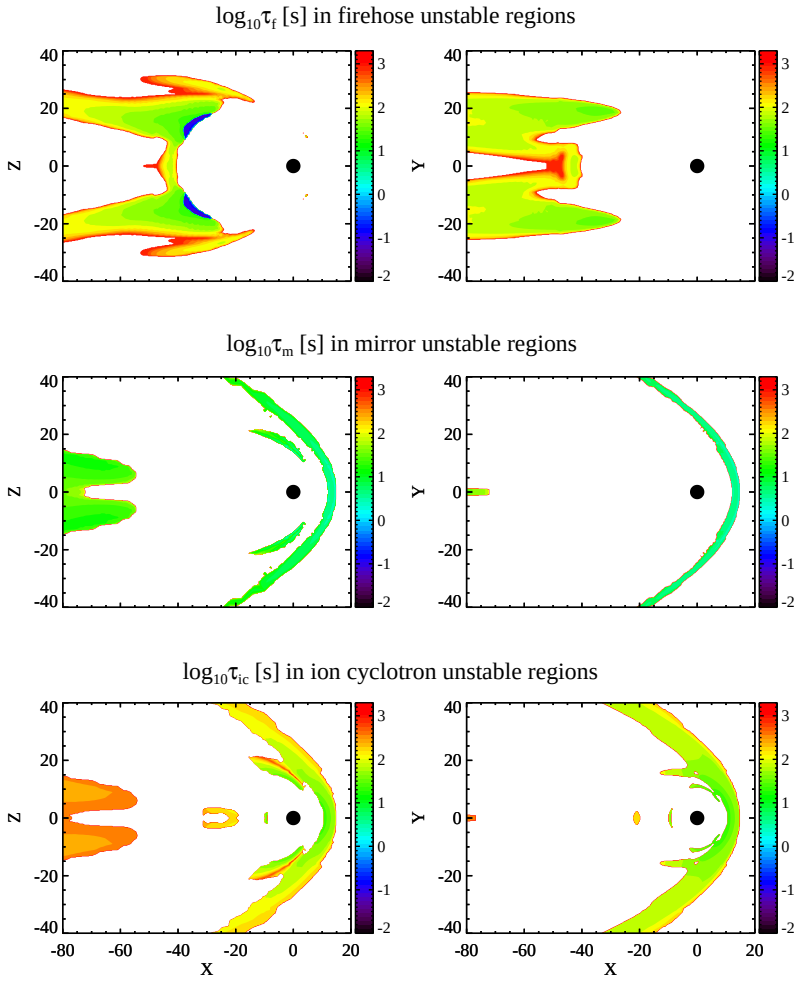

Figure 3.11: Same as Figure 3.2 for the northward IMF case.

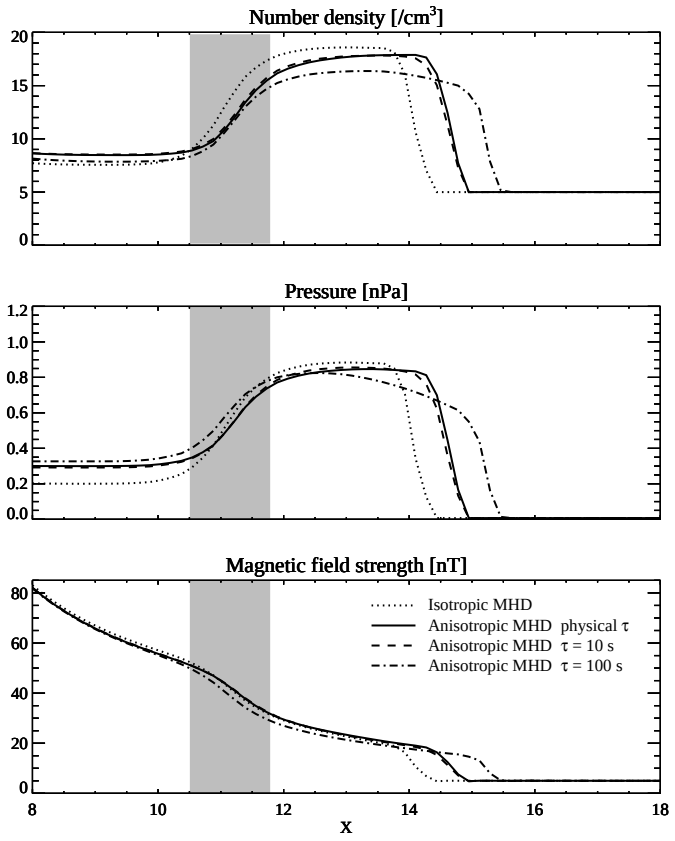

Figure 3.12: Same as Figure 3.4 for the northward IMF case.

the northward IMF than for the southward IMF.

With northward IMF, a plasma depletion layer just outside of the magnetopause forms. The depletion layer is identified by decreased plasma density and increased magnetic field strength relative to the adjacent magnetosheath plasma [*Zwan and Wolf*, 1976], as marked by the shadowed region in Figure 3.12. The comparison between the isotropic MHD and the anisotropic MHD with growth-rate based τ, $\tau = 10\,\mathrm{s}$ and $\tau = 100\,\mathrm{s}$ reveals that pressure anisotropy increases the density depletion, although the overall effect is very small. The same conclusion has been drawn by Denton from the study of a 2D magnetosheath model [*Denton and Lyon*, 2000].

3.3 Non-idealized Quiet Time Magnetospheric Simulations

To further validate our model, we perform magnetospheric simulations driven by real solar wind and IMF conditions. As we do not couple any ring current model to anisotropic BATS-R-US for this study, we only simulate the quiet time magnetosphere. Two time periods are selected based on the geomagnetic activity level indicated by the Dst index, the positions of the THEMIS satellites and the data availability. Both the dayside and nightside magnetosphere are covered in our validation. We apply the global relaxation term in the simulations. Comparisons between the simulations and measurements are reported.

3.3.1 Dayside validation – 16 June 2008

The first time interval we choose is from 12 to 24UT on 16 June 2008, when two THEMIS satellites B and C went across the dayside magnetosheath and the bow shock. The solar wind and IMF conditions measured by the ACE satellite are shown in Figure 3.13. The IMF B_z component varies a bit between positive and negative values, yet the magnitude is small. The average Dst index during this period is about $-13\,\mathrm{nT}$. Therefore the magnetosphere basically stays in a quiet state.

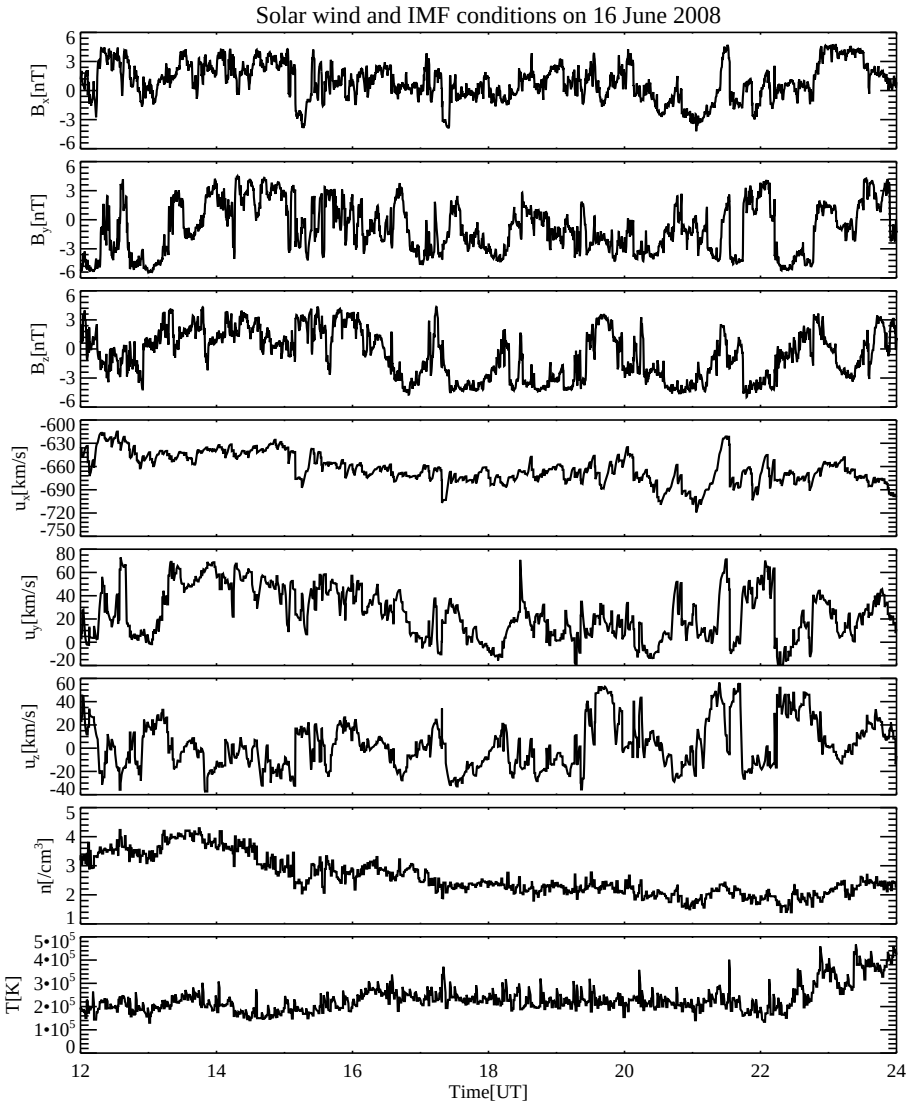

Figure 3.13: The solar wind and IMF conditions from ACE data for 12-24UT on 16 June 2008.

The 3D computational domain extends from $X = -224\,\mathrm{R}_E$ to $X = 32\,\mathrm{R}_E$, from $Y = -128\,\mathrm{R}_E$ to $Y = 128\,\mathrm{R}_E$, and from $Z = -128\,\mathrm{R}_E$ to $Z = 128\,\mathrm{R}_E$. To better capture the magnetosheath where THEMIS B and C cross, we increase the grid resolution to $1/8\,\mathrm{R}_E$ in that region. Other parameters are the same as they are in the idealized simulations. We perform two simulations with anisotropic and isotropic BATS-R-US respectively. We use the growth-rate based relaxation time and the global relaxation time of 200 seconds in the anisotropic MHD run.

First we look at the pressure anisotropy. In the top panel of Figure 3.14, we plot the anisotropy ratio $p_\perp/p_\parallel$ at 18UT in the meridional and the equatorial planes, with the trajectories of THEMIS B and C overplotted. The lower two panels show the anisotropy ratio extracted along the satellite orbits from the simulation against the actual data. The comparison indicates that the simulation does fairly well in reproducing the anisotropy ratio in the magnetosheath, including the anisotropy jumps near the magnetopause.

Second, as the idealized simulations show the evidence of the mirror and ion cyclotron instabilities across the magnetosheath, we plot the criteria and relaxation times of these two instabilities along the satellite orbits in Figure 3.15. The first and third row from top show the variations of the anisotropy factor $A = p_\perp/p_\parallel - 1$ with red lines representing the mirror and ion cyclotron unstable bound respectively. An instability is excited if A is larger than the unstable bound, i.e., the black line is higher than the red one, under which circumstance the relaxation times are shown in the second and fourth row. The mirror and ion cyclotron instabilities are found in the time interval of 13UT-16.5UT during the magnetosheath crossing by THEMIS B, and in the time interval of 16.5UT-23UT for THEMIS C. The mirror instability plays a more important role, because its bound is exceeded by approximately the same amount as the ion cyclotron instability bound is exceeded, but the relaxation time of the mirror instability is much smaller than that of the ion cyclotron instability, so

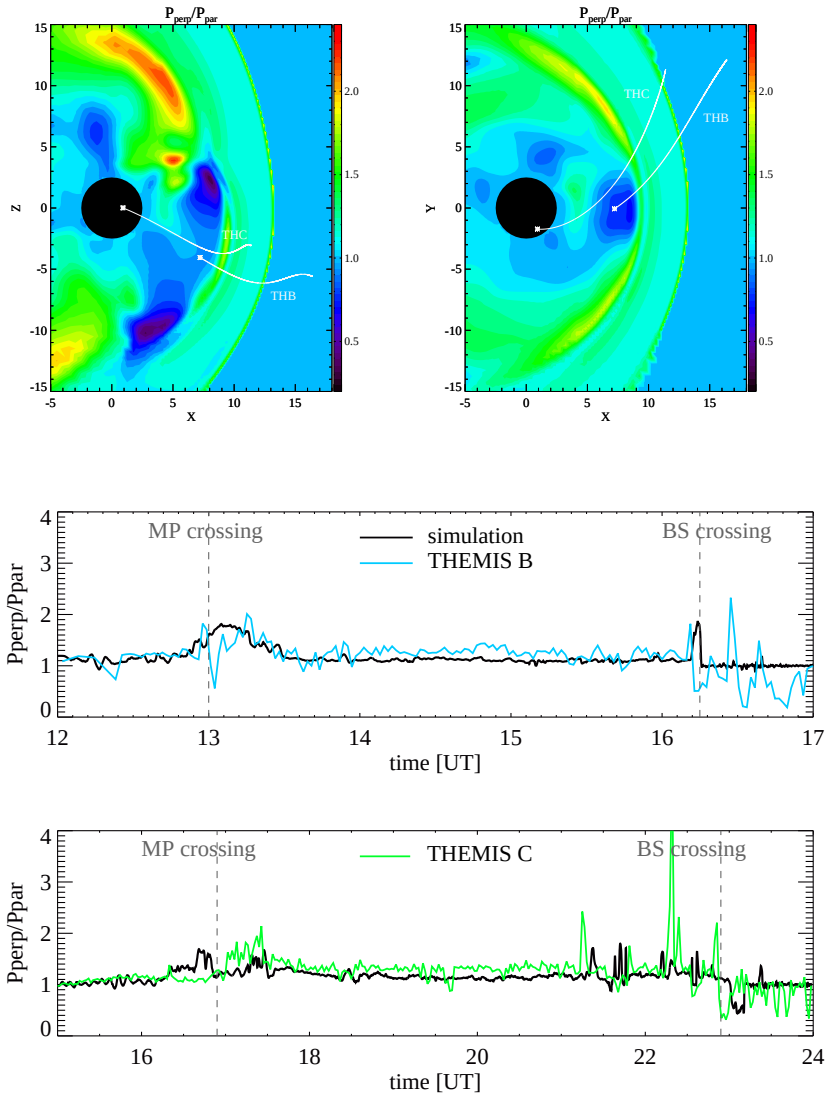

Figure 3.14: The pressure anisotropy ratio $p_\perp/p_\parallel$ in the $Y = 0$ (top left panel) and $Z = 0$ (top right panel) planes at 18UT on 16 June 2008. Trajectories of THEMIS B and C during 12-24UT are shown by white lines started from the stars. The bottom two panels show the simulated $p_\perp/p_\parallel$ (black lines) against the actual data along the satellite trajectories.

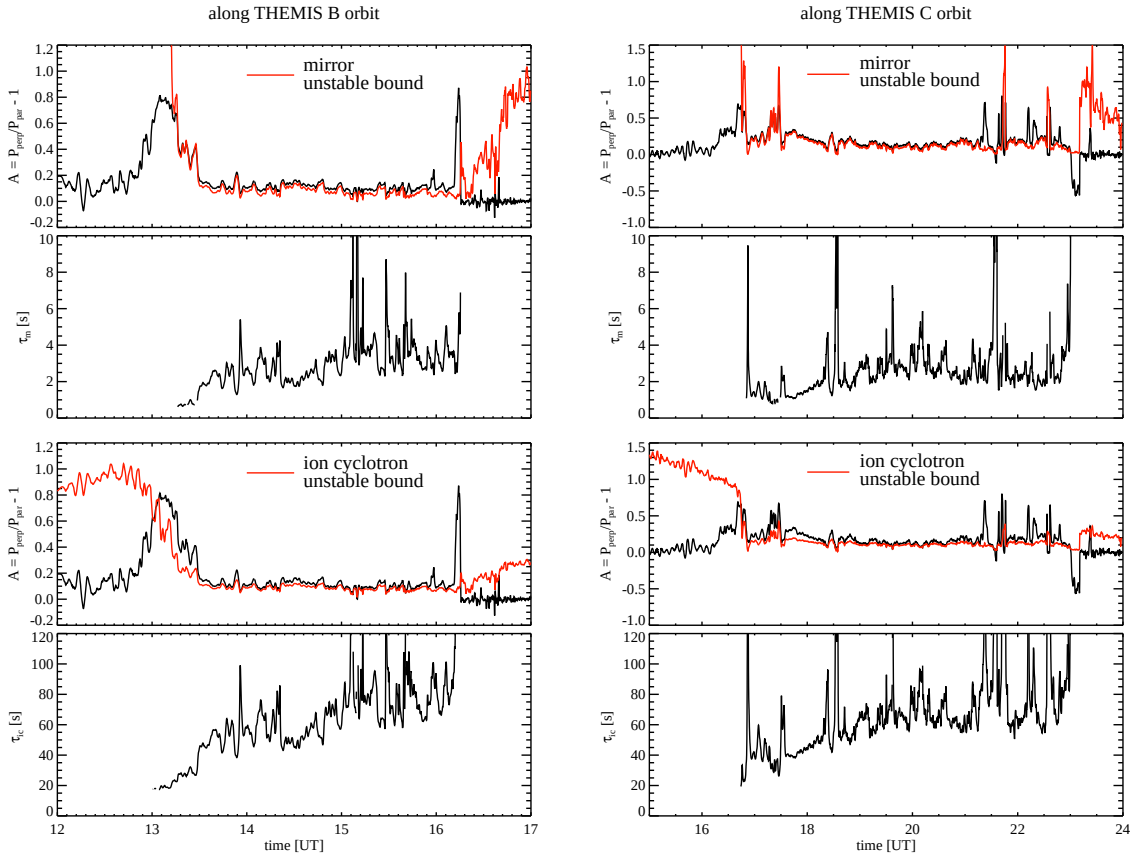

Figure 3.15: The simulated anisotropy factor A (black lines in the first and the third row from top), the unstable bounds (red lines) and the relaxation time (the second and fourth row from top) along THEMIS B and C orbits during 12-24UT on 16 June 2008.

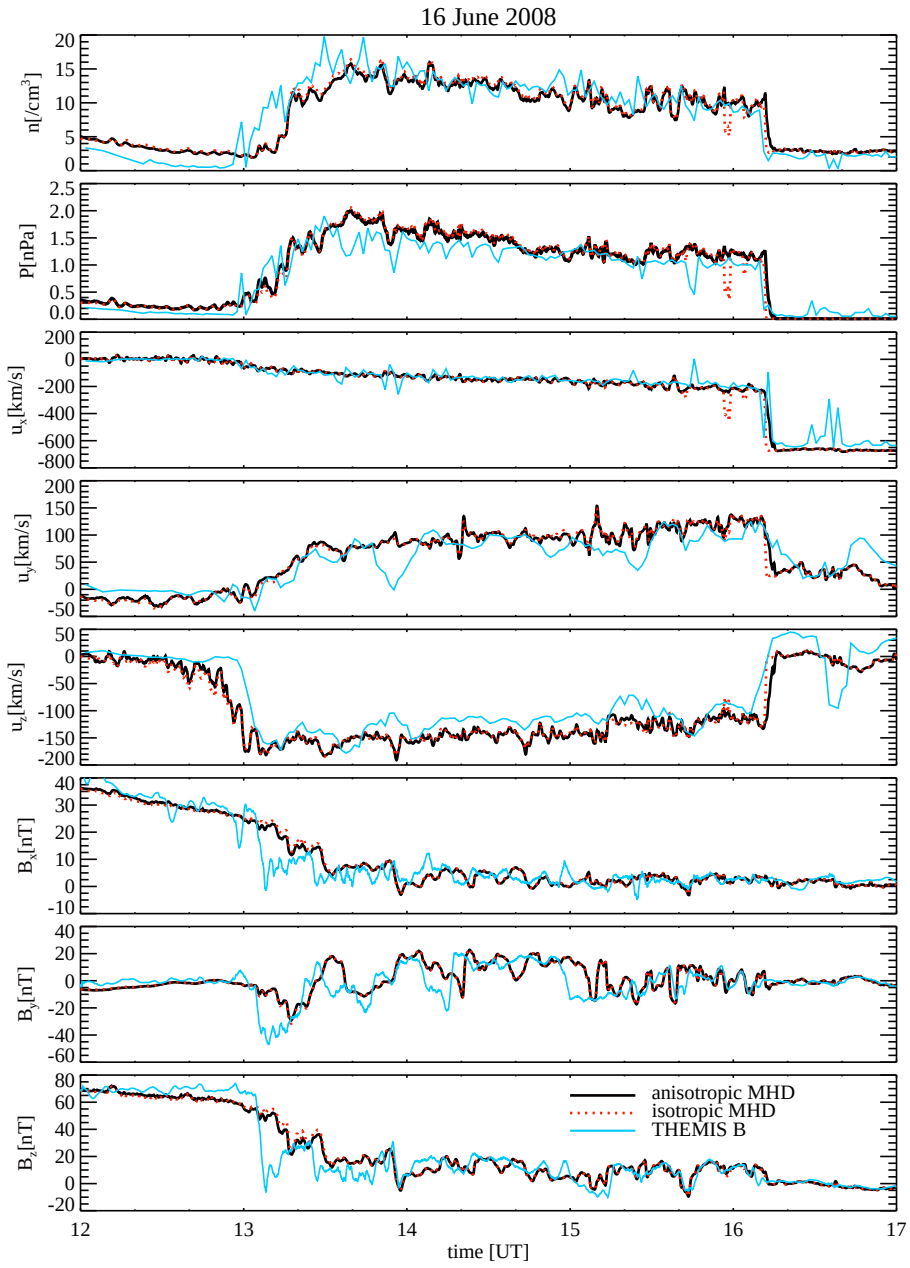

Figure 3.16: The simulated and measured variables along the THEMIS B orbit during 12-24UT on 16 June 2008.

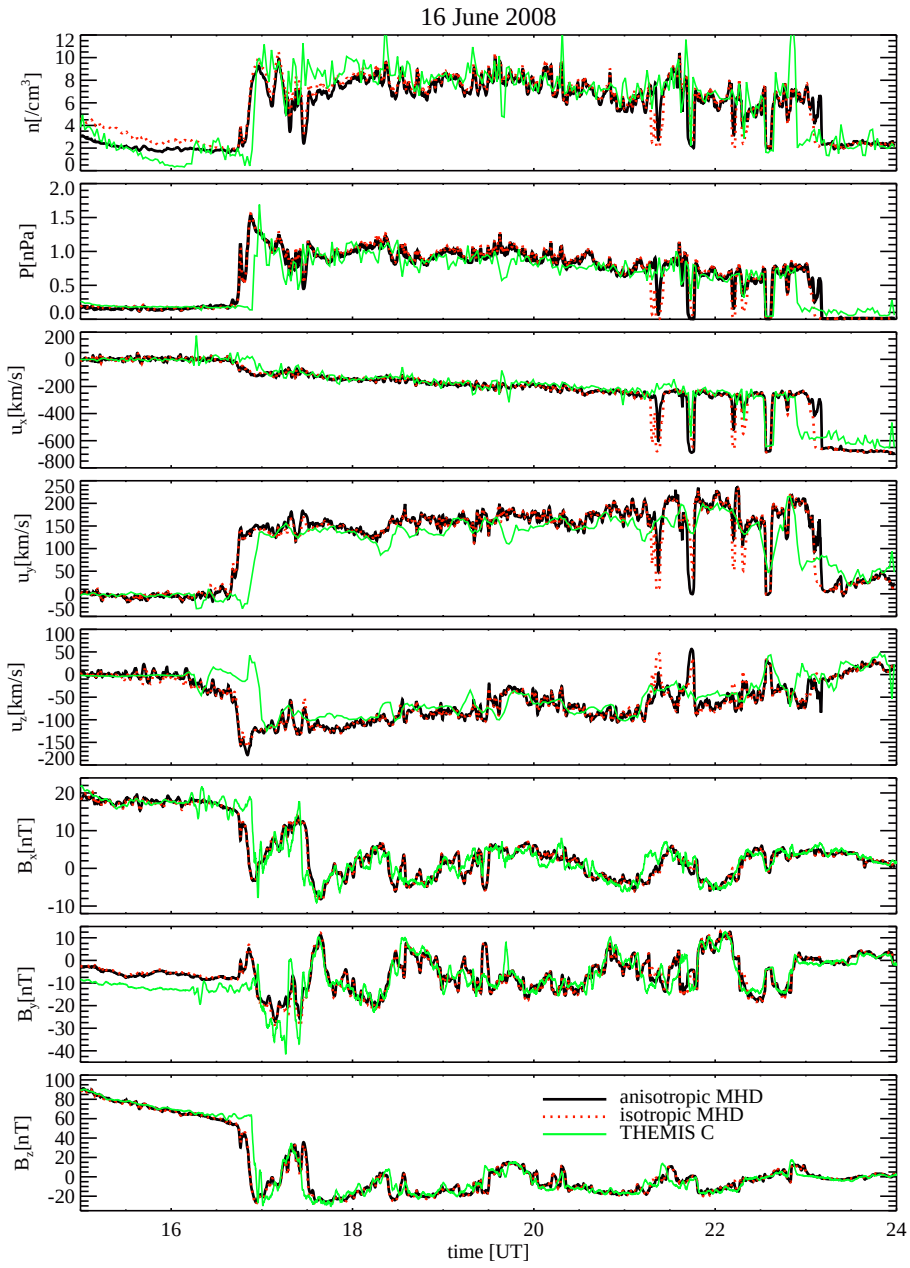

Figure 3.17: The simulated and measured variables along the THEMIS C orbit during 12-24UT on 16 June 2008.

	THEMIS B		THEMIS C	
	Isotropic MHD	Anisotropic MHD	Isotropic MHD	Anisotropic MHD
n [/cc]	2.18	2.29	1.66	1.66
p [nPa]	0.25	0.24	0.22	0.21
u_x [km/s]	63.37	52.93	80.21	74.22
u_y [km/s]	37.67	36.45	46.68	45.23
u_z [km/s]	45.48	46.12	42.52	42.30
b_x [nT]	5.81	5.52	3.95	3.93
b_y [nT]	11.75	11.77	6.85	6.70
b_z [nT]	11.57	10.86	10.13	10.32

Table 3.1: RMS errors of the simulated variables in comparison to the THEMIS data for the 16 June 2008 event

the former results in larger changes in the parallel pressure.

Finally, we extract the number density, average pressure, velocity and magnetic field from the anisotropic MHD simulation to compare with the data from the ESA instrument and the isotropic MHD solutions, as shown in Figure 3.16 and Figure 3.17. The root-mean-square (RMS) errors with respect to the data are presented in Table 3.1. Overall the anisotropic and isotropic MHD simulations give very similar variations of the MHD variables across the magnetosheath. The simulations both resemble the measurements reasonably. However, we are more interested in any improvements or drawbacks brought by the anisotropic MHD simulation. One improvement we observe from the figures is that the anisotropic MHD simulation reduces or even eliminates some sudden drops in the density, the average pressure and especially the velocity behind the bow shock, leading to better agreement with the data. The RMS errors reveal an obvious improvement on the velocity. Note both the anisotropic and isotropic MHD simulations do not predict the location of the bow shock well especially for THEMIS C crossing. But the discrepancy between simulated and measured bow shock locations can also be caused by the plane parallel solar wind conditions based on a point measurement by ACE. We checked that the agreement with data is

improved if the satellite positions are shifted slightly (by $0.2\,\mathrm{R}_E$) towards the positive X direction.

3.3.2 Nightside validation – 6 February 2009

The second time interval is from 14 to 24UT on 6 February 2009, during which the THEMIS satellites were in the nightside magnetosphere. Both THEMIS B and C were close to the tail current sheet. Figure 3.18 shows the solar wind and IMF conditions from the combined ACE and WIND data. B_z has small variations around 0. The averaged Dst index is about $-14\,\mathrm{nT}$.

We compute the simulations in a manner similar to the dayside study, except that we do not have a high resolution magnetosheath, but $1/8\,\mathrm{R}_E$ resolution in the tail where the satellites cross. Both the anisotropic MHD with growth-rate depended τ and isotropic MHD simulations are conducted.

We plot $p_\perp/p_\parallel$ in the $Y = 0$ and $Z = 0$ planes and overplot the satellite trajectories in the top panels of Figure 3.19. A direct comparison between the simulation and the data is shown in lower panels. The overall results are much worse than the dayside comparison, as the tail dynamics cannot be fully described by MHD.

The number density, average pressure, velocity and magnetic field profiles along the satellite orbits are shown in Figures 3.20 and 3.21. Table 3.2 shows the RMS errors. The agreement looks poor compared to the dayside case. However, compared to the isotropic simulation, the anisotropic MHD simulation improves the agreement with data on u_y and u_z for THEMIS B and u_x and u_z for THEMIS C. This matches with the results we have seen in the idealized simulations, as the anisotropic MHD model reduces the plasma speed in the tail. But the u_x agreement is worse in the anisotropic case for THEMIS B. The anisotropic MHD simulation also sightly improves the magnetic field agreement with the data, particularly B_z for THEMIS C. Note a major contradiction to the measurement occurs at around 19UT, when both the

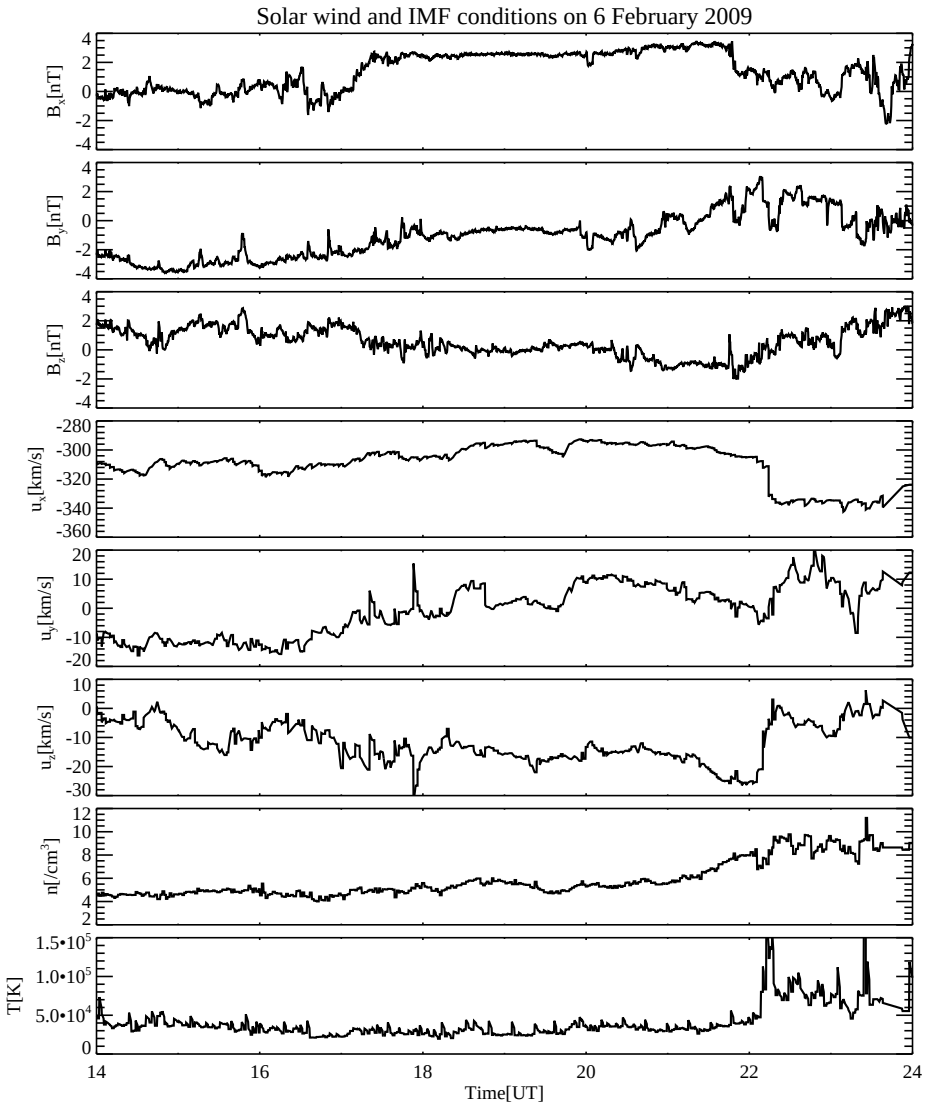

Figure 3.18: The solar wind and IMF conditions from ACE data for 12-24UT on 6 February 2009.

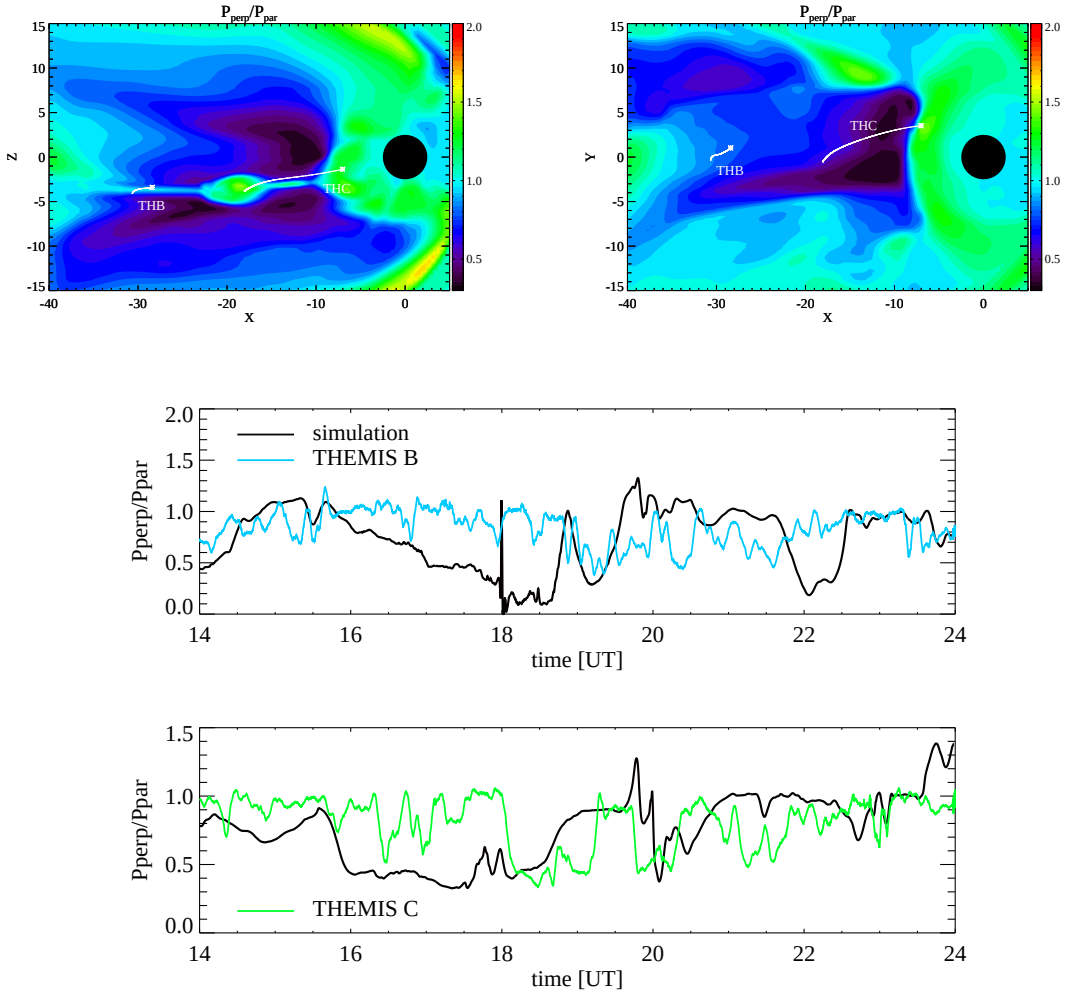

Figure 3.19: The pressure anisotropy ratio $p_\perp/p_\parallel$ in the $Y = 0$ (top left panel) and $Z = 0$ (top right panel) planes at 24UT on 6 February 2009. Trajectories of THEMIS B and C during 14-24UT are shown by white lines started from the stars. The bottom two panels show the simulated $p_\perp/p_\parallel$ (black lines) against the actual data along the satellite trajectories.

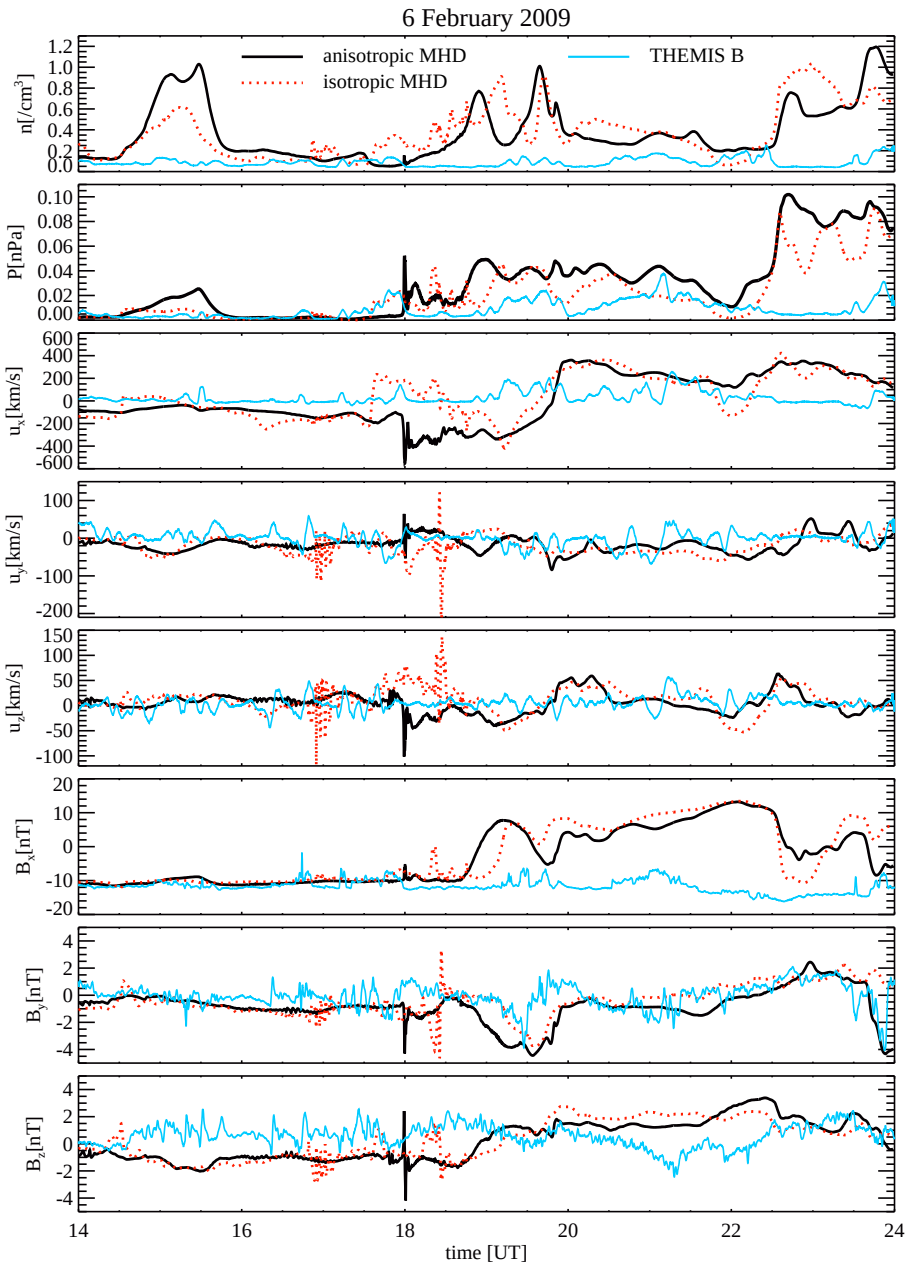

Figure 3.20: The simulated and measured variables along the THEMIS B orbit during 14-24UT on 6 February 2009.

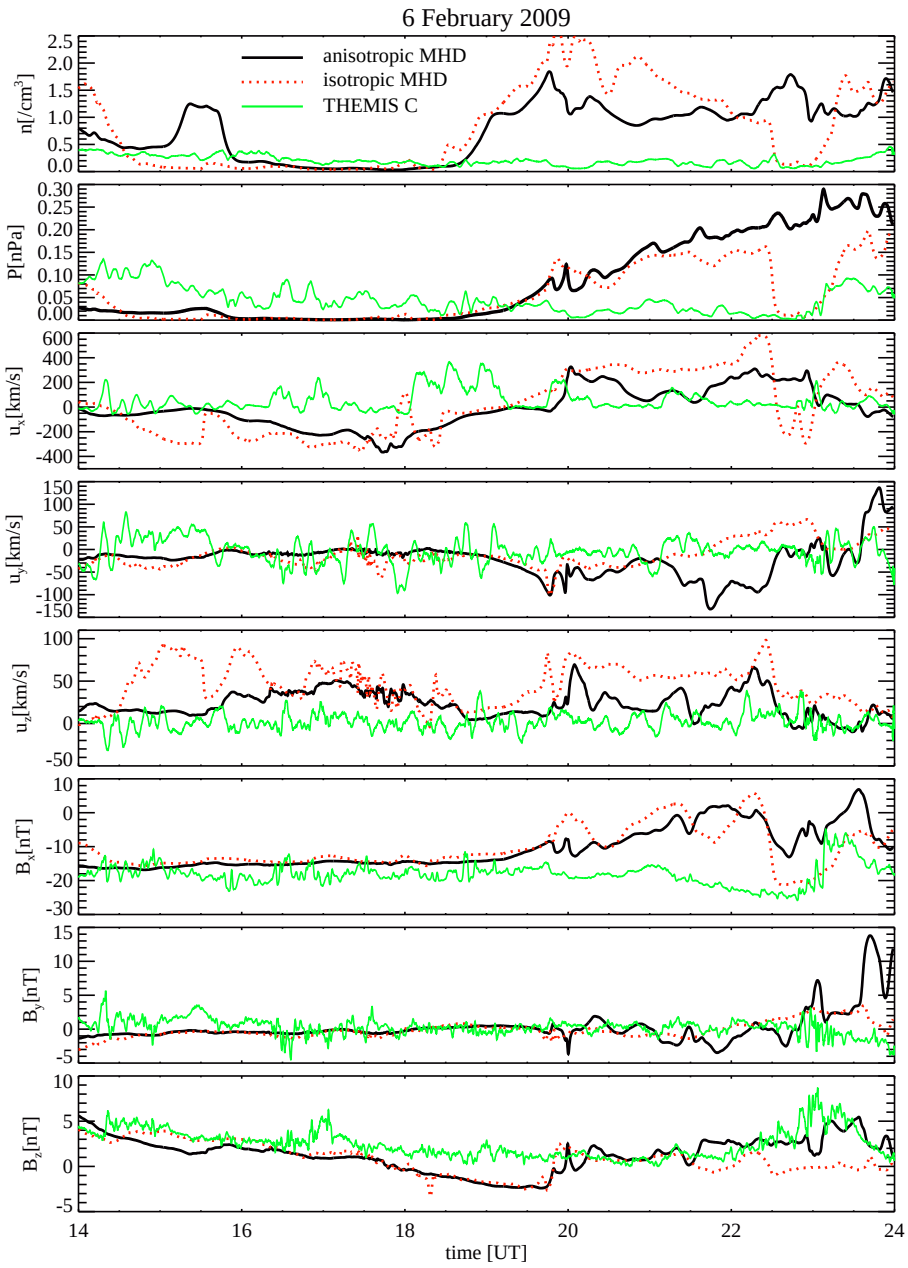

Figure 3.21: The simulated and measured variables along the THEMIS C orbit during 14-24UT on 6 February 2009.

	THEMIS B		THEMIS C	
	Isotropic MHD	Anisotropic MHD	Isotropic MHD	Anisotropic MHD
n [/cc]	0.39	0.40	1.00	0.78
p [nPa]	0.025	0.035	0.08	0.11
u_x [km/s]	195.07	222.87	272.14	201.28
u_y [km/s]	40.78	37.39	49.98	59.27
u_z [km/s]	32.89	28.45	53.57	32.07
b_x [nT]	13.37	12.46	10.10	10.10
b_y [nT]	1.30	1.38	1.98	3.11
b_z [nT]	1.93	1.89	2.44	2.04

Table 3.2: RMS errors of the simulated variables in comparison to the THEMIS data for the 6 February 2009 event

isotropic and anisotropic MHD simulations predict that THEMIS B crosses the current sheet, identified by the sign change of B_x. The incorrect position of the simulated current sheet closely relates to the bad data-model agreement on other variables.

3.4 Summary

In this chapter we apply Anisotropic BATS-R-US to 3D global magnetospheric simulations. We have neglected the electron pressure in the model, and the resulting pressure equations that Anisotropic BATS-R-US solves are equivalent to the double adiabatic formulation. The model is further improved and specified to magnetospheric simulations by setting the pressure anisotropy relaxation time τ based on the growth rates of the firehose, mirror and ion cyclotron instabilities, which in turn depend on local plasma parameters, for the instability related pressure anisotropy relaxation term. We have also implemented a global pressure anisotropy relaxation term that limits pressure anisotropy everywhere in the magnetosphere with some constant relaxation time τ_g set externally.

We have performed both idealized and real quiet time magnetospheric simulations with Anisotropic BATS-R-US. The idealized magnetosphere simulations with

southward IMF show several interesting differences between anisotropic and isotropic MHD in modeling the magnetosphere, further revealing the effects of pressure anisotropy. First of all, pressure anisotropy thickens the magnetosheath and changes the shape of the magnetosphere. Second, pressure anisotropy reduces the reconnection rate and consequently the flow speed in the tail significantly. Third, pressure anisotropy increases the nightside plasma pressure and forms a pressure peak away from the Earth. The increase in the nightside pressure strengthens the region 2 currents. The steepened pressure distribution results in a stronger ring current. Some of these results are supported by previous studies that obtained similar features. The idealized magnetosphere simulations with northward IMF confirms the increased density depletion near the magnetopause resulting from pressure anisotropy that has been found by past studies.

The simulations of the real magnetosphere during geomagnetic quiet time provides a direct evaluation of Anisotropic BATS-R-US when comparing the simulations to the measurements. In general the model predicts the dayside magnetosheath better than the nightside magnetosphere. Compared to the isotropic MHD simulations, the anisotropic MHD simulations improve the model-data agreement on the velocity. Not much improvement has been seen in the other variables.

Despite of its many advantages, our anisotropic MHD model exhibits several limitations that may require improvements in the future. First of all, the anisotropic pressure equations are formulated equivalently to the double adiabatic equations. However, the double adiabatic approximation is not applicable to some processes, for example mirror instability [*Kulsrud*, 1982; *Shi et al.*, 1987]. Although the pressure relaxation term mimics the effect of instabilities on pressure, it is still an approximation. Second, like isotropic MHD, anisotropic MHD based on the double adiabatic approximation is not appropriate to describe the inner magnetospheric dynamics, since it cannot capture the diamagnetic drift and neglects the heat flux [*Wolf et al.*,

2009; *Heinemann and Wolf*, 2001]. To better describe the near-Earth plasma and perform geomagnetic storm simulations, we couple Anisotropic BATS-R-US to inner magnetospheric models that capture various kinetic processes. The details will be reported in the following chapter.

CHAPTER IV

Global Magnetospheric Simulations with Coupled Anisotropic BATS-R-US and Ring Current Models

We have successfully applied Anisotropic BATS-R-US to quiet time magnetospheric simulations. Although Anisotropic BATS-R-US is more advanced than the standard isotropic MHD model BATS-R-US, it is still not appropriate in describing the inner magnetospheric dynamics. In fact, neither the isotropic nor the anisotropic MHD equations can properly capture gradient-curvature drift [*Wolf et al.*, 2009], which is energy-dependent and leads to the formation of the ring current. Therefore, MHD models are not applicable to simulate various physical processes of the near-Earth plasma. A better approach is to employ kinetic models, especially during time periods of strong geomagnetic activity, when the hot ring current plasma plays an important role.

In this chapter we report the two-way couplings between Anisotropic BATS-R-US and both the Rice Convection Model (RCM) [*Toffoletto et al.*, 2003] and the Comprehensive Ring Current Model (CRCM) [*Fok et al.*, 2001], which are somewhat different from the existing couplings between BATS-R-US and the two ring current models in the SWMF. The coupling between Anisotropic BATS-R-US and the RCM is simple and straightforward, given the coupling of the isotropic MHD version has been established already. However, since the RCM assumes pitch angle isotropy, this coupling

will reduce or even eliminate pressure anisotropy in the inner magnetosphere, thus greatly limits the capability of Anisotropic BATS-R-US. Alternatively, the CRCM can resolve pitch angle anisotropy. Therefore it is more meaningful to couple Anisotropic BATS-R-US with the CRCM to obtain self-consistent solutions of pressure anisotropy throughout the whole magnetosphere. This coupling requires a new algorithm. Again, we neglect the electron pressure in the magnetosphere, so Anisotropic BATS-R-US does not use electron pressure for its coupling with ring current models.

The following content of the chapter consists of four sections. In Section 4.1 we briefly review the past work on coupling magnetospheric models with ring current models, as well as the two ring current models involved in this study. In Section 4.2 we describe the coupling algorithms. In Section 4.3 and Section 4.4 we present idealized quiet time and real storm time magnetospheric simulations, respectively. We also compare the results from the RCM and CRCM-coupled models. Our conclusions are in section 4.5.

4.1 Background

4.1.1 Previous work on ring current model coupling

Several global MHD models have been coupled with ring current models, mainly the RCM and the CRCM. The Lyon-Fedder-Mobarry (LFM) MHD model [*Lyon et al.*, 2004] is two-way coupled with the RCM [*Toffoletto et al.*, 2004; *Pembroke et al.*, 2012]. The LFM model is also used to drive the CRCM [*Fok et al.*, 2006; *Moore et al.*, 2008]. The Open Geospace General Circulation Model (OpenGGCM) [*Raeder et al.*, 2001] is one-way coupled to RCM [*Hu et al.*, 2010]. The BATS-R-US MHD model is two-way coupled with both the RCM [*De Zeeuw et al.*, 2004] and the CRCM [*Buzulukova et al.*, 2010; *Glocer et al.*, 2012]. These coupled models successfully combine global MHD models with kinetic ring current models, providing a key step towards constructing a

global general circulation model.

No coupling between a global anisotropic MHD model and a ring current model has been reported to date. However, from a broader perspective of magnetospheric modeling, equilibrium models with pressure anisotropy have been coupled to ring current models. *Zaharia et al.* [2005] fed their 3-D equilibrium code with anisotropic pressure in the equatorial plane from the UNH-RAM ring current model [*Jordanova et al.*, 1997] and analyzed the computed magnetic fields and electric fields during a geomagnetic storm. *Wu et al.* [2009] extended another equilibrium code, RCM-E, which has already been coupled with the RCM, to include anisotropic pressure. They also proposed the possibility of coupling the equilibrium code with the CRCM. These studies are very insightful in examining the impact of pressure anisotropy in the inner magnetosphere.

4.1.2 RCM and CRCM

Both the RCM and CRCM are kinetic models of the Earth's ring current, which is carried primarily by tens of keV ions drifting westward in the closed field line region surrounding the Earth. Both models are based on the bounce-averaged calculation that treats the particle distribution as a result of averaging over the particle bounce motions along the closed field lines. The underlying assumption is that the time scale of the variation for inner magnetospheric plasma properties is much larger than the particle bounce periods. Furthermore, both models compute the magnetospheric electric fields self-consistently with the plasma distribution. In addition, they use similar computational grids set in the ionosphere based on longitudes and latitudes.

Despite of their many common features, the RCM assumes isotropic pitch angle distribution while the CRCM solves full pitch angle distribution. This is the major difference between the RCM and the CRCM, which results in different pictures of the inner magnetosphere. Observations have found that the ring current region is

characterized by anisotropic ion and electron distributions during both quiet time and disturbed time [*Lui and Hamilton*, 1992]. Even the plasma sheet, which has long been considered to have an isotropic particle distribution, contains electrons with anisotropic pitch angle distribution, according to *Walsh et al.* [2011].

4.2 Algorithm

The general concept of the coupling between two components is to interchange variables between the two components periodically. In a typical GM-IE-IM combination in the SWMF, GM-IE and GM-IM are two-way coupled, while IE-IM is one-way coupled. More specifically, GM sends the field-aligned currents to IE and the magnetic field topology to IM. IE solves for the ionospheric electric potential on a 2D height-integrated spherical surface and passes the electric potential to GM and IM. IM sends the pressure of the inner magnetosphere to GM. The three components connect together tightly by the messages passed around regularly. In terms of computational efficiency, one practical task is to determine the optimal frequency of coupling one component to another so that the states of the two components have changed significantly but not dramatically during the time interval of two successive couplings.

Although the two-way coupling algorithms between BATS-R-US and both the RCM and the CRCM have been developed [*De Zeeuw et al.*, 2004; *Glocer et al.*, 2012], these algorithms need to be modified to accommodate the coupling between Anisotropic BATS-R-US and the two ring current models.

4.2.1 Anisotropic BATS-R-US and the RCM Coupling

The majority of the coupling between BATS-R-US and the RCM [*De Zeeuw et al.*, 2004] can be migrated directly to the coupling between the Anisotropic BATS-R-US and the RCM, except the pressure feedback from the RCM to BATS-R-US.

The RCM computes on a 2D longitude-latitude grid, on which closed field lines are rooted. For BATS-R-US with isotropic pressure, the RCM passes the total particle pressure (the sum of pressures of different species) for each closed field line to BATS-R-US, and the BATS-R-US pressure in every grid cell along that closed field line is nudged towards the same RCM pressure, assuming the pressure is constant along each closed field line. In Anisotropic BATS-R-US, both the parallel and total pressures along a closed field line are nudged towards the same RCM isotropic pressure for that field line, given the RCM does not resolve pressure anisotropy. This leads to a significant reduction of the pressure anisotropy in the closed field line region in Anisotropic BATS-R-US. The RCM can also provide BATS-R-US the density, which is coupled the same way as the total pressure, i.e., the BATS-R-US density along a closed field line is nudged towards the RCM density, assuming the density is constant along each closed field line. The density coupling is the same for Anisotropic BATS-R-US.

The coupling between Anisotropic BATS-R-US and the RCM implants a ring current model into the global anisotropic MHD model, yet the pressure anisotropy in the inner magnetosphere cannot be completely resolved due to the pitch angle isotropy assumption in the RCM. In order to take full advantage of the anisotropic MHD model, we seek coupling with another ring current model that allows for anisotropic pressure.

4.2.2 Anisotropic BATS-R-US and the CRCM Coupling

Recently, *Buzulukova et al.* [2010] and *Glocer et al.* [2012] introduced the CRCM into the Inner Magnetosphere component of the SWMF and implemented the one-way and two-way coupling between BATS-R-US and the CRCM, respectively. Since the CRCM can resolve pitch angle anisotropy, it can calculate the parallel and perpendicular pressure distributions in the inner magnetosphere. This provides a perfect

opportunity of combining the CRCM with Anisotropic BATS-R-US to obtain self-consistent solutions of pressure anisotropy in the global magnetosphere.

The two-way coupling between Anisotropic BATS-R-US and the CRCM requires a quite different algorithm from the one addressing the two-way coupling between BATS-R-US and the CRCM. In the *Glocer et al.* [2012] algorithm, BATS-R-US sends the CRCM the 3D magnetic field configuration, and density and isotropic pressure as boundary conditions, while the CRCM feeds BATS-R-US the density and the total pressure at the magnetic equator for each closed field line. The BATS-R-US density and pressure along a closed field line are thus pushed towards the magnetic equatorial CRCM values on that field line. Same as the coupling with the RCM, the assumption of constant density and pressure along every closed field line is applied to avoid field-aligned flows in the isotropic MHD model.

Anisotropic MHD, on the other hand, has a different requirement in order to maintain force balance along field lines. More specifically, the force along the magnetic field can be obtained from the momentum equation (3.2) as

$$\begin{aligned}
\mathbf{F}_{\parallel} &= \mathbf{b}\cdot\mathbf{F} \\
&= \mathbf{b}\cdot\left[\nabla\left(p_{\perp}+\frac{B^2}{2\mu_0}\right)+\nabla\cdot\left((p_{\parallel}-p_{\perp})\mathbf{bb}-\frac{\mathbf{BB}}{\mu_0}\right)\right] \\
&= (p_{\parallel}-p_{\perp})B\nabla_{\parallel}(B^{-1})+\nabla_{\parallel}p_{\parallel} \qquad (4.1)
\end{aligned}$$

where $\mathbf{b}=\mathbf{B}/|\mathbf{B}|$ and $\nabla_{\parallel}=\mathbf{b}\cdot\nabla$. In the case of MHD with isotropic pressure, (4.1) is simply $\nabla_{\parallel}p$, which is zero with our assumption of no pressure gradient along the magnetic field. If the pressure is anisotropic, the first term of the final expression in (4.1), which basically describes a mirror force, i.e., adiabatic focusing, has to be balanced by the parallel pressure gradient along the magnetic field. Otherwise the non-zero force will result in flows moving along closed field lines in the anisotropic MHD solutions.

Bearing the pressure gradient requirement in mind, we look for an efficient coupling algorithm connecting Anisotropic BATS-R-US and the CRCM. A natural approach would be to pass the pressure distributions along each closed field line from the CRCM to Anisotropic BATS-R-US. Although this is doable, it is computationally expensive as it requires additional arrays to be passed between the two components that store the pressure values and their locations along field lines. In addition, the parallel and total pressures obtained in the CRCM do not necessarily satisfy the force balance condition in the anisotropic MHD model. To reduce the amount of information exchanged between the two models and maintain force balance in Anisotropic BATS-R-US, we build the algorithm based on Liouville's Theorem with the conservation of the first adiabatic invariant and energy, so the density and pressure profiles along magnetic field lines can be obtained from equatorial values following *Spence et al.* [1987],*Olsen et al.* [1994], *Liemohn* [2003], and *Xiao and Feng* [2006] as shown in Appendix B.

The two-way coupling consists of two parts as shown in Figure 4.1. On one hand, Anisotropic BATS-R-US sends the magnetic field information to the CRCM. Also, the CRCM uses the density and pressures (parallel pressure and total pressure) at the minimum magnetic field point on each closed field line from Anisotropic BATS-R-US as boundary conditions to construct a bi-Maxwellian distribution at the outer boundary, i.e., the furthest closed field lines from the Earth within an ellipse, the size and position of which varies in different simulations. On the other hand, the CRCM passes Anisotropic BATS-R-US the density, the parallel and total pressures computed at the minimum magnetic field point of every closed field line, which are used by Anisotropic BATS-R-US to derive the density and pressures at "non-minimum B" locations along the closed field lines according to the following relations (see

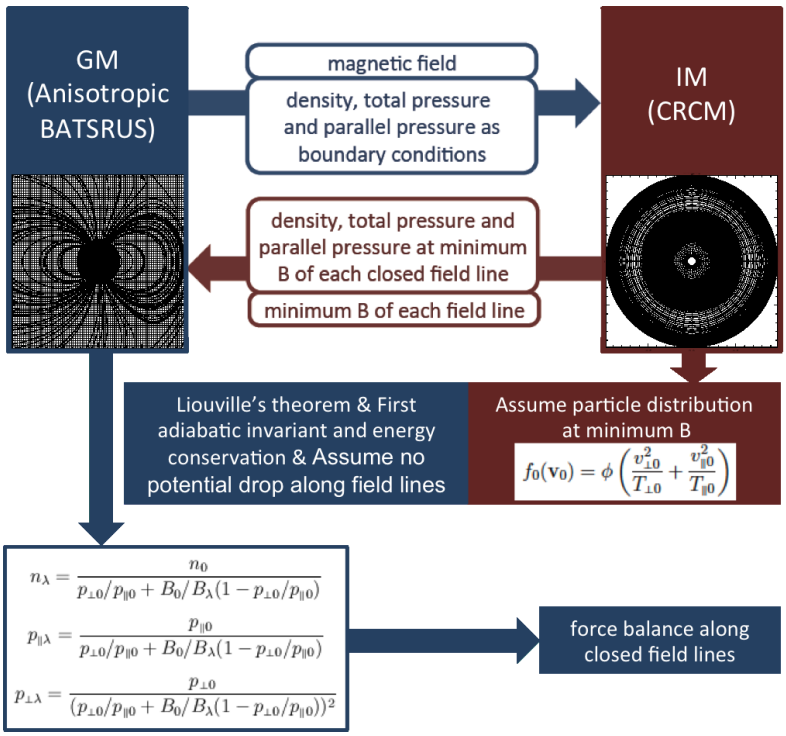

Figure 4.1: The flow chart for the two-way coupling between Anisotropic BATS-R-US and the CRCM.

Appendix B for a derivation).

$$n_\lambda = \frac{n_0}{p_{\perp 0}/p_{\parallel 0} + B_0/B_\lambda(1 - p_{\perp 0}/p_{\parallel 0})} \tag{4.2}$$

$$p_{\parallel\lambda} = \frac{p_{\parallel 0}}{p_{\perp 0}/p_{\parallel 0} + B_0/B_\lambda(1 - p_{\perp 0}/p_{\parallel 0})} \tag{4.3}$$

$$p_{\perp\lambda} = \frac{p_{\perp 0}}{(p_{\perp 0}/p_{\parallel 0} + B_0/B_\lambda(1 - p_{\perp 0}/p_{\parallel 0}))^2} \tag{4.4}$$

The subscript 0 denotes for the location of the minimum magnetic field on a closed field line, and λ indexes an arbitrary point along that field line. The relation (2.2) is employed to calculate the corresponding total pressure p_λ. Substituting equation (4.3) and (4.4) into equation (4.1) gives $\mathbf{F}_{\parallel\lambda} = 0$ (also shown in Appendix B), therefore the pressure distributions obey the force balance condition along the magnetic field lines.

The derivation of equation (4.2), (4.3) and (4.4) is based on two assumptions.

First, there is no potential drop between the "minimum B" point and the point at latitude λ along the field line. Second, the distribution function at the "minimum B" point is a function of $v_{\parallel}^2/T_{\parallel} + v_{\perp}^2/T_{\perp}$ dependence, where $v_{\parallel}$ and $v_{\perp}$ are the parallel and perpendicular velocities, and $T_{\parallel}$ and $T_{\perp}$ are the parallel and perpendicular temperatures, respectively. This means that the relations are satisfied for a variety of distribution functions, including bi-Maxwellian and bi-Kappa distributions, that are reasonable approximations of the particle distribution in the inner magnetosphere.

4.3 Idealized Quiet Time Magnetosphere

To validate Anisotropic BATS-R-US and its couplings with the two ring current models RCM and CRCM, we perform global magnetospheric simulations and analyze the differences between the anisotropic MHD and isotropic MHD simulations, as well as the differences between the RCM and the CRCM-coupled simulations. We first present the idealized simulations.

We have performed six idealized magnetospheric simulations with different model combinations in the SWMF:

1. Anisotropic MHD Model + RIM
2. Isotropic MHD Model + RIM
3. Anisotropic MHD Model + RIM + RCM
4. Isotropic MHD Model + RIM + RCM
5. Anisotropic MHD Model + RIM + CRCM
6. Isotropic MHD Model + RIM + CRCM

The first two simulations do not contain any ring current models, thus they serve as the baselines for comparisons. All six simulations use identical parameters for the same models.

The global MHD model is set up in a 3D box extended from -224 R_E to 32 R_E in the X direction and from -128 R_E to 128 R_E in the Y and Z directions in the GSM coordinate system. The inner boundary is at 2.5 R_E from the center of the Earth. The grid resolution varies from the smallest 1/8 R_E grid cells close to the Earth to the largest 8 R_E grid cells far down the magnetotail. The total number of cells is 1.8 million. As idealized conditions, we align the magnetic axis with the ecliptic north direction, and drive the MHD model with constant solar wind condition and southward IMF: number density $n_{sw} = 5\,\mathrm{cm}^{-3}$, temperature $T_{sw} = 10^5\,\mathrm{K}$, velocity $u_{xsw} = -400\,\mathrm{km/s}$, $u_{y,zsw} = 0$, magnetic field $B_{x,ysw} = 0$, and $B_{zsw} = -5\,\mathrm{nT}$. We use TVD Lax-Friedrich scheme [*Rusanov*, 1961] with the Koren limiter [*Koren*, 1993], explicit time stepping and Boris factor 0.02, i.e., the reduced speed of light is 6000 km/s.

For the ionosphere model RIM, we assume a constant Pedersen conductance of 5 mho and zero Hall conductance. For the RCM, its initial particle distribution is calculated from the MHD solutions of the density and temperature in steady state. For the CRCM, its initial particle distribution is based on quiet time ring current data from the AMPTE/CCE spacecraft [*Sheldon and Hamilton*, 1993].

All simulations are started with 5000 iterations using local time stepping in the MHD code that is coupled with RIM every 10 time steps to achieve steady states. Then they are switched to the time accurate mode, and for the last four simulations, are coupled with the RCM or the CRCM. The time accurate simulations last for 8 hours.

4.3.1 Force balance along closed field lines

As mentioned in section 4.2, the coupling between Anisotropic BATS-R-US and the CRCM is built in a way that the force balance condition along closed field lines is satisfied in the presence of pressure anisotropy. This can be verified by extracting closed field lines in the MHD solution of simulation 5: Anisotropic MHD + RIM +

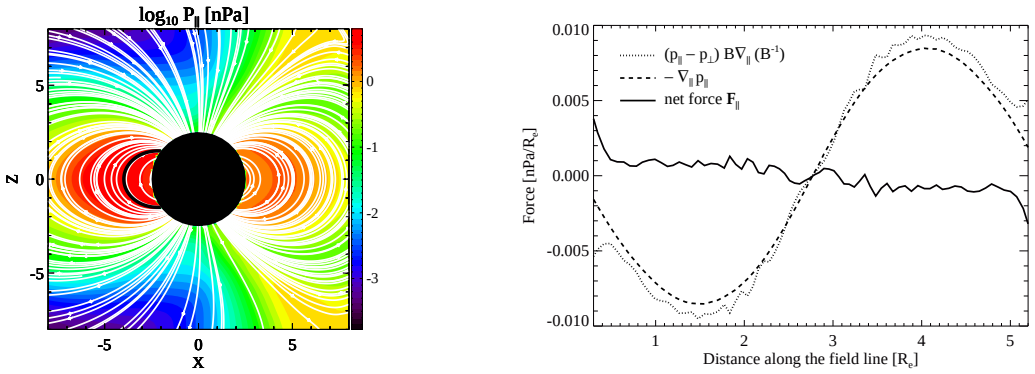

Figure 4.2: Force balance along the field lines for the idealized simulation with Anisotropic MHD + RIM + CRCM at time $t = 4\,\mathrm{hr}$. The left plot shows the logarithmic parallel pressure (colors) and the field lines in the noon-midnight meridional plane from the MHD model. The black line represents the closed field line for which the force balance condition is shown in the right plot.

CRCM, and calculate the forces along these field lines based on the force expression (4.1).

Figure 4.2 shows an example of the force balance analysis. The left plot displays the logarithmic parallel pressure and the magnetic field lines in the noon-midnight meridional ($Y = 0$) plane at $t = 4\,\mathrm{hr}$ from simulation 5. We extract a closed field line on the nightside marked by the black line. Using the parallel and perpendicular pressures and the magnetic field strength in each grid cell along this field line, we calculate the force contributions from the mirror force, i.e., the first term in (4.1), and from the gradient of the parallel pressure, i.e., the second term in (4.1). The right plot shows the forces along this field line starting from near the inner boundary of the MHD model in the northern hemisphere. The mirror force represented by the dotted line and the negative parallel pressure gradient represented by the dashed line are very close to each other. The resulting net force represented by the solid line is approximately zero. The plot demonstrates that the force balance condition is satisfied along the particular field line, with some limited discretization errors.

4.3.2 Pressure distribution

The plasma pressure distribution in the inner magnetosphere is a direct indication of the ring current. We expect higher inner magnetospheric pressure in the ring current model-coupled simulations 3, 4, 5 and 6 compared to the simulations without ring current models. Figure 4.3 displays the plasma pressure, in the case of anisotropic MHD, the total plasma pressure, from the global MHD model in the equatorial ($Z = 0$) plane at $t = 8\,\mathrm{hr}$. The top three plots are from the three simulations with the anisotropic MHD model, and the bottom ones are from the three simulations with the isotropic MHD model. The comparison among the three top plots shows a much stronger nightside pressure from the RCM or the CRCM-coupled anisotropic MHD simulations than from the anisotropic MHD simulation without any ring current model. This validates the effect of the couplings with the RCM and the CRCM, which is consistent with the results from the isotropic MHD simulations shown in the bottom plots. Comparing the anisotropic MHD and isotropic MHD simulation results, we observe higher nightside pressure in the MHD-only simulations (left column) and in the CRCM-coupled simulations (right column), but lower nightside pressure in the RCM-coupled simulations (middle column) for the anisotropic MHD model than for the isotropic MHD model. Comparing the RCM and the CRCM-coupled simulations, the latter produces stronger pressure in the anisotropic MHD model but weaker pressure in the isotropic MHD model. Compared to the RCM-coupled simulations, the CRCM-coupled simulations also show more dawn-dusk asymmetry (dusk preferred) in the pressure distributions, which implies stronger gradient-curvature drift in the CRCM than in the RCM. Although the RCM and the CRCM-coupled simulations react oppositely in terms of changes in the pressure magnitude resulted from the inclusion of pressure anisotropy in the MHD model, they exhibit similar changes in the size of the inner magnetosphere. When comparing the top and bottom plots in the middle and right columns, we find the influence of the IM pressure is greatly reduced

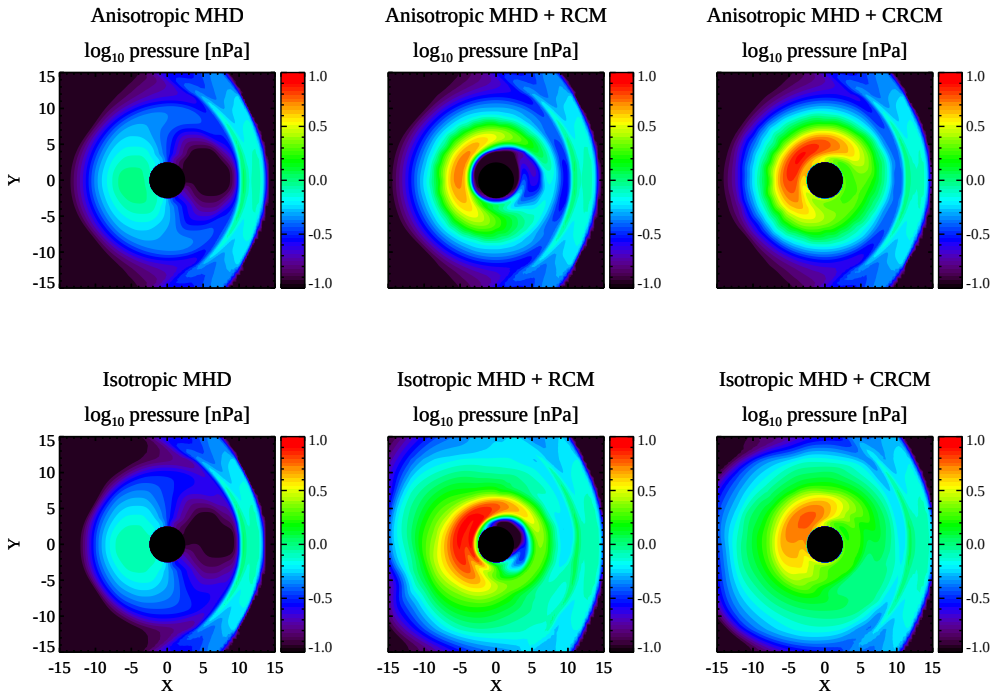

Figure 4.3: The logarithm of the total pressure in nPa in the equatorial ($Z = 0$) plane from the MHD model at $t = 8$ hr.

with anisotropic MHD in comparison with isotropic MHD. We have also noticed that the position of the bow shock varies in these simulations, which will be addressed in section 4.3.3.

A more straightforward comparison of the nightside pressure strengths from different simulations is shown in Figure 4.4. In this figure we plot the nightside pressure along the Sun-Earth line, i.e., the X axis, from the global MHD model. The solid lines represent anisotropic MHD, and the dotted lines represent isotropic MHD. Compared to the two simulations without ring current models identified by the black lines, we see significant pressure increases in the simulations with the RCM and the CRCM, identified by the blue and orange lines respectively. The plot clearly shows a little pressure increase in the anisotropic MHD only simulation, a large pressure increase in the CRCM-coupled anisotropic MHD simulation but a large pressure decrease in the RCM-coupled anisotropic MHD simulation compared to the corresponding isotropic

MHD simulations. Both the RCM and the CRCM coupled anisotropic MHD simulations produce a single pressure peak at around $x = -5\,\mathrm{R}_E$. The pressure gradient towards the Earth (which leads to eastward inner ring current), is not very distinctive in the isotropic MHD simulations especially the CRCM-coupled one (orange dotted line) in which the pressure gradient towards the Earth is very small.

In the anisotropic MHD simulations we can also look into pressure anisotropy. Figure 4.5 shows the pressure anisotropy ratio $P_\perp/P_\parallel$ in the $Z = 0$ plane at $t = 8\,\mathrm{hr}$ from the MHD model. In the inner magnetosphere region within $8\,\mathrm{R}_E$ radius, the RCM-coupled simulation has the least amount of pressure anisotropy with an exception of a parallel pressure dominated small region close to the Earth, while the CRCM-coupled simulation has the strongest pressure anisotropy with the perpendicular pressure dominating in general. This is expected, since the coupling with the isotropic RCM drives the pressure towards isotropy in the closed field line region. Therefore, the RCM-coupled simulation produces less pressure anisotropy than the anisotropic MHD-only simulation does. The CRCM-coupled simulation, on the other hand, produces more pressure anisotropy than the anisotropic MHD-only simulation does, behind the magnetosheath particularly, which implies that the CRCM itself generates more perpendicular preferred pressure anisotropy than the anisotropic MHD model does.

4.3.3 Magnetosheath thickness and magnetopause position

In the previous study (Chapter III) we have found thicker magnetosheath when including pressure anisotropy in global MHD simulations. However, this changes for simulations coupled with the RCM or the CRCM. Figure 4.6 plots the number density, pressure (total pressure in the anisotropic MHD cases) and magnetic field strength variations along the Sun-Earth line on the dayside from the MHD solutions at $t = 8\,\mathrm{hr}$. For the two MHD only simulations represented by the black lines, we

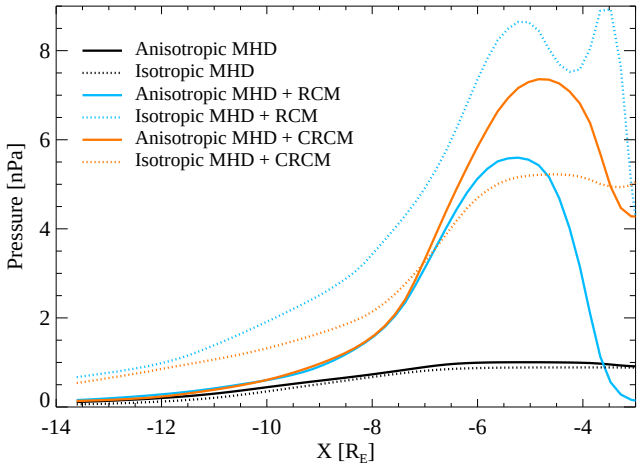

Figure 4.4: The nightside total pressure profile extracted along the X axis from the MHD model at $t = 8\,\mathrm{hr}$.

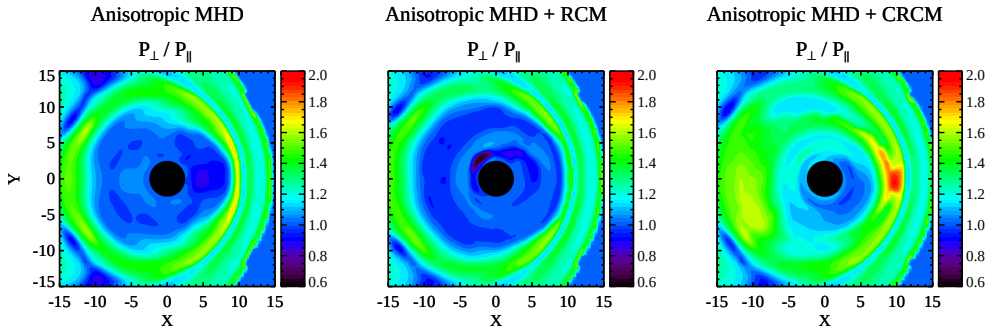

Figure 4.5: Pressure anisotropy ratio in the $X = 0$ plane from the MHD model at $t = 8\,\mathrm{hr}$.

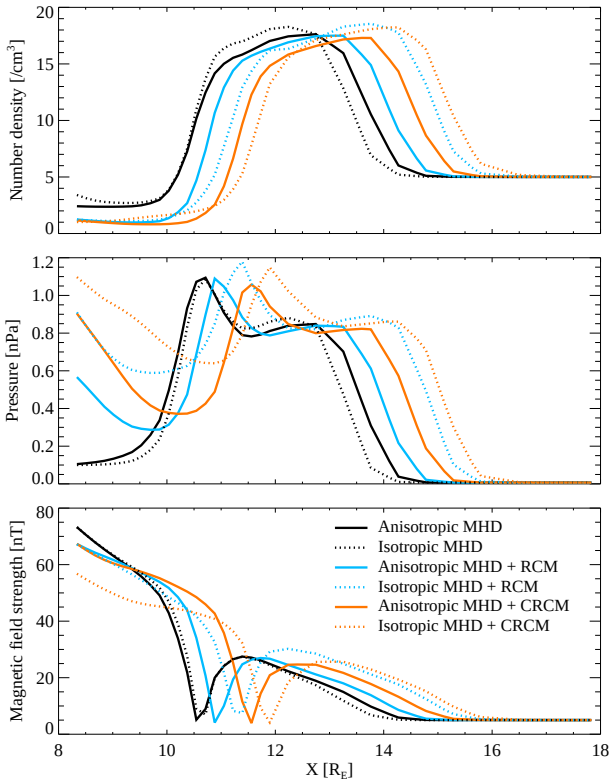

Figure 4.6: The magnetosheath number density (top panel), total pressure (middle panel) and magnetic field strength (bottom panel) profiles extracted along the X axis from the MHD model at $t = 8\,\mathrm{hr}$.

see a larger bow shock stand-off distance from the Earth and a wider magnetosheath in the case of anisotropic MHD. In addition, the position of the magnetopause is not affected much by pressure anisotropy. On the contrary, for the RCM and the CRCM-coupled simulations, pressure anisotropy brings both the magnetopause and the bow shock closer to the Earth, resulting in a thinner magnetosheath as the change of the bow shock stand-off distance is larger than the change of the magnetopause position, which can be seen from the number density and pressure profiles. The thickness of the magnetosheath from different simulations can be ordered from the thinnest to the thickest as follows: Isotropic MHD, Anisotropic MHD + CRCM, Anisotropic MHD, Anisotropic MHD + RCM, Isotropic MHD + CRCM, Isotropic MHD + RCM.

The magnetopause positions from the RCM and the CRCM-coupled simulations

are further away from the Earth compared to the ones in MHD only simulations. This could be easily explained by the larger inner magnetospheric pressure in the ring current model-coupled simulations, which blows up the size of the whole magnetosphere. The closer magnetopause from the Earth in the RCM and the CRCM-coupled simulations in the anisotropic MHD case than in the isotropic MHD case is consistent with the pressure distribution plots in the middle and right columns of Figure 4.3, which shows a reduced pressure just inside the magnetopause and thus a smaller magnetosphere in the anisotropic MHD case.

4.3.4 Earthward tail flow and the magnetic field topology

Another conclusion from the previous study is that the inclusion of pressure anisotropy in the global MHD model reduces the reconnection rate thus the Earthward flow speed in the tail. This holds true for the ring current model-coupled MHD simulations, too. Figure 4.7 displays the X direction flow speed as well as the magnetic field lines in the $Y = 0$ plane from the MHD solutions at $t = 8\,\mathrm{hr}$. The comparison between the top and bottom plots in each column shows greatly reduced Earthward flow speeds in the cases of anisotropic MHD compared to isotropic MHD. For the RCM and the CRCM-coupled simulations (middle and right columns), this flow speed reduction is more significant than the MHD only simulations (left column). For anisotropic MHD (top row), the Earthward flow in the RCM or the CRCM-coupled case is even slower than the one in the MHD only case, which brings the simulated flow speed closer to the observed typical speed of 300 km/s during quiet time [*Baumjohann and Pashmann*, 1989]. In terms of modeling the realistic Earthward tail flow, including pressure anisotropy in the ring current model-coupled MHD simulations improves the results a lot.

Figure 4.7 also shows the change in magnetic field topology when including pressure anisotropy in the MHD model coupled with the RCM or the CRCM. In the

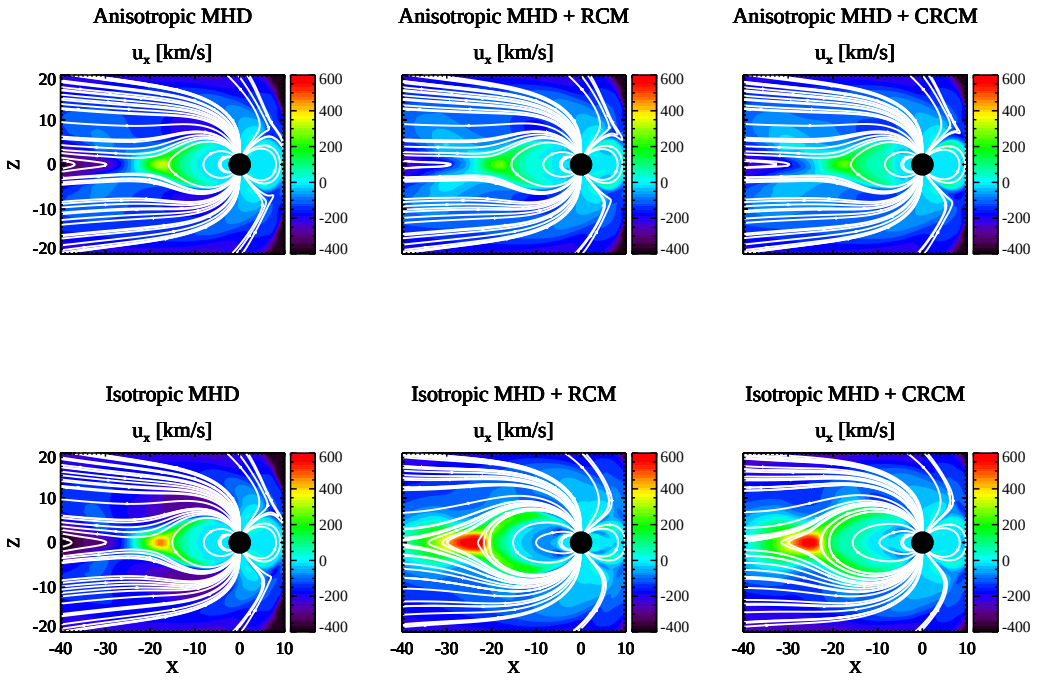

Figure 4.7: The X direction velocity contour overplotted with the magnetic field lines in the noon-midnight meridional $Y = 0$ plane from the MHD model at $t = 8$ hr.

anisotropic MHD only simulation, the magnetic field topology is barely different from the one in the isotropic MHD only simulation. However, with the coupling of the ring current models, the tail reconnection site in anisotropic MHD is much closer to the Earth than in isotropic MHD, and the overall shape of the closed field lines is compressed in anisotropic MHD. This, again, is consistent with the reduced size of the inner magnetosphere in anisotropic MHD that we discussed previously. An interesting feature of the three bottom plots is that the coupling of the ring current models changes the magnetic field topology significantly in the isotropic MHD case. But this effect is almost eliminated in the anisotropic MHD case, for which the coupling of the ring current models does not seem to impact the magnetic field topology, at least not distinguishable in the plots. This implies the importance of pressure anisotropy in controlling magnetic field topology. Even though the pressure anisotropy in the global MHD model might be small in the inner magnetosphere, for instance

in the anisotropic MHD + RCM simulation, it still has a strong effect on the closed magnetic field region.

4.4 Geomagnetic Storms

Geomagnetic storm simulations require incorporating a kinetic inner magnetosphere model with the global MHD model in order to capture the dynamics of the ring current during storm evolutions, thus can be used to validate the coupling between the anisotropic MHD model and the RCM or the CRCM.

We set up the storm simulations the same way as we do the idealized magnetospheric simulations, except that real physical parameters replace the idealized conditions. For the global MHD model, we set orientations of the magnetic and the rotational axes based on the actual time and date to be simulated. The input time-varying solar wind and IMF conditions are taken from the ACE and/or WIND measured values that are time-shifted based on the solar wind propagation time from the satellite to the upstream boundary of the simulation. For the RIM, we use the actual solar $F10.7$ flux to calculate the ionospheric conductance. For the RCM, we use a 10-hour artificial SYM-H decay to mimic the SYM-H recovery, as the RCM does not model physical processes that decay the ring current in the recovery phase. This artificial term is not added to the CRCM because charge exchange loss is already incorporated in that model.

In this study we simulate two moderate storm events, one in 2009 and the other in 2010. For each event, we conduct four simulations:

Run I: Anisotropic MHD Model + RIM + RCM

Run II: Isotropic MHD Model + RIM + RCM

Run III: Anisotropic MHD Model + RIM + CRCM

Run IV: Isotropic MHD Model + RIM + CRCM

4.4.1 21-22 July 2009 storm

The first event we select is the 21-22 July 2009 CIR-driven storm. The time interval we simulate is from 18 UT on July 21st to 0 UT on July 23rd. The upstream condition input for the global MHD model is shown in Figure 4.8. The IMF z component slowly decreases, accompanied by a density increase starting at 0 UT, July 22, which triggers the storm. Later B_z changes from southward to northward, then southward, then northward again, which continues to disturb the magnetosphere.

The SYM-H index reflects the variation of ring current strength during the storm. Figure 4.9 compares the simulated SYM-H indexes by the global MHD model from different simulations and the measured 1-minute SYM-H index. For the RCM-coupled simulations represented by the blue lines, we see differences in the storm growth phase and the recovery phase between the anisotropic MHD simulation and the isotropic MHD simulation. The anisotropic MHD simulation has a slightly deeper SYM-H decrease in the growth phase, which matches the data better. The same conclusion can be drawn for the recovery phase between 10 UT and 14 UT. For the CRCM-coupled simulations, the anisotropic MHD and the isotropic MHD make a big difference in the main phase, with the anisotropic MHD predicts much less SYM-H. In the recovery phase, the SYM-H of the anisotropic MHD case recovers faster than the SYM-H of the isotropic MHD case. We have also noticed that the SYM-H recovers much slower in the CRCM-coupled simulations than it does in the RCM-coupled simulations. On one hand, we have applied the 10-hour SYM-H decay for the RCM-coupled simulations, which is not physical-based. On the other hand, the CRCM underestimates the decay rate of the ring current even though it includes a physical loss term.

4.4.1.1 CRCM solutions

Since the coupling between Anisotropic BATS-R-US and the CRCM provides the first opportunity for the CRCM to be driven by an anisotropic MHD model self-

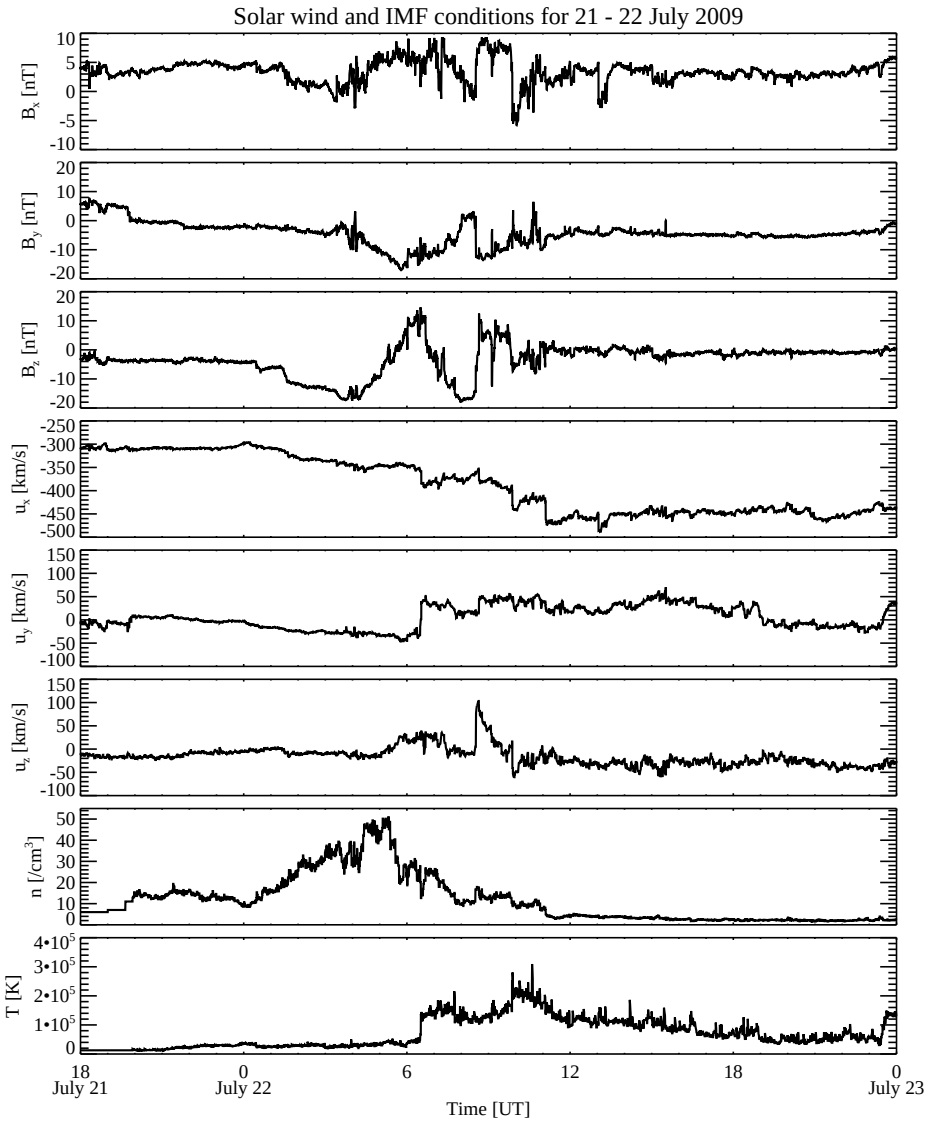

Figure 4.8: The input solar wind and IMF conditions of the MHD model for the 21-22 July 2009 storm.

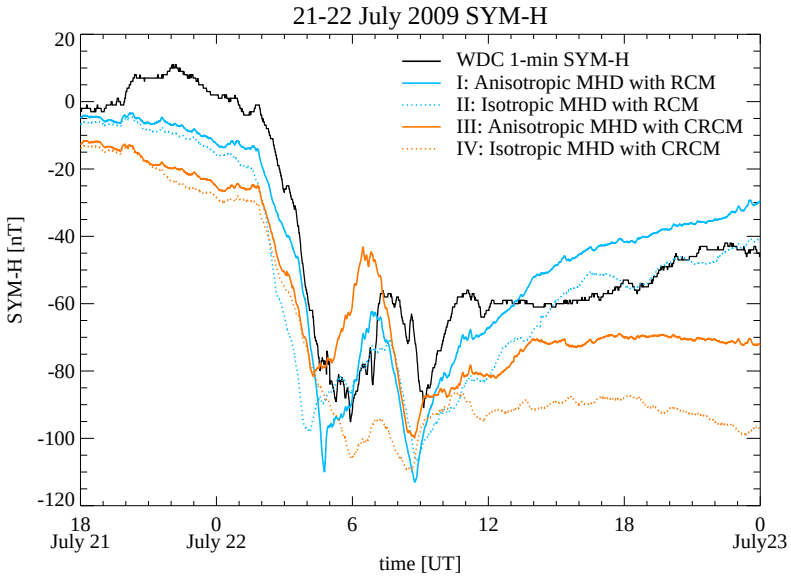

Figure 4.9: The measured 1-minute SYM-H and the simulated SYM-H for the 21-22 July 2009 storm. The blue lines represent the RCM-coupled simulations, and the orange ones represent the CRCM-coupled simulations. The solid lines are for anisotropic MHD, while the dashed ones are for isotropic MHD.

consistently, we are also interested in the differences in the CRCM solutions when driven by the anisotropic MHD model compared to the solutions when driven by the isotropic MHD model.

Figure 4.10 displays the total pressure in the equatorial plane from the CRCM in simulations III and IV. A series of plots at different times during the storm is shown, which represents the evolution of the ring current. The anisotropic MHD-driven case (top panel) and the isotropic MHD-driven case (bottom panel) generate very different ring current patterns at same times. At 0 UT just before the storm begins, the anisotropic MHD-driven case gives a very similar, though very weak, pressure distribution as the isotropic MHD-driven case does. At 4 UT when the storm grows, the anisotropic MHD-driven case has a weaker ring current than the isotropic MHD-driven case has, but in both cases the ring current has a strong duskside preference. From 6 UT to 8 UT during the storm main phase, the anisotropic MHD-driven case shows a much weaker and more dawn-dusk symmetric ring current than the other

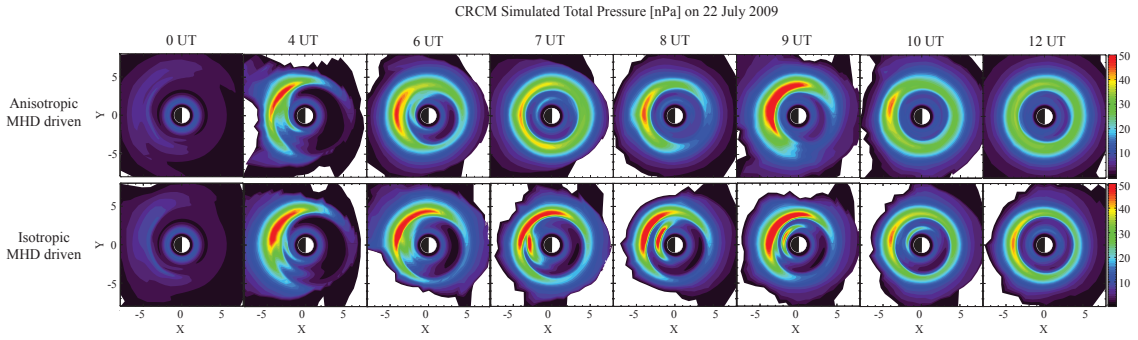

Figure 4.10: The CRCM simulated total pressure in the $Z = 0$ plane for different times on 22 July 2009. The top panel shows results from the anisotropic MHD-driven case, while the bottom panel shows results from the isotropic MHD-driven case.

simulation. Moreover, the ring current undergoes a strong-weak-strong change from 6 UT to 8 UT in the anisotropic MHD-driven case, yet this variation is not distinctive in the isotropic MHD-driven case. This difference can also be seen from the SYM-H variations in Figure 4.9. Between 6 UT and 8 UT, the SYM-H index in simulation III increases then decreases, while the SYM-H in simulation IV has a much smaller change. The consistency between the results from the global MHD model and from the CRCM also verifies the correct coupling between these models. After 9 UT, the start of the recovery, the ring current patterns in the anisotropic MHD and isotropic MHD-driven cases become closer. However, the anisotropic MHD case shows a faster ring current decay, so that at 12 UT, the pressure is obviously less and its distribution is more symmetric surrounding the Earth. An overview of the ring current strength at all times in Figure 4.10 tells us that the CRCM produces weaker ring current when driven by the anisotropic MHD model than by the isotropic MHD model for this storm.

As a further exploration, we plot the equatorial electric potential contours from the CRCM at 6 UT for both the anisotropic MHD and isotropic MHD-driven simulations in Figure 4.11. The potential distribution in the equatorial plane is traced along the closed field lines from the potential pattern in the high latitude ionosphere solved by

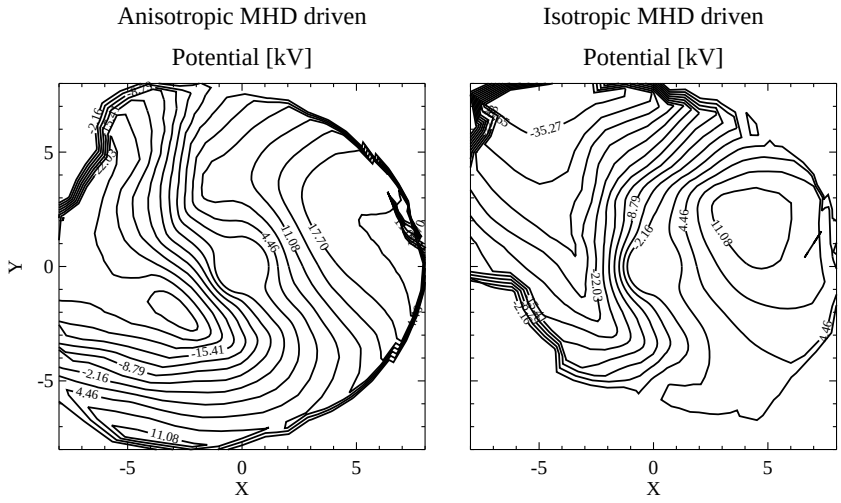

Figure 4.11: The equatorial electric potential contour from the CRCM at 6 UT on 22 July 2009, mapped along field lines from the solution of the ionospheric electrodynamics model RIM.

the RIM. This potential is due to the convection electric field, thus the equipotential lines represent drift paths of zero (or very low) energy particles. For high energy particles, their motions are also governed by the azimuthal gradient-curvature drift that is energy-dependent. In the anisotropic MHD-driven case shown on the left of Figure 4.11, the equipotential lines are less dense than in the isotropic MHD-driven case shown on the right, which indicates that the convection electric field is weaker in the anisotropic MHD-driven simulation. Therefore, for particles of the same energy in the two simulations, which means that they have the same gradient-curvature drift speed, they can penetrate closer to the Earth in the isotropic MHD-driven case because of larger $\mathbf{E} \times \mathbf{B}$ drift speed.

Including pressure anisotropy in the global MHD model also modifies the pressure anisotropy in the CRCM for the coupled simulations. Figure 4.12 plots the pressure anisotropy in the $Z = 0$ plane in the CRCM at three different times. The left column shows the anisotropic MHD-driven case, and the right column shows the isotropic MHD-driven case. Overall the anisotropic MHD-driven CRCM produces much less

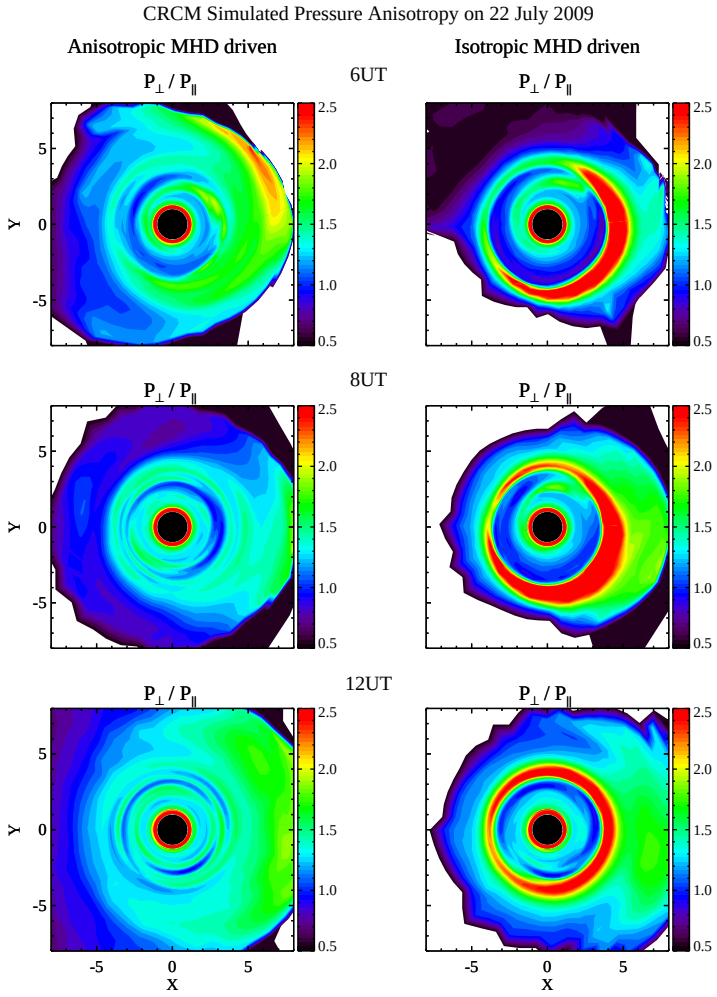

Figure 4.12: The CRCM simulated pressure anisotropy in the $Z = 0$ plane at 6 UT (top panel), 8 UT (middle panel) and 12 UT (bottom panel) on 22 July 2009 for the anisotropic MHD-driven (left column) and the isotropic MHD-driven (right column) cases.

pressure anisotropy than the isotropic MHD-driven CRCM does. This results from the deeper penetration of the particles in the isotropic MHD-driven case, which leads to more perpendicular pitch angle distribution due to the strong gradient-curvature drift and charge exchange loss that prefer to remove particles moving along the field lines. In the more self-consistent simulation (anisotropic MHD with the CRCM), we observe pressure anisotropy variation during the storm. At 6 UT when the storm enters the main phase, the pressure is highly perpendicular, especially on the dayside. At a later time 8 UT, the anisotropy becomes less. At 12 UT during the recovery phase, the pressure anisotropy increases, and the region with perpendicular preferred pressure grows larger.

4.4.1.2 Comparison with satellite data

We trace a number of satellites in the global MHD model and extract the variables along the satellite trajectories for the four simulations. The simulated results are compared to the actual data.

Figure 4.13 shows the GOES11 and GOES12 orbits during the storm and the comparison between the simulated and measured magnetic field along the geosynchronous orbit. We use the same line types and colors to distinguish different simulations as we use in Figure 4.9. We calculate the root-mean-square errors for quantitative comparisons, also shown in the figure. For both the RCM-coupled and the CRCM-coupled simulations, the anisotropic MHD model matches the measured X and Y components of the magnetic field better but does worse for the Z component than the isotropic MHD model does. In terms of the topology of the magnetic field, the anisotropic MHD model predicts less stretched magnetic field lines than the isotropic MHD model does during the main phase and the recovery phase of the storm. For the anisotropic MHD case, the RCM-coupled and the CRCM-coupled simulations are competitive in terms of reproducing the magnetic field.

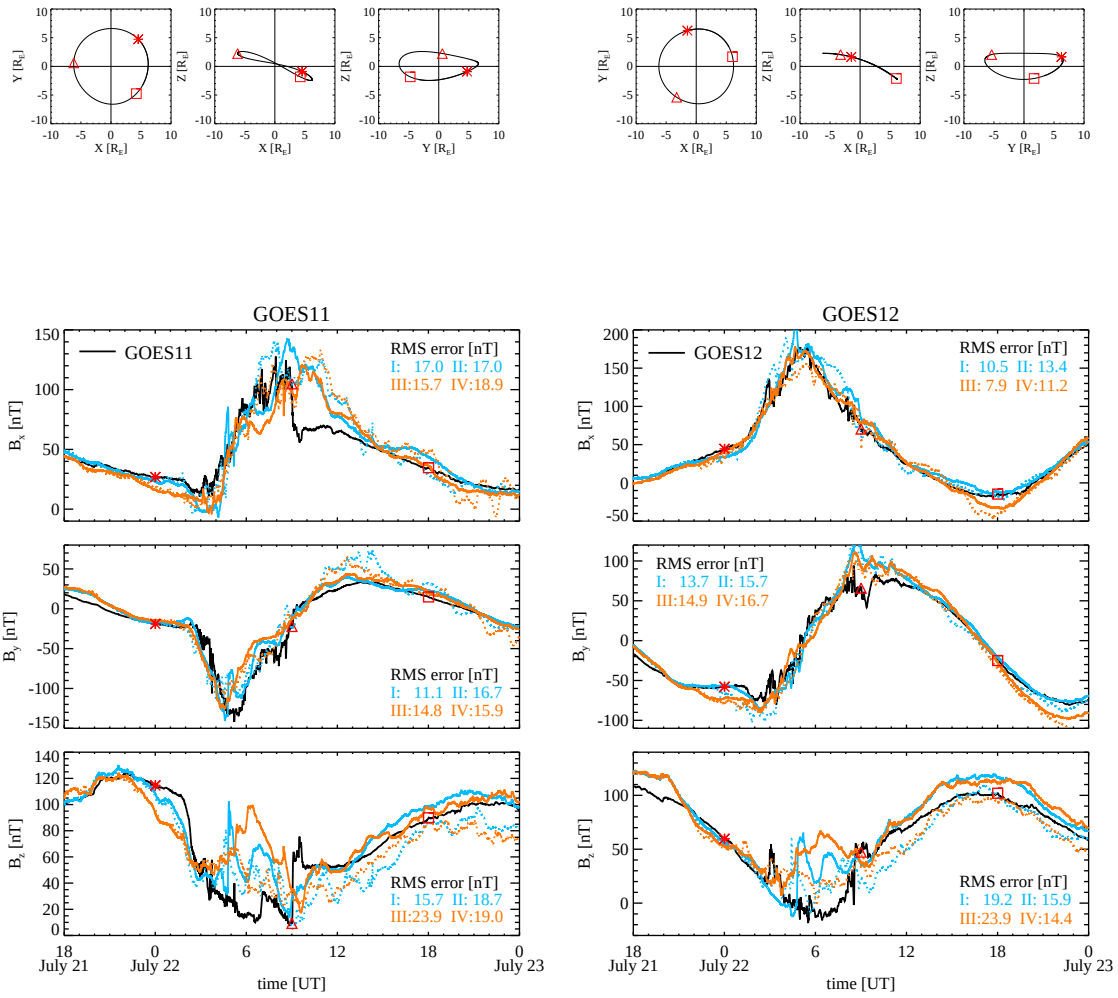

Figure 4.13: The orbits of GOES11 (top left) and GOES12 (top right) from 18 UT on July 21 to 0 UT on July 23rd and the measured and simulated magnetic field with the root-mean-square (RMS) errors written on the plots. The line representations of the four simulations are the same as in Figure 4.9.

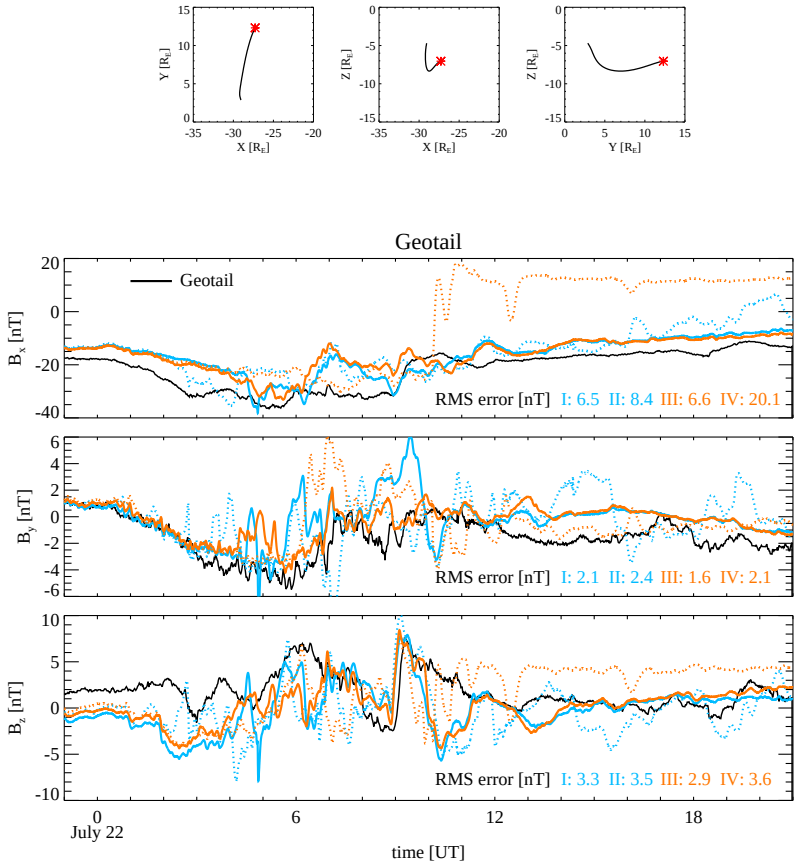

Figure 4.14: The orbits of Geotail (top panel) from 18 UT on July 21 to 0 UT on July 23rd and the measured and simulated magnetic field with the root-mean-square errors. The line representations of the four simulations are the same as in Figure 4.9.

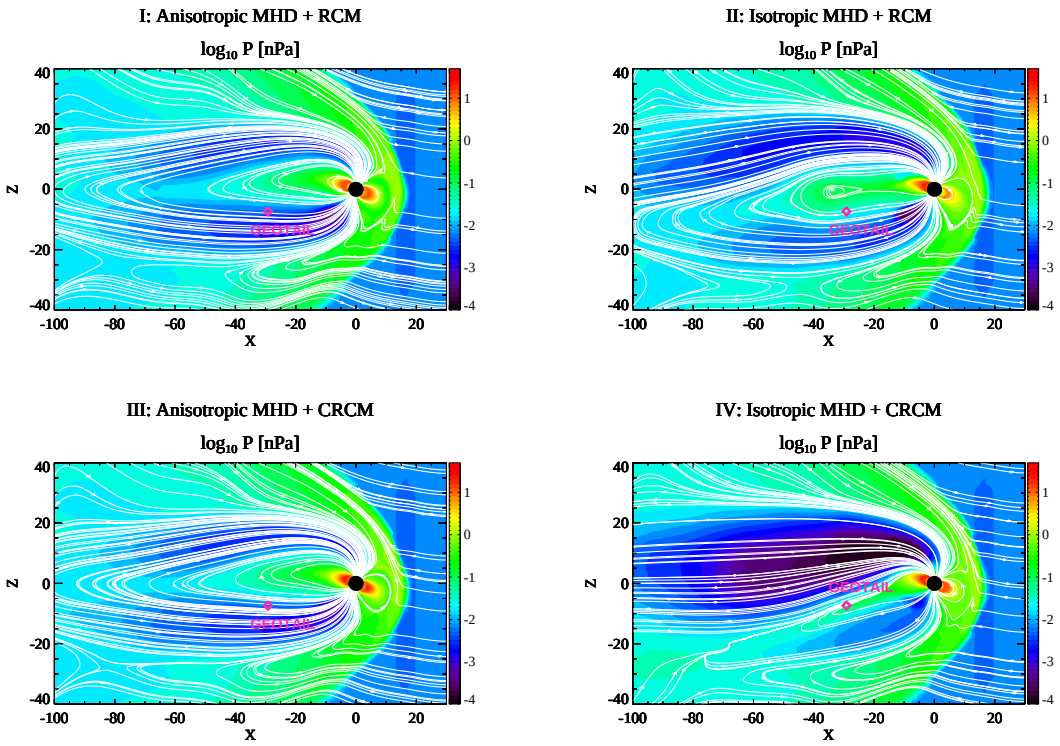

Figure 4.15: The logarithm of the total pressure and the magnetic field lines in the $Y = 0$ plane at 12 UT on July 22 from the MHD solutions.

The comparison with the Geotail data indicates significant improvements when using the anisotropic MHD model instead of the isotropic MHD model for ring current-coupled simulations, as shown in Figure 4.14. During this storm time interval, Geotail was down in the tail at about $X = -30\,\mathrm{R}_E$. For both the RCM and the CRCM-coupled cases, the anisotropic MHD model produces better agreement with data for all three components of the magnetic field than the isotropic MHD model does. Moreover, the CRCM-coupled anisotropic MHD simulation matches the measured magnetic field in the tail best among the four simulations. We have also noticed that the CRCM-coupled isotropic MHD simulation predicts B_x with the wrong sign from 10 UT, July 22 to 0 UT, July 23. To further investigate this problem, we look into the simulated magnetic field topology at 12 UT on July 22nd when simulation IV has a very different B_x from the other simulations and the data, shown in Figure 4.15. We overplot the field lines on the logarithmic pressure contour in the $Y = 0$ plane, as well as the Geotail location at 12 UT projected to this plane, represented by the magenta diamond. In simulation IV, the tail is very tilted towards the minus Z direction, so that Geotail is on the opposite side of the current sheet to where it is in the other three simulations. Hence, the simulated B_x is positive instead of negative in simulation IV.

During the July 2009 storm the THEMIS data is also available. Since THEMIS satellites measure the perpendicular and parallel temperatures, we could compare the simulated pressure anisotropy to the measurement directly. Figure 4.16 shows the orbits of THEMIS A, D and E projected in the $Y = 0$ and $Z = 0$ planes with the simulated pressure anisotropy from simulation III at 16 UT on July 22nd, and the simulated pressure anisotropy ratio extracted along the satellite trajectories compared with the actual data. All three satellites are in the dusk sector of the dayside magnetosphere. THEMIS D and E have very close trajectories. The pressure anisotropy contour plots show that perpendicular pressure dominates the polar regions,

the magnetosheath, and the region close to the Earth. The simulated $P_\perp/P_\parallel$ matches the data reasonably for both the RCM and the CRCM-coupled simulations except the pressure anisotropy jump between 8 UT and 9 UT seen by THEMIS A. Later we will see that during this time interval THEMIS A went across the magnetopause and into the magnetosheath where the pressure anisotropy is high.

We also compare the other variables measured by the THEMIS satellites with the simulated ones. Figure 4.17, 4.18 and 4.19 display the data-model comparisons of the number density, pressure, velocity and magnetic field for THEMIS A, D and E respectively. For THEMIS A, both the RCM and the CRCM-coupled anisotropic MHD simulations (I and III) improve the comparisons for almost every variable, especially for the velocity, relative to the isotropic MHD simulations (II and IV). In the velocity comparison, the isotropic MHD simulations predict large flows after 13 UT, which are not observed. The RCM and the CRCM-coupled anisotropic MHD simulations are very competitive with each other in terms of matching the actual data. At 8 UT, B_z has a sudden decrease and the number density has a sudden increase, which implies that the satellite flew into the magnetosheath. Although the simulations capture the change in the magnetic field, they miss the anisotropy jump. For THEMIS D and E, the anisotropic MHD simulations do not show improvements as large as they are for THEMIS A. For the RCM-coupled simulations, anisotropic MHD produces even worse results than isotropic MHD does for some variables, for example the number density. For the CRCM-coupled simulations, the anisotropic MHD model still has better results than the isotropic MHD model has for most variables. Interestingly, for these satellite trajectories, the RCM-coupled isotropic MHD simulation II seems to do a better job than the CRCM-coupled anisotropic MHD simulation III.

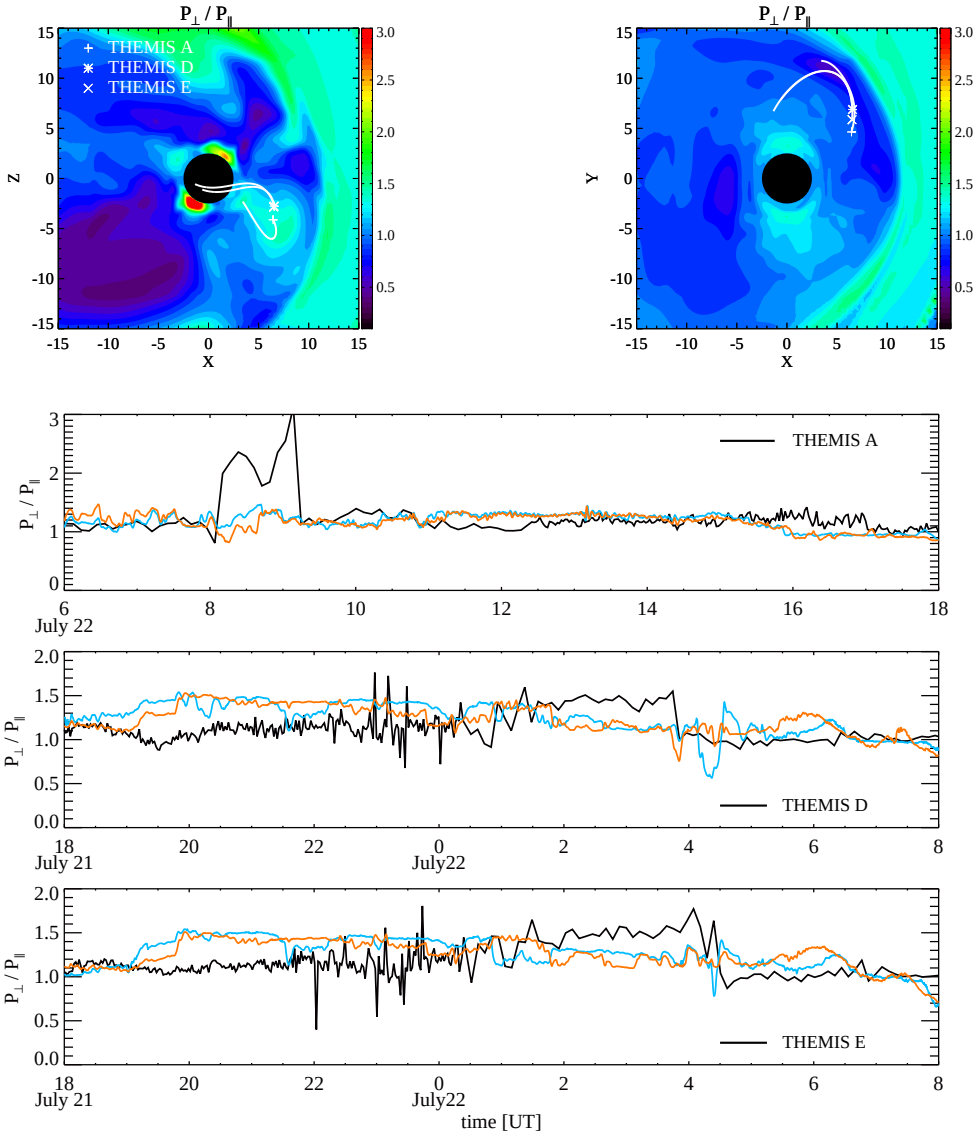

Figure 4.16: The pressure anisotropy in the $Y = 0$ (top left) and $Z = 0$ (top right) planes at 16 UT on July 22, overplotted with the orbits of THEMIS A, D and E (white lines) during the 21-22 July 2009 storm. The lower three panels show the measured and simulated pressure anisotropy. The blue line represents the RCM-coupled anisotropic MHD simulation, and the orange line represents the CRCM-coupled anisotropic MHD simulation.

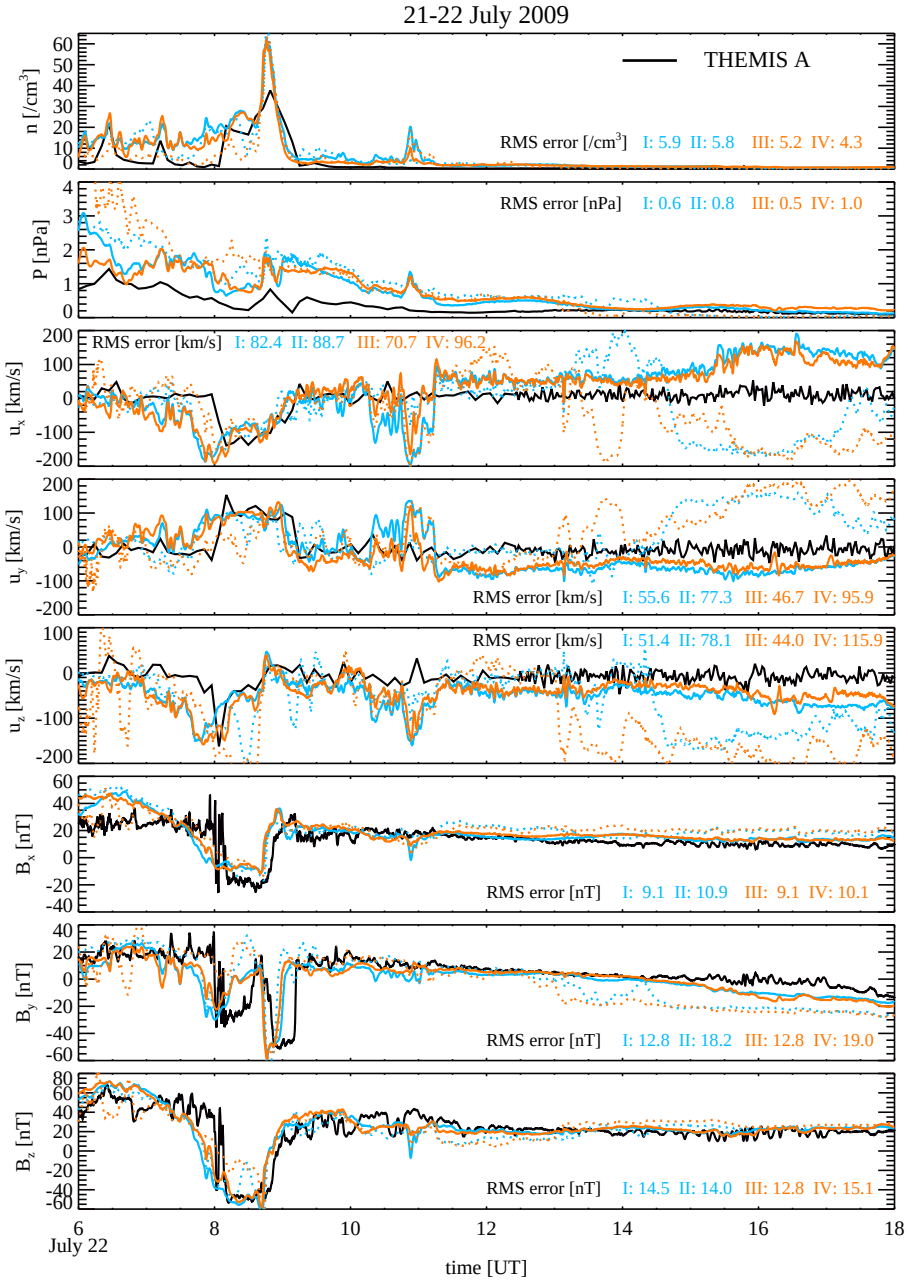

Figure 4.17: The simulated density, pressure, velocity and magnetic field along the THEMIS A trajectory from the MHD solutions and the actual measurement for the 21-22 July 2009 storm. The line representations of the four simulations are the same as in Figure 4.9.

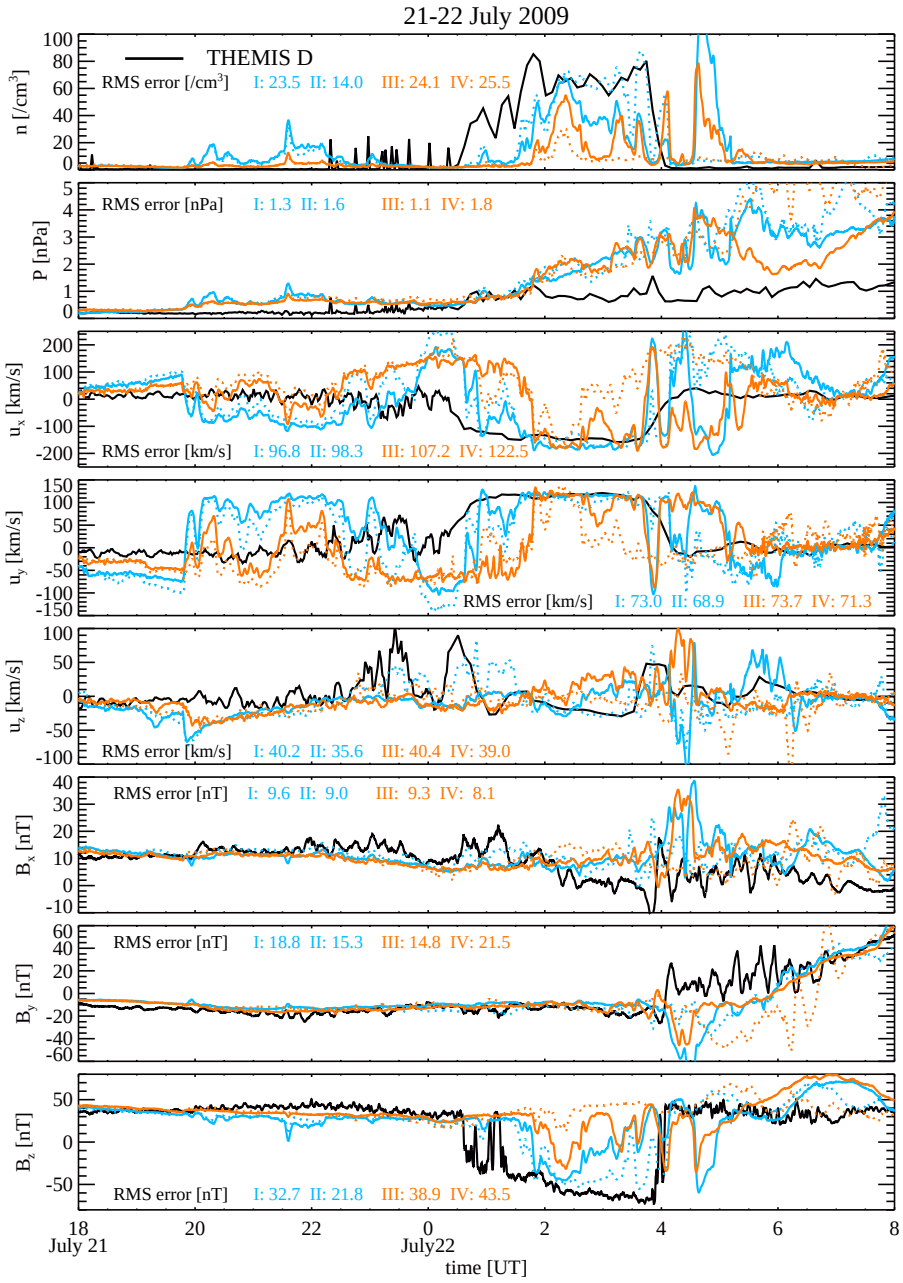

Figure 4.18: Same as Figure 4.17 for THEMIS D.

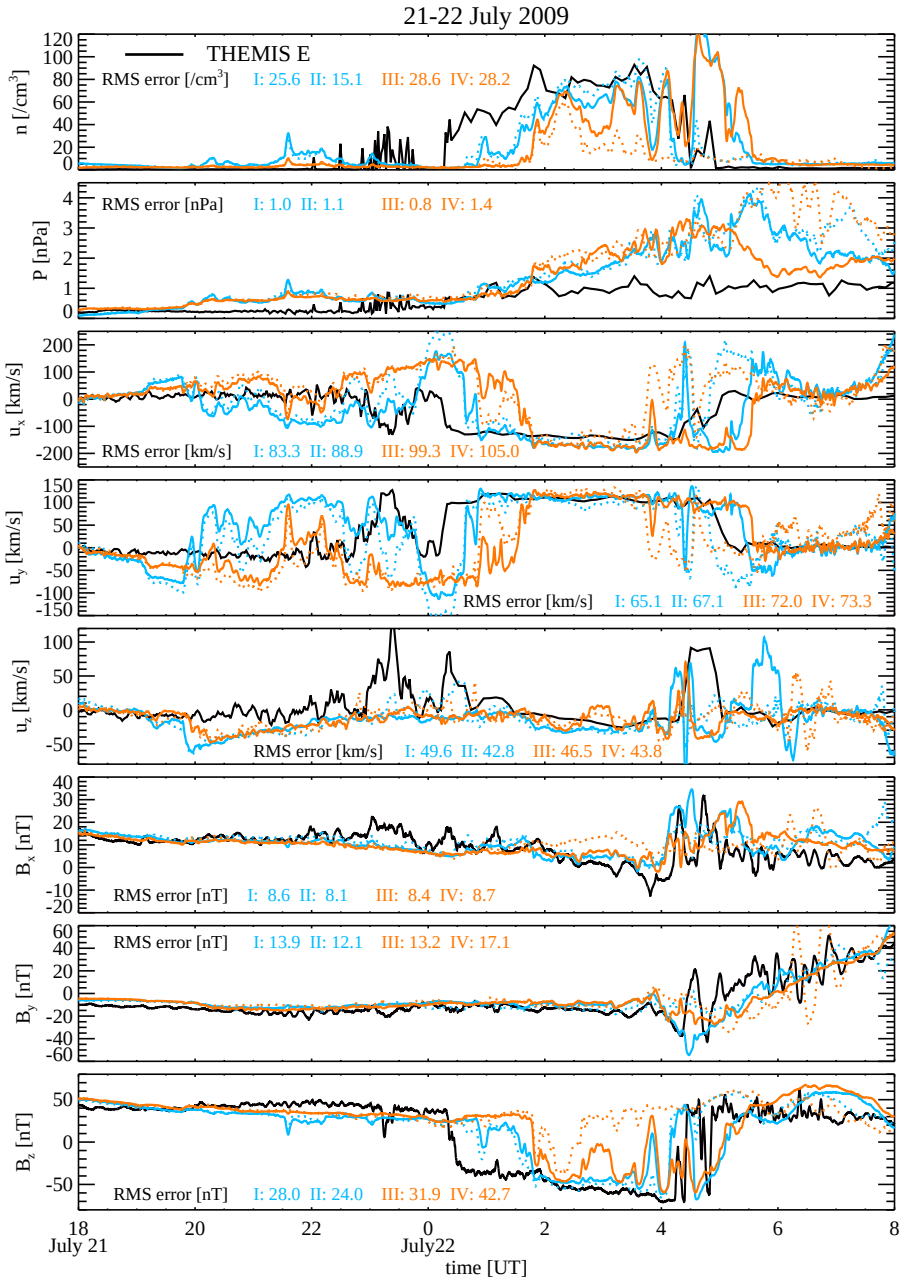

Figure 4.19: Same as Figure 4.19 for THEMIS E.

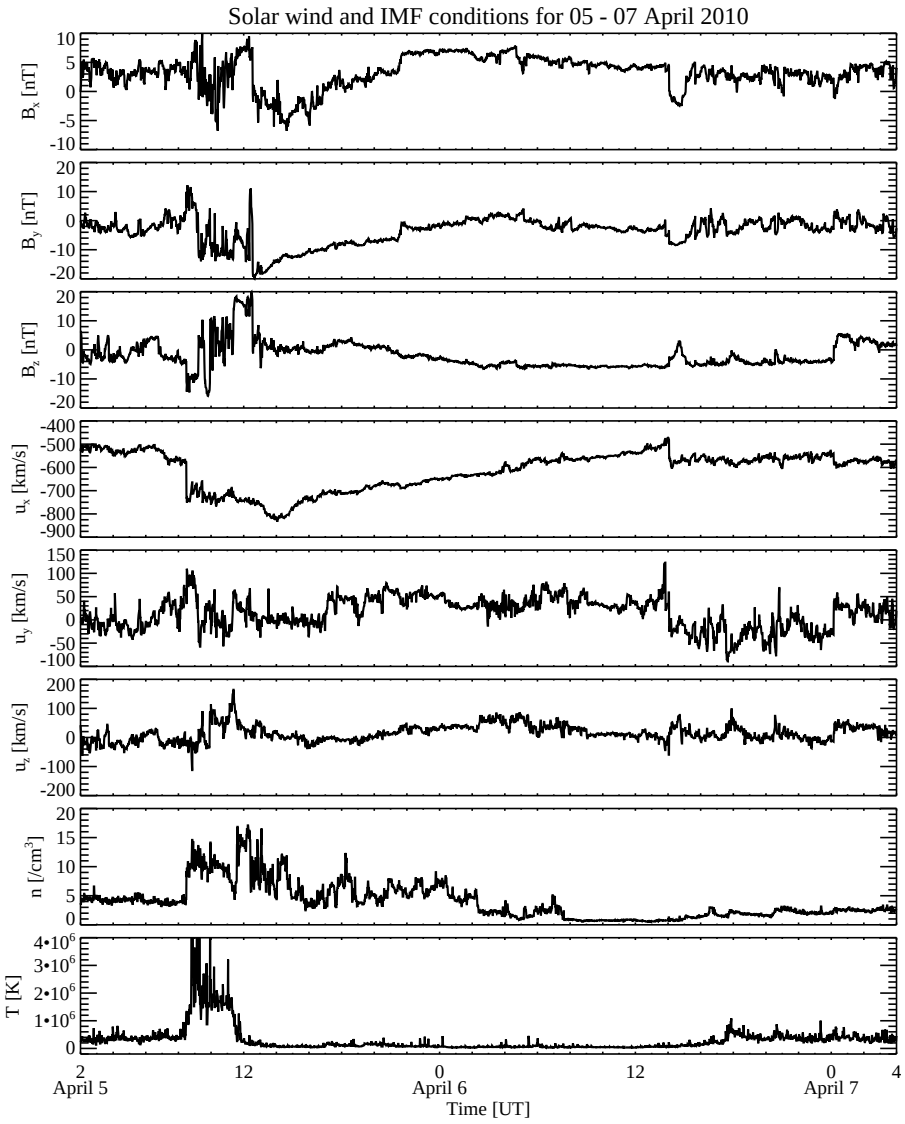

Figure 4.20: The input solar wind and IMF conditions of the MHD model for the 5-7 April 2010 storm.

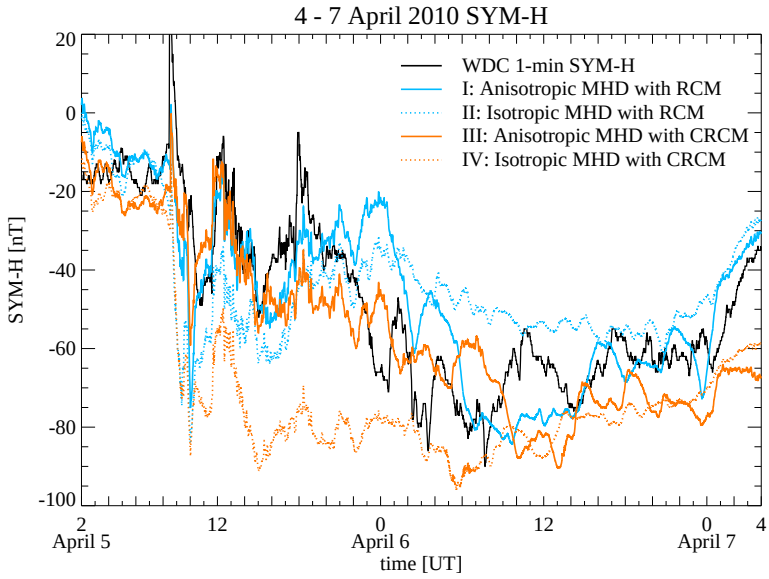

Figure 4.21: The measured 1-minute SYM-H and the simulated SYM-H for the 5-7 April 2010 storm. The blue lines represent the RCM-coupled simulations, and the orange ones represent the CRCM-coupled simulations. The solid lines are for anisotropic MHD, while the dashed ones are for isotropic MHD.

4.4.2 5-7 April 2010 storm

The second event we select is the 5-7 April 2010 CME-driven storm. The simulated time interval is from 2 UT on April 5th to 4 UT on April 7th. The input solar wind and IMF conditions are from the ACE satellite measurement, shown in Figure 4.20. The CME arrives shortly after 8 UT, when the IMF B_z starts to decrease, the solar wind speed suddenly increases, and the number density and temperature suddenly increase.

Figure 4.21 shows the simulated and measured SYM-H index, from which we could tell that the anisotropic MHD simulations predict better SYM-H for this storm than the isotropic MHD simulations do. In particular, for the CRCM-coupled simulations, the anisotropic MHD case produces much closer SYM-H to the measurement than the isotropic MHD case does. The CRCM-coupled isotropic MHD simulation produces overly-large negative SYM-H, which indicates that it overestimates the ring current

strength. The two anisotropic MHD simulations are competitive, with the RCM-coupled simulation matching the measured SYM-H after 12 UT on April 6th better than the CRCM-coupled one, but the SYM-H recovery simulated by the RCM-coupled simulation could be mostly due to the 10-hour SYM-H decay we added.

Comparisons of the simulated magnetic field at geosynchronous orbit to the GOES satellite measurements are presented in Figure 4.22. In general, for the CRCM-coupled simulations, the anisotropic MHD model captures the variations in the data better than the isotropic MHD model does. On the contrary, for the RCM-coupled simulations, the anisotropic MHD model does slightly worse. Of the two anisotropic MHD simulations, the CRCM-coupled one does better than the RCM-coupled one, particularly for B_x. However, all simulations produce less stretched field lines than as seen by GOES11.

The comparison with the Geotail data is shown in Figure 4.23. During the storm, Geotail moved from outside the bow shock to the inner magnetosphere. All four simulations reproduce the measured magnetic field well. Between the two CRCM-coupled simulations, the anisotropic MHD simulation matches the data better according to the root-mean-square errors. The CRCM-coupled anisotropic MHD simulation and the two RCM-coupled simulations are competitive.

4.5 Summary

In order to address the ring current dynamics during the geomagnetic disturbed time with our newly developed anisotropic MHD model, we couple Anisotropic BATS-R-US with the RCM and the CRCM. Since the CRCM can resolve pitch angle anisotropy while the RCM cannot, the coupling between Anisotropic BATS-R-US and the CRCM is more self-consistent. For the first time, we provide two-way coupling between a global anisotropic MHD model and an anisotropic ring current model, which allows us to study the global pattern of pressure anisotropy in the terrestrial

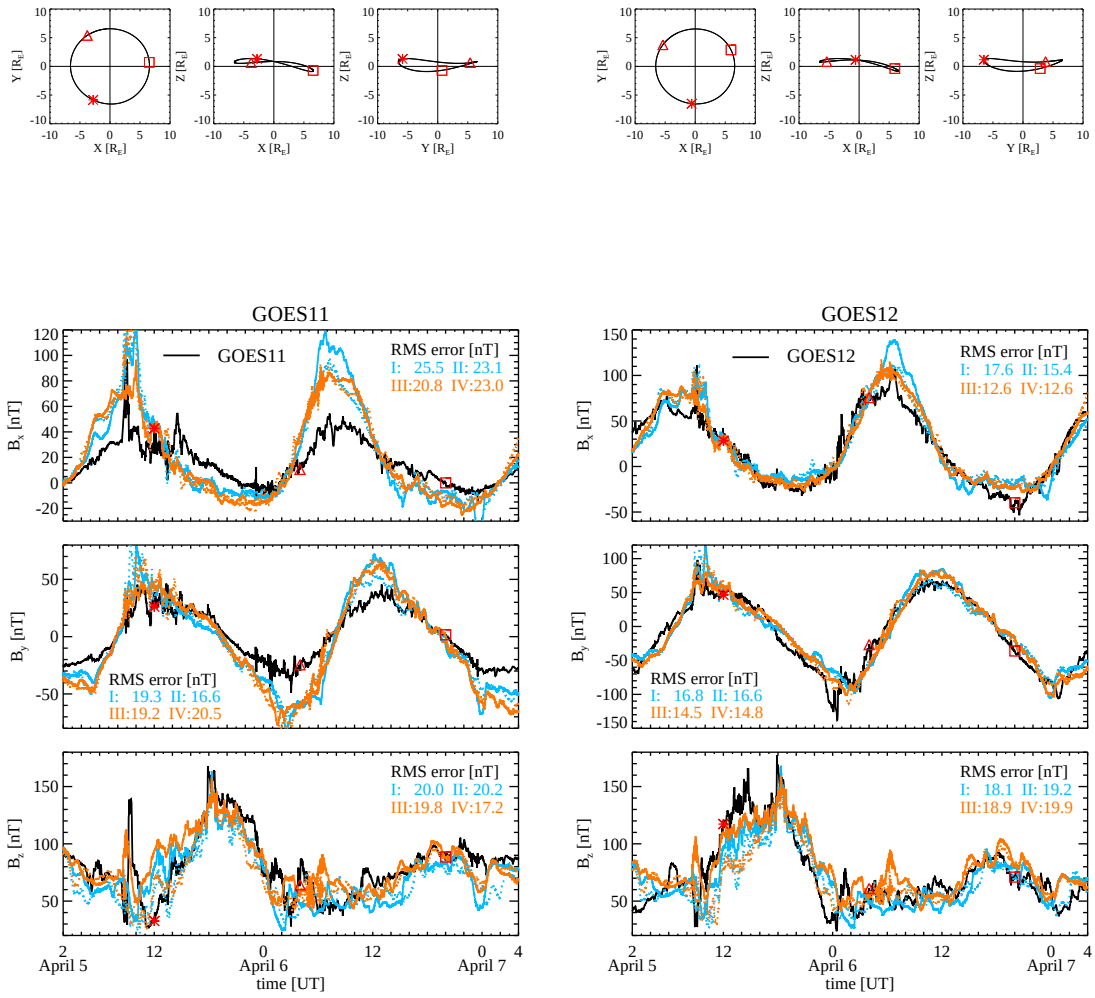

Figure 4.22: The orbits of GOES11 (top left) and GOES12 (top right) from 2 UT on April 5 to 4 UT on April 7 and the measured and simulated magnetic field with the root-mean-square errors written on the plots. The line representations of the four simulations are the same as in Figure 4.21.

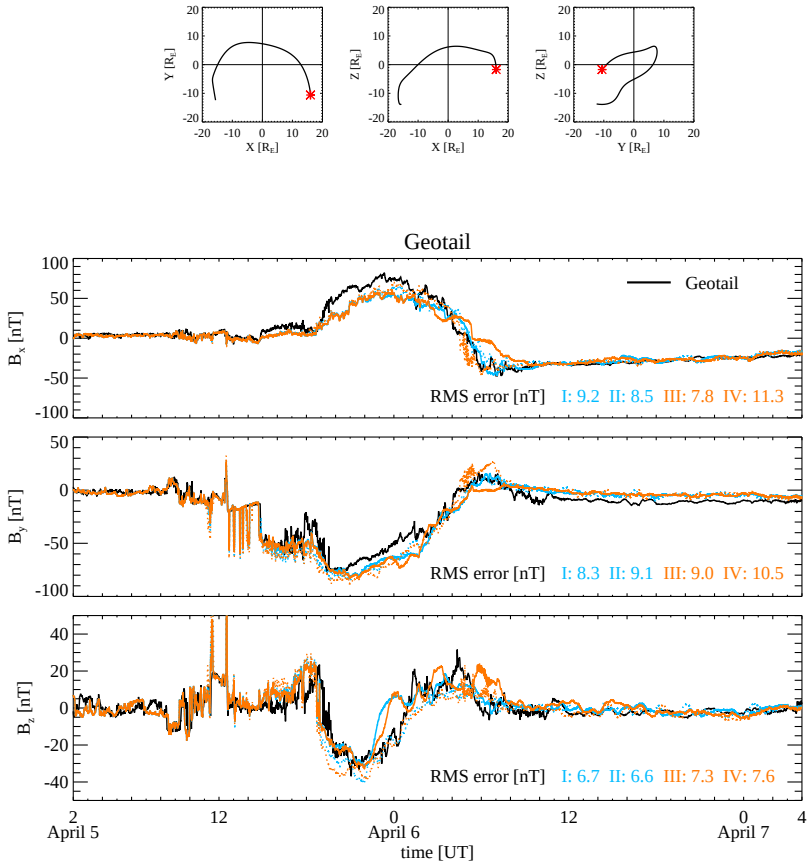

Figure 4.23: The orbits of Geotail (top panel) from 2 UT on April 5 to 4 UT on April 7 and the measured and simulated magnetic field with the root-mean-square errors. The line representations of the four simulations are the same as in Figure 4.21.

magnetosphere more completely.

The two-way coupling between Anisotropic BATS-R-US and the RCM is adopted from the coupling between BATS-R-US and the RCM. Since the RCM assumes isotropic pressure, both the total and parallel pressures along the closed field lines in the anisotropic MHD model are nudged towards the RCM pressure with the assumption that the pressures are constant along field lines.

The two-way coupling between Anisotropic BATS-R-US and the CRCM is more sophisticated. For the CRCM to Anisotropic BATS-R-US coupling, by feeding Anisotropic BATS-R-US with the CRCM density and pressures at "minimum B" points on closed field lines, we calculate the density and pressures at "non-minimum B" points along closed field lines in Anisotropic BATS-R-US based on the relations (4.2), (4.3) and (4.4), which are obtained by Liouville's Theorem and based on a set of assumptions. For Anisotropic BATS-R-US to the CRCM coupling, in addition to the magnetic field information, the CRCM also uses the density and pressures from Anisotropic BATS-R-US to set boundary conditions.

The coupled Anisotropic BATS-R-US and ring current models are validated through global magnetospheric simulations and compared to the standard coupled BATS-R-US and ring current models. In the idealized quiet time simulations, we find significantly increased nightside pressure and pressure gradient towards the Earth in the MHD solutions for both the RCM and the CRCM-coupled anisotropic MHD cases than for the anisotropic MHD-only case. However, compared to the corresponding isotropic MHD simulations, the RCM-coupled anisotropic MHD gives less nightside pressure, while the CRCM-coupled anisotropic MHD gives more nightside pressure. In the anisotropic MHD solutions, the pressure anisotropy in the inner magnetosphere is the largest for the CRCM-coupled simulations, and the smallest for the RCM-coupled simulations as expected. We also find that the inclusion of pressure anisotropy in the global MHD model that is coupled with the RCM or the CRCM brings

the subsolar magnetopause and the bow shock towards the Earth, and the resulting magnetosheath is thinner. In addition, we find the RCM or the CRCM-coupled anisotropic MHD simulation produces a shorter tail, more compressed closed field lines on the nightside, and a much slower Earthward flow jet from the tail reconnection site, compared to the corresponding isotropic MHD simulations. The conclusions from the idealized simulations imply that pressure anisotropy plays an important role in controlling the magnetic field topology and maybe some other physical processes in the global magnetosphere.

In two geomagnetic storm simulations, we observe less ring current during the main and recovery phases produced by the anisotropic MHD model than by the isotropic MHD model for the CRCM-coupled simulations. For the 2009 storm, the anisotropic MHD-driven CRCM produces less anisotropic plasma for the ring current compared to the isotropic MHD-driven CRCM does. For the comparisons with the satellite data, we see mostly improvements, but also drawbacks from the anisotropic MHD simulations compared to the isotropic MHD simulations. In particular, anisotropic MHD improves the magnetic field agreement with the Geotail data and the velocity agreement with the THEMIS A data a lot for the 2009 storm. In most cases, the CRCM-coupled anisotropic MHD simulation and the two RCM-coupled simulations produce competitive results. Moreover, for the RCM-coupled simulations, the isotropic MHD case sometimes shows better match with the data than the anisotropic MHD case does. In our opinion, this reveals the importance of consistency between the global MHD model and the ring current model. The RCM assumes isotropic pressure, so does the isotropic MHD model. In principle, the RCM-coupled isotropic MHD model is more consistent than the RCM coupled anisotropic MHD model. This might also explain the incorrect tail tilt seen in the CRCM-coupled isotropic MHD simulation in Figure 4.15, as the coupling between a isotropic MHD model with an anisotropic ring current model is inconsistent.

CHAPTER V

Coronal and Heliospheric Simulations with Anisotropic BATS-R-US

As the last application of Anisotropic BATS-R-US presented in this thesis, we have generalized a recent coronal and heliospheric model [*Sokolov et al.*, 2013] to account for the observed proton temperature anisotropy based on Anisotropic BATS-R-US. This chapter describes the current state of this solar wind model and shows some preliminary results. Given that the electron thermal pressure is equally important as the ion thermal pressure in the corona and the solar wind, we consider the electron pressure as well, which is different from the magnetospheric simulations presented in Chapter III and IV.

The content of the chapter is as following. Section 5.1 describes the anisotropic MHD model for the solar wind, including the governing equations and boundary conditions. Section 5.2 presents an idealized coronal simulation. Section 5.3 presents the coronal and heliospheric simulations for three Carrington rotations during solar minimum and maximum. Section 5.4 summarizes the chapter.

5.1 An Anisotropic MHD Model for the Corona and Heliosphere

Since both the SC and IH components in the SWMF are represented by BATS-R-US, Anisotropic BATS-R-US can be easily incorporated into the coronal and heliospheric models available in SC and IH, so that these solar wind models can account for ion temperature anisotropy in the corona and the solar wind. In this study we extend the newly developed Alfvén wave driven solar wind model [*Sokolov et al.*, 2013; *van der Holst et al.*, 2010] to include the ion pressure anisotropy. Note that the ions only include protons in the model.

The governing equations for the Alfvén wave driven solar wind model with anisotropic ion pressure are written as

$$\frac{\partial \rho}{\partial t} + \nabla \cdot (\rho \mathbf{u}) = 0 \tag{5.1}$$

$$\frac{\partial \rho \mathbf{u}}{\partial t} + \nabla \cdot \left[\rho \mathbf{u}\mathbf{u} + p_\perp \mathbf{I} + p_e \mathbf{I} + (p_\parallel - p_\perp)\mathbf{b}\mathbf{b} - \frac{1}{\mu_0}\left(\mathbf{B}\mathbf{B} - \frac{B^2}{2}\mathbf{I} \right) \right] + \nabla \left(\frac{w_+ + w_-}{2} \right) = 0 \tag{5.2}$$

$$\frac{\partial \mathbf{B}}{\partial t} + \nabla \times [-(\mathbf{u} \times \mathbf{B})] = 0 \tag{5.3}$$

$$\frac{\partial p_\parallel}{\partial t} + \nabla \cdot (p_\parallel \mathbf{u}) + 2 p_\parallel \mathbf{b} \cdot (\mathbf{b} \cdot \nabla)\mathbf{u} = \frac{2}{3\tau_{ei}}(p_e - p_\parallel) + \frac{2}{3} Q_{p\parallel} + \frac{\delta p_\parallel}{\delta t} \tag{5.4}$$

$$\frac{\partial p}{\partial t} + \nabla \cdot (p \mathbf{u}) + \frac{2}{3} p_\perp (\nabla \cdot \mathbf{u}) + \frac{2}{3}(p_\parallel - p_\perp)\mathbf{b} \cdot (\mathbf{b} \cdot \nabla)\mathbf{u} = \frac{2}{3\tau_{ei}}(p_e - p) + \frac{2}{3} Q_p \tag{5.5}$$

$$\frac{\partial p_e}{\partial t} + \nabla \cdot (p_e \mathbf{u}) + \frac{2}{3} p_e (\nabla \cdot \mathbf{u}) + \frac{2}{3} \nabla \cdot \mathbf{q}_e = \frac{2}{3\tau_{ei}}(p - p_e) + \frac{2}{3} Q_e - \frac{2}{3} Q_{rad} \tag{5.6}$$

$$\frac{\partial w_\pm}{\partial t} + \nabla \cdot (\mathbf{u} w_\pm \pm \mathbf{b} V_A w_\pm) + \frac{1}{2} w_\pm \nabla \cdot \mathbf{u} = -\Gamma_\pm w_\pm \tag{5.7}$$

Again, ρ and $\mathbf{u}$ are the density and velocity, $\mathbf{I}$ is the unit tensor, $\mathbf{B}$ is the magnetic field, $\mathbf{b}$ is the unit vector along the direction of the magnetic field, and μ_0 is the vacuum permeability. The polytropic index is taken to be 5/3. We still use $p_\parallel$ and

p to represent the ion parallel pressure and ion average scalar pressure, which are related by equation (2.2), while p_e represents the electron pressure that is assumed to be isotropic. The ion pressure anisotropy relaxation term on the right-hand-side of 5.4 has been discussed in detail in Chapter III and can be expressed by

$$\frac{\delta p_{\parallel}}{\delta t} = \max\left(\frac{\overline{p}_{\parallel} - p_{\parallel}}{\tau}, \frac{p - p_{\parallel}}{\tau_g}\right) \quad . \tag{5.8}$$

The definitions of $\overline{p}_{\parallel}$, τ and τ_g are the same as for equations (3.12) and (3.13).

Comparing to the anisotropic MHD equations used in previous chapters, the new equations (5.7) are specific to coronal and heliospheric modeling. They describe the propagation and dissipation of the Alfvén wave energy densities $w_{\pm}$. The + subscript indicates the propagating Alfvén waves in the direction of $\mathbf{B}$, and similarly the $-$ subscript indicates the Alfvén waves antiparallel to $\mathbf{B}$. The Alfvén wave speed can be written as $\mathbf{V}_A = \mathbf{B}/\sqrt{\mu_0 \rho}$. The wave energy dissipation rates are expressed as

$$\Gamma_{\pm} = \frac{\sqrt{|\mathbf{B}|}}{(L_{\perp} \cdot \sqrt{|\mathbf{B}|})} \sqrt{\frac{\max\left(w_{\mp}, C_{refl}^2 w_{\pm}\right)}{\rho}} \quad , \tag{5.9}$$

where $L_{\perp}$ is the transverse correlation length of the turbulence. $(L_{\perp} \cdot \sqrt{|\mathbf{B}|})$ and C_{refl} are free parameters that can be set externally.

There are also some new terms on the right-hand-sides of equations (5.2), (5.4) - (5.6) that are absent in the anisotropic MHD equations employed in previous chapters. First, $\nabla((w_+ + w_-)/2)$ in equation (5.2) represents the contribution from wave pressures. Second, $2(p_e - p_{\parallel})/(3\tau_{ei})$ in equation (5.4), $2(p_e - p)/(3\tau_{ei})$ in equation (5.5), and $2(p - p_e)/(3\tau_{ei})$ in equation (5.6) describe the heat exchanges between the electrons and the ions due to their collisions, where τ_{ei} represents the relaxation time. Third, the terms with $Q_{p\parallel} = \alpha_{\parallel} Q_w$, $Q_p = (1 - \alpha_e) Q_w$, and $Q_e = \alpha_e Q_w$ represent the coronal heating by the Alfvén waves, where $Q_w = \Gamma_- w_- + \Gamma_+ w_+$ is the Alfvén wave dissipation. Hence, the total wave energy dissipation is divided into three parts: two

for the parallel and perpendicular directions (relative to the magnetic field direction) in the ions and one for the electrons. $\alpha_{\parallel}$ is the ratio of the wave energy dissipated in the parallel direction of the ions against the total wave energy, while α_e is the ratio for the part of the wave energy dissipated in the electrons. The default ratios are that the electrons get 40% of the total energy, while the rest of the energy goes into ions and is partitioned to the parallel and perpendicular directions with a ratio of $1:2$. For now these ratios are set to be constants, and they are also input parameters. Third, $\nabla \cdot \mathbf{q}_e$ in equation (5.6) is the field-aligned electron heat conduction term, where $\mathbf{q}_e = -\boldsymbol{\kappa} \cdot \nabla T_e$, T_e is the electron temperature, and $\boldsymbol{\kappa}$ is the field-aligned heat conduction tensor that is proportional to $T_e^{5/2}$. Lastly, Q_{rad} in equation (5.6) represents the radiation energy loss from an optically thin plasma: $Q_{rad} = n_e n_p \Lambda(T_e)$, where n_e and n_p are the electron and proton number densities, respectively, and $\Lambda(T_e)$ is a function of T_e that can be obtained from the Chianti tables [*Dere et al.*, 1997].

The new model described by equations (5.1) - (5.7) has been implemented into both the SC and IH components. Same as the original Alfvén wave driven solar wind model, we can either run the SC component only to model the corona, or run the coupled SC+IH to resolve both the corona and the inner heliosphere. The original Alfvén wave driven solar wind model sets its inner boundary at the top of the chromosphere, where the ion and electron temperatures are assumed to be the same constant and uniform value. In our anisotropic MHD model, we adopt the same inner boundary conditions, with the assumption that the ion pressure is isotropic at the boundary, i.e., the ion parallel temperature is the same as the ion average temperature and the electron temperature. This assumption is approximately valid due to the abundant particle collisions in the relatively dense plasma at the top of the chromosphere, which can drive the plasma pressure to be isotropic. The treatment of the transition region remains unchanged, i.e., modifying the electron heat conduction, the radiation loss rate, and the wave dissipation rate [*Sokolov et al.*, 2013].

5.2 Idealized Coronal Simulation

To validate the Alfvén wave driven solar wind model with ion pressure anisotropy, we first apply the model to simulate the solar corona under idealized conditions and compare the results to previous 1D and 2D anisotropic MHD modeling results.

The simulation is performed with the SC component only. Our computational domain is a sphere centered at the Sun with a radius of 24 solar radii (R_S). We use spherical grids, and the grid resolution varies from about $0.001\,R_S$ very close to the surface of the Sun, to about $1\,R_S$ further away from the Sun, with refined grids in the current sheet region. The total number of cells is about 2.85 millions. The idealized condition is that we assume the solar magnetic field is a pure dipole field as the initial condition and keep the radial magnetic field at the inner boundary fixed during the simulation. Some other important input parameters include: the electron and ion temperatures at the inner boundary, i.e., the top of the chromosphere, are set to a uniform value $5.0 \times 10^4\,\mathrm{K}$, and the inner boundary number density is set to $2.0 \times 10^{17}\,\mathrm{m}^{-3}$ uniformly. For wave dissipation rates, we set $(L_\perp \cdot \sqrt{|\mathbf{B}|}) = 75\,\mathrm{km\ T}^{1/2}$ and $C_{refl} = 0.04$. For wave energy dissipation ratios, we use the default values, i.e., $\alpha_e = 0.4$ and $\alpha_\parallel = 0.2$. For the pressure anisotropy relaxation, we use the default instability-growth-rate based term, and do not apply global pressure anisotropy relaxation, namely, $\tau_g = \infty$.

For comparisons we also perform an isotropic MHD simulation with the original Alfvén wave driven solar wind model. This simulation is set up identically as the anisotropic MHD simulation except for the parameters related to anisotropic pressure.

Both simulations are computed in the local time stepping mode for 60000 iterations, when the solutions are converged to near steady state. We look into the results at the end of the simulations.

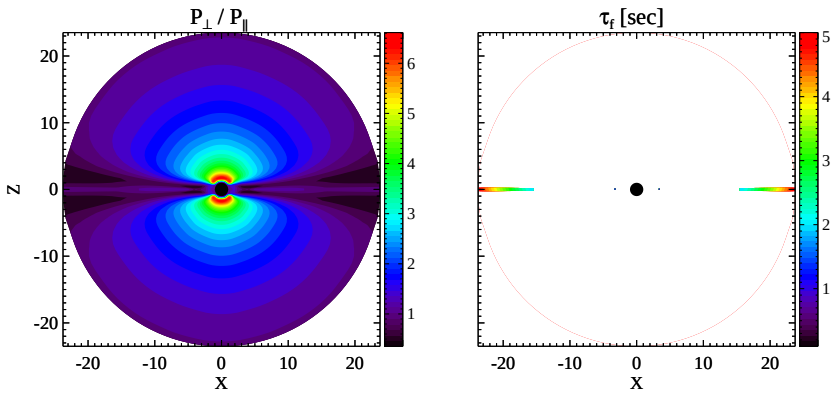

Figure 5.1: The ion pressure anisotropy ratio (left) and the firehose unstable region with the firehose instability relaxation time (right) in the $Y = 0$ plane from the anisotropic MHD simulation of the idealized corona.

5.2.1 Ion pressure anisotropy

For the anisotropic MHD simulation, we are most interested in the ion pressure anisotropy. The left plot of Figure 5.1 shows the ion pressure anisotropy ratio $p_\perp/p_\parallel$ in the $Y = 0$ plane. Close to the Sun, we observe highly perpendicular pressure in the two polar regions where open field lines are rooted, while much less pressure anisotropy near the equator where closed field lines dominate. The pressure anisotropy in the polar regions gradually reduces away from the Sun, while in the equatorial region the variation with radius is small. The pressure anisotropy variation along the open field lines can be explained by adiabatic focusing, which results in a more perpendicular pitch-angle distribution towards the stronger magnetic field region along the magnetic field lines. Close to the outer boundary of the simulation domain, the perpendicular pressure slightly dominates over the parallel pressure except near the equatorial plane where the parallel pressure develops to be higher than the perpendicular pressure. Since the fast solar wind originated from coronal holes with open field lines is frequently observed to have $T_\perp/T_\parallel > 1$, our results qualitatively agree with it.

Instabilities could be excited by the ion pressure anisotropy. During the simulation, the ion cyclotron and firehose instabilities are excited, but the former disappears after some iterations as the pressure anisotropy is being limited through the pressure relaxation term. At the end of the simulation we find that only the firehose instability is present due to the large parallel pressure and small magnetic field strength near the equatorial plane. The right plot of Figure 5.1 displays the firehose unstable region in the $Y = 0$ plane and its growth-rate-based relaxation time τ_f applied in the simulation. The two very narrow regions that align with the X axis are firehose unstable. Comparing with the pressure anisotropy contour on the left, we notice that the pressure anisotropy ratio in these two regions does not deviate much from 1. However, these two regions are actually part of the current sheet as we shall see later, where the magnetic field is very small, such that the firehose instability can be excited even when the parallel pressure is only slightly higher than the perpendicular pressure.

To better understand the ion pressure anisotropy variation in the simulated coronal hole, we extract the ion parallel and perpendicular temperatures along the positive Z axis and plot the temperature profiles in the left plot of Figure 5.2. This plot can be directly compared to the results obtained by the 2D anisotropic MHD model (Figure 2(c) in *Li et al.* [2004]) and 1D anisotropic MHD model (Figure 4 in *Chandran et al.* [2011]). Our ion temperature profiles in the fast solar wind are very close to theirs in terms of the shapes and magnitudes, as well as the measured values between $1\,\mathrm{R}_S$ and $3\,\mathrm{R}_S$ (shown in *Chandran et al.* [2011]). Furthermore, *Chandran et al.* [2011] obtains isotropic temperature at a radial distance of about $40\,\mathrm{R}_S$, while *Li et al.* [2004] has the perpendicular temperature always higher than the parallel temperature. In comparison to their results, we get approximately isotropic temperature at about $24\,\mathrm{R}_S$.

The middle plot of Figure 5.2 shows the ion temperature anisotropy profile, which

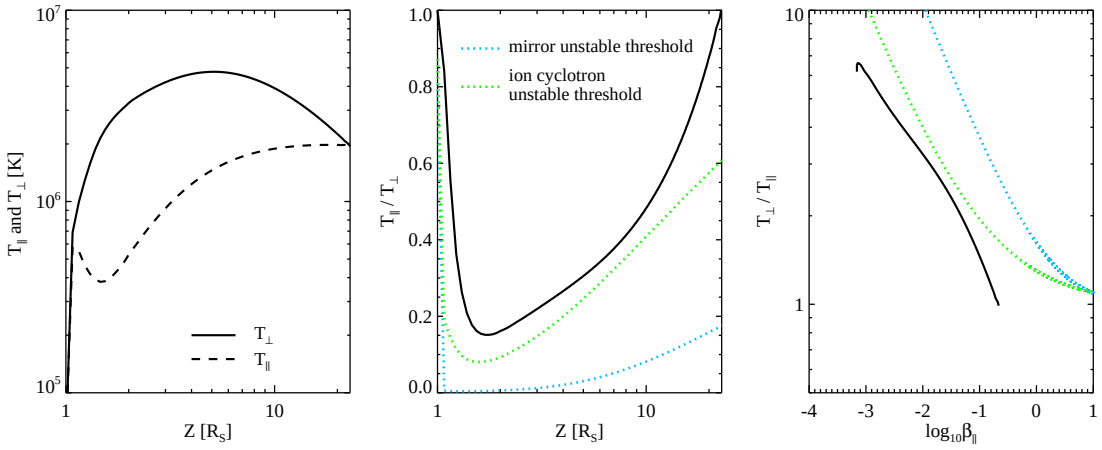

Figure 5.2: The ion parallel and perpendicular temperature (left), the ion pressure anisotropy ratio (middle), and the relation between ion parallel plasma beta and ion pressure anisotropy (right) along the positive Z axis in anisotropic MHD simulation of the idealized corona. The blue and green dotted lines in the middle and right plots represent the mirror and firehose instability thresholds, respectively.

can also be compared to Figure 2(e) in *Li et al.* [2004]. Although we get similar variation of $T_\parallel/T_\perp$ as the 2D anisotropic MHD modeling obtains, in our simulation the location of minimum $T_\parallel/T_\perp$ is closer to the Sun, and the temperature returns to isotropy much faster. We overplot the mirror and ion cyclotron instability criterion in the plot, and the region below the dotted lines is unstable. As mentioned earlier, the ion cyclotron instability has been excited during the simulation, but the solution at the end of the simulation is ion cyclotron stable.

Observations [*Marsch et al.*, 2004; *Hellinger et al.*, 2006] have shown that the ion temperature anisotropy and the ion parallel plasma beta are closely related in the solar wind. The ion parallel plasma beta is defined by the ratio between the ion parallel pressure and the magnetic pressure: $\beta_\parallel = 2\mu_0 p_\parallel/B^2$. We extract $\beta_\parallel$ along the $Z > 0$ axis and plot $log_{10}\beta_\parallel$ against $T_\perp/T_\parallel$ in the right plot of Figure 5.2. From left to right along the black line, the location of the extraction point along the Z axis increases from around $1.5\,\mathrm{R}_S$ to $24\,\mathrm{R}_S$. For $\beta_\parallel > 0.01$, our result is very similar to the one obtained by 1D anisotropic MHD simulations [*Chandran et al.*, 2011]. The mirror and ion cyclotron instability thresholds are also shown in the plot. Again, we can see that the simulated $T_\perp/T_\parallel - \beta_\parallel$ relation is bounded by the ion cyclotron instability criteria.

5.2.2 Comparison with isotropic MHD results

It is also important to compare the anisotropic MHD simulation with an isotropic MHD simulation, which will indicate how pressure anisotropy affects the coronal solution. Below we compare the solar wind speed, the ion and electron temperatures, and the plasma beta at the end of the two simulations.

Figure 5.3 displays the flow speed with the magnetic field lines in the $Y = 0$ plane. In both simulations, the flow from the polar regions with open field lines gradually accelerates radially and forms the fast solar wind, while the flow from the

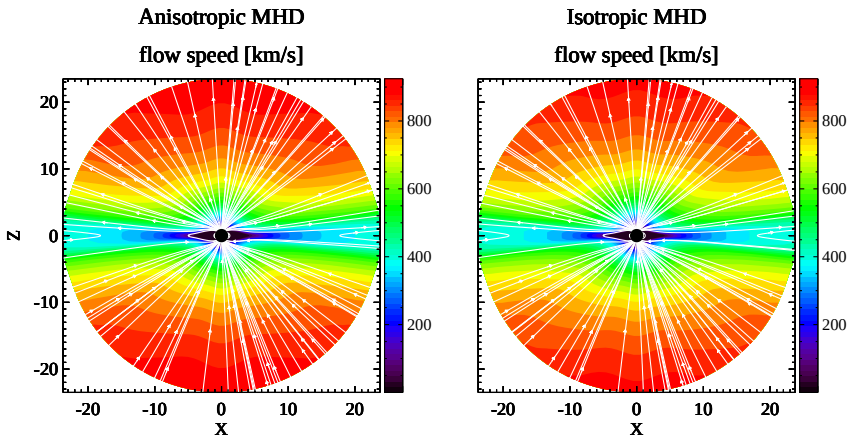

Figure 5.3: The flow speed contour and magnetic field lines (white) in the $Y = 0$ plane from the idealized coronal simulations.

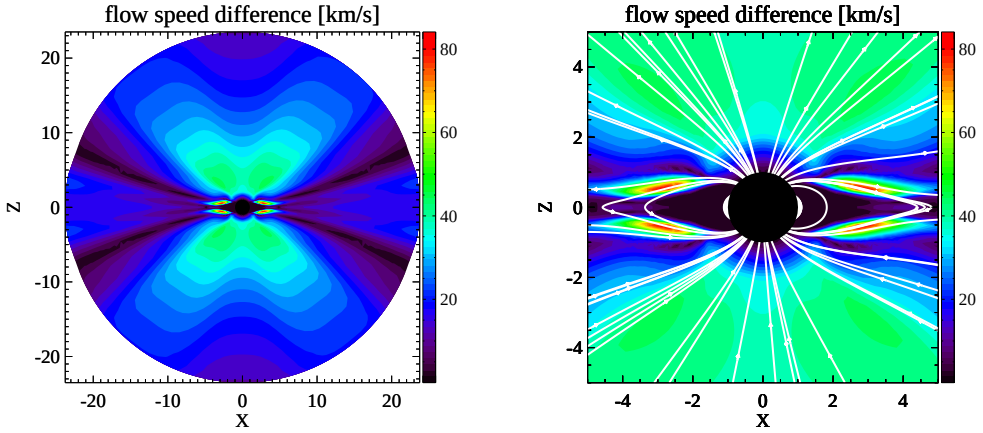

Figure 5.4: Left: The flow speed difference by subtracting the isotropic MHD simulated speed from the anisotropic MHD simulated speed shown in Figure 5.3. Right: A zoom-in view with magnetic field lines in white.

equatorial region with closed field lines accelerates in a much slower pace and forms the slow solar wind. Note that both simulations produce solar wind speeds larger than 850 km/s, while in reality, the fast solar wind speed hardly exceeds 800 km/s. The difference between the anisotropic MHD and isotropic MHD simulations can hardly be seen from the figure. In fact, the anisotropic MHD simulation gives larger solar wind speed than the isotropic MHD simulation gives, as seen in Figure 5.4, in which we subtract the isotropic MHD simulated flow speed from the anisotropic MHD simulated flow speed. As we can see from the left plot the speed difference is positive everywhere, and the difference becomes smaller away from the Sun. The right plot shows that the largest difference of more than 80 km/s occurs close to the Sun and at the interfaces of open and closed field lines, where the slow solar wind can originate. Our results partially agree with *Li et al.* [2004], who have found faster solar wind speed in anisotropic MHD than in isotropic MHD simulations for 2D models. Yet we do not observe a reversed trend beyond 10 R_S as has been seen in 2D simulations, at least within 24 R_S in our simulations.

Figure 5.5 compares the ion temperature T_i, the electron temperature T_e and the plasma beta in the $Y = 0$ plane from the two simulations. For the anisotropic MHD simulation, T_i is the average scalar ion temperature: $T_i = (2T_\perp + T_\parallel)/3$, and the plasma beta is the ratio of the average scalar ion pressure to the magnetic pressure. From this figure we find the following differences between the anisotropic and isotropic MHD simulations. First of all, the ion temperature from the anisotropic MHD simulation is lower than from the isotropic MHD simulation, especially for the region close to the equatorial plane. Second, the electron temperature given by the anisotropic MHD simulation is slightly higher than given by the isotropic MHD simulation, but the difference is small. Third, the plasma beta in the anisotropic MHD simulation is smaller than in the isotropic MHD simulation, particularly along the X axis. Since the distinctively high plasma beta region indicates the location of the current sheet where

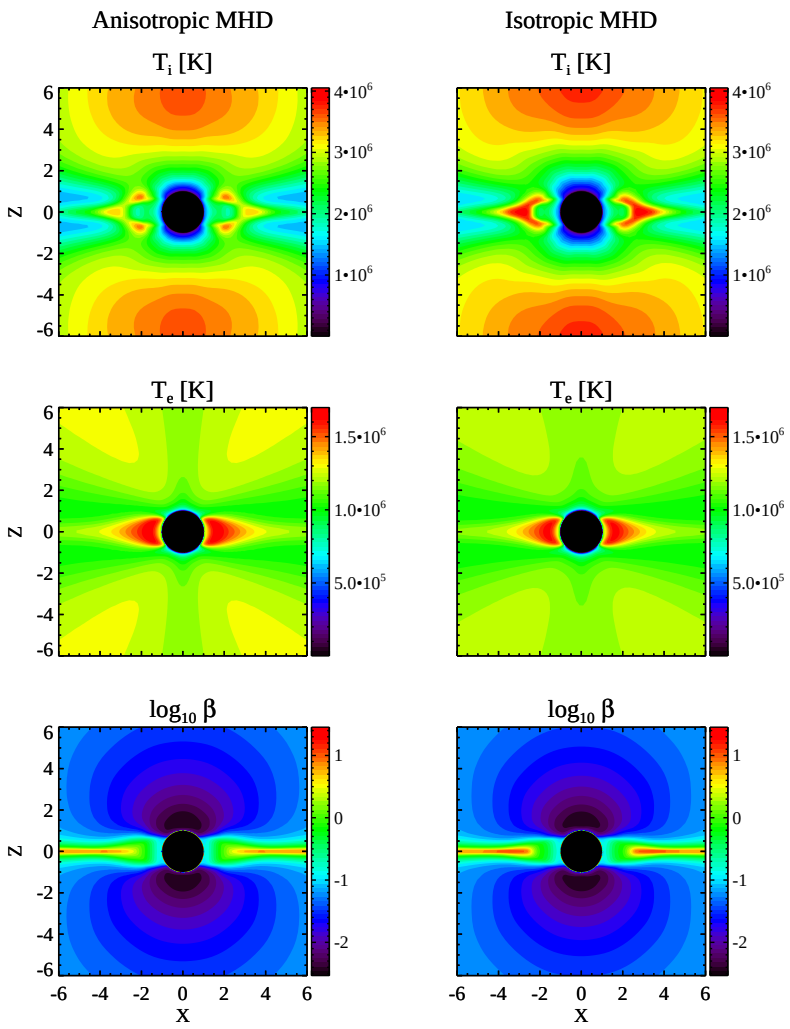

Figure 5.5: The ion temperature, electron temperature, and the logarithmic plasma beta in the $Y = 0$ plane from the idealized coronal simulations.

the magnetic field is close to zero, the simulation results imply that the anisotropic MHD simulation produces a somewhat thinner current sheet than the isotropic MHD simulation does.

A straightforward comparison of the ion and electron temperatures between the anisotropic and isotropic MHD simulations can be found in Figure 5.6, in which we plot the profiles of T_i and T_e along the positive X and Z axes. While the differences in the electron temperatures from the two simulations are almost negligible, the differences in the ion temperatures are considerable. In the polar region, the ion

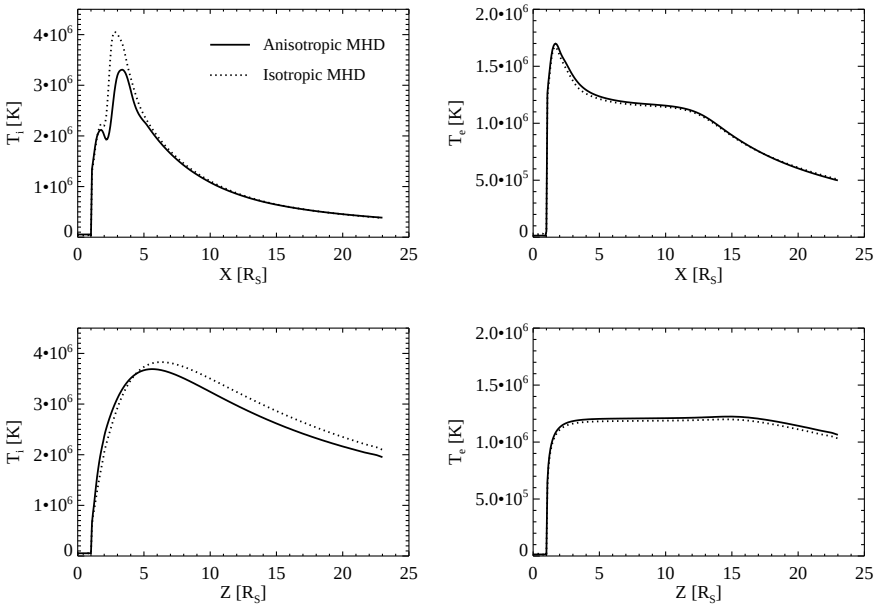

Figure 5.6: The ion temperature (left column) and electron temperature (right column) profiles along the X axis (top panel) and the Z axis (bottom panel) from the idealized coronal simulations.

temperature in the anisotropic MHD simulation is lower than in the isotropic MHD simulation beyond $5\,\mathrm{R}_S$. This was also obtained by 2D simulations [*Li et al.*, 2004].

5.3 Non-idealized Coronal and Heliospheric Simulations

For further validation, we apply the anisotropic MHD solar wind model to simulate several real Carrington rotations (CR) during the solar minimum (CR2077 and CR2058) and the solar maximum (CR2107), and compare the simulation results with isotropic MHD simulation results, as well as in-situ satellite measurement at 1 AU.

The simulations couple the IH component to the SC component to propagate the solar wind solution to 1 AU. For the SC component, the computational domain, grid, and inner boundary conditions are set to be the same as those used in the idealized coronal simulations, except that we use real magnetograms to obtain the magnetic field at the inner boundary of SC, instead of assuming a dipole field. We use the same wave dissipation rate and reflection coefficient as in the idealized simulations. The

wave dissipation ratios are: $\alpha_e = 0.4$ and $\alpha_{\parallel} = 0.05$. Here, a much smaller $\alpha_{\parallel}$ is used than in the idealized simulation, because we have found too much parallel pressure compared to measurement at 1 AU with the default $\alpha_{\parallel}$ in our initial experiments. In addition to the growth-rate-based pressure anisotropy relaxation, we also apply the global relaxation term with a relaxation time $\tau_g = 10^5$ s.

For the IH component, the computational domain is a square box surrounding the spherical domain of SC. The box extends from -250 R_S to 250 R_S along each of the X, Y and Z directions. We use Cartesian grids that vary from less than 1 R_S to about 8 R_S in resolution. Again, the current sheet region is with higher grid resolution than the rest of the domain. The total number of cells is about 2.1 million. The IH component uses exactly the same wave dissipation rate, dissipation ratio, and the pressure anisotropy relaxation as the SC component uses.

Similar to the idealized case, the isotropic MHD simulations with the same settings as the anisotropic MHD simulations have also been performed.

For all simulations presented in this section, we first run the SC component in the steady state mode for 60000 iterations, then couple the IH component with the SC component, switch off SC, and advance IH from the steady state SC solution for 4000 iterations in the steady state mode.

5.3.1 CR2077 Simulation

The Carrington rotation CR2077 (November 20th through December 16th, 2008) is a very quiet period during the solar minimum of solar cycle 23. The input magnetogram is obtained from the National Solar Observatory's Global Oscillation Network Group (GONG). Figure 5.7 shows the magnetogram used by our simulations, which has very few active regions and their magnetic field strength is small (compared to the other two Carrington rotations that we will show later).

Figure 5.8 displays the ion pressure anisotropy and solar wind speed at the end

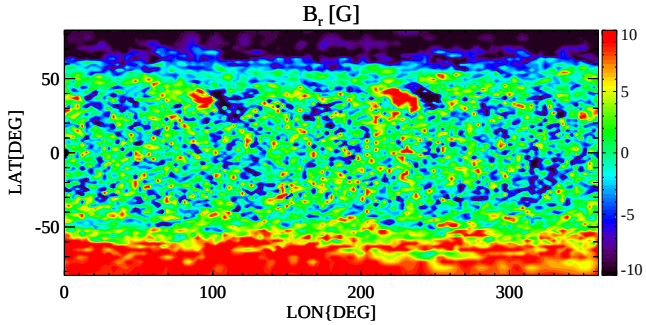

Figure 5.7: The input radial magnetic field for CR2077 simulations.

of the anisotropic MHD simulation from the IH component. The black circle in the middle of each plot represents the domain of the SC component. Away from the boundary between SC and IH, the ion pressure anisotropy ratio $p_\perp/p_\parallel$ gradually drops from greater than 1 to smaller than 1. Near the outer boundary of IH, $p_\perp/p_\parallel$ gets larger again, and the value is very close to 1. Comparing the ion pressure anisotropy with the solar wind speed in the $Z = 0$ plane, the region with lowest $p_\perp/p_\parallel$ is in the fast solar wind region represented by red in the flow speed plot.

We extract the ion pressure anisotropy along the Earth trajectory from the simulation with anisotropic MHD, and compare it with the WIND satellite measurement. Although WIND is at the L1 point instead of the Earth, we neglect this difference since the distance between the L1 point and the Earth is small compared to the heliospheric scale. Also, the grid resolution in our simulation is about $8\,\mathrm{R}_S$ near 1 AU, which is even larger than the distance between the L1 point and Earth (less than $3\,\mathrm{R}_S$). The comparison is shown in Figure 5.9. From the plot we could see that the simulated pressure anisotropy ratio is basically smaller and with less variation than the data.

Furthermore, we extract the magnetic field magnitude, the solar wind speed, the number density, and the ion temperature along the Earth orbit from both the anisotropic and isotropic MHD simulations, and compare them with the OMNI data,

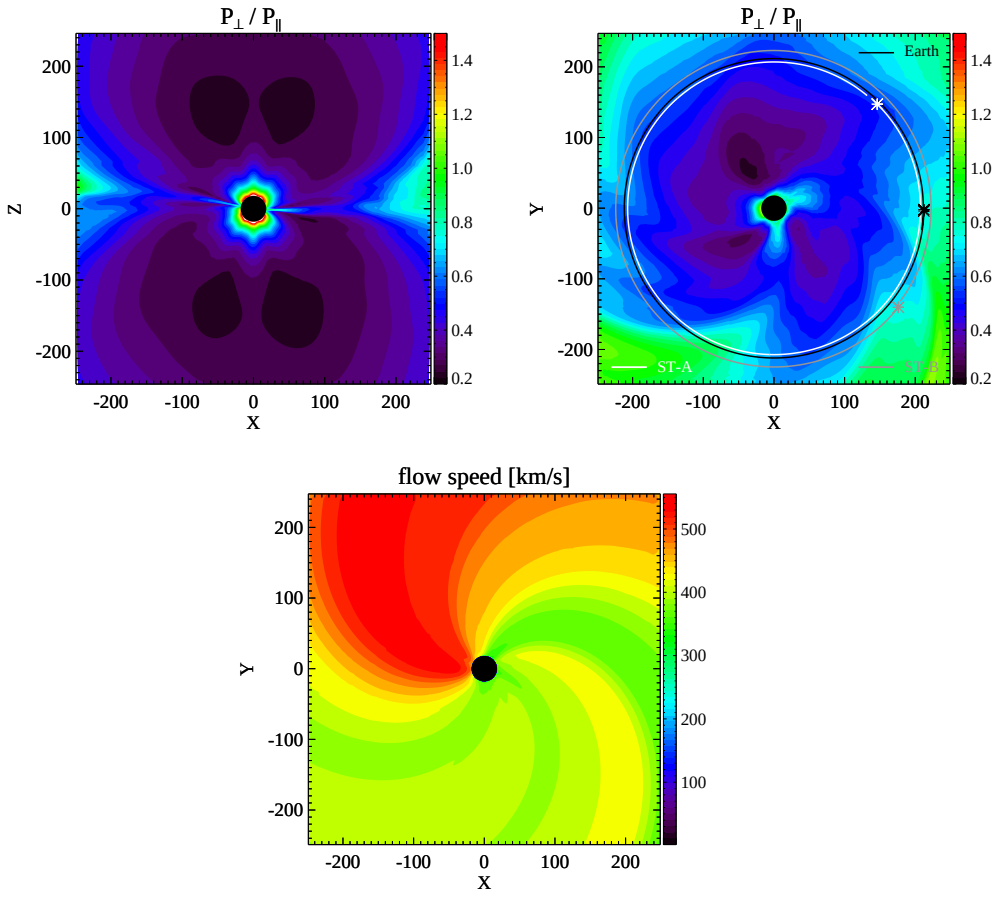

Figure 5.8: The ion pressure anisotropy ratio in the $Y = 0$ (top left) and $Z = 0$ (top right) planes, as well as the flow speed in the $Z = 0$ plane (bottom) at the end of the IH iterations for the anisotropic MHD simulation of CR2077. The trajectories of the Earth and the two STEREO satellites are projected onto the $Z = 0$ plane in the top right plot. The stars represent the locations of the Earth and the satellites at the beginning of CR2077.

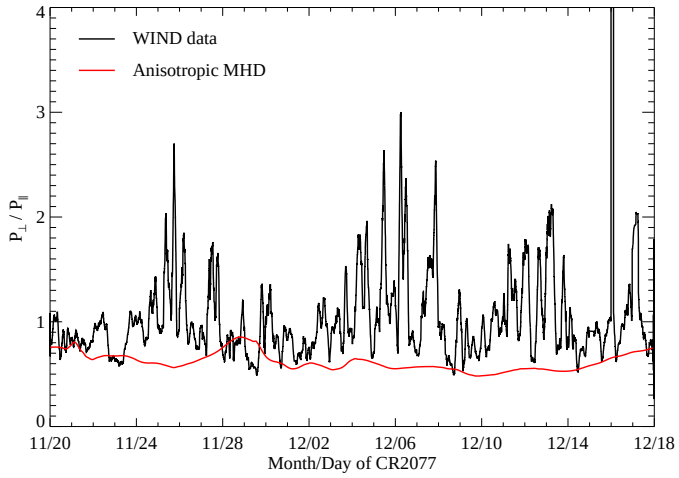

Figure 5.9: The comparison of simulated ion pressure anisotropy with the WIND data for CR2077.

which contains the solar wind and IMF conditions at 1 AU. The comparisons are shown in Figure 5.10. The anisotropic and isotropic MHD simulations produce very similar magnetic field strength and solar wind properties. However, they do not properly capture the corotating interaction regions (CIRs) that appear as sudden increase of the solar wind speed, accompanied by simultaneous jumps in the magnetic field magnitude, the number density and the temperature on November 25th. The failure in reproducing the CIRs can also been seen in the flow speed plot in Figure 5.8, where the transitions between slow and fast solar winds are rather smooth without any sharp interface. The anisotropic MHD model predicts higher ion temperature (average scalar temperature) at 1 AU than the isotropic MHD model does, which also provides a better agreement with the OMNI data. Interestingly, this is opposite to the effect of pressure anisotropy in the idealized coronal simulation, in which the anisotropic MHD simulation produces lower ion temperature than the isotropic MHD simulation does.

We also compare the simulations with the STEREO-A (STA) and STEREO-B (STB) data in Figure 5.11 and Figure 5.12, respectively. As shown in the top right panel of Figure 5.9, the STEREO-A satellite orbits a little bit closer to the Sun, and

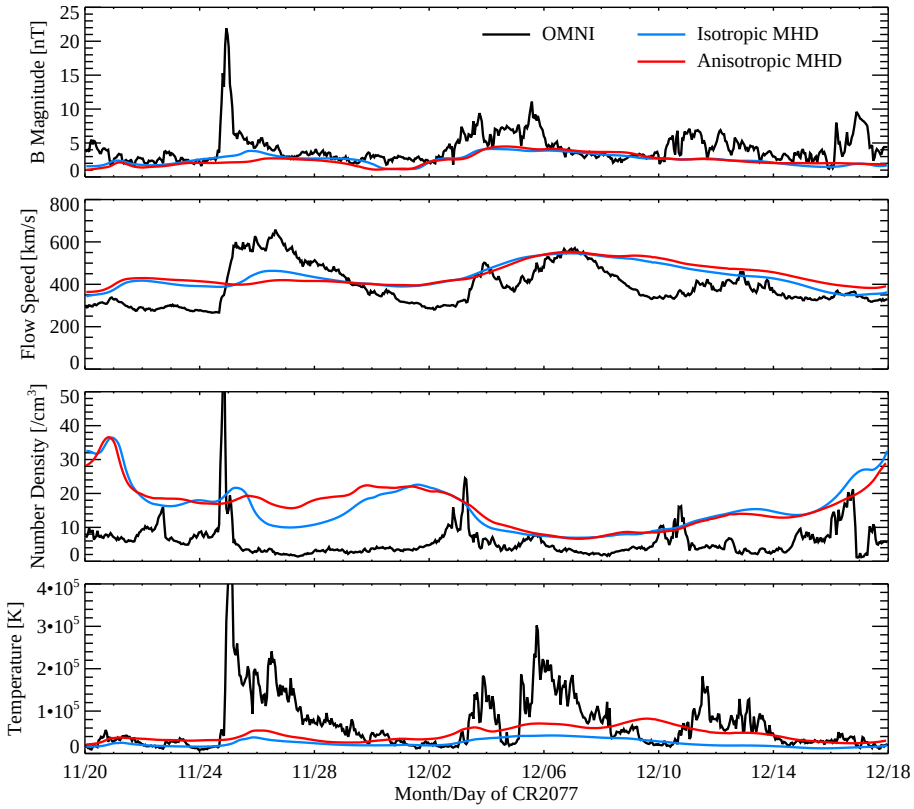

Figure 5.10: The comparison of anisotropic and isotropic MHD simulated magnetic field magnitude, solar wind speed, number density and ion temperature with the OMNI data for CR2077.

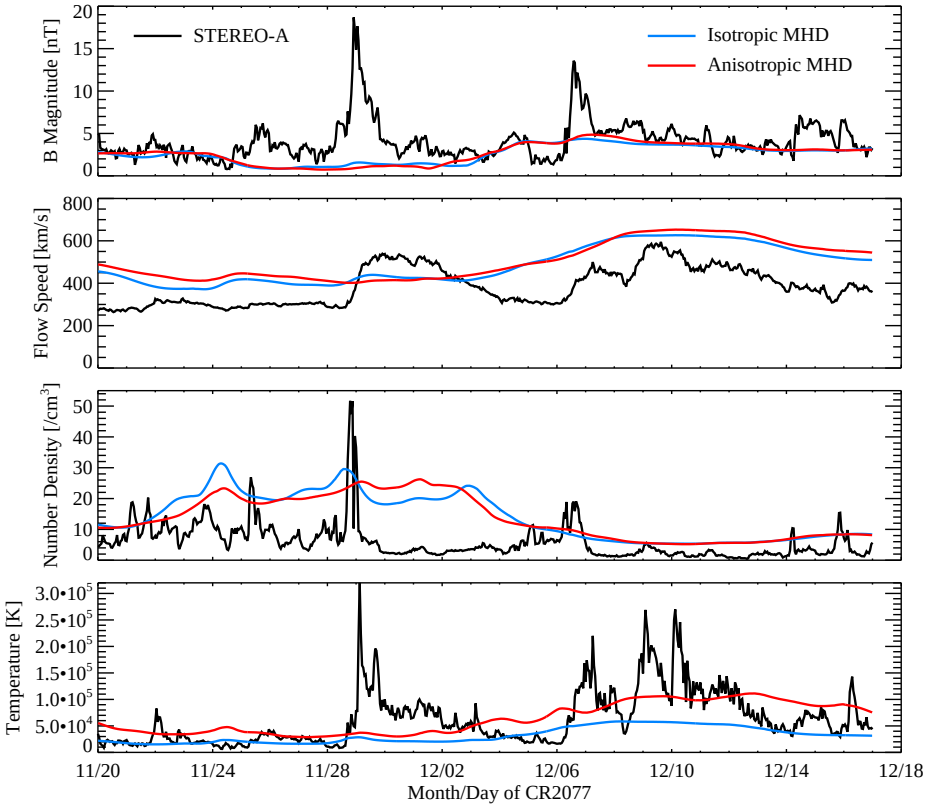

Figure 5.11: The comparison of anisotropic and isotropic MHD simulated magnetic field magnitude, solar wind speed, number density and ion temperature with the STEREO-A data for CR2077.

the STEREO-B satellite orbits further away from the Sun, compared to the trajectory of the Earth. The locations of the STEREO satellites and the Earth are quite far away from each other. Thus the comparison with the two STEREO satellites can help evaluate the models from different perspectives relative to the Sun.

Similar to the comparison with the OMNI data, comparisons with the STEREO-A and STEREO-B measurements indicate that the anisotropic MHD and isotropic MHD simulations have very similar results in the magnetic field magnitude and the solar wind speed, while the anisotropic MHD simulated ion temperature is constantly higher than the isotropic MHD simulated one, and the former agrees with the data slightly better. Again, both simulations miss the CIRs as seen by STEREO-A and

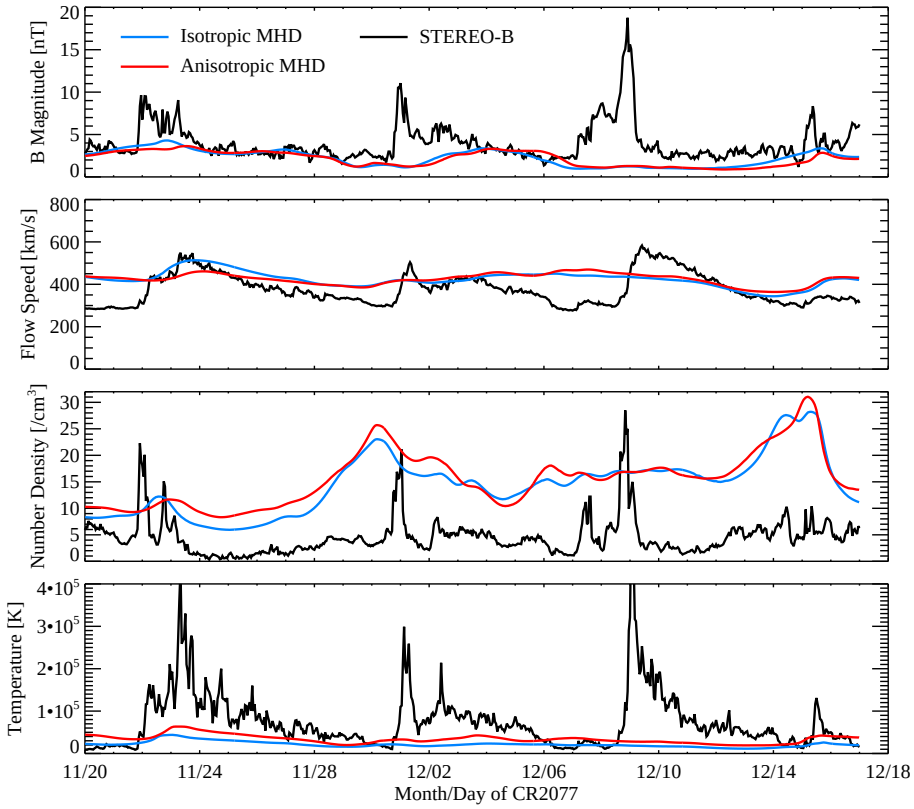

Figure 5.12: The comparison of anisotropic and isotropic MHD simulated magnetic field magnitude, solar wind speed, number density and ion temperature with the STEREO-B data for CR2077.

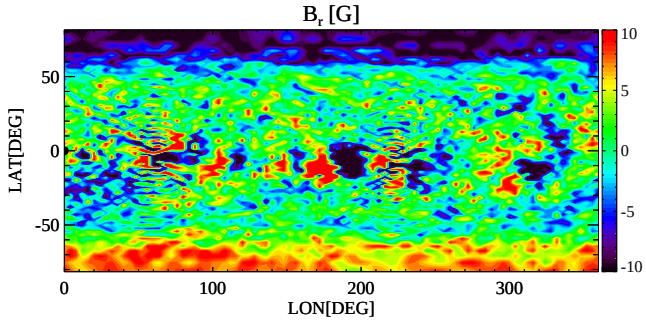

Figure 5.13: The input radial magnetic field for CR2058 simulations.

STEREO-B.

5.3.2 CR2058 Simulation

The second Carrington rotation we select is CR2058 from June 21st to July 18th in 2007. This time interval is also during the solar minimum, however there are more active regions on the Sun than during CR2077. The input magnetogram from GONG is displayed in Figure 5.13. There are a few active regions that can be identified by several pairs of large red and blue dots representing the strong magnetic field regions with bi-polarity.

Figure 5.14 plots the anisotropic MHD model simulated ion pressure anisotropy ratio $p_\perp/p_\parallel$ and the solar wind speed. Compared to the pressure anisotropy for CR2077 in Figure 5.8, we observe a more interesting pressure anisotropy distribution here. First, the current sheet region is characterized by higher $p_\perp/p_\parallel$ than the polar regions as shown in the top left plot. Second, pressure anisotropy exhibits corotational structure in the $Z = 0$ plane. When comparing with the solar wind speed shown in the bottom plot, we find that the region with highest $p_\perp/p_\parallel (> 1.4)$ in the $Z = 0$ plane corresponds to the sharp interface between regions with slow and fast solar wind, i.e., the CIR.

We extract the ion pressure anisotropy along the Earth orbit and compare it with

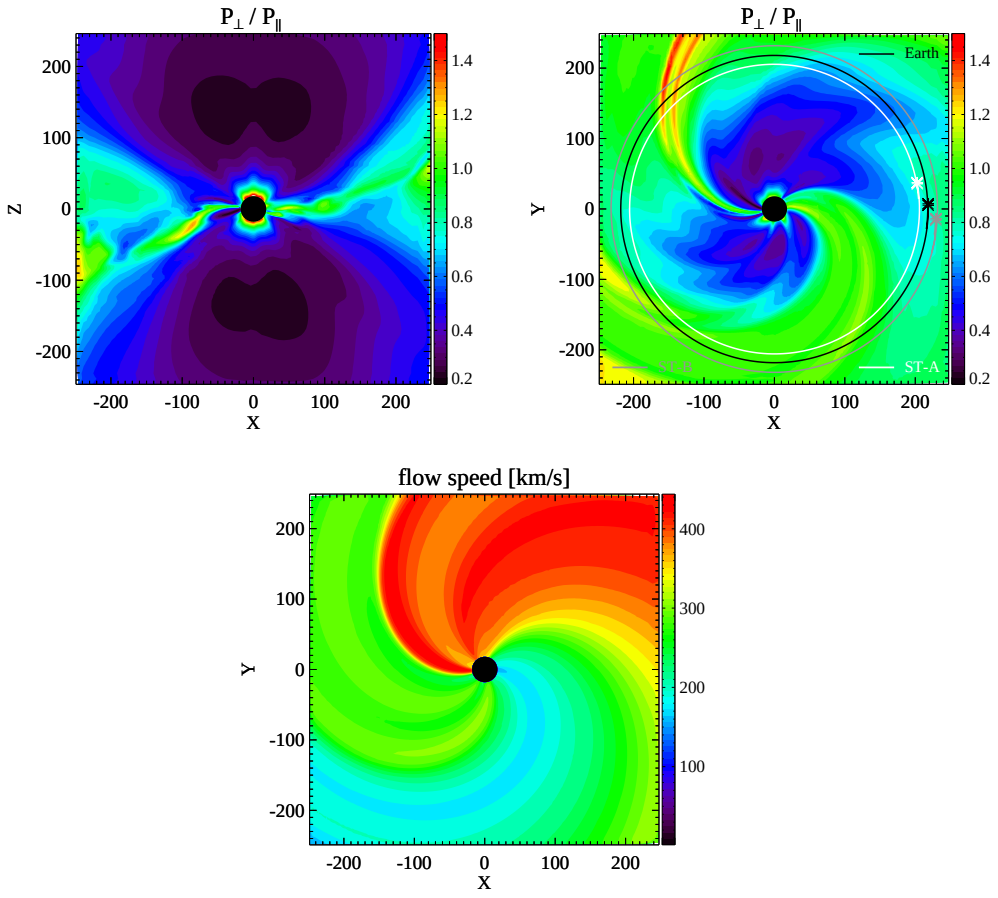

Figure 5.14: The ion pressure anisotropy ratio in the $Y = 0$ (top left) and $Z = 0$ (top right) planes, and the flow speed in the $Z = 0$ plane (bottom) at the end of the IH iterations for the anisotropic MHD simulation of CR2058. The trajectories of the Earth and the two STEREO satellites are projected onto the $Z = 0$ plane in the top right plot. The stars represent the locations of the Earth and the satellites at the beginning of CR2058.

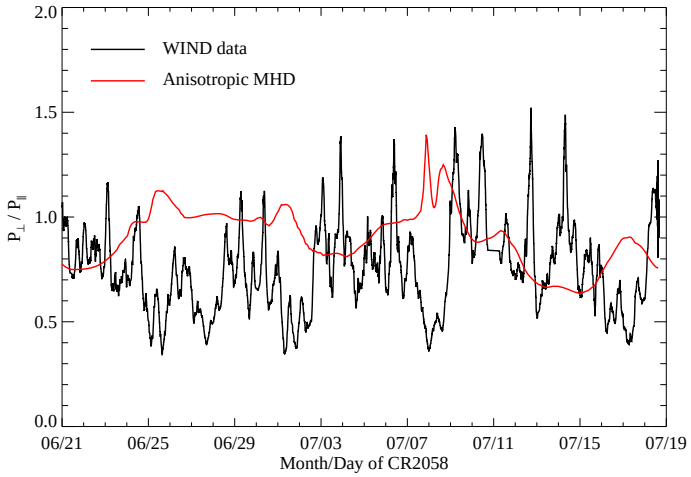

Figure 5.15: The comparison of simulated ion pressure anisotropy with the WIND data for CR2058.

the WIND data in Figure 5.15. This time we have more variations in the simulated $p_\perp/p_\parallel$ compared to Figure 5.9. Although the simulation produces quite different $p_\perp/p_\parallel$ from the measurement during June 23rd and July 3rd, the agreement after July 10th is good. Also, the simulated $p_\perp/p_\parallel$ variation seems to be shifted ahead by a few days compared to the data. This time shift is observed in the comparisons with other data as well.

Figure 5.16 compares the anisotropic and isotropic MHD simulations with the OMNI data. The two simulations are competitive in reproducing the magnetic field magnitude and the solar wind plasma properties. However, the anisotropic MHD model does a worse job than the isotropic MHD model does in capturing the CIR feature on July 11th. In addition, the anisotropic MHD simulation predicted CIR, shown as a red peak in every quantity in the figure, is a few days ahead of the isotropic MHD simulated one, as well as the actual data. This is the same time shift we have seen in the pressure anisotropy comparison. Once again, the anisotropic MHD simulation gives higher ion temperature than the isotropic MHD simulation during most of the time interval.

The comparisons with the STEREO-A and STEREO-B satellite measurements in

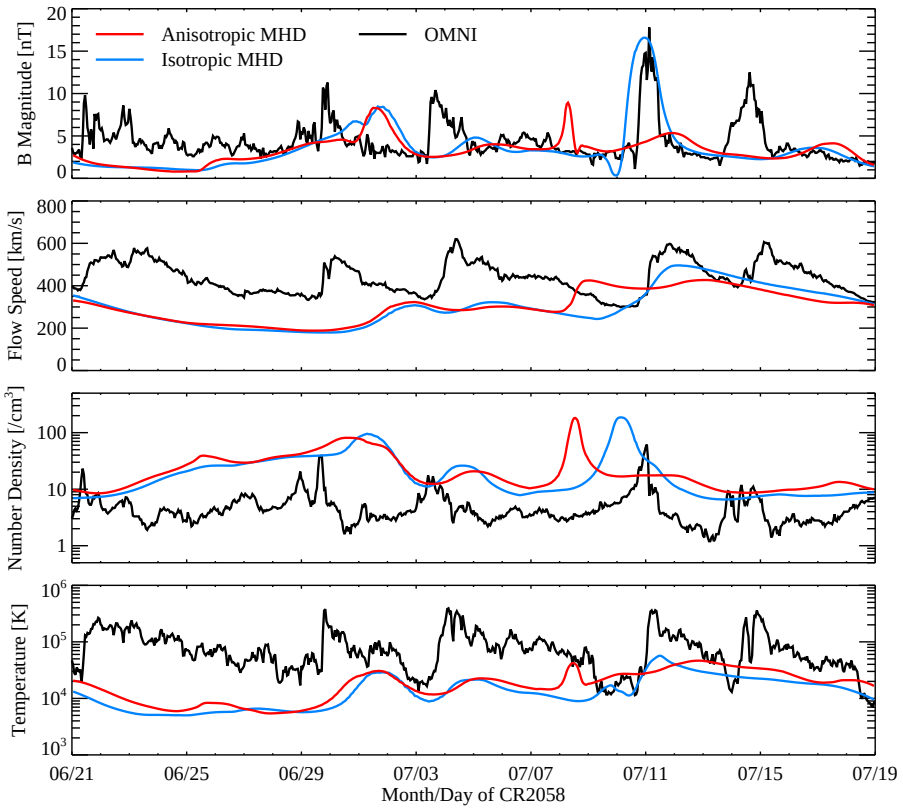

Figure 5.16: The same as Figure 5.10 for CR2058.

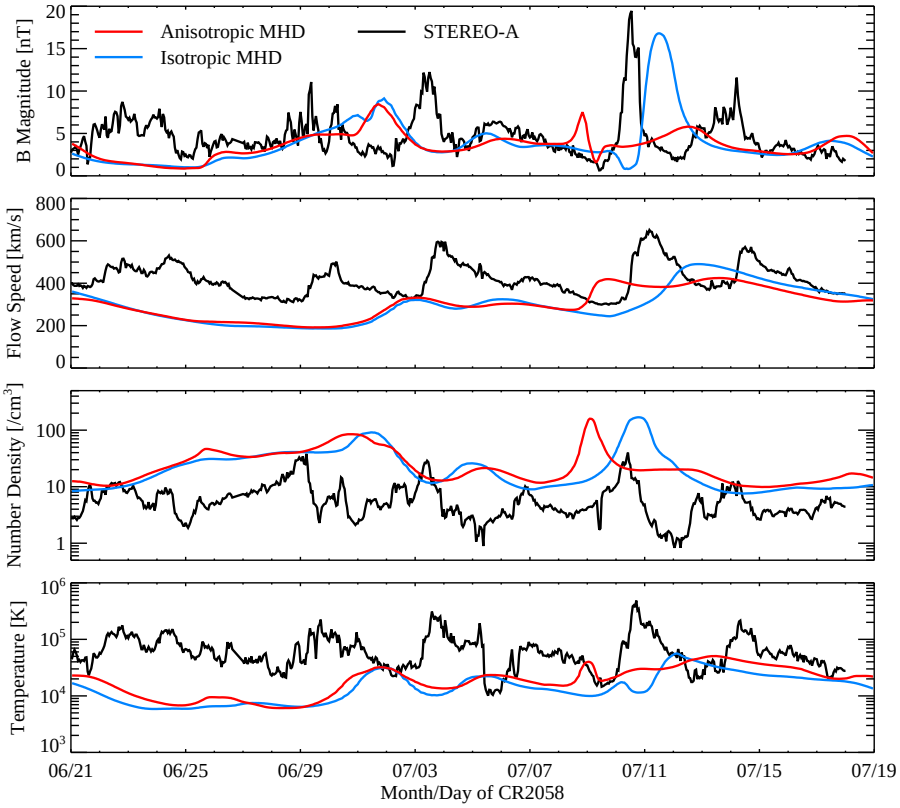

Figure 5.17: The same as Figure 5.11 for CR2058.

Figure 5.17 and Figure 5.18 have very similar features to the comparison with the OMNI data, given the positions of the two satellites and the location of the Earth are very close, as shown in Figure 5.14. The very same time shift appears in the comparisons with both STEREO satellites.

5.3.3 CR2107 Simulation

The last time period that we simulate is CR2107 from February 16th through March 16th in 2011. This is a solar maximum time, and a lot of active regions with strong magnetic fields appear in the magnetogram, as shown by Figure 5.19.

The simulated ion pressure anisotropy and flow speed are shown in Figure 5.20. The pressure anisotropy ratio varies between 0.5 and 1.5 in most of the domain. In

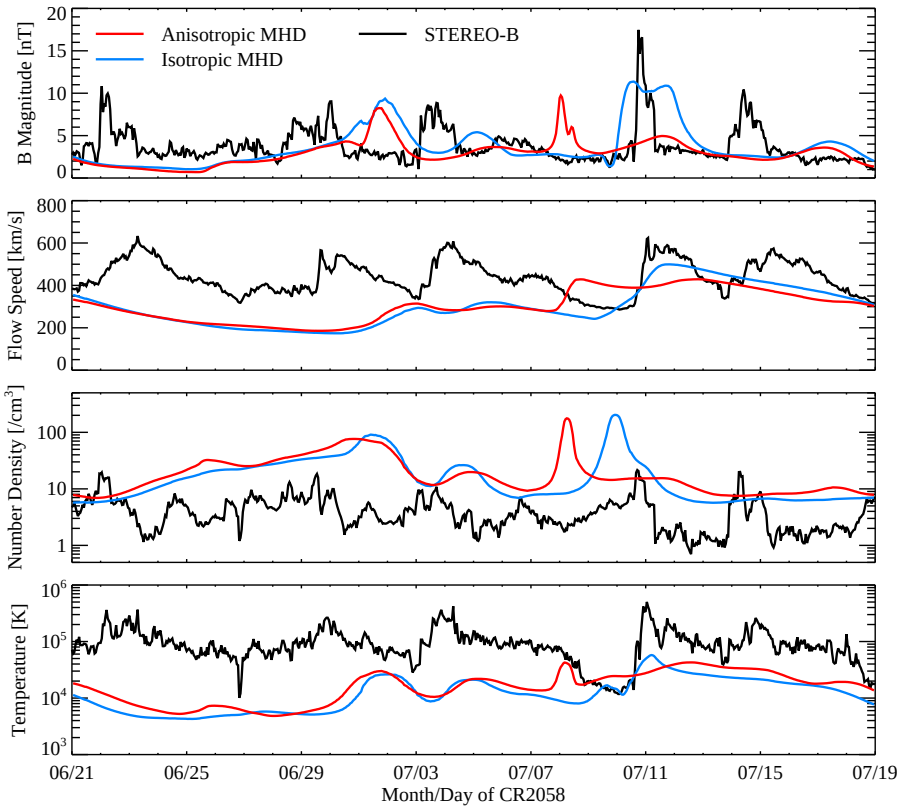

Figure 5.18: The same as Figure 5.12 for CR2058.

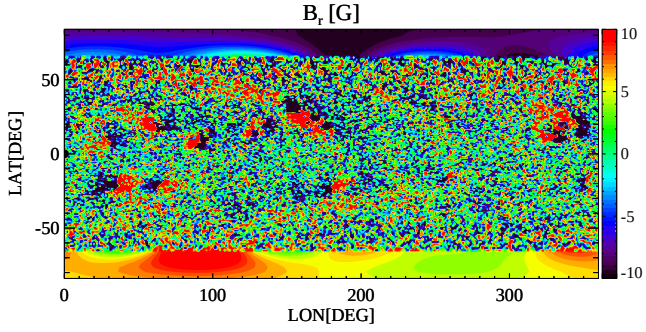

Figure 5.19: The input radial magnetic field for CR2107 simulations.

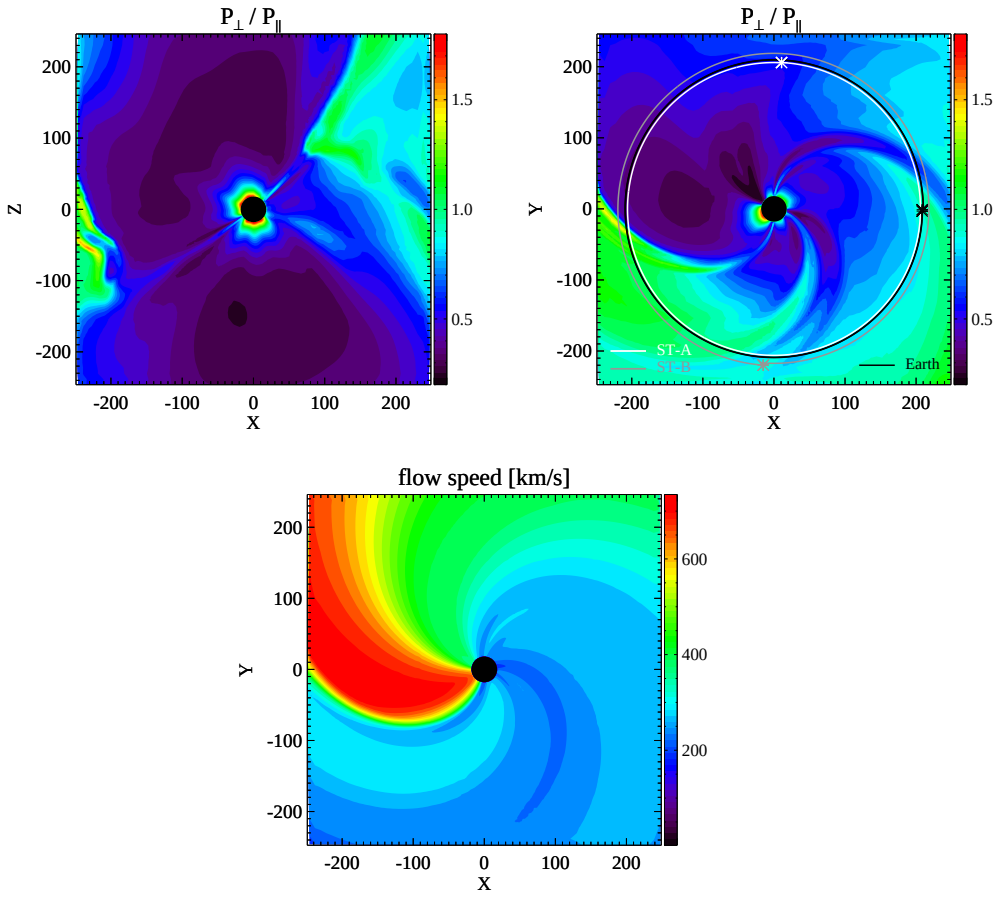

Figure 5.20: The ion pressure anisotropy ratio in the $Y = 0$ (top left) and $Z = 0$ (top right) planes, and the flow speed in the $Z = 0$ plane (bottom) at the end of the IH iterations for the anisotropic MHD simulation of CR2107. The trajectories of the Earth and the two STEREO satellites are projected onto the $Z = 0$ plane in the top right plot. The stars represent the locations of the Earth and the satellites at the beginning of CR2107.

the $Z = 0$ plane, the distribution of $p_\perp/p_\parallel$ appears to be cororating with the Sun, and the largest $p_\perp/p_\parallel$ away from the Sun occurs at the CIR and close to the outer boundary of the IH domain. The CIR is very distinct in the solar wind speed plot.

Figure 5.21 shows the comparison of the simulations with the WIND measurements. The anisotropic MHD simulation matches the peak in the magnetic field magnitude at the CIR better than the isotropic MHD simulation does. The solar wind speed from the anisotropic MHD simulation also agrees with the data better, though not by much, than the isotropic MHD simulation does. For the solar wind

number density, the two simulations are competitive. The last panel in Figure 5.21 shows that the anisotropic MHD simulation gives reasonable ion pressure anisotropy compared to the measurement, but in the fast solar wind region during March 2rd and March 6th, the simulated pressure anisotropy ratio is significantly lower than the measured one. Unfortunately the anisotropic MHD simulation does not capture the pressure anisotropy jump on February 18th, yet the corresponding jumps in the magnetic field magnitude, speed and density are not well reproduced by either the isotropic MHD or the anisotropic MHD simulation. Given that the ACE satellite is at the same location as the WIND satellite, the comparison with the ACE measured magnetic field strength and flow speed in Figure 5.22 confirms the features we observe in the comparison with the WIND data.

In the last two data-model comparisons for CR2107 shown in Figure 5.23 and 5.24, we compare the IMF and solar wind quantities along the STEREO-A and STEREO-B trajectories with the actual data. The comparison with the STEREO-A measurement indicates that both the anisotropic and isotropic MHD simulations predict the jump in the magnetic field strength and the solar wind speed about one day earlier than measured. In general, the anisotropic MHD and isotropic MHD produces similar results, but the anisotropic MHD simulation matches the measured solar wind speed and ion temperature better. The comparison with the STEREO-B measurement shows that the anisotropic MHD model predicts worse magnetic field magnitude than the isotropic MHD model does, for instance, the jump during March 7th and March 9th is well captured by the isotropic MHD simulation but not by the anisotropic MHD simulation. However, in the flow speed and ion temperature comparisons, the anisotropic MHD simulation does a better job than the isotropic MHD simulation does, particularly from February 28th to March 8th.

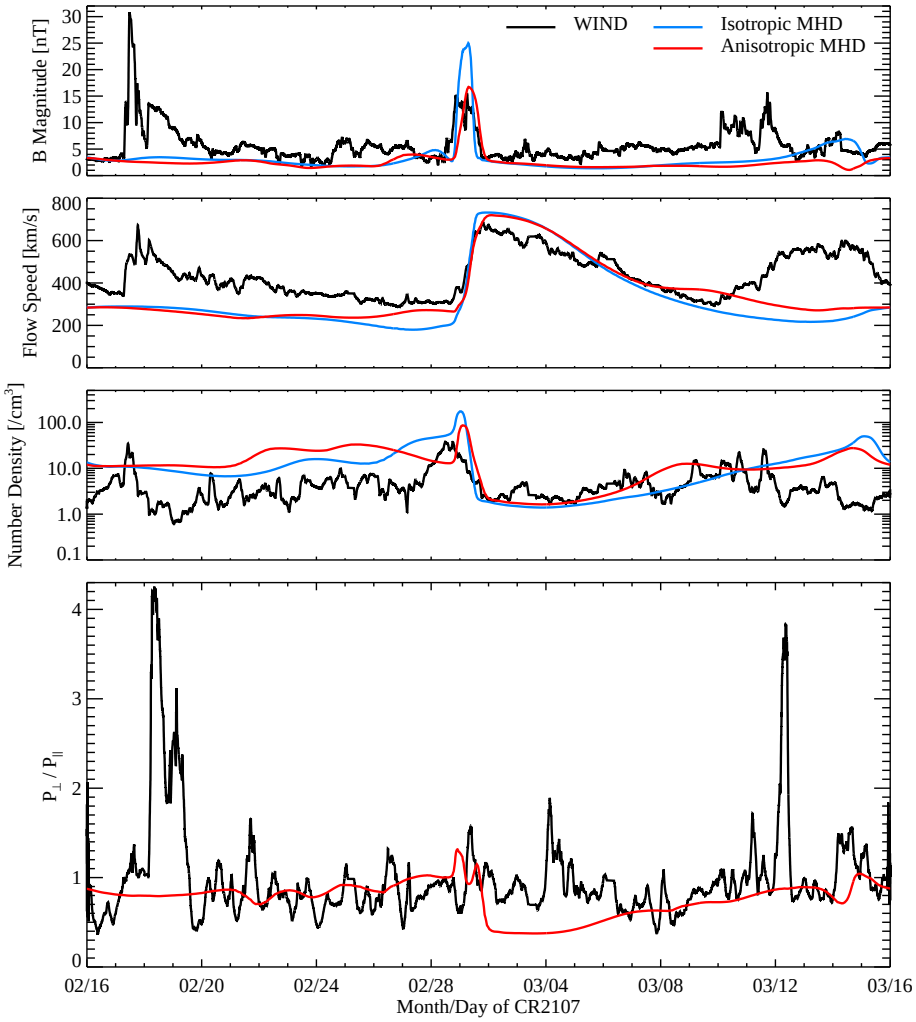

Figure 5.21: The comparison of simulated magnetic field magnitude, solar wind speed, number density by anisotropic and isotropic MHD, and the simulated ion pressure anisotropy by anisotropic MHD with the WIND data for CR2107.

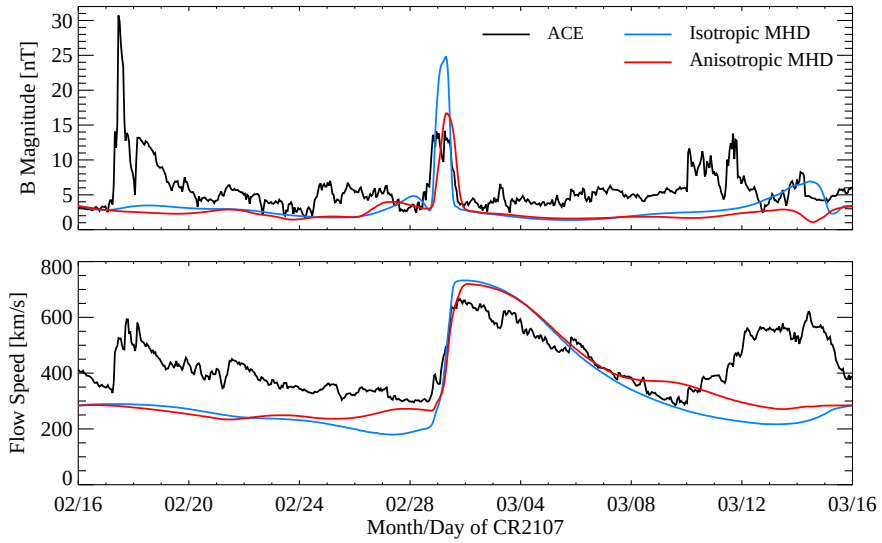

Figure 5.22: The comparison of anisotropic and isotropic MHD simulated magnetic field magnitude, and solar wind speed with the ACE data for CR2107.

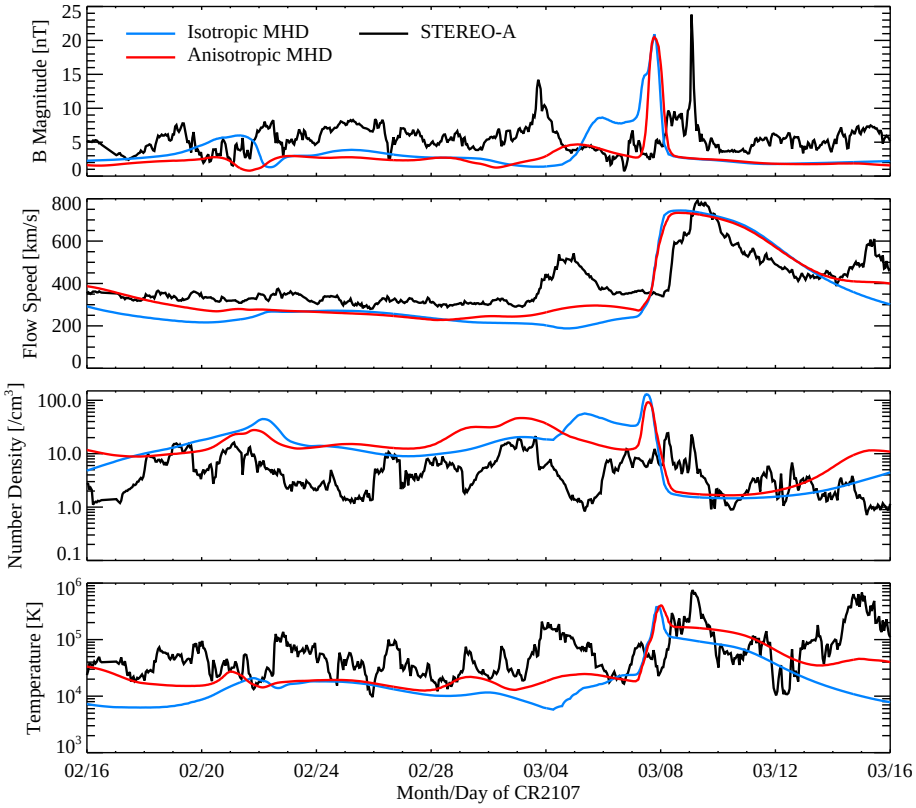

Figure 5.23: The same as Figure 5.11 for CR2107.

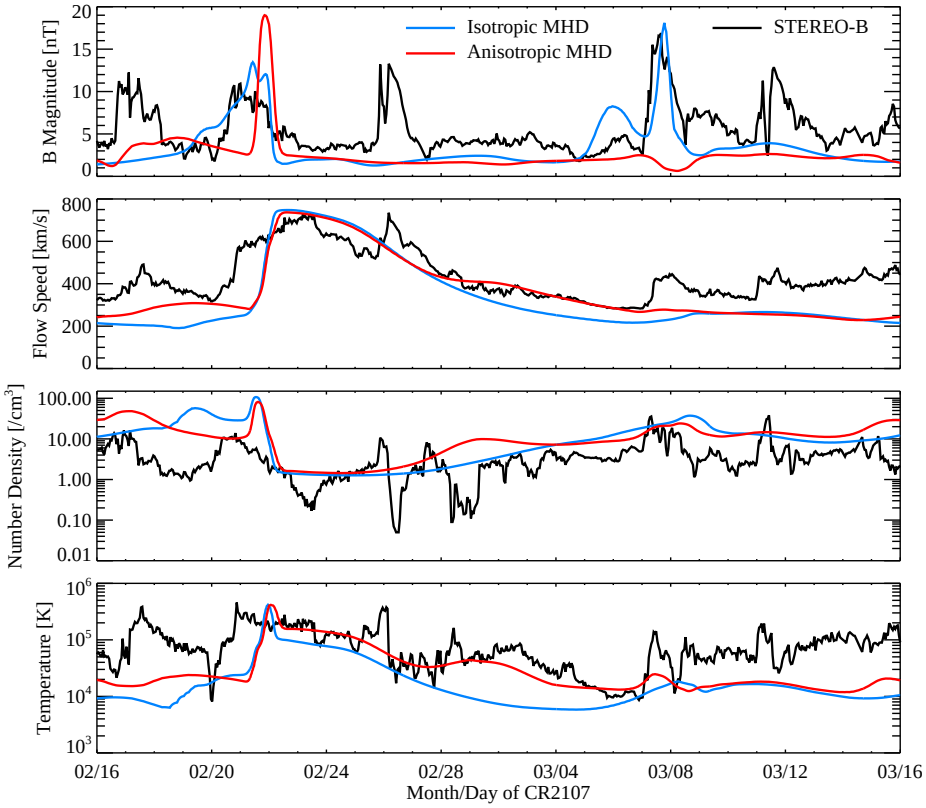

Figure 5.24: The same as Figure 5.12 for CR2107.

5.4 Summary

We have successfully incorporated Anisotropic BATS-R-US into the Alfvén wave driven solar wind model in the SWMF and applied the new anisotropic MHD solar wind model to coronal and heliospheric simulations.

The anisotropic MHD solar wind model keeps most of the treatments in the original Alfvén wave driven solar wind model and in Anisotropic BATS-R-US. We assume anisotropic ion pressure and isotropic electron pressure. The Alfvén wave energy dissipation goes into the ion parallel pressure, ion perpendicular pressure, and the electron pressure. For now we use uniform and constant ratios for the energy partition. At the top of the chromosphere where the inner boundary of the model lies, we assume that the ion pressure is isotropic.

In the idealized simulation of the corona with the anisotropic MHD model, most of our results agree with the 1D and 2D anisotropic MHD modeling results, and the ion parallel and perpendicular temperature profiles for the fast solar wind agree with available measurements. By comparing the anisotropic MHD simulation with the isotropic MHD simulation, we have found the following effects of the ion pressure anisotropy in the idealized solar corona. First, the ion pressure anisotropy results in larger solar wind speeds, especially close to the Sun and at the interface of the open and closed field line regions. Second, including the ion pressure anisotropy in the MHD model leads to lower ion average temperatures, particularly near the equatorial plane. Third, the ion pressure anisotropy leads to smaller plasma beta and a thinner current sheet in the equatorial region.

In the simulations of the corona and the heliosphere for three separated Carrington rotations, we have observed corotational structures in the ion pressure anisotropy distributions in the heliosphere, and the regions with the highest $p_\perp/p_\parallel$ corresponds to the CIRs. The comparisons between the simulation results and the satellite measurements indicates both improvements and drawbacks of the anisotropic MHD model.

Overall, the anisotropic MHD and isotropic MHD simulations produce very similar magnetic field strength and solar wind speed around 1 AU, but the anisotropic MHD simulations give higher ion temperatures that match the measured values better than the isotropic MHD simulations do. This is also opposite of the idealized simulations, which might be due to the different heating ratios used in idealized and non-idealized runs. The simulated ion pressure anisotropy also reproduces the WIND observations reasonably well.

The results presented in this chapter are mostly preliminary, and more work will be carried out in the future. For instance, since the ion pressure anisotropy matters most in the coronal region, we will compare it against the UVCS observational data of the ion pressure anisotropy in the corona to further validate our model. Also, the anisotropic MHD solar wind model itself needs to be improved. For example, we will implement the physics-based wave energy dissipation ratios $\alpha_{\parallel}$ and α_e that depend on local plasma parameters to replace the uniform dissipation ratios in the current model.

CHAPTER VI

Conclusions

This dissertation research focuses on MHD modeling of space plasmas with pressure anisotropy. I have successfully extended the existing 3D MHD model BATS-R-US to account for ion pressure anisotropy and applied Anisotropic BATS-R-US to model the terrestrial magnetosphere as well as the solar corona and heliosphere.

The analytical model for Anisotropic BATS-R-US is the MHD equations with anisotropic ion pressure and isotropic electron pressure under both non-relativistic and semirelativistic approximations. The ion pressure equations basically follow the double adiabatic approximation except for the pressure anisotropy limiting term. The characteristic waves for the equations are derived in order to calculate the numerical fluxes. Utilizing the available temporal and spatial schemes in BATS-R-US, I have implemented the anisotropic MHD equations and performed a variety of numerical tests to verify the implementation.

The major application of Anisotropic BATS-R-US presented in this dissertation is the global magnetospheric modeling. I have performed quiet time magnetosphere simulations and explored the effects of pressure anisotropy in the magnetosphere from different results seen in the anisotropic and isotropic MHD simulations. The results from idealized magnetospheric simulations confirm previous studies: pressure anisotropy widens the magnetosheath, increases the density depletion in the vicinity of the

magnetopause, enhances the nightside plasma pressure, and produces an eastward ring current. In addition, the flow speed in the magnetotail is significantly reduced by including pressure anisotropy in MHD simulations. In the non-idealized magnetospheric simulations the results are validated against the THEMIS data on both the dayside and nightside of the magnetosphere during quiet times. The comparison to the results from isotropic MHD simulations implies that although anisotropic MHD is comparable to isotropic MHD in matching the measurement, it improves the simulated plasma velocity in some cases.

Since the inner magnetosphere dynamics cannot be fully described even by anisotropic MHD, I have coupled Anisotropic BATS-R-US with two ring current models: the RCM and the CRCM. The coupled models provide better representations of the near Earth plasma, especially during geomagnetic storms. In particular, we have developed the two-way coupling algorithm between Anisotropic BATS-R-US and the CRCM. Global magnetosphere simulations are performed with the coupled models, and the results are compared to the results given by the coupled isotropic MHD and ring current models. I find that in the global MHD simulations coupled with ring current models, pressure anisotropy results in a thinner magnetosheath, a shorter tail, a much smaller Earthward plasma jet from the tail reconnection site, and is also important in controlling the magnetic field topology. The comparisons with satellite data for the magnetospheric event simulations show improvements on reproducing the measured tail magnetic field and inner magnetospheric flow velocity when including pressure anisotropy in the ring current model coupled global MHD model.

The last application of Anisotropic BATS-R-US addressed in the dissertation is the coronal and heliospheric modeling. By incorporating Anisotropic BATS-R-US into the Alfvén wave driven solar wind model, I have performed idealized coronal simulations, as well as coronal and heliospheric simulations during real Carrington rotations. In idealized simulations, I find that the ion pressure anisotropy results in

faster solar wind speeds, lower ion average temperatures, and smaller plasma beta near the current sheet in the corona. The simulated ion parallel and perpendicular temperature profiles in the fast solar wind agree with measurements and 1D and 2D anisotropic MHD modeling results. In simulations of real Carrington rotations, I find that in the CIRs the ion pressure is more perpendicular than in other regions. The simulated ion pressure anisotropies are reasonable compared to the observed values at 1 AU. The anisotropic MHD and isotropic MHD simulated magnetic field strengths and solar wind speeds at 1 AU are similar and competitive in matching the in-situ measurements, while the anisotropic MHD simulated ion average temperatures better agree with the data than the isotropic MHD simulated ones.

6.1 Originality and Contributions

Anisotropic BATS-R-US is the first 3D global MHD model developed to account for space plasma pressure anisotropy. It drops the assumption of pressure isotropy that has been used by the modeling community for a long time, which makes a large step forward towards accurately describing features of space plasmas.

During the model development, I have derived the characteristic wave speeds for the semirelativistic anisotropic MHD equations, which is original and contributes to the anisotropic MHD theory. Also, the semirelativistic formulation for anisotropic MHD is implemented into a numerical model for the first time.

In the global magnetospheric simulations, I have examined the effects of pressure anisotropy in the magnetosphere, confirmed several features observed in regional anisotropic MHD simulations, and found new features with our model. The coupled Anisotropic BATS-R-US and the CRCM provides the first self-consistent Earth's magnetospheric model resolving both the ring current and the pressure anisotropy, which improves geomagnetic storm simulations and benefits space weather prediction potentially. The application of Anisotropic BATS-R-US on the coronal and heliospheric

modeling also leads to development of the first 3D Alfvén wave driven anisotropic MHD model for the solar wind.

6.2 Future Work

A lot of future research can be carried out beyond this dissertation study. An obvious follow-up work is to further improve the anisotropic MHD solar wind model as discussed in Chapter V. Beside this, possible future work includes:

1. Apply the anisotropic MHD solar wind model to time-dependent simulations with the presence of CMEs.

2. For the Earth's magnetosphere, we could do a more systematic study with Anisotropic BATS-R-US or the coupled Anisotropic BATS-R-US+CRCM model to explore how pressure anisotropy affects the magnetosphere, such as studying the global magnetospheric dynamics under different solar wind and IMF conditions, investigating the role pressure anisotropy plays in the magnetosheath, and modeling substorm periods.

3. We can use Anisotropic BATS-R-US to model planetary magnetospheres other than the Earth's, for example, Jupiter's and Saturn's magnetospheres. Since Jupiter's and Saturn's intrinsic magnetic fields are much stronger than the terrestrial magnetic field, we expect that the pressure anisotropy is more important in Jupiter's and Saturn's magnetospheres.

4. Anisotropic BATS-R-US itself can be extended to account for electron pressure anisotropy and pressure anisotropy for multi-ion modeling. The extended model will have even more applications.

APPENDICES

APPENDIX A

Marginally Unstable States for Plasmas with Ion Pressure Anisotropy

The marginally unstable states of $p_{\|}$ for the firehose, mirror and ion cyclotron instabilities are obtained as following.

We denote the marginally unstable ion parallel and perpendicular pressures as $\overline{p}_{\|}$ and $\overline{p}_{\perp}$, respectively. The following relation is always true,

$$\overline{p}_{\|} + 2\overline{p}_{\perp} = 3p \tag{A.1}$$

A.1 Firehose Instability

For the firehose instability, based on (2.15), plasmas are marginally unstable when

$$\frac{\overline{p}_{\|}}{\overline{p}_{\perp}} = 1 + \frac{\mathbf{B}^2}{\mu_0 \overline{p}_{\perp}} \tag{A.2}$$

which can also be written as

$$\overline{p}_{\|} = \overline{p}_{\perp} + \frac{\mathbf{B}^2}{\mu_0} \tag{A.3}$$

Combining equation (A.1) and (A.3) and eliminating $\overline{p}_\perp$ gives

$$\overline{p}_\parallel = \frac{3}{2}p - \frac{1}{2}\overline{p}_\parallel + \frac{\mathbf{B}^2}{\mu_0} \tag{A.4}$$

Thus the ion parallel pressure in marginally firehose unstable plasmas is

$$\overline{p}_{\parallel f} = p + \frac{2\mathbf{B}^2}{3\mu_0} \tag{A.5}$$

and the marginally unstable ion perpendicular pressure is

$$\overline{p}_{\perp f} = p - \frac{\mathbf{B}^2}{3\mu_0} \tag{A.6}$$

From (A.5) and (A.6), we observe the following interesting relation

$$p_\parallel - \overline{p}_{\parallel f} = 2(\overline{p}_{\perp f} - p_\perp) \tag{A.7}$$

where we have used equation (2.2). The relation (A.7) basically says that for an arbitrary plasma state (stable or unstable), the difference between the parallel pressure and its marginally firehose unstable value is twice of the difference between the perpendicular pressure and its marginally firehose unstable value.

A.2 Mirror Instability

For the mirror instability, based on (2.16), the marginally unstable condition is given by

$$\frac{\overline{p}_\perp}{\overline{p}_\parallel} = 1 + \frac{\mathbf{B}^2}{2\mu_0\overline{p}_\perp} \tag{A.8}$$

or equivalently,

$$\overline{p}_\perp = \overline{p}_\parallel + \frac{\mathbf{B}^2}{2\mu_0}\frac{\overline{p}_\parallel}{\overline{p}_\perp} \tag{A.9}$$

from which $\overline{p}_\perp$ can be eliminated with the help of equation (A.1) to obtain

$$3\overline{p}_\parallel^2 - \left(\frac{2\mathbf{B}^2}{\mu_0} + 12p\right)\overline{p}_\parallel + 9p^2 = 0 \tag{A.10}$$

The above equation can be easily solved for $\overline{p}_\parallel$ as

$$\overline{p}_\parallel = \frac{1}{3}\left[\frac{\mathbf{B}^2}{\mu_0} + 6p \pm \sqrt{\left(\frac{\mathbf{B}^2}{\mu_0} + 6p\right)^2 - 27p^2}\right] \tag{A.11}$$

The root with the plus sign is not physically valid, since it yields

$$\begin{aligned}
\overline{p}_\parallel &= \frac{1}{3}\left[\frac{\mathbf{B}^2}{\mu_0} + 6p \pm \sqrt{\left(\frac{\mathbf{B}^2}{\mu_0} + 3p\right)^2 + \frac{6\mathbf{B}^2 p}{\mu_0}}\right] \\
&> \frac{1}{3}\left(\frac{\mathbf{B}^2}{\mu_0} + 6p + \frac{\mathbf{B}^2}{\mu_0} + 3p\right) \\
&= \frac{2\mathbf{B}^2}{3\mu_0} + 3p
\end{aligned} \tag{A.12}$$

for positive $|\mathbf{B}|$ and p. This further gives $\overline{p}_\parallel > \overline{p}_\perp$, which contradicts with the fact that the ion perpendicular pressure is larger than the ion parallel pressure when the mirror instability is excited. Therefore the remaining root with the minus sign gives the ion parallel pressure in marginally mirror unstable plasmas

$$\overline{p}_{\parallel m} = \frac{1}{3}\left[\frac{\mathbf{B}^2}{\mu_0} + 6p - \sqrt{\left(\frac{\mathbf{B}^2}{\mu_0}\right)^2 + \frac{12\mathbf{B}^2 p}{\mu_0} + 9p^2}\right] \tag{A.13}$$

that is always positive. $\overline{p}_{\perp m}$ can be obtained from (A.1).

A.3 Ion Cyclotron Instability

From the criterion of the ion cyclotron instability (2.17), we obtain the marginally unstable condition

$$\frac{\overline{p}_{\perp}}{\overline{p}_{\parallel}} = 1 + 0.3\sqrt{\frac{\mathbf{B}^2}{2\mu_0\overline{p}_{\parallel}}} \tag{A.14}$$

It can be written as

$$\overline{p}_{\perp} = \overline{p}_{\parallel} + 0.3\sqrt{\frac{\mathbf{B}^2\overline{p}_{\parallel}}{2\mu_0}} \tag{A.15}$$

With equation (A.1), we eliminate $\overline{p}_{\perp}$ and get

$$\overline{p}_{\parallel} + 0.2\sqrt{\frac{\mathbf{B}^2\overline{p}_{\parallel}}{2\mu_0}} - p = 0 \tag{A.16}$$

$\sqrt{\overline{p}_{\parallel}}$ can be solved from the above equation as

$$\sqrt{\overline{p}_{\parallel}} = -0.1\sqrt{\frac{\mathbf{B}^2}{2\mu_0}} \pm \sqrt{0.01\frac{\mathbf{B}^2}{2\mu_0} + p} \tag{A.17}$$

The root with the minus sign is meaningless as it gives $\sqrt{\overline{p}_{\parallel}} < 0$. Hence, from the root with the plus sign we get

$$\overline{p}_{\parallel ic} = \frac{1}{2}\left(-0.1\sqrt{\frac{\mathbf{B}^2}{\mu_0}} + \sqrt{0.01\frac{\mathbf{B}^2}{\mu_0} + 2p}\right)^2 \tag{A.18}$$

as the marginally unstable ion parallel pressure for the ion cyclotron instability.

APPENDIX B

Particle Distribution and Force Balance Along Closed Field Lines in the Inner Magnetosphere

B.1 Particle Distribution Along Closed Field Lines

Let us assume that the particle distribution at the "minimum B" point (represented by subscript "0") of a closed field line can be written as

$$f_0(\mathbf{v}_0) = \phi\left(\frac{v_{\perp 0}^2}{T_{\perp 0}} + \frac{v_{\parallel 0}^2}{T_{\parallel 0}}\right) \tag{B.1}$$

where v is particle speed, T is temperature, and the subscript "$\perp$" and "$\parallel$" stand for the directions perpendicular to and along with the magnetic field, and ϕ is an arbitrary function of $v_\perp^2/T_\perp + v_\parallel^2/T_\parallel$. For bi-Maxwellian distribution, $\phi(x) = A\exp(-mx/2k)$; For bi-Kappa distribution, $\phi(x) = B(1 + mx/(k(2\kappa - 3)))^{-\kappa-1}$, or in terms of characteristic energy, $\phi(y) = B(1 + my/(2\kappa))^{-\kappa-1}$ with $y = v_\parallel^2/E_{ch\parallel} + v_\perp^2/E_{ch\perp}$, where $E_{ch\parallel}$ and $E_{ch\perp}$ are parallel and perpendicular characteristic energy, respectively. Both A and B are normalization factors, m is particle mass, and k is Boltzmann constant.

Liouville's theorem gives the particle distribution at an arbitrary "non-minimum

B" point (represented by subscript "λ") as

$$f_\lambda(\mathbf{v}_\lambda) = f_0(\mathbf{v}_0(\mathbf{v}_\lambda)) \tag{B.2}$$

To find $\mathbf{v}_0(\mathbf{v}_\lambda)$, we connect the components of $\mathbf{v}_0$ and $\mathbf{v}_\lambda$ through the conservation of the first adiabatic invariant as

$$\mu = \frac{mv_{\perp 0}^2}{2B_0} = \frac{mv_{\perp \lambda}^2}{2B_\lambda} \tag{B.3}$$

and the conservation of energy with neglecting potential drop along the field line as

$$E = \frac{1}{2}mv_{\perp 0}^2 + \frac{1}{2}mv_{\parallel 0}^2 = \frac{1}{2}mv_{\perp \lambda}^2 + \frac{1}{2}mv_{\parallel \lambda}^2 \tag{B.4}$$

where m is particle mass and B is magnetic field strength. From equation (B.3) we obtain

$$v_{\perp 0}^2 = v_{\perp \lambda}^2 \frac{B_0}{B_\lambda} \tag{B.5}$$

which can be substituted into equation (B.4) to get

$$v_{\parallel 0}^2 = v_{\perp \lambda}^2 \left(1 - \frac{B_0}{B_\lambda}\right) + v_{\parallel \lambda}^2 \tag{B.6}$$

Therefore,

$$f_\lambda(\mathbf{v}_\lambda) = \phi\left(\frac{v_{\perp \lambda}^2 \frac{B_0}{B_\lambda}}{T_{\perp 0}} + \frac{v_{\perp \lambda}^2(1 - \frac{B_0}{B_\lambda}) + v_{\parallel \lambda}^2}{T_{\parallel 0}}\right) \tag{B.7}$$

Defining

$$T_{\perp \lambda} = \frac{T_{\perp 0}}{T_{\perp 0}/T_{\parallel 0} + B_0/B_\lambda(1 - T_{\perp 0}/T_{\parallel 0})} \tag{B.8}$$

$$T_{\parallel \lambda} = T_{\parallel 0} \tag{B.9}$$

the distribution function at "λ" can be written into the same form as the distribution

function at "0" (equation (B.1)):

$$f_\lambda(\mathbf{v}_\lambda) = \phi\left(\frac{v_{\perp\lambda}^2}{T_{\perp\lambda}} + \frac{v_{\parallel\lambda}^2}{T_{\parallel\lambda}}\right) \tag{B.10}$$

We can obtain the number density at "0" and "λ" through

$$n_0 = \iiint_{\mathbf{v_0}} f_0(\mathbf{v}_0)\, d\mathbf{v}_0 = \iiint_{\mathbf{v_0}} \phi\left(\frac{v_{\perp 0}^2}{T_{\perp 0}} + \frac{v_{\parallel 0}^2}{T_{\parallel 0}}\right) d\mathbf{v}_0 \tag{B.11}$$

and

$$n_\lambda = \iiint_{\mathbf{v}_\lambda} f_\lambda(\mathbf{v}_\lambda)\, d\mathbf{v}_\lambda = \iiint_{\mathbf{v}_\lambda} \phi\left(\frac{v_{\perp\lambda}^2}{T_{\perp\lambda}} + \frac{v_{\parallel\lambda}^2}{T_{\parallel\lambda}}\right) d\mathbf{v}_\lambda \tag{B.12}$$

$f_0(\mathbf{v}_0)$ and $f_\lambda(\mathbf{v}_\lambda)$ are identical except that the velocities are scaled with different $\sqrt{T_\perp}$, given $T_{\parallel\lambda} = T_{\parallel 0}$. So the volumes wrapped by the distribution functions over velocity space, i.e., n_0 and n_λ, are different by a factor of $(\sqrt{T_{\perp 0}}/\sqrt{T_{\perp\lambda}})^2$, where the square accounts for the two perpendicular directions. Hence,

$$n_\lambda = \frac{T_{\perp\lambda}\sqrt{T_{\parallel\lambda}}}{T_{\perp 0}\sqrt{T_{\parallel 0}}} n_0 = \frac{T_{\perp\lambda}}{T_{\perp 0}} n_0 \tag{B.13}$$

Then we can rewrite n_λ with the help of (B.8) as

$$n_\lambda = \frac{n_0}{T_{\perp 0}/T_{\parallel 0} + B_0/B_\lambda(1 - T_{\perp 0}/T_{\parallel 0})} \tag{B.14}$$

Finally, using $p_{\parallel 0} = n_0 k T_{\parallel 0}$, $p_{\parallel\lambda} = n_\lambda k T_{\parallel\lambda}$, $p_{\perp 0} = n_0 k T_{\perp 0}$ and $p_{\perp\lambda} = n_\lambda k T_{\perp\lambda}$, we can express the number density, the parallel and perpendicular pressures at "λ" as

$$n_\lambda = \frac{n_0}{p_{\perp 0}/p_{\parallel 0} + B_0/B_\lambda(1 - p_{\perp 0}/p_{\parallel 0})} \tag{B.15}$$

$$p_{\parallel\lambda} = \frac{p_{\parallel 0}}{p_{\perp 0}/p_{\parallel 0} + B_0/B_\lambda(1 - p_{\perp 0}/p_{\parallel 0})} \tag{B.16}$$

$$p_{\perp\lambda} = \frac{p_{\perp 0}}{(p_{\perp 0}/p_{\parallel 0} + B_0/B_\lambda(1 - p_{\perp 0}/p_{\parallel 0}))^2} \tag{B.17}$$

The above relations, also given as equation (4.2), (4.3) and (4.4), agree with previous studies [*Spence et al.*, 1987; *Olsen et al.*, 1994; *Liemohn*, 2003; *Xiao and Feng*, 2006]. They are valid for any distribution function $\phi(x)$ with $x = v_\perp^2/T_\perp + v_\parallel^2/T_\parallel$ at the "minimum B" point of a closed field line.

B.2 Force Balance Along Closed Field Lines

We now show that the pressures given by (B.16) and (B.17) satisfy the force balance condition along closed field lines in anisotropic MHD. The force parallel to a field line at an arbitrary point λ is given by:

$$\mathbf{F}_{\parallel\lambda} = (p_{\parallel\lambda} - p_{\perp\lambda})B_\lambda \nabla_\parallel (B_\lambda^{-1}) + \nabla_\parallel p_{\parallel\lambda} \tag{B.18}$$

We can write (B.16) and (B.17) as $p_{\parallel\lambda} = p_{\parallel 0}/g$ and $p_{\perp\lambda} = p_{\perp 0}/g^2$, where $g = (p_{\perp 0}/p_{\parallel 0} + B_0/B_\lambda(1 - p_{\perp 0}/p_{\parallel 0}))$. Substituting into the first term of (B.18), we get

$$\begin{aligned}
(p_{\parallel\lambda} - p_{\perp\lambda})B_\lambda \nabla_\parallel (B_\lambda^{-1}) &= \left(\frac{p_{\parallel 0}}{g} - \frac{p_{\perp 0}}{g^2}\right) B_\lambda \nabla_\parallel (B_\lambda^{-1}) \\
&= \frac{(g p_{\parallel 0} - p_{\perp 0})B_\lambda}{g^2} \nabla_\parallel (B_\lambda^{-1}) \\
&= \frac{(p_{\parallel 0} - p_{\perp 0})B_0}{g^2} \nabla_\parallel (B_\lambda^{-1})
\end{aligned} \tag{B.19}$$

while the second term of (B.18) gives

$$\nabla_\parallel p_{\parallel\lambda} = -\frac{p_{\parallel 0}}{g^2} g'(B_\lambda^{-1}) \nabla_\parallel (B_\lambda^{-1}) = -\frac{(p_{\parallel 0} - p_{\perp 0})B_0}{g^2} \nabla_\parallel (B_\lambda^{-1}) \tag{B.20}$$

where we used the fact that B_λ is the only non-constant variable in g along the field line. (B.19) and (B.20) cancels out, thus the net force $\mathbf{F}_{\parallel\lambda}$ is zero. The force balance condition is achieved.

BIBLIOGRAPHY

BIBLIOGRAPHY

Abraham-Shrauner, B. (1967), Shock jump conditions for an anisotropic plasma, *Journal of Plasma Physics*, *1*(03), 379–381.

Anderson, B. J., S. A. Fuselier, S. P. Gary, and R. E. Denton (1994), Magnetic spectral signatures in the earth's magnetosheath and plasma depletion layer, *J. Geophys. Res.*, *99*(A4), 5877–5891, doi:10.1029/93JA02827.

Anderson, D., D. Decker, and C. Valladares (1996), Modeling boundary blobs using a time-varying convection model, *Geophys. Res. Lett.*

Angelopoulos, V., et al. (1994), Statistical characteristics of bursty bulk flow events, *J. Geophys. Res.*, *99*, 21,257.

Antonucci, E., M. A. Dodero, and S. Giordano (2000), Fast solar wind velocity in a polar coronal hole during solar minimum, *Sol. Phys.*, *197*, 115–134.

Baker, D. N., et al. (2013), A long-lived relativistic electron storage ring embedded in Earth's outer van allen belt, *Science*, doi:10.1126/science.1233518.

Baranov, V. B. (1970), Simple waves in a plasma with anisotropic pressure, *Fluid Dynamics*, *5*(2), 181–186.

Barnes, A. (1966), Collisionless damping of hydromagnetic waves, *Physics of Fluids*, *9*(8).

Baumjohann, W., and G. Pashmann (1989), Average plasma properties in the central plasma sheet, *J. Geophys. Res.*, *94*(A6), 6,597–6,606.

Birn, J., S. P. Gary, and M. Hesse (1995), Microscale anisotropy reduction and macroscale dynamics of the magnetotail, *J. Geophys. Res.*, *100*, 19,211.

Birn, J., et al. (2001), Geospace Environmental Modeling (GEM) magnetic reconnection challenge, *J. Geophys. Res.*, *106*(A3), 3715–3720, doi:10.1029/1999JA900449.

Boris, J. P. (1970), A physically motivated solution of the Alfvén problem, *Tech. Rep. NRL Memorandum Report 2167*, Naval Research Laboratory, Washington, D.C.

Buzulukova, N., M.-C. Fok, A. Pulkkinen, M. Kuznetsova, T. E. Moore, A. Glocer, P. C. Brandt, G. Toth, and L. Rastatter (2010), Dynamics of ring current and electric fields in the inner magnetosphere during disturbed periods: CRCM–BATS-R-US coupled model, *J. Geophys. Res.*, *115*, A05,210, doi:doi:10.1029/2009JA014621.

Chandran, B. D. G., T. J. Dennis, E. Quataert, and S. D. Bale (2011), Incorporating kinetic physics into a two-fluid solar-wind model with temperature anisotropy and low-frequency Alfvén-wave turbulence, *Astrophys. J.*, *743*, doi:10.1088/0004-637X/743/2/197.

Chandrasekhar, S., A. N. Kaufman, and K. M. Watson (1958), The stability of the pinch, *Proceedings of the Royal Society of London. Series A*, *245*, 435–455.

Chao, J. K., and B. Goldstein (1972), Modification of the rankine-hugoniot relations for shocks in space, *J. Geophys. Res.*, *77*(28), 5455–5466.

Chapman, S., and V. Ferraro (1930), A new theory of magnetic storms, *Nature*, *126*, 129–130.

Cheng, A. F. (1992a), A model of convection and corotation in Jupiter's magnetosphere: Ulysses predictions, *J. Geophys. Res.*, *19*, 221–224.

Cheng, C. Z. (1992b), Magnetospheric equilibrium with anisotropic pressure, *J. Geophys. Res.*, *97*, 1497–1510.

Chew, G. F., M. L. Goldberger, and F. E. Low (1956), The boltzmann equation and the one-fluid hydromagnetic equations in the absence of particle collisions, *Proceedings of the Royal Society of London. Series A, Mathematical and Physical Sciences*, *236*(1204), 112–118.

Cohen, O., et al. (2007), A semi-empirical magnetohydrodynamical model of the solar wind, *Astrophys. J.*, *654*, L163–L166, doi:10.1086/511154.

Crooker, N. U., G. L. Siscoe, and R. B. Geller (1976), Persistent pressure anisotropy in the subsonic magnetosheath region, *Geophys. Res. Lett.*, *3*(2), 65–68.

Daglis, I. A. (2001), The storm-time ring current, *Space Sci. Rev.*, *98*, 343–363.

Daglis, I. A. (2006), Ring current dynamics, *Space Sci. Rev.*, *124*, 183–202.

Daglis, I. A., R. M. Thorne, W. Baumjohann, and S. Orsini (1999), The terrestrial ring current: Origin, formation, and decay, *Reviews of Geophysics*, *37*, 407, doi: 10.1029/1999RG900009, (c) 1999: American Geophysical Union.

De Michelis, P., I. A. Daglis, and G. Consolini (1999), An average image of proton plasma pressure and of current systems in the equatorial plane derived from AMPTE/CCE-CHEM measurements, *J. Geophys. Res.*, *104*, 28,615–28,624.

De Zeeuw, D., S. Sazykin, R. Wolf, T. Gombosi, A. Ridley, and G. Tóth (2004), Coupling of a global MHD code and an inner magnetosphere model: Initial results, *J. Geophys. Res.*, *109*(A12), A12,219, doi:10.1029/2003JA010366.

De Zeeuw, D. L., T. I. Gombosi, C. P. T. Groth, K. G. Powell, and Q. F. Stout (2000), An adaptive MHD method for global space weather simulations, *IEEE Trans. Plasma Sci.*, *28*, 1956.

DeCoster, R. J., and L. A. Frank (1979), Observations pertaining to the dynamics of the plasma sheet, *J. Geophys. Res.*, *84*(A9), 5099–5121.

Denton, R. E., and J. G. Lyon (2000), Effect of pressure anisotropy on the structure of a two-dimensional magnetosheath, *J. Geophys. Res.*, *105*(A4), 7545–7556.

Denton, R. E., B. J. Anderson, S. P. Gary, and S. A. Fuselier (1994), Bounded anisotropy fluid model for ion temperatures, *J. Geophys. Res.*, *99*(A6), 11,225–11,241, doi:10.1029/95JA00656.

Dere, K. P., E. Landi, H. E. Mason, B. C. M. Fossi, and P. R. Young (1997), CHIANTI - an atomic database for emission lines, *Astron. Astrophys. Suppl. Ser.*, *125*, 149–173.

Erkaev, N. V., C. J. Farrugia, and H. K. Biernat (1999), Three-dimensional, one-fluid, ideal mhd model of magnetosheath flow with anisotropic pressure, *J. Geophys. Res.*, *104*(A4), 6877–6887.

Erkaev, N. V., D. F. Vogl, and H. K. Biernat (2000), Solution for jump conditions at fast shocks in an anisotropic magnetized plasma, *Journal of Plasma Physics*, *64*(05), 561–578, doi:10.1017/S002237780000893X.

Feldman, W. C., J. R. Asbridge, S. J. Bame, and M. D. Montgomery (1974), Interpenetrating solar wind streams, *Rev. Geophys. and Space Phys.*, *12*(4).

Fok, M., R. A. Wolf, R. W. Spiro, and T. E. Moore (2001), Comprehensive computational model of earth's ring current, *J. Geophys. Res.*, *106*(A5), 8,417–8,424.

Fok, M., T. E. Moore, P. C. Brandt, D. C. Delcourt, S. P. Slinker, and J. A. Fedder (2006), Impulsive enhancements of oxygen ions during substorms, *J. Geophys. Res.*, *111*, A10,222.

Gary, J., R. Heelis, and J. Thayer (1995), Summary of field-aligned poynting flux observations from de 2, *Geophys. Res. Lett.*, *22*, 1861.

Gary, S. P. (1976), Proton temperature anisotropy instabilities in the solar wind, *J. Geophys. Res.*, *81*(7).

Gary, S. P. (1992), The mirror and ion-cyclotron anisotropy instabilities, *J. Geophys. Res.*, *97*(A6), 8519–8529.

Gary, S. P., M. E. Mckean, and D. Winske (1993), Ion cyclotron anisotropy instabilities in the magnetosheath: Theory and simulations, *J. Geophys. Res.*, *98*(A3), 3963–3971.

Gary, S. P., M. E. Mckean, D. Winske, B. J. Anderson, R. E. Denton, and S. A. Fuselier (1994), The protom cyclotron instability and the anistotropy/beta-inverse correlation, *J. Geophys. Res.*, *99*(A4), 5903–5914, doi:10.1029/93JA03583.

Gary, S. P., H. Li, S. O'Rourke, and D. Winske (1998), Proton resonant firehose instability: Temperature anisotropy and fluctuating field constraints, *J. Geophys. Res.*, *103*(A7), 14,567–14,574.

Gary, S. P., R. M. Skoug, and J. T. Steinberg (2001), Proton temperature anisotropy constraint in the solar wind: ACE observations, *Geophys. Res. Lett.*, *28*(14), 2759–2762.

Gary, S. P., B. E. Goldstein, and M. Neugebauer (2002), Signatures of wave-ion interactions in the solar wind: Ulysses observations, *J. Geophys. Res.*, *107*(A8), 1169, doi:10.1029/2001JA000269.

Glocer, A., M. Fok, X. Meng, G. Tóth, N. Buzulukova, S. Chen, and K. Lin (2012), CRCM + BATS-R-US two way coupling, *J. Geophys. Res.*, submitted.

Godunov, S. K. (1959), A difference scheme for numerical computation of discontinuous solutions of hydrodynamic equations, *Mat. Sb.*, *47*(3), 271–306, (in Russian).

Gombosi, T., and C. Rasmussen (1991), Transport of gyration-dominated space plasmas of thermal origin I - generalized transport equations, *J. Geophys. Res.*, *96*, 7759–7778, doi:10.1029/91JA00012.

Gombosi, T. I. (1991), The plasma environment of comets, *Rev. Geophys.*, *29*, 976.

Gombosi, T. I., G. Tóth, D. L. De Zeeuw, K. C. Hansen, K. Kabin, and K. G. Powell (2002), Semirelativistic magnetohydrodynamics and physics-based convergence acceleration, *J. Comput. Phys.*, *177*, 176–205, doi:10.1006/jcph.2002.7009.

Gombosi, T. I., et al. (2004), Solution-adaptive magnetohydrodynamics for space plasmas: Sun-to-Earth simulations, *Computing in Science and Engineering*, *06*(2), 14–35.

Hall, A. N. (1979), Finite ion larmor radius modifications to the firehose and mirror instabilities, *Journal of Plasma Physics*, *21*, 431–443.

Hall, A. N. (1980), On the origin of long time-scale pulsar scintillations - ii. growth of the mirror instability, and non-linear amplitude limitation, *Mon. Not. R. astr. Soc.*, *190*, 371–383.

Hall, A. N. (1981), The firehose instability in interstellar space, *Mon. Not. R. astr. Soc.*, *195*, 685–696.

Harten, A., P. D. Lax, and B. van Leer (1983), On upstream differencing and Godunov-type schemes for hyperbolic conservation laws, *SIAM Rev.*, *25*(1), 35–61.

Hau, L. N., and B. U. O. Sonnerup (1993), On slow-mode waves in an anisotropic plasma, *Geophys Res Lett*, *20*(17), 1763–1766, doi:10.1029/93GL01706.

Hau, L. N., T. D. Phan, B. U. O. Sonnerup, and G. Paschmann (1993), Double-polytropic closure in the magnetisheath, *Geophys Res Lett*, *20*(20), 2255–2258, doi:10.1029/93GL02491.

Heinemann, M., and R. A. Wolf (2001), Relationships of models of the inner magnetosphere to the rice convection model, *J. Geophys. Res.*, *106*(A8), 15,545 – 15,554.

Hellinger, P., O. Trávníček, J. C. Kasper, and A. J. Lazarus (2006), Solar wind proton temperature anisotropy: Linear theory and WIND/SWE observations, *Geophys. Res. Lett.*, *33*(L09101), doi:10.1029/2006GL025925.

Hesse, M., and J. Birn (1992), MHD modeling of magneototail instability for anisotropic pressure, *J. Geophys. Res.*, *97*, 10,643–10,654.

Horton, W., L. Cheung, J.-Y. Kim, and T. Tajima (1993), Self-consisent plasma pressure tensors from the tsyganenko magnetic field models, *J. Geophys. Res.*, *98*(A10), 17,327–17,343.

Hu, B., F. R. Toffoletto, R. A. Wolf, S. Sazykin, J. Raeder, D. Larson, and A. Vapirev (2010), One-way coupled OpenGGCM/RCM simulation of the 23 March 2007 substorm event, *J. Geophys. Res.*, *115*, A12,205.

Hu, Y. Q., R. Esser, and S. R. Habbal (1997), A fast solar wind model with anisotropic proton temperature., *J. Geophys. Res.*, *102*, 14,661–14,676.

Hudson, P. D. (1970), Discontinuities in an anisotropic plasma and their identification in the solar wind, *Planet. Space Sci.*, *18*, 1611–1622.

Hundhausen, A. J. (1968), Direct observations of solar-wind particles, *Space Sci. Rev.*, *8*, 690–749.

Jordanova, V. K., J. U. Kozyra, A. F. Nagy, and G. V. Khazanov (1997), Kinetic model of the ring current - atmosphere interactions, *J. Geophys. Res.*, *102*, 14,279.

Kasper, J. C., A. J. Lazarus, S. P. Gary, and A. Szabo (2003), Solar wind temperature anisotropies, in *Solar wind ten: proceedings of the tenth international solar wind conference*, edited by M. Velli, R. Bruno, and F. Malara, pp. 538–541, AIP.

Kennel, C. F., and H. E. Petschek (1966), Limit on stably trapped particle fluxes, *J. Geophys. Res.*, *71*(1).

Kivelson, M. G., and C. T. Russell (Eds.) (1995), *Introduction to Space Physics*, Cambridge University Press, Cambridge, UK.

Kohl, J. L., et al. (1998), UVCS/SOHO empirical determinations of anisotropic velocity distributions in the solar corona, *Astrophys. J.*, *501*, L127–L131.

Kohl, J. L., G. Noci, S. R. Cranmer, and J. C. Raymond (2006), Ultraviolet spectroscopy of the extended solar corona, *Astron. Astrophys. Rev.*, *13*, 31–157.

Koren, B. (1993), A robust upwind discretisation method for advection, diffusion and source terms, in *Numerical Methods for Advection-Diffusion Problems*, edited by C. Vreugdenhil and B.Koren, p. 117, Vieweg, Braunschweig.

Kulsrud, R. M. (1982), Mhd description of plasma, in *Handbook of Plasma Physics Volume I: Basic Plasma Physics 1*, edited by A. A. Galeev and R. N. Sudan, North-Holland Publishing Company.

Lazar, M., and S. Poedts (2009a), Limits for the firehose instability in space plasmas, *Sol Phys*, *258*(1), 119–128.

Lazar, M., and S. Poedts (2009b), Firehose instability in space plasmas with bi-kappa distributions, *A&A*, *494*(1), 311–315.

Leer, E., and W. I. Axford (1972), A two-fluid solar wind model with anisotropic proton temperature, *Sol. Phys.*, *23*, 238–250.

Li, B., X. Li, Y.-Q. Hu, and S. R. Habbal (2004), A two-dimensional Alfvén wave-driven solar wind model with proton temperature anisotropy, *J. Geophys. Res.*, *109*(A07103), doi:10.1029/2003JA010313.

Li, X. (1999), Proton temperature anisotropy in the fast solar wind: A 16-moment bi-Maxwellian model, *J. Geophys. Res.*, *104*(A9), 19,773–19,785.

Li, X., S. R. Habbal, J. L. Kohl, and G. Noci (1998), The effect of temperature anisotropy on observations of doppler dimming and pumping in the inner corona, *Astrophys. J.*, *501*, L133–L137.

Liemohn, M. W. (2003), Yet another caveat to the Dessler-Parker-Sckopke relation, *J. Geophys. Res.*, *108*(A6), doi:10.1029/2003JA009839.

Lucek, E. A., D. Constantinescu, M. L. Goldstein, J. Pickett, J. L. Pincon, F. Sahraoui, R. A. Treumann, and S. N. Walker (2005), The magnetosheath, *Space Sci. Rev.*, *118*, 95–152.

Lui, A., and D. Hamilton (1992), Radial profiles of quiet time magnetospheric parameters, *J. Geophys. Res.*, *97*, 19,325.

Lui, A. T. Y., H. E. Spence, and D. P. Stern (1994), Empirical modeling of the quiet time nightside magnetosphere, *J. Geophys. Res.*, *99*, 151–157.

Lynn, Y. M. (1967), Discontinuities in an anisotropic plasma, *Physics of Fluids*, *10*, 2278.

Lyon, J., J. Fedder, and C. Mobarry (2004), The Lyon-Fedder-Mobarry (LFM) global MHD magnetospheric simulation code, *J. Atmos. Sol-Terr. Phys.*, *66*, 1333.

Lyu, L. H., and J. R. Kan (1986), Shock jump conditions modified by pressure anisotropy and heat flux for earth's bowshock, *J. Geophys. Res.*, *91*(6), 6771–6775.

Märk, E. (1974), Growth rates of the ion cyclotron instability in the magnetosphere, *J. Geophys. Res.*, *79*(22), 3218–3220.

Marsch, E., K.-H. Mühlhäuser, R. Schwenn, H. Rosenbauer, W. Pilipp, and F. M. Neubauer (1982), Solar wind protons: Three-dimensional velocity distributions and derived plasma parameters measured between 0.3 and 1 AU, *J. Geophys. Res.*, *87*(A1), 52–72.

Marsch, E., X.-Z. Ao, and C.-Y. Tu (2004), On the temperature anisotropy of the core part of the proton velocity distribution function in the solar wind, *J. Geophys. Res.*, *109*(A04102), doi:10.1029/2003JA010330.

Meng, X., G. Tóth, I. V. Sokolov, and T. I. Gombosi (2012a), Classical and semirelativistic magnetohydrodynamics with anisotropic ion pressure, *J. Comput. Phys.*, *231*, 3610–3622, doi:10.1016/j.jcp.2011.12.042.

Meng, X., G. Tóth, M. W. Liemohn, T. I. Gombosi, and A. Runov (2012b), Pressure anisotropy in global magnetospheric simulations: A magnetohydrodynamics model, *J. Geophys. Res.*, *117*, A08,216, doi:10.1029/2012JA017791.

Miyoshi, T., and K. Kusano (2005), A multi-state HLL approximate Riemann solver for ideal magnetohydrodynamics, *J. Comput. Phys.*, *208*, 315–344, doi:10.1016/j.jcp.2005.02.017.

Moore, T. E., M. Fok, D. C. Delcourt, S. P. Slinker, and J. A. Fedder (2008), Plasma plume circulation and impact in an MHD substorm, *J. Geophys. Res.*, *113*, A06,219.

Neubauer, F. (1970), Jump relations for shocks in an anisotropic plasma, *Z. Physik*, *237*, 205–223.

Olsen, R. C., L. J. Scott, and S. A. Boardsen (1994), Comparison between liouville's theorem and observed latitudinal distributions of trapped ions in the plasmapause region, *J. Geophys. Res.*, *99*(A2), 2191–2203.

Pembroke, A., F. Toffoletto, S. Sazykin, M. Wiltberger, J. Lyon, V. Merkin, and P. Schmitt (2012), Initial results from a dynamic coupled magnetosphere-ionosphere-ring current model, *J. Geophys. Res.*, *117*, A02,211.

Phan, T.-D., G.Paschmann, W. Baumjohann, and N.Sckopke (1994), The magnetosheath region adjacent to the dayside magnetopause: AMPTE/IRM observations, *J. Geophys. Res.*, *99*(A1), 121–141.

Pokhotelov, O. A., R. Z. Sagdeev, M. A. Balikhim, and R. A. Treumann (2004), Mirror instability at finite ion-larmor radius wavelengths, *J. Geophys. Res.*, *109*(A9).

Powell, K., P. Roe, T. Linde, T. Gombosi, and D. L. De Zeeuw (1999), A solution-adaptive upwind scheme for ideal magnetohydrodynamics, *J. Comp. Phys.*, *154*, 284–309.

Pudovkin, M. I., S. A. Zaitseva, L. L. Lebedeva, A. A. Samsonov, B. P. Besser, and C. V. Meister (2002), Some problems of magnetosheath physics, *International Journal of Geomagnetism and Aeronomy*, *3*(2), 93–107.

Raeder, J., et al. (2001), Global simulation of the Geospace Environment Modeling substorm challenge event, *J. Geophys. Res.*, *106*, 281.

Ridley, A., T. Gombosi, and D. Dezeeuw (2004), Ionospheric control of the magnetosphere: conductance, *Annales Geophysicae*, *22*, 567–584.

Roe, P. L. (1981), Approximate Riemann solvers, parameter vectors, and difference schemes, *J. Comput. Phys.*, *43*, 357–372.

Rusanov, V. (1961), Calculation of interaction of non-steady schock waves with obstacles, *J. Comp. Math. and Phys.*, *1*, 267.

Russell, C. T. (1972), The configuration of the magnetosphere, in *Critical Problems of Magnetospheric Physics*, edited by E. R. Dyer, pp. 1–16, National Academy of Sciences, Washington, D.C.

Russell, C. T. (Ed.) (1994), *The magnetosheath: Advances in Space Research*, vol. 14, Pergamon Press, Oxford.

Russell, C. T., R. C. Snare, J. D. Means, D. Pierce, D. Dearborn, M. Larson, G. Barr, and G. Le (1995), The GGS/POLAR magnetic fields investigations, *Space Sci. Rev.*, *71*, 563–582.

Samsonov, A. A., and M. I. Pudovkin (2000), Application of the bounded anisotropy model for the dayside magnetosheath, *J. Geophys. Res.*, *105*(A6), 12,859–12,867.

Samsonov, A. A., M. I. Pudovkin, S. P. Gary, and D. Hubert (2001), Anisotropic mhd model of the dayside magnetosheath downstream of the oblique bow shock, *J. Geophys. Res.*, *106*, 21,689.

Samsonov, A. A., O. Alexandrova, C. Lacombe, M. Maksimovic, and S. P. Gary (2007), Proton temperature anisotropy in the magnetosheath: comparison of 3-d mhd modelling with cluster data, *Ann. Geophys.*, *25*, 1157.

Sheldon, R. B., and D. C. Hamilton (1993), Ion transport and loss in the earth's quiet ring current 1. data and standard model, *J. Geophys. Res.*, *98*(A8), 13,491–135,08.

Shi, Y., L. C. Lee, and Z. F. Fu (1987), A study of tearing instability in the presence of a pressure anisotropy, *J. Geophys. Res.*, *92*(A11), 12,171–12,179.

Shoji, M., Y. Omura, B. T. Tsurutani, O. P. Verkhoglyadova, and B. Lembege (2009), Mirror instability and l-mode electromagnetic ion cyclotron instability: Competition in the earth's magnetosheath, *J. Geophys. Res.*, *114*.

Sokolov, I., E. V. Timofeev, J. Sakai, and K. Takayama (2002), Artificial wind – a new framework to construct simple and efficient upwind shock-capturing schemes, *J. Comput. Phys.*, *181*, 354–393, doi:10.1006/jcph.2002.7130.

Sokolov, I. V., K. G. Powell, and T. I. G. aand I. I. Roussev (2006), A TVD principle and conservative TVD schemes for adaptive Cartesian grids, *J. Comput. Phys.*, *220*, 1–5, doi:10.1016/j.jcp.2006.07.021.

Sokolov, I. V., B. van der Holst, R. Oran, C. Downs, I. I. Roussev, M. Jin, W. B. Manchester, R. M. Evans, and T. I. Gombosi (2013), Magnetohydrodynamic waves and coronal heating: Unifying empirical and MHD turbulence models, *Astrophys. J.*, *764*(1), doi:10.1088/0004-637X/764/1/23.

Song, P., and C. T. Russell (1997), What do we really know about the magnetosheath?, *Advances in Space Research*, *20*, 747–765.

Soper, G. K., and E. G. Harris (1965), Effect of finite ion and electron temperatures on the ion-cyclotron resonance instability, *Phys. Fluids*, *8*(5).

Southwood, D. J., and M. G. Kivelson (1993), Mirror instability: 1. physical mechanism of linear instability, *J. Geophys. Res.*, *98*, 9181–9187.

Spence, H. E., M. G. Kivelson, and R. J. Walker (1987), Static magnetic field models consistent with nearly isotropic plasma pressure, *Geophys. Res. Lett.*, *14*(8), 872–875.

Tajiri, M. (1967), Propagation of hydromagnetic waves in collisionless plasma, ii, kinetic approach, *J. Phys. Soc. Japan*, *22*(6).

Takahashi, K., and J. E. W. Hones (1988), ISEE 1 and 2 observations of ion distributions at the plasma sheet-tail lobe boundary, *J. Geophys. Res.*, *93*(A8), 8558–8582.

Telloni, D., E. Antonucci, and M. A. Dodero (2007), Oxygen temperature anisotropy and solar wind heating above coronal holes out to 5 $R_{\odot}$, *Astron. Astrophys.*, *476*, 1341–1346.

Toffoletto, F., S. Sazykin, R. Spiro, and R. Wolf (2003), Inner magnetospheric modeling with the Rice Convection Model, *Space Sci. Rev.*, *107*, 175–196.

Toffoletto, F., S. Sazykin, R. Spiro, R. Wolf, and J. Lyon (2004), RCM meets LFM: initial results of one-way coupling, *J. Atmos. Sol-Terr. Phys.*, *66*, 1361.

Tóth, G., et al. (2005), Space Weather Modeling Framework: A new tool for the space science community, *J. Geophys. Res.*, *110*, A12,226, doi:10.1029/2005JA011126.

Tóth, G., D. L. De Zeeuw, T. I. Gombosi, and K. G. Powell (2006), A parallel explicit/implicit time stepping scheme on block-adaptive grids, *J. Comput. Phys.*, *217*, 722–758, doi:10.1016/j.jcp.2006.01.029.

Tóth, G., X. Meng, T. I. Gombosi, and A. Ridley (2011), Reducing numerical diffusion in magnetospheric simulations, *J. Geophys. Res.*, *116*, A07,211, doi: 10.1029/2010JA016370.

Tóth, G., et al. (2012), Adaptive numerical algorithms in space weather modeling, *J. Comput. Phys.*, *231*, doi:10.1016/j.jcp.2011.02.006.

van der Holst, B., W. M. IV, R. Frazin, A. Vásquez, G. Tóth, and T. Gombosi (2010), A data-driven, two-temperature solar wind model with alfvén waves, *Astrophys. J.*, *725*, 1373–1383, doi:10.1088/0004-637X/725/1/1373.

Vogl, D. F., H. K. Biernat, N. V. Erkaev, C. J. Farrugia, and S. Mühlbachler (2001a), Jump conditions for pressure anisotropy and comparison with the earth's bow shock, *Nonlinear Proc Geoph*, *8*(3), 167–174.

Vogl, D. F., N. V. Erkaev, H. K. Biernat, S. Mühlbachler, and C. J. Farrugia (2001b), Jump conditions at fast shocks in an anisotropic magnetized plasma, *Advances in Space Research*, *28*(6), 851–856, doi:10.1016/S0273-1177(01)00503-8.

Walsh, A. P., C. J. Owen, A. N. Fazakerley, C. Forsyth, and I. Dandouras (2011), Average magnetotail electron and proton pitch angle distributions from Cluster PEACE and CIS observations, *Geophys. Res. Lett.*, *38*, L06,103.

Whang, Y. C. (1972), A solar-wind model including proton thermal anisotropy, *Astrophys. J.*, *178*, 221–239.

Wolf, R. A., Y. Wan, X. Xing, J.-C. Zhang, and S. Sazykin (2009), Entropy and plasma sheet transport, *J. Geophys. Res.*, *114*, A00D05, doi: 10.1029/2009JA014044.

Wu, L., F. Toffoletto, R. A. Wolf, and C. Lemon (2009), Computing magnetospheric equilibria with anisotropic pressures, *J. Geophys. Res.*, *114*(A5), A05,213.

Xiao, F., and X. Feng (2006), Modeling density and anisotropy of energetic electrons along magnetic field lines, *Plasma Science and Technology*, *8*(3).

Zaharia, S., C. Z. Cheng, and K. Maezawa (2004), 3-d force-balanced magnetospheric configurations, *Ann. Geophys.*, *22*, 251–266.

Zaharia, S., M. F. Thomsen, J. Birn, M. H. Denton, V. K. Jordanova, and C. Z. Cheng (2005), Effect of storm-time plasma pressure on the magnetic field in the inner magnetosphere, *Geophys. Res. Lett.*, *32*, L03,102.

Zwan, B. J., and R. A. Wolf (1976), Depletion of solar wind plasma near a planetary boundary, *J. Geophys. Res.*, *81*(10), 1636–1648.